

DURVILLE CASTING OF NICKEL-IRON VALVE BARS

by

JASON DAVID SWAN

A Thesis Submitted to the University of Birmingham for the Degree  
of DOCTOR OF PHILOSOPHY

School of Metallurgy and Materials  
The University of Birmingham  
Edgbaston  
Birmingham  
B15 2TT  
United Kingdom  
2014

UNIVERSITY OF  
BIRMINGHAM

**University of Birmingham Research Archive**

**e-theses repository**

This unpublished thesis/dissertation is copyright of the author and/or third parties. The intellectual property rights of the author or third parties in respect of this work are as defined by The Copyright Designs and Patents Act 1988 or as modified by any successor legislation.

Any use made of information contained in this thesis/dissertation must be in accordance with that legislation and must be properly acknowledged. Further distribution or reproduction in any format is prohibited without the permission of the copyright holder.

## Abstract

The production of valve bars by the Durville tilt casting process has various manufacturing stages. As a wrought product it is initially cast as a larger diameter, within a mould, where it is allowed to solidify before further thermo-mechanical work. The formation of an air-gap at the casting-mould interface during solidification significantly affects local cooling rates and the magnitude of heat transfer mechanisms; this gap was investigated experimentally and numerically for the aluminium alloy, LM25, and a nickel-iron alloy XD1102.

A numerical model has been used to predict the size of the air-gap and the temperature distribution along the metal-mould interface given an initial Interfacial Heat Transfer Coefficient. Validation of the numerical model was conducted experimentally by measuring the thickness of the air-gap during solidification using optical techniques and also temperatures within the mould and casting using thermocouples. Agreement between the numerical, ProCAST, model and experimental results gives some confidence in the model's ability to predict the magnitude of the air-gap and temperature distribution in new situations.

Valve bar ingots of XD1102 were extruded after dwelling in an air furnace held at the extrusion temperature prior to ingot loading; however, these conditions have proved problematic for some ingots in which cracks have been observed across their bases. After extrusion, a large longitudinal split was observed running down the front of many of the bars. SEM and EDX analysis around and beyond the split

were conducted, and the structure of the oxide skin formed during pre-heating was characterised.

After extrusion the bars are hot rolled with a total length reduction ratio close to 1:200 from the as-cast ingot. Due to this combined large amount of work received, it has been discussed whether a turbulent-free filling of a mould is beneficial over a simple top pouring. Emphasis is focused on oxides and if the amount of work received to the ingot is sufficient to prevent the deleterious effects oxides usually have on cast structures. The statistical approach of the Weibull modulus is used to evaluate the two casting techniques.

*The one who follows the crowd will usually go no further than the crowd.  
The one who walks alone is likely to find himself in places no one has ever  
been before*

*Albert Einstein*

# ACKNOWLEDGEMENTS

---

I would like to express my gratitude to my supervisor, Dr R M Ward, for his invaluable support over my three years at the University of Birmingham. He has always been there providing his help and guidance throughout my studies no matter what time of the day. In particular he showed patience as I made the transition from a Mechanical Engineering undergraduate degree into the field of Metallurgy and Materials.

Secondly, a thank you to my co-supervisor Professor Roger Reed for having faith in me from the beginning and giving me the opportunity to further my studies at the university. On Roger's departure to the University of Oxford, Dr W D Griffiths kindly provided his wealth of knowledge in the casting and solidification of alloys, so a big thank you goes to him.

On a practical note I am indebted to Mr Adrian Caden and Mr Peter Cranmer for their guidance and expertise within the foundry, and an always enjoyable Christmas meal.

A special thank you goes to Precision Castparts Corporation for making this PhD possible and to Special Metals Wiggin Limited with their industrial capability.

A final thank you to my partner, Kate, for her unquestionable support throughout the difficult times.

# Table of Contents

---

Chapter 1.	Introduction.....	1
Chapter 2.	Durville Tilt Casting .....	4
2.1	Introduction.....	4
2.2	Durville Tilt Casting at SMWL .....	4
2.2.1	Induction Furnace .....	6
2.2.2	Ladle .....	6
2.2.3	Durville Tilt Casting Machine .....	6
2.2.4	Receiver .....	7
2.2.5	Vermiculite .....	8
2.2.6	Tilting.....	8
2.2.7	Moulds .....	9
2.2.8	Bitop.....	10
2.2.9	Post Processing .....	10
2.3	Alloy XD1102.....	13
2.3.1	Thermo-Calc Predictions .....	16
2.3.2	Alloy XD1102 Characteristics .....	17
Chapter 3.	Solidification Theory .....	23
3.1.1	Undercooling.....	23
3.1.2	Constitutional Undercooling.....	24

3.1.3	Curvature undercooling .....	26
3.1.4	Thermal Undercooling .....	27
3.1.5	Kinetic Undercooling .....	27
3.1.6	Pressure Undercooling .....	27
3.1.7	Undercooling Combined .....	28
3.1.8	Grain Nucleation .....	28
3.1.9	Growth Kinetics: .....	31
3.1.10	Solute Redistribution Models .....	32
3.1.11	Effect of Solidification Rate .....	33
Chapter 4.	Air-Gap Formation and Heat Transfer between Casting and Mould Interface	35
4.1	Introduction .....	35
4.2	Experimental Set-Up .....	39
4.3	Temperature and Displacement Results for LM25 .....	44
4.3.1	Calculations of IHTC .....	49
4.3.2	Radiative to Conductive Ratio, $Q_r:Q_c$ .....	50
4.3.3	Including a Numerical Model – ProCAST .....	51
4.3.3.1	Mesh Size Sensitivity Study .....	55
4.3.3.2	Stress Sensitivity Study .....	57
4.3.3.3	Inputs into the Model .....	58
4.4	Temperature and Displacements Results for XD1102 .....	69



4.4.1	Q <sub>r</sub> to Q <sub>c</sub> Ratio.....	72
4.5	Comparing the Two Alloys Cast.....	73
4.6	Emissivity Trials for Improved Simulation Data, XD1102.....	74
4.6.1	Experimental Process.....	75
4.6.2	ProCAST Simulations.....	76
4.7	Conclusions.....	81
4.8	Future Work.....	83
Chapter 5.	Valve Bar Feature – Identification, Origin, Root Cause Analysis and Mitigation	86
5.1	Introduction.....	86
5.2	The Valve Bar Feature.....	88
5.3	Extruded Bar “Crocodile“.....	90
5.3.1	Metallographic Technique.....	90
5.3.2	Section 1: Start of Crack.....	91
5.3.3	Section 2: Middle of Crack.....	93
5.3.4	Section 3: Crack Tip.....	95
5.3.5	Section 4: Sub Crocodile Crack 1.....	96
5.3.6	Section 5: Sub Crocodile Crack 2.....	99
5.4	Oxidation of an Non-Extruded Sample.....	100
5.4.1	Surface Oxidation.....	100
5.4.2	Treating a Lap Defect as a Crack.....	103

5.5	Analysis of Thermal Shocked Ingot .....	104
5.5.1	Longitudinal Crack – “Primary” .....	104
5.6	Crack Formation Hypothesis .....	110
5.6.1	ProCAST .....	111
5.7	Circumferential “Secondary” Crack .....	114
5.8	Conclusions.....	116
5.9	Future Work.....	117
Chapter 6.	Is the Bifilm Defect Detrimental to Wrought Product? .....	119
6.1	Introduction.....	119
6.2	Entrainment of Oxides in the Production of XD1102 ingots.....	122
6.2.1	Dip Sample.....	124
6.2.2	Entrainment within the Durville Machine .....	127
6.2.3	Cast Ingot Slice .....	130
6.2.4	Ingot After Extrusion Pre-Heat – But not Extruded .....	133
6.2.5	Forward.....	133
6.3	Casting Trials.....	134
6.3.1	Method .....	134
6.3.2	Results.....	137
6.4	Investigation into the Differences in Strength between Casting Methods 144	
6.4.1	Chemistry.....	144

6.4.2	Fractured Surface .....	145
6.4.3	Carbides .....	148
6.5	Conclusions.....	162
6.6	Future Work .....	164
6.6.1	Nucleation on Oxides True Cause for Increased Strength? .....	165
6.6.2	Chemistry Alterations .....	165
Chapter 7.	Final Remarks .....	170
Appendix A.	Oxidation of a Lap Defect.....	173
A.1.1	Experimental Set-Up.....	173
A.1.2	Results.....	174
Appendix B.	MATLAB.....	179
B.1	Introduction.....	179
B.2	Converting Thermocouple Voltage into Temperature.....	179
B.3	Prediction of the Mould's Inner Surface Temperature .....	182
B.4	Air and Water Quenching of the XD1102 at SMWL .....	186
B.5	Sub functions of the Code.....	192
B.6	Possible Extension to the MATLAB Code .....	198
Appendix C.	ProCAST Run Parameters .....	199
REFERENCES	.....	200

# LIST OF FIGURES

Figure 2-1 - The Durville tilt casting process at Special Metals Wiggin Limited, Hereford.....	5
Figure 2-2 Durville tilt casting machine at SMWL.....	7
Figure 2-3 – Cross-section of a SMWL mould .....	9
Figure 2-4 – Schematic of four different types of flow patterns during extrusion (Kurt and Helmut, 1976).....	11
Figure 2-5 – Fe-Ni-Cr ternary phase diagram at a) 1050°C and b) 650°C (Pickering, 1976).....	15
Figure 2-6 – Fe-Ni-Cr-Nb quaternary phase diagram at 1200 °C (Takeyama et al., 2001).....	15
Figure 2-7 – Thermo-Calc phase predictions for XD1102.....	16
Figure 2-8 – Interdendritic carbides in an as-cast ingot of XD1102 .....	20
Figure 2-9 – Time-temperature transformation diagram in IN-718 (Donachie, 2002) ..	21
Figure 3-1 – Linearised phase diagram displaying the solid and liquid solute compositions (Chilton, 2002) .....	25
Figure 3-2 – Formation of a constitutionally undercooled region (dashed area) in the liquid next to the solid/liquid interface because of lower liquidus temperature produced by the higher solute content. (Stefanescu and Ruxanda, 2004).....	26
Figure 3-3 – Effects of different mechanisms of undercooling during solidification in a linearised binary phase diagram (Kurz and Fisher, 1998).....	28
Figure 3-4 – Gibbs free energy change associated with homogeneous nucleation with a spherical shape (Kurz and Fisher, 1998) .....	29

Figure 3-5 – Schematic diagram displaying the heterogeneous nucleation of a nuclei (Kurz and Fisher, 1998).....	30
Figure 3-6 – Solute redistribution during equilibrium solidification: (a) at the start of solidification, (b) at temperature $T^*$ , (c) when solidification is complete, (d) the corresponding phase diagram (Flemings, 1974).....	32
Figure 3-7 – An construct demonstrating the partitioning of liquid from the interface to the liquid in the Gulliver-Scheil model of segregation (Dantzig and Rappaz, 2009). ...	33
Figure 4-1 – Metal–mould interface at an early stage when solid is nucleating at points of good thermal contact. Overall macroscopic contact is good at this stage (a). Later (b) the casting gains strength, and casting and mould both deform, reducing contact to isolated points at greater separations on non-conforming rigid surfaces (Campbell, 2011b).....	37
Figure 4-1 – Schematic diagrams displaying the dimensions of the H13 steel mould used during the air-gap experiments and the laser triangulation and tungsten rod set up to capture the displacement of the melt. ....	42
Figure 4-2 – Thermocouple locations set into the mould wall at 3, 10 and 18 mm from the moulds outer surface.....	42
Figure 4-3 – Photograph of the air-gap experimental set-up displaying the mould and housings for the laser triangulation sensors sitting on top of the slab of fireclay. ....	43
Figure 4-4 – Photograph of the air-gap experiments displaying the internal configuration of the Type K melt thermocouple and the protruding tungsten rod. ....	43
Figure 4-5 – Graph to show the first 500 seconds of the measured temperature readings for the LM25 casting. ....	44

Figure 4-6 – Graph to show the first 500 seconds of the measured experimental displacements for the LM25 casting.....	44
Figure 4-7 – Graph to show the full length of experimental temperature readings for the LM25 casting.....	46
Figure 4-8 – Graph to show the full length of experimental displacement readings for the LM25 casting.....	46
Figure 4-9 – Graph to show the predictions of the internal moulds surface temperature for the first 500 seconds using the inverse, finite difference and extrapolation techniques.....	48
Figure 4-10 – Graph to show the fluctuations of $\pm 5^{\circ}\text{C}$ when using the finite difference method.....	49
Figure 4-11 – Graph to show the calculated interfacial heat transfer coefficient for the LM25 casting.....	50
Figure 4-12 – Graph to show the ratio of radiative to conductive heat transfer with the size of air-gap for the LM25 casting. ....	51
Figure 4-13 – Screen shot of the 4 mm surface mesh used on the H13 mould .....	52
Figure 4-14 – Mesh sensitivity study graphically showing the predicted mould temperatures for the LM25 casting using ProCAST with a constant tetrahedral mesh size of 2, 4, 8 and 16 mm.....	57
Figure 4-15 – Percentage deviation of the 4, 8 and 16 mm mesh sizes in comparison to the 2 mm mesh size. After 911 seconds the computer shut down for the 2 mm mesh and hence the values start to diverge beyond this point.....	57

Figure 4-16 – Stress sensitivity study graphically showing the predicted air-gap for the LM25 casting using ProCAST with a constant tetrahedral mesh size of 4 mm and the elastic, elastic-plastic and visco-elastic plastic stress models. ....	58
Figure 4-17 – Time steps taken from ProCAST simulation (left) and the casting experiment (right) for LM25 casting. ....	63
Figure 4-18 – Illustration to show the locations of nodes selected in ProCAST for the extraction of predicted temperatures within the mould’s wall and melt concurring with experimental locations. ....	64
Figure 4-19 – Graph to show the ProCAST temperature predictions (dashed lines) and the experimental measurements of the thermocouples 10 and 18 mm within the mould wall and the melt thermocouples for the LM25 casting. ....	65
Figure 4-20 – Graph to show the ProCAST air-gap predictions (dashed lines) and the experimentally measured air-gap for the LM25 casting. ....	65
Figure 4-21 – Photograph to show the location of thermocouple tip solidified within the LM25 casting. ....	67
Figure 4-22 – Graph to show the comparison of the predicted interfacial heat transfer coefficient using ProCAST and the calculated values from the LM25 casting. ....	68
Figure 4-23 – Graph to show the full length of experimental temperature readings for the XD1102 casting. ....	70
Figure 4-24 – Graph to show the full length of experimental displacement measurements and the magnitude of the air-gap for the XD1102 casting. ....	71
Figure 4-25 – Graph to show the calculated IHTC for the experimental XD1102 casting. ....	72

Figure 4-26 – Graph to show the ratio of radiative to conductive heat transfer with the size of air-gap for the XD1102 casting.....	72
Figure 4-27 – Thermal image of the as-cast XD1102 at temperature. ....	75
Figure 4-28 – Graph to show the measured emissivity of XD1102 up to 700°C .....	76
Figure 4-29 - Graph to show the ProCAST temperature predictions (solid lines) and the experimental measurements of the thermocouples 10 and 18 mm within the mould wall and the melt thermocouple for the XD1102 casting.....	77
Figure 4-30 – Illustration of the ProCAST simulation showing the moving interface between the casting and the mould.....	80
Figure 4-31 – Graph to show the ProCAST predictions for the displacements of the casting and the mould and the magnitude of the air-gap compared to the experimentally measured displacements and size of the air-gap for the XD1102 casting. ....	81
Figure 5-2 – SEM back scattered image at 2,000 magnification of the feature region within a valve bar of XD1102. Dark in contrast particles are rich in aluminium – light in contrast are titanium rich particles. <i>Blank entries within the attached table indicates that no detection of that element was found</i> .....	89
Figure 5-4 – SEM image and elemental mapping at x1,000 magnification of the start of the crocodiled region of an extruded bar - Section 1 .....	92
Figure 5-5 – SEM image and elemental mapping at x1,800 magnification at the mid crocodiled region of a extruded bar - Section 2.....	94
Figure 5-6 – SEM image and elemental mapping at x2,500 magnification at the crack tip of the crocodiled extruded bar - Section 3. ....	95
Figure 5-7 – SEM image x2,000 magnification of a sub crocodiled region of a extruded bar -. Section 4.....	97



Figure 5-8 – Elemental maps of the surface of the void as shown by the large rectangular purple box annotated within Figure 5-7 .....	97
Figure 5-9 – Elemental maps at the location sub-surface of the void as shown by the small yellow square annotated within Figure 5-7.....	98
Figure 5-10 – Optical image displaying regions of dark in contrast particles AlN and Light in contrast, TiN particles - Section 5 .....	99
Figure 5-11 – SEM image and elemental mapping at x600 magnification displaying the oxidation characteristics of XD1102. ....	101
Figure 5-12 – SEM image and elemental mapping at x7,500 magnification displaying sub-surface nitridation. ....	102
Figure 5-13 – SEM image at x400 magnification displaying oxidation in front of a crack.....	103
Figure 5-14 – Photograph illustrating the longitudinal crack on the base of an ingot after being withdrawn from the furnace prior to extrusion.....	104
Figure 5-15 – SEM image at x400 magnification illustrating the oxidation at the base of cracked ingot.....	105
Figure 5-16 – SEM image at x500 magnification displaying the oxidation and nitridation of aluminium and titanium at the end of primary crack.....	106
Figure 5-17 – Schematic diagram showing the morphology of an oxidised crack in the alloy .....	107
Figure 5-18 – Graph to show the ProCAST simulation predictions of the stress distribution along the base of the ingot which has the standard pre-heating process...	112
Figure 5-19 – Graph to show the ProCAST simulation predictions of the stress distribution along the base of the ingot which has an alternative heating regime.....	112

Figure 5-20 – Schematic diagram displaying the heat transfer distribution into the ingot from the furnace environment during the pre-heat furnace prior to extrusion. ....	113
Figure 5-21 – Photograph displaying the primary and secondary crack of an XD1102 ingot which has been withdrawn from the pre-heat furnace prior to extrusion.....	114
Figure 5-22 – SEM image at x100 magnification displaying that no oxidation of the secondary crack has occurred. ....	115
Figure 6-1 – Schematic diagram displaying surface turbulence within a liquid metal causing entrainment of the oxide skin and gas bubbles (Campbell, 2006) .....	120
Figure 6-2 – Photographs taken during the Durville tilt casting process. ....	122
Figure 6-3 – Optical macrograph x10 magnification displaying an example of an “old” oxide film entrained within a dip sample of the XD1102 alloy. ....	125
Figure 6-4 – SEM images illustrating the entrainment events witnessed within the dip sample of a XD1102 casting.....	125
Figure 6-5 – Graph to show a potential improvement to the Durville tilt casting rotation to allow a constant fluid velocity throughout the tilt.....	127
Figure 6-6 – Photographs of the Durville tilt casting process displaying a return wave as the melt hits the base of the mould and back up. Note the position of the annotated red line to aid in the visualisation of the return wave.....	129
Figure 6-7 – Screen shot of a simulation displaying the free surface area of melt during the Durville tilt casting method. ....	130
Figure 6-9 – SEM image (left) and Element mapping of the entrained oxide/bubble feature as illustrated in Figure 6-8.....	132
Figure 6-10 – Optical image at x50 magnification of a section of a cracked ingot displaying an oxide film decorated with niobium carbides. ....	133

Figure 6-11 – Schematic diagram of the tensile test piece dimensions.....	136
Figure 6-12 – Graph displaying the predicted machine strain during tensile testing...	137
Figure 6-13 – Graph to display the probability of survival for Durville cast and top poured cast tensile properties. ....	141
Figure 6-14 – Graph to display the 0.2% yield strength of Durville and top poured tests split into lead, middle and discard ends.....	142
Figure 6-15 - Graph to display the ascending 0.2% yield strength of Durville and top poured tests. ....	142
Figure 6-16 – Graph to show the percentage chemistry deviation from the elemental average wt% in the lead, middle and discards ends of both Durville and top poured end of test pieces. ....	144
Figure 6-17 – SEM image of an oxide film on the fractured surface middle location top poured test piece. ....	146
Figure 6-18 – SEM images at x500 magnification displaying regions of ductile and brittle failure mechanisms on a fractured surface.....	147
Figure 6-19 – Graph illustrating the typical types of fracture during tensile testing....	148
Figure 6-20 – SEM image of a fracture surface displaying the existence of niobium carbides at the base of each large pore. ....	149
Figure 6-21 – Illustration of particle detection using ImageJ.....	150
Figure 6-22 – Graph to illustrate 0.2% yield strength vs. NbC volume fraction for both Durville and top poured casts. ....	151
Figure 6-23 – SEM images at x2,000 magnification displaying the grain size in relation to the size of NbC (etched in Kallings No.2 reagent).....	153

Figure 6-24 – Graph to illustrate the NbC volume fraction vs. radial position of the as-cast ingot.....	155
Figure 6-25 – Graph to show the average top 10 largest NbC vs. radial position.....	156
Figure 6-26 – Simplified flow diagram displaying the steps within the MATLAB code .....	157
Figure 6-28 – Graph illustrating the time for each cell to reach the solidus temperature of the alloy for an air-cooled and water-cooled mould. ....	160
Figure 6-29 – Graph to show the cooling rate going through the solidus temperature for each cell for an air-cooled and water-cooled mould.....	160
Figure 6-30 – Predicted displacements for the XD1102 ingot comparing the standard air-cooling of the mould and water-cooling. ....	162
Figure 6-31 – Optical images at x20 magnification displaying a central feature within many of the larger NbC. ....	164
Figure 6-32 – Thermo-Calc phase predictions for XD1102,.....	166
Figure 6-33 – Schematic diagram displaying solidification paths in Alloy 625 (Floreen et al.) .....	168
Figure 6-34 – Thermo-Calc phase predictions with modified XD1102 composition. .	169
Figure A-1 – Schematic diagram of the samples analysed.....	173
Figure A-2 – Photograph of an as-cast billet containing entrained oxide surfaces (i.e. laps) .....	174
Figure A-3 – SEM image and elemental mapping at x10,000 magnification of the middle of as-cast lap .....	175
Figure A-4 – SEM image at x1,000 magnification middle of an oxidised lap.....	177

Figure A-5 – Elemental mapping of an oxidised surface of lap (large purple rectangular box within Figure A-4).....	177
Figure A-6 – Elemental mapping displaying sub-surface of oxidised lap (small yellow box within Figure A-4).....	178
Figure B-1 – Schematic diagram displaying the variables used for the finite difference calculation.....	185
Figure B-2 – Schematic diagram displaying cell sizes used in the MATLAB code ....	187
Figure B-3 – Thermal Conductivity of Grey Cast Iron used in the MATLAB code ...	192
Figure B-4 – Thermal Conductivity of XD1102 used in the MATLAB code .....	193
Figure B-5 – Enthalpy of Grey Cast Iron used in the MATLAB code .....	194
Figure B-6 – enthalpy of XD1102 used in the MATLAB code .....	195
Figure B-7 – Emissivity of Grey Cast Iron used in the MATLAB code.....	195
Figure B-8 – Emissivity of XD1102 used in the MATLAB code.....	196
Figure B-9 – Conductivity of air used in the MATLAB code.....	196
Figure B-10 – Heat Transfer Coefficient during water quenching used in the MATLAB code.....	197
Figure B-11 – 1-D finite difference model including the air-gap formation and the carbon layer .....	198

# LIST OF TABLES

Table 2-1 – Nominal compositions of a selection of nickel alloys (wt%) .....	14
Table 2-2 – Summary of the potential phases in the alloy XD1102 (Smith, 1999). .....	22
Table 4-1 – Simulation Time for Differing Mesh Sizes.....	56
Table 6-1 – EDX analysis of points identified within Figure 6-4b).....	126
Table 6-2 - Results from the tensile testing <i>*Indicates the 3 tensiles which had the extensometer attached</i> .....	138
Table 6-3 – Calculated Weibull modulus of Durville cast and top poured tensile properties. ....	140
Table 6-4 - Trends in mechanical properties of the tensile tests .....	143
Table 6-5 – EDX analysis corresponding to the points annotated in Figure 6-17.....	146
Table 6-6 – Thermo-Calc phase predictions with varying niobium and carbon contents .....	167

# Chapter 1. Introduction

This thesis describes work carried out during a three year period at the University of Birmingham in collaboration with the Specials Metals Corporation group, Special Metals Wiggin Limited (SMWL). Special Metals Corporation is the world's leading manufacturer of nickel-based superalloys and supplies to all major industries: aerospace, automotive, petrochemical and marine just to name a few.

This work examined, with the view to optimise, the manufacture of valve bars which are initially air melted and Durville tilt cast prior to thermo-mechanically working. In particular the impact of the air-gap formed, between the casting and the mould, has on the magnitude of heat transfer has been investigated. An additional aim was to identify a valve bar feature containing oxides and trace it back to its origin; recommendations have been suggested to prevent the feature from re-occurring. The final aim was to investigate whether the substantial thermo-mechanical work received by an ingot after casting minimised the benefits of a carefully poured cast via the Durville method. This was in comparison to a chaotic in nature top-poured casting. If the latter process yielded equivalent final mechanical properties then it could be argued that the Durville casting method and additional process controls is an unnecessary cost.

This study was focused on the alloy XD1102, a customer specific nickel-iron based superalloy manufactured into valve bars for use in the commercial automotive diesel engine market to replace traditional stainless steel valves such 21-4N.

The application of nickel-based superalloys is becoming more commonly used in the automotive industry, much like the aerospace industry did in the 1950s, to cope with the increased combustion temperatures and pressures of the engine. Alternative nickel grades for automotive valve applications include Nimonic alloy 80A (Zhu et al., 2009) and Pyromet alloy 31 (Scott et al., 1995), which have been used in the heavy duty diesel engine market. However, for the commercial automotive market such alloys are not cost effective due to the high nickel content 75 wt% and 57 wt% respectively for Nimonic alloy 80A and Pyromet alloy 31. The alloy XD1102 has approximately half the nickel content of the above mentioned alloys, but still retains the principal characteristics of nickel-based superalloys at elevated temperature: high resistance to corrosion, mechanical and thermal fatigue, mechanical and thermal shock, creep and erosion (Novovic et al., 2004).

Nickel-based superalloys are not the only alternative to stainless steel valves and the use of titanium based alloys, such as Ti-834, are increasing in popularity. Having a density of nearly a half the nickel-based alloy rewards its benefits, however with low formability and difficulties in production these valves are typically used in race engines. Centrifugal casting has been promising (Fu et al., 2008), which produces a near net shape valve in a minimal amount of process steps. However the amount of valves cast per batch is currently limited and hence will not appeal to the mass commercial market.

This thesis is split into three main experimental chapters, all of which are relevant to the manufacture of a valve bar by the Durville tilt casting process; this process, and alloy XD1102 characteristics are covered in Chapter 2.

Chapter 3 summarises the relevant literature on solidification.



Chapter 4 describes the influence of an air-gap on the Interfacial Heat Transfer Coefficient between the melt and mould during casting. Measurements of temperature and the size of air-gap for two alloys cast within the same size mould are presented. These measurements were used to validate numerical 3D simulations using the commercially available software ProCAST.

Chapter 5 describes a root cause analysis of particular feature found within the heads of a selection of valves. The feature was identified by metallographic techniques which aided in tracing them back to their origin. The characteristics of formation of the feature have then been discussed and recommendations for feature mitigation have been presented.

Chapter 6 compares the Durville tilt casting method with a basic top poured casting. The Durville tilt casting is used to provide the tranquil fill of a mould preventing turbulence and the entrainment of oxide films, known to be detrimental to castings. The possibility as to whether thermo-mechanically working the cast ingot nullified the benefit of tranquil filling has been explored.

## Chapter 2. Durville Tilt Casting

### 2.1 Introduction

The Durville tilt casting process was originally used for the casting of aluminium-bronze coinage, patented by Durville in 1914 (Durville, 1914). It is the casting method used by Special Metals Wiggin Limited (SMWL) for the production of XD1102 ingots for valve bar applications. It is an idealised process as it minimises the turbulence induced into the flowing melt promoting a cleaner ingot.

### 2.2 Durville Tilt Casting at SMWL

The process steps involved to produce ingots at SMWL by Durville tilt casting are summarised by the pictures in Figure 2-1 and are described below.



a) Air-melt in an induction furnace



b) Transfer melt from furnace into pre-heated ladle



c) Crane ladle over to Durville machines



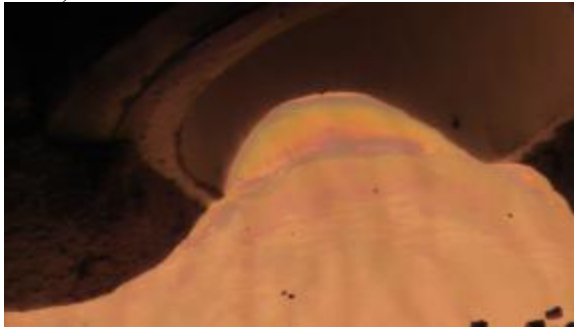
d) Bottom pouring from ladle into receiver.



e) Allow melt to dwell



f) Tilt Durville machines



g) Melt filling the mould



h) Durville machine passed through horizontal



i) Tilt complete – Addition of Exothermic Powder



j) Allow ingots to solidify in moulds.

Figure 2-1 - The Durville tilt casting process at Special Metals Wiggin Limited, Hereford.

### 2.2.1 Induction Furnace

A weighed charge ( $\approx 4500\text{Kg}$ ) is air-melted in an induction furnace, which consists of water-cooled copper coils surrounding the furnace crucible. The induced eddy currents provide a platform for melting and ensure the complete mixing of the melt. Once the melt is sufficiently superheated and mixed the melt is ready to be transferred to the ladle.

### 2.2.2 Ladle

The purpose of the ladle is to transfer the liquid metal from the furnace into the receivers of the Durville machines. The ladle is pre-heated to between  $700$  and  $800^{\circ}\text{C}$  to minimise the amount of solidification on the ladle walls. This is known as “skull” and reduces the efficiency of the process, but it can be used to make up part of the next weighed furnace charge. The ladle is transferred by an overhead crane with an attached scale, to ensure that the correct mass of liquid metal can be transferred into the Durville receivers. The ladle bottom pours into the receivers to prevent the oxide/slag layer on top of the liquid metal from being transferred into the receiver and ultimately into the mould. The bottom pouring process also minimises the liquid metals exposure to environment; thus limiting the size of new oxides which will form on the surface of the liquid metal.

### 2.2.3 Durville Tilt Casting Machine

The Durville machine comprises of a receiver and two parallel mounted grey cast iron moulds as pictured in Figure 2-2. The receiver and moulds are mechanically joined so during tilt the whole system rotates together.

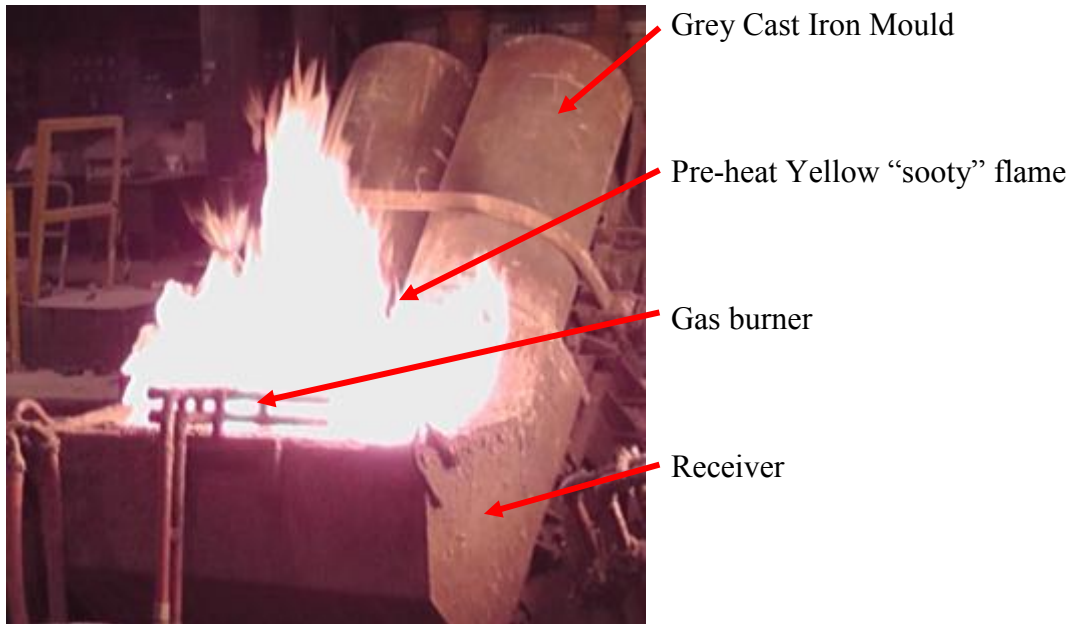


Figure 2-2 - Durville tilt casting machine at SMWL

#### 2.2.4 Receiver

In order to minimise the production of skull in the receiver, this and the moulds are pre-heated by gas torches with a minimal air supply promoting a yellow sooty flame. This also coats the internal walls of the mould with carbon, which aids with fluidity of the melt and improves the surface finish of the ingot. Due to the flame position the mould temperature is non-uniform and localised regions of high temperature can lead to the boiling of the melt surface; to prevent this, the pre-heating process is terminated between the range of 60 and 120 minutes before the transfer of the melt to allow for the mould temperatures to equilibrate.

Each receiver has 700 kg of melt teemed into it; with the given charge weight of the furnace this allows for six Durville receivers to be filled. As each Durville machine has two moulds attached a total of twelve ingots per cast are produced.

### 2.2.5 Vermiculite

Each receiver has Vermiculite added before the melt is teemed into it. Vermiculite is a hydrated laminar mineral consisting of dense aluminium-iron-magnesium silicates. It is an inert material which when heated expands up to 30 times its original volume by conversion of the dense flakes into porous granules containing many minute air layers. As it is less dense than the liquid melt, it will float up through the liquid where it can engulf any inclusions. Once on the top of the melt it provides a high insulation factor reducing heat loss to the surroundings.

### 2.2.6 Tilting

Before tilting the liquid melt is allowed to dwell in the receiver until two criteria are met. Firstly a minimum dwell period is required to ensure the vermiculite has sufficient time to float and settle on top of the receiver's melt; this prevents it from becoming transferred into the mould during tilt. Secondly the tilt temperature is to be reached. A maximum dwell period is also in place to prevent excessive amounts of skull forming leading to short ingots.

These criteria are applied on the first of the six Durville machines with the second to sixth being tilted on the completion of the preceding tilt. Tilting of the Durville machines consists of rotating through a central axis, by 135° in less than 60 seconds, so that the moulds are standing vertically

### 2.2.7 Moulds

Each mould will produce an ingot of 280 mm diameter by 635 mm in height. An additional 150 mm in height of melt is protected by an insulating collar retarding heat loss in the upper section of the mould. This region then provides sufficient feeding to the solidifying ingot preventing the formation of pipe within the main body of the ingot; after solidification this region is discarded. A round is present at the base of each mould to allow the smooth flow of the melt through the mould geometry.

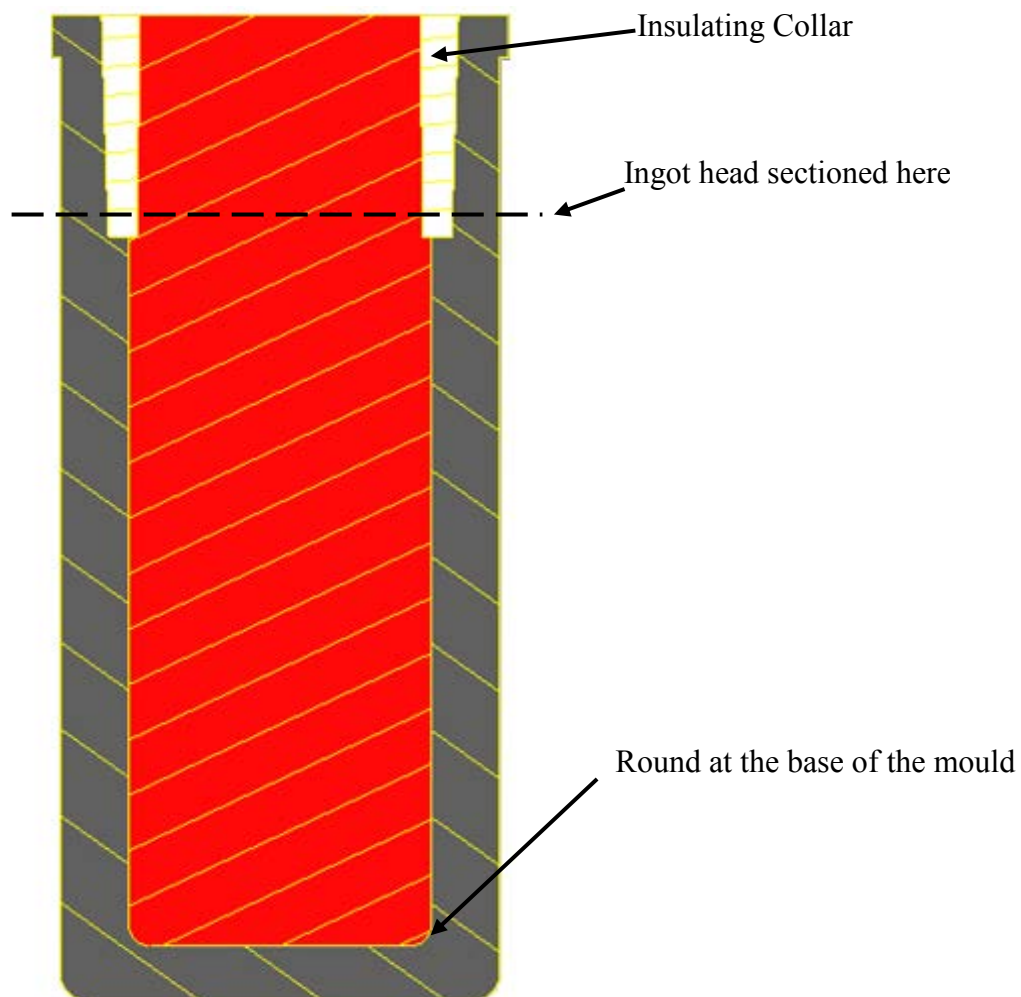


Figure 2-3 – Cross-section of a SMWL mould

### 2.2.8 Bitop

Once the tilt is complete the proprietary substance Bitop is added to the top of the melt. This reacts with the melt exothermically, and in combination with the insulating collar further retards the heat loss from the top of the melt, to its surroundings, ensuring that sufficient feeding to the ingot is provided. The ingots are left to cool naturally in air for a minimum of 80 minutes before extraction from the moulds.

### 2.2.9 Post Processing

Once the ingot is fully solidified and removed from the mould it is identified, inspected for imperfections and the excess head is removed prior to extrusion.

The ingots are extruded by the conventional direct extrusion method by pre-heating the ingots to slightly below the solidus temperature, and using a hydraulic ram to force the ingot through a die. Due to the compressive nature of extrusion, this is an attractive method for forming difficult to form alloys such as stainless steels, nickel-based alloys and other high temperature alloys (K. L. Narayana, 2010). Alternative extrusion methods include billet-on-billet extrusion which is used to create continuous lengths of product, and indirect extrusion where the die moves relative to the ingot. In the conventional direct extrusion method, used in this study, the ingot moves relative to the die. Typical flow patterns observed through the extrusion routes are illustrated in Figure 2-4 (Kurt and Helmut, 1976).



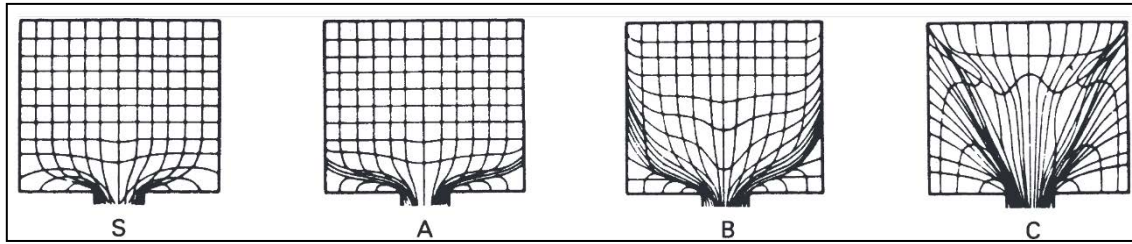


Figure 2-4 – Schematic of four different types of flow patterns during extrusion (Kurt and Helmut, 1976)

The illustrations within Figure 2-4 have the following characteristics, as discussed by (Saha, 2000):

1. Flow pattern S resembles the extrusion of a homogeneous material in the absence of friction at both the die-ingot interface, and the ingot-container interface.
2. Flow pattern A is obtained when extruding a homogeneous ingot with frictional forces at the die-ingot interface only; a conical dead metal zone is created at the leading edge of the ingot due to the frictional force causing the ingot to plastically deform via shear in this location. This flow pattern is typical for the indirect extrusion process.
3. Flow pattern B consists of a homogeneous ingot which has frictional forces at both the ingot-die interface and the ingot-container interface. This leads to an increased dead metal zone when compared to flow pattern A; this is typical of the direct extrusion process.
4. Flow pattern C is obtained with ingots having inhomogeneous material properties, or with non-uniform temperature distribution in the ingot resulting in increased shear and an increased dead metal zone.

Ingots extruded at SMWL are wrapped circumferentially with glass lubricating sheets prior to extrusion; this is to minimise the dead metal zone caused at the ingot-container interface as described by flow pattern B.

For valve bars manufactured at SMWL, the extrusion process is an intermediate operation which is followed by hot-rolling to the final product diameter. A sequence of steps must be taken to ensure that the final valve bar is conforming. Firstly, due to the asymmetric frictional forces and temperature distributions (Bauser and Siegert, 2006) the extruded bar is usually distorted, and due to the temperatures involved a scale of surface oxides is present. Therefore, the bars are straightened and peeled (ground) prior to hot-rolling to prevent the ingress of the surface oxide. After pre-heating the extruded bars in an InductoForge induction heater, they are hot-rolled via a series of reductions to the final diameter of 25 mm (for the given valve bar discussed in this study). In a similar fashion to the extruded bar, each hot-rolled bar is straightened and ground representing the final product. Each bar receives the volumetric non-destructive eddy current test ensuring no out of specification internal defects exist. This is the final manufacturing step completed by SMWL before the bar is shipped to their customers. It is not until this point that the valve bar is sectioned and forged into valve heads. This is followed by a standard solution anneal to remove any residual stresses and detrimental secondary phases which may have formed during the manufacturing process, precipitation hardened, and final machining.

## **2.3 Alloy XD1102**

SMWL by name are manufactures of high-value nickel-based superalloys such as the Inconel, Nimonic and the Monel families. The alloy which forms the basis of this study is XD1102; this alloy is a precipitation hardenable, niobium stabilised, nickel-iron chromium alloy which provides high mechanical strength with good oxidation and corrosion resistance at high temperatures. It has a similar composition to Inconel 706 (Table 2-1) which has characteristics akin to Inconel 718. However, further reductions of nickel, molybdenum and niobium in comparison to Inconel 718 and substantially reduced levels compared to other nickel-based alloys, such as Waspaloy and Alloy X-750, leads to an increase in machinability and formability of the alloy. This selective reduction in elements also lowers costs, both due to the lower raw material costs and the decreased demand on tooling, and thirdly reduces the tendency of the alloy range to develop macrosegregation, which enables the alloy to be cast with large cross sections. However, these reductions also lower the strength of the material compared to Inconel 718; increased weight percentages of Al and Ti have been included to mitigate this (Smith and Patel, 2005). Inconel 706 is the basis of the alloy XD1102 with further reductions in the nickel content, but with increased amount of carbon, aluminium and titanium to provide extra strength.

Table 2-1 – Nominal compositions of a selection of nickel alloys (wt%)

Element	Nickel-iron based alloys		Nickel based alloys	
	Inconel 706	Inconel 718	Waspaloy	Udimet 520
Ni	39.0-44.0	50.00-55.00	~ 60%	~60%
Cr	14.5-17.5	17.00-21.00	18.00-21.00	18.0-20.0
Fe	Balance	Balance	2.00 Max	-
Nb	2.5-3.3	4.75-5.50	-	-
Mo	-	2.80-3.30	3.50-5.00	5.5-7.0
Ti	1.5-2.0	0.65-1.15	2.75-3.25	2.9-3.25
Al	0.40 max	0.20-0.80	1.20-1.60	1.8-2.3
Co	0.06 Max	1.00 Max	12.00-15.00	11.0-14.0
C	0.06 Max	0.08 Max	0.02-0.10	0.02-0.06
Mn	0.35 Max	0.35 Max	1.00 Max	-
Si	0.35 Max	0.35 Max	0.75 Max	-
P	0.020 max	0.015 Max	0.030 Max	-
S	0.015 Max	0.015 Max	0.030 Max	-
B	0.006 Max	0.006 Max	0.003-0.010	0.004-0.010
Cu	0.30 Max	0.30 Max	0.50 Max	-
Zr	-	-	0.02-0.12	-

Due to the complexity of these alloys, the phase diagrams are difficult to present. Therefore as an example the ternary phase diagram for iron-chromium-nickel at two temperatures is presented in Figure 2-5, and the quaternary phase diagram for iron-nickel-chromium-niobium at 1473K is presented in Figure 2-6 displaying a selection of deleterious phases which can form in the nickel-based superalloys. The phases present within the alloy XD1102 will be discussed in more detail below.

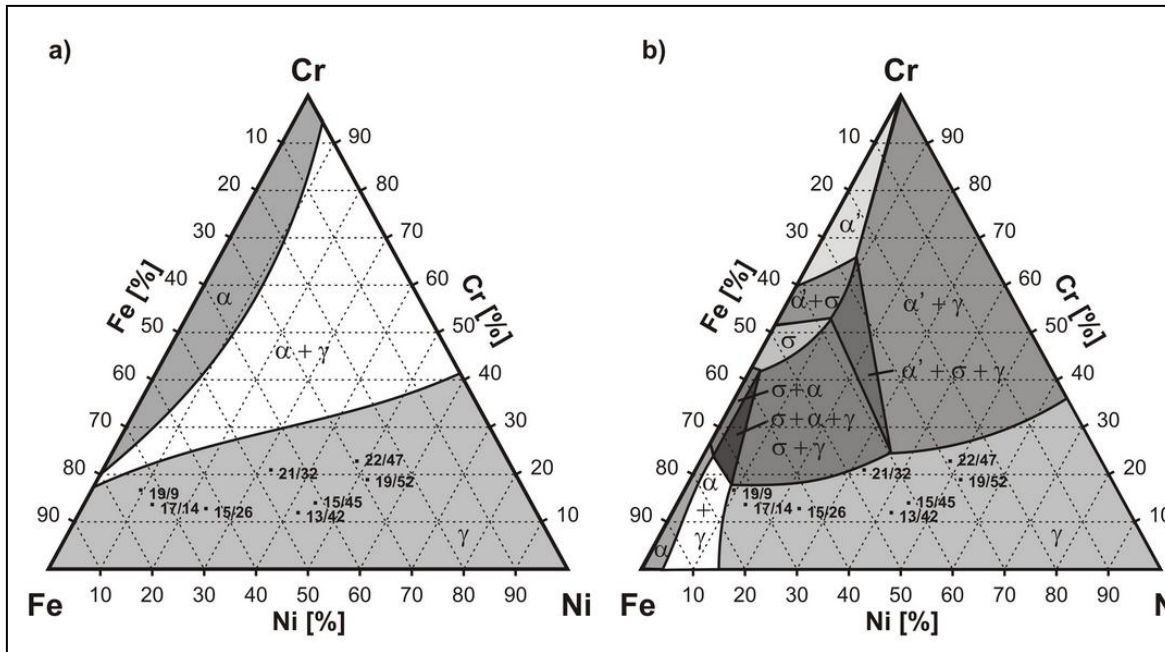


Figure 2-5 – Fe-Ni-Cr ternary phase diagram at a) 1050°C and b) 650°C (Pickering, 1976)

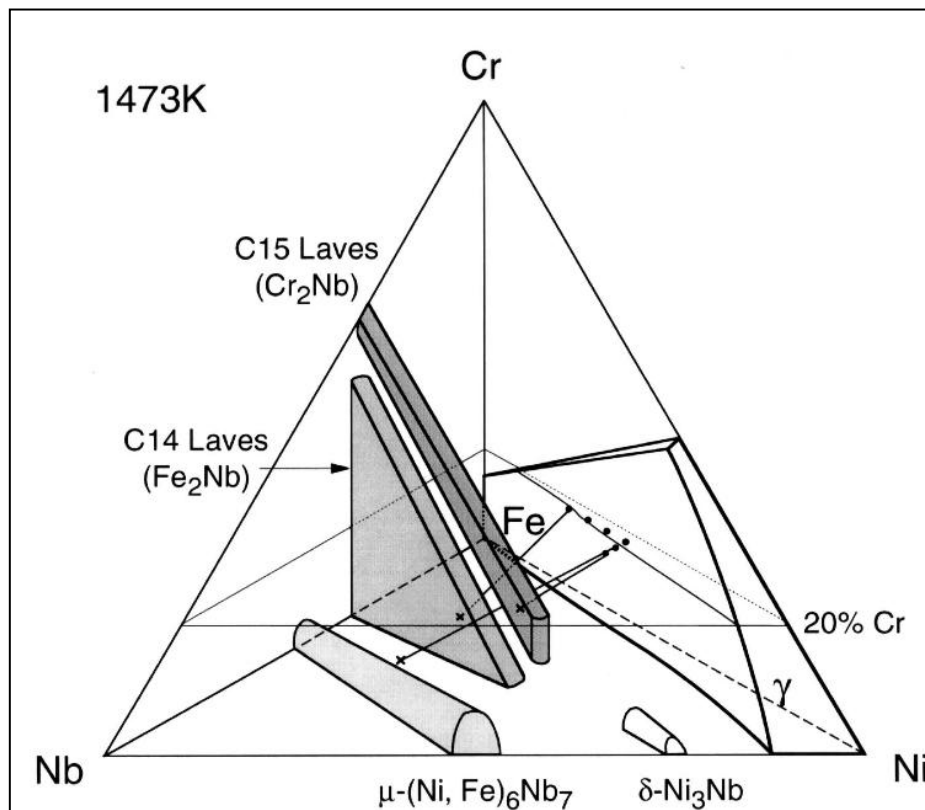
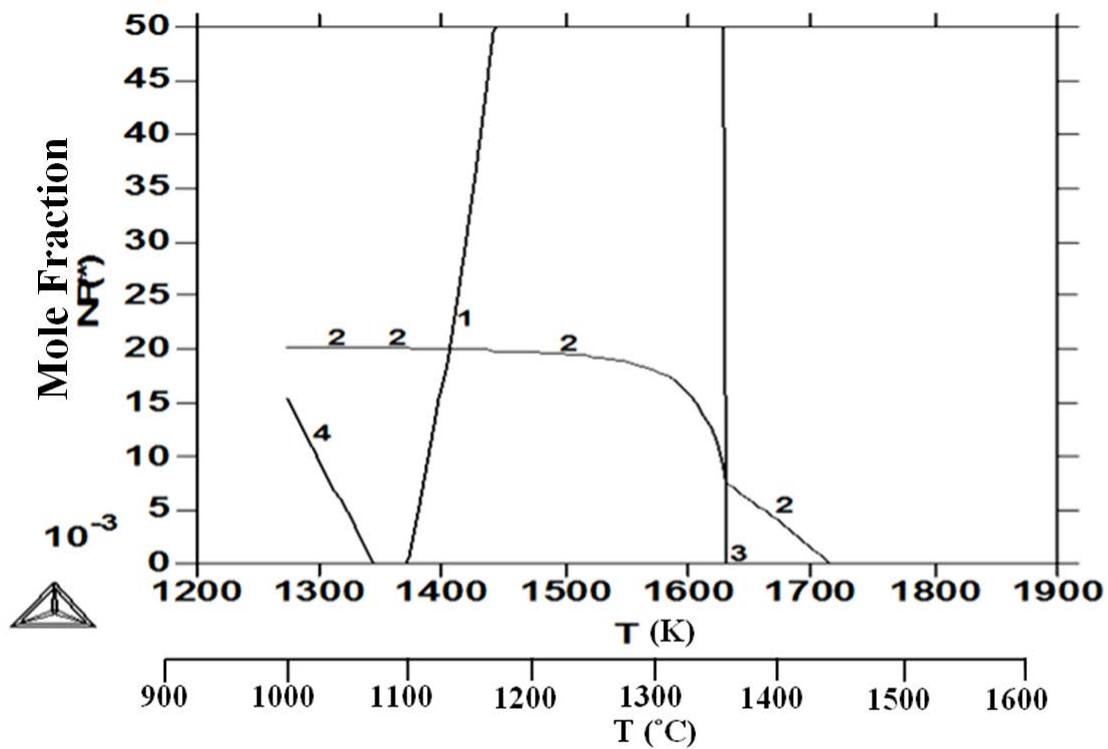


Figure 2-6 – Fe-Ni-Cr-Nb quaternary phase diagram at 1200 °C (Takeyama et al., 2001).

### 2.3.1 Thermo-Calc Predictions

The software Thermo-Calc has been used to predict the phases present in alloy XD1102 by the use of an average alloy composition (29 heats), and the TCFE7 database (Thermo-Calc Software). The predicted phases formed during solidification for alloy XD1102 is displayed in Figure 2-7 which shows that the first phase to form is the Face-Centered Cubic (FCC) MC phase, niobium carbide, followed by the FCC gamma matrix. The predictions also illustrates that after the solidus point, the undesirable Laves phase is formed.



1 – liquid    2 – FCC - NbC phase    3 – FCC bulk matrix phase    4 – Laves phase

Figure 2-7 – Thermo-Calc phase predictions for XD1102

### 2.3.2 Alloy XD1102 Characteristics

XD1102 forms a FCC, austenitic gamma matrix which is strengthened primarily by the Body-Centred Tetragonal (BCT) phase  $\text{Ni}_3\text{Nb}$ ,  $\gamma''$ . This is the preferred strengthening phase in this alloy due to the increased niobium content (Reed and Rae, 2014) although it becomes unstable above  $650^\circ\text{C}$ , limiting the service temperature of the alloy (Kirman and Warrington, 1970). Due to high coherency strains of this phase it is sluggish to form (Reed, 2006, Donachie, 2002) which increases the weldability of the material as precipitation hardening is initially minimal (Gordine). During post weld heat treatments the material is effectively stress relieved prior to strengthening leading to the reduced probability of strain age cracking (Lucas Jr, 1970).

Due to the chemistry of XD1102, the primary MC carbide niobium carbide ( $\text{NbC}$ ) forms; within this alloy and in similar alloys, the presence of  $\text{NbC}$  can aid in structural refinement during fabrication by assisting grain size control (Smith and Patel, 2005). When present at the grain boundaries these carbides are also known to inhibit slip, and when intragranular will aid in strengthening the matrix. The addition of the carbides also increases the wear resistance of the material which makes it suitable for a valve bar application; Wilmes reported a hardness of 2,556 HV for  $\text{NbC}$  (Wilmes and Zwick, 2002).

However, it is known that carbides can also be detrimental as they can act as a source of dislocations and fatigue crack initiation (Cocks, 1985, Pelloux and Stoloff, 1980, Smith and Patel, 2005)

During service or heat treatments, MC type carbides can transform into  $\text{M}_{23}\text{C}_6$  and  $\text{M}_6\text{C}$  types which can be undesirable as the carbides coarsen rapidly and the constituent “M”

elements are removed from the matrix; this depletion leads to local regions of the alloy with loss of strength and corrosion resistance. Whilst no publications were found in automotive valve application, an example of this type of failure was observed on Alloy 600 where chromium diffused into the carbide via the grain boundaries; this ultimately left the grain boundaries vulnerable to environmentally assisted stress corrosion cracking (Was, 1990). Due to the low diffusivity of chromium within the matrix, compared to diffusion along the grain boundaries, lengthy thermal treatments are often used to replenish the grain boundaries, with chromium, before going into service. This is less of a problem for XD1102, as niobium stabilisation enables the chromium to be maintained within the matrix and at grain boundaries providing efficient resistance to oxidation.

Conversely Wen Sun found that the transformation of MC carbides to  $M_6C$  and  $M_{23}C_6$  increased the stress-rupture life of the nickel-based alloy, Alloy 800, as this transformation suppressed the formation of the  $\mu$  and  $\sigma$  phases, which are non-coherent with the gamma matrix (Sun et al., 2015). For the niobium containing nickel superalloys it is known that this addition delays the transformation from MC to  $M_6C$  and  $M_{23}C_6$  (Smith and Patel, 2005).

For many compositions of nickel-based alloys the carbides form after the gamma matrix (Bouse, 1989, Cieslak et al., 1989, Zhao et al., 2008) to name a few for Inconel 718. Etching a sample of XD1102 in the as-cast state illustrates carbides are positioned interdendritically (Figure 2-8), but it cannot be determined whether the carbides nucleated first and were pushed to the interdendritic regions or formed by the liquid present interdendritically after the matrix has begun to solidify. As identified in the Thermo-Calc prediction (Figure 2-7) the first phase to form is the niobium carbide,



which indicates a reduced solubility of carbon within liquid XD1102 over alloy 718. Taking a cross-section through the as-cast structure reveals that the carbides increase in size as you traverse from the edge to the centre of the ingot. As the ingot cools, the centre will experience increased time at temperature and thereby the carbides in this region will have relatively a longer time to grow than carbides which either form, or are trapped, interdendritically within regions near the surface of the ingot. This gives rise to the larger carbides in the centre of the ingot. Mitchell found that the nucleation of NbC on TiN led to an increased size of the carbide as they nucleated earlier and therefore had additional time to grow (Mitchell et al., 1994). TiN will form in the liquid increasing the temperature at which the carbide will form over a “pure” NbC carbide which has spontaneously nucleated. This was also found by Heck in the alloy 706 where TiN was detected centrally on large blocky carbides (Heck, 1994).

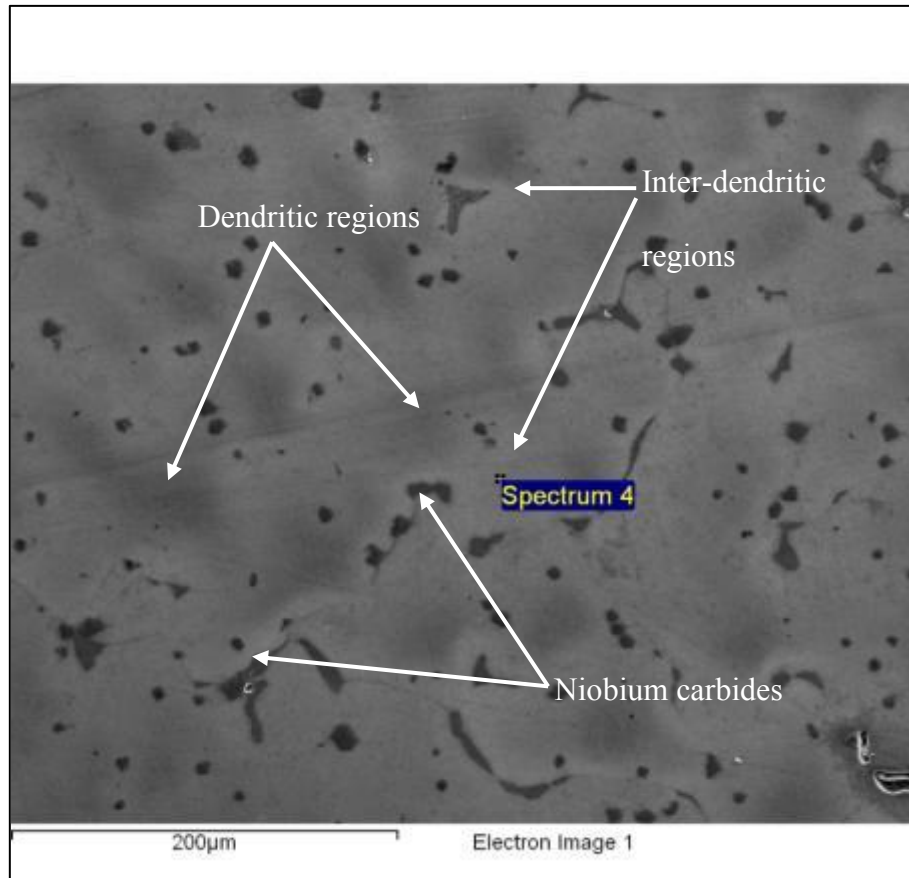


Figure 2-8 – Interdendritic carbides in an as-cast ingot of XD1102

In addition to the transformation of MC to either  $M_{23}C_6$  or  $M_6C$  type carbides, other transformations can occur. These are the topologically closed packed phases, discussed below, which form and coarsen at the expense of the strengthening  $\gamma$  or  $\gamma''$  phases, or in the expense of oxidation and corrosion resistance. Unlike the  $\gamma''$  phase they are non-coherent with the  $\gamma$  matrix so must be kept to a minimum.

The precipitation of the delta ( $\delta$ ) phase, a needle-shaped orthorhombic  $Ni_3Nb$  structure, forms and coarsens at the expense of the  $\gamma''$  phase. This transformation is caused by over-aging or extended service at precipitation hardening temperatures between 650 to 980°C, as illustrated in Figure 2-9 for the alloy Inconel 718. The characteristics of the

formation depend strongly on this temperature range as described by Reed (Reed, 2006) and Donachie (Donachie, 2002).

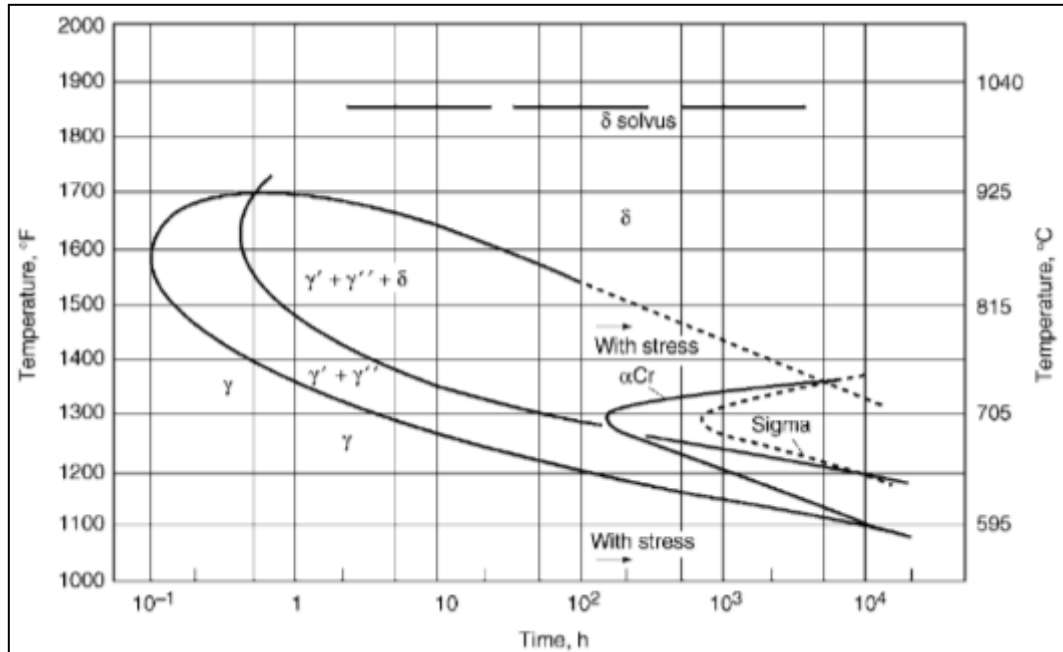


Figure 2-9 – Time-temperature transformation diagram in IN-718 (Donachie, 2002)

The sigma ( $\sigma$ ) phase FeCr, inherent to nickel-iron superalloys can form in service under stress as illustrated in Figure 2-9. If found as thin continuous films precipitated on grain boundaries, dislocation pile-up can lead to crack initiation and the loss of ductility (Geddes et al., 2010). However small spherical particles may increase creep resistance (Matysiak et al., 2013).

The eta ( $\eta$ ) phase,  $\text{Ni}_3(\text{Ti}, \text{Nb})$ , has a hexagonal structure that forms as platelets or cells on grain boundaries, which is known to reduce ductility if large amounts are present. Small amounts of  $\eta$  phase were found not to be detrimental in alloy 740 (Shingledecker and Pharr, 2012) but should be avoided in large quantities. However this has less impact on toughness than the Laves phase.

Of the inter-metallic phases the Laves phase, hexagonal  $\text{Fe}_2(\text{Ti,Nb})$ , is the most well known; it has generally been accepted that the presence of this phase is deleterious to the mechanical properties. It usually forms at the grain boundaries either as a continuous or semi-continuous network reducing ductility and weldability of the material (Chang et al., 1994). The Laves phase is usually attributed to segregation during casting or welding of the alloys; this is discussed by Radhakrishna (Radhakrishna and Rao, 1997). It has also been reported that a reduction in silicon to below 0.10 wt% helps to minimise Laves precipitation (Schilke et al., 1994, Schirra et al., 1991).

Solution heat treating the material will dissolve all phases other than NbC; this includes  $\gamma''$  which can be subsequently precipitated back out during aging heat treatments. Care must be taken during solution annealing to avoid excessive grain growth and maintain material properties (Brooks and Bridges, 1988).

The main strengthening and deleterious phases which may exist within XD1102 are summarised in Table 2-2 ; this table includes the Greek symbol, stoichiometry, structure, space group, Pearson symbol and the Strukturbericht symbol.

Table 2-2 – Summary of the potential phases in the alloy XD1102 (Smith, 1999).

Common Name	Greek Symbol	Stoichiometry	Structure	Space group	Pearson Symbol	Strukturbericht symbol
Gamma	$\gamma$	$\text{Ni}_3(\text{Al,Ti})$	Ordered FCC	Fm3m	cF4	A1
Gamma Double Prime	$\gamma''$	$\text{Ni}_3\text{Nb}$	Ordered BCT	I4/mmm	tI8	D0 <sub>22</sub>
Delta	$\delta$	$\text{Ni}_3\text{Nb}$	Orthorhombic	Pnmm	oP8	D0 <sub>a</sub>
Sigma	$\sigma$	FeCr	Tetragonal	P4 <sub>2</sub> /mnm	tP30	D8 <sub>b</sub>
Eta	$\eta$	$\text{Ni}_3(\text{Ti,Nb})$	HCP	P6 <sub>3</sub> /mmc	hP16	D0 <sub>24</sub>
Laves		$\text{Fe}_2(\text{Ti,Nb})$	HCP	P6 <sub>3</sub> /mmc	hP12	C14

## Chapter 3. Solidification Theory

To understand the microstructures, thermal histories and defects which may arise from a casting process, it is important to understand the theory of solidification. The solidification process is the phase transformation of a liquid phase into one or several solid phases which involves solute diffusion and latent heat (Kurz and Fisher, 1998). There are two basic phenomena which need to occur for solidification to begin; undercooling and nucleation, for which thermodynamics dictates that a level of undercooling must exist for nucleation (Stefanescu and Ruxanda, 2004). If a stable nucleus has formed and reaches a critical size, it can begin to grow and understanding the growth kinetics and the microstructural evolution, allows for a better understanding of the final materials structure and properties.

Although for the alloy XD1102, where the final materials strengths is largely a resultant of the amount of work received during the extrusion and the hot-rolling process, combined with the precipitating heat treatment; it is still prudent to understand the solidification kinetics of the ingot to ensure segregation is minimised and casting defects such as cracks, or laps can be avoided. Such scenarios could lead to loss of yield during the manufacturing stages of the valve bar.

### 3.1.1 Undercooling

The phenomenon of undercooling,  $\Delta T$ , is described as the local temperature difference of the liquid-to-solid interface to the equilibrium melting point temperature. Undercooling has contributions from constitutional undercooling,  $\Delta T_C$ , curvature undercooling,  $\Delta T_\gamma$ , thermal undercooling,  $\Delta T_t$ , kinetic undercooling,  $\Delta T_K$ , and pressure undercooling,  $T_P$ , which can largely determine the growth rate and the dendrite

morphology (Herlach, 2006). The summation of the individual contributions to the undercooling gives the total undercooling,  $\Delta T$ :

$$\Delta T = \Delta T_C + \Delta T_\gamma + \Delta T_t + \Delta T_K + \Delta T_P \quad \text{Eq. 3-1}$$

### 3.1.2 Constitutional Undercooling

During solidification, solute can diffuse from either the solid into the liquid, when the liquid has increased solubility of the solute than the solid, or from the liquid into the solid. Therefore at a given temperature the composition of the solid,  $C_s$ , and the liquid,  $C_L$ , differ and deviate from the starting composition,  $C_0$ . A typical linearised phase diagram is illustrated in Figure 3-1, which shows in this instance that the composition of the solid is lower than the liquid; i.e. solute has been rejected to the liquid. The ratio of  $C_s$  to  $C_L$  is known as the partition coefficient, as expressed in Eq. 3-2:

$$k = \frac{C_s}{C_L} \quad \text{Eq. 3-2}$$

Treating the phase diagram as a linear relationship, the partition coefficient can be expressed as the gradient of the liquidus slope,  $m_L$ , to the solidus slope,  $m_s$ , (Eq. 3-3) as illustrated in Figure 3-1.

$$k = \frac{m_L}{m_s} \quad \text{Eq. 3-3}$$

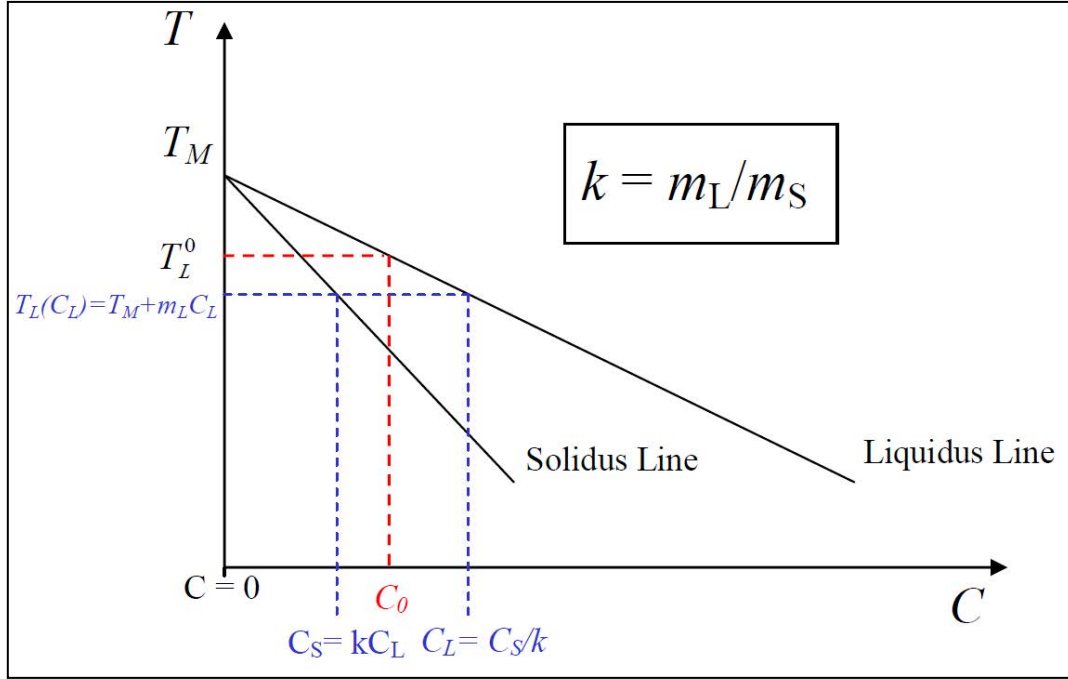


Figure 3-1 – Linearised phase diagram displaying the solid and liquid solute compositions (Chilton, 2002)

For partition coefficients  $k < 1$ , i.e. where solute is rejected into the liquid, a boundary layer of liquid richer in solute in comparison to the bulk liquid is present. A consequence to this is that the liquidus temperature is lower next to the liquid-to-solid interface than away from it, as illustrated in Figure 3-2 (Stefanescu and Ruxanda, 2004). Additionally, Figure 3-2 illustrates that the heat flow from the bulk liquid to the solid imposes a thermal gradient,  $G_T$ , and a liquidus gradient,  $G_L$ , which is the tangent to the temperature of the liquid in the boundary layer,  $T_L$ , at the liquid-to-solid interface. If  $G_T$  is lower than  $G_L$ , the temperature in the boundary layer will be below the equilibrium liquidus temperature; thus a constitutional undercooled region will result. This can be calculated by:

$$\Delta T_C = T_L - T^* = m_L(C_0 - C_L^*) \quad \text{Eq. 3-4}$$

where  $T^*$  is the liquid-to-solid interface temperature,  $C_L^*$  is the concentration in the liquid side of the interface and the remainder as previously defined.

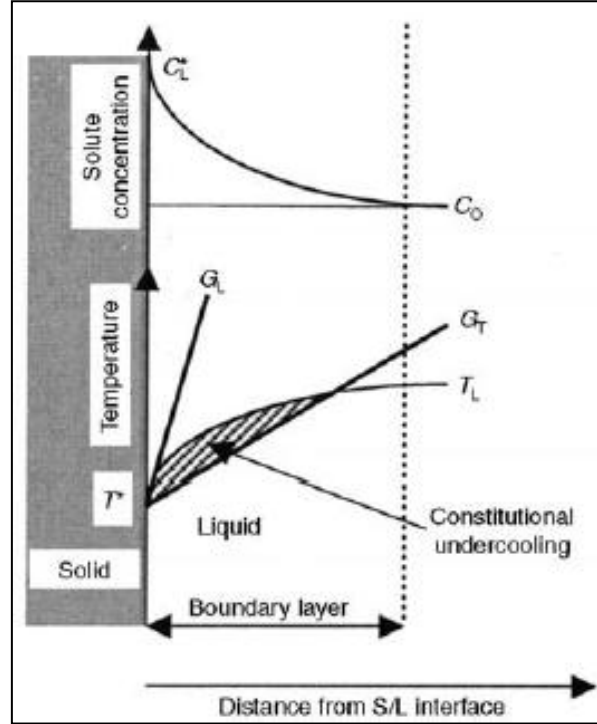


Figure 3-2 – Formation of a constitutionally undercooled region (dashed area) in the liquid next to the solid/liquid interface because of lower liquidus temperature produced by the higher solute content. (Stefanescu and Ruxanda, 2004)

### 3.1.3 Curvature undercooling

The curvature undercooling,  $T_\gamma$ , is a result of the excess energy through the formation of the curved liquid-to-solid interface and it is given by the Gibbs-Thomson equation:

$$\Delta T_\gamma = K k_{GT} \quad \text{Eq. 3-5}$$

where  $k_{GT}$  is the Gibbs-Thompson coefficient, and  $K$  is the average surface curvature.

For isotropic surface energies  $K$  can be expressed as:

$$K = \frac{1}{r_1} + \frac{1}{r_2} \quad \text{Eq. 3-6}$$



where  $r_1$  and  $r_2$  are the principle radii of curvature and therefore the smaller the radius, resulting in increased surface-to-volume ratio, leads to an increased amount of undercooling.

### 3.1.4 Thermal Undercooling

Thermal undercooling,  $\Delta T_t$ , is attributed to pure metals when nucleation has not occurred and the temperature of the liquid at the liquid-to-solid interface is below the equilibrium temperature through the extraction of heat.

$$\Delta T_t = T_e - T^* \quad \text{Eq. 3-7}$$

where  $T_e$  is the equilibrium temperature at the interface.

### 3.1.5 Kinetic Undercooling

The kinetic undercooling,  $\Delta T_K$ , is attributed to the net driving force for atoms to transfer from the liquid state to the solid state, or from the solid state to the liquid state. In materials which have low entropy, the kinetic undercooling is in the order of 0.01 to 0.05 K (Stefanescu and Ruxanda, 2004) and therefore can be deemed negligible.

### 3.1.6 Pressure Undercooling

The pressure undercooling,  $\Delta T_p$ , is the result of applied pressure,  $\Delta P$ , on the liquid causing an increased level of undercooling; however it is relatively small, in the order of  $10^{-2}$  K/atm, and therefore can usually be neglected (Stefanescu and Ruxanda, 2004).

$\Delta T_p$  can be calculated by:

$$\Delta T_p = \frac{\Delta P \Delta v}{\Delta S_f} \quad \text{Eq. 3-8}$$

where  $\Delta v$  is the change in volume, and  $\Delta S_f$  is the entropy of fusion.

### 3.1.7 Undercooling Combined

The combination of the mechanisms of undercooling can be illustrated as in Figure 3-3 (Kurz and Fisher, 1998), where the kinetic and pressure undercooling has been neglected and the curvature undercooling is designated as  $T_R$ .

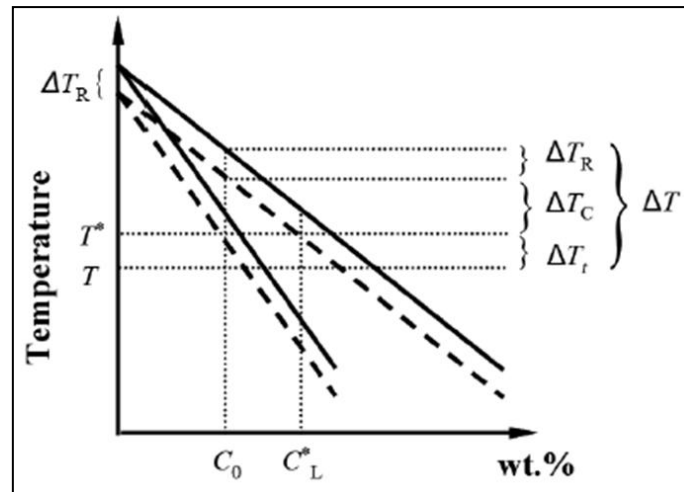


Figure 3-3 – Effects of different mechanisms of undercooling during solidification in a linearised binary phase diagram (Kurz and Fisher, 1998).

### 3.1.8 Grain Nucleation

There are two basic types of grain nucleation which will be briefly discussed, homogeneous and heterogeneous nucleation.

#### 3.1.8.1 Homogeneous Nucleation

Homogeneous nucleation is the spontaneous and random creation of a nucleus within a substrate of the same chemistry. Homogeneous nucleation is driven by the change in Gibbs free energy,  $\Delta G$ , of the new phase that has just formed. The energy balance is formed by taking into account the decrease in energy through the formation of the solid phase with a given volume,  $G_V$ , and the increase in energy through the new interface  $G_I$ . The simplest case is assuming the nucleus as a sphere; this allows the energy balance to

be derived by the addition of the volume and interface terms (Dantzig and Rappaz, 2009):

$$\Delta G = \Delta G_I + \Delta G_V = 4\pi r^2 \sigma + \frac{4\pi r^3}{3} \Delta g \quad \text{Eq. 3-9}$$

where  $r$  is the radius of the nucleus,  $\sigma$  is the liquid-to-solid interfacial energy and  $\Delta g$  is the Gibbs free energy difference as a function of the undercooling,  $\Delta T$ , between the liquid and the solid phase per unit volume. Figure 3-4 displays the change in the free energies of the volume of the nucleus and the interfacial energy for a given level of undercooling. This figure shows that for a nucleus to be stable and grow it must be of a critical radius,  $r^0$ .

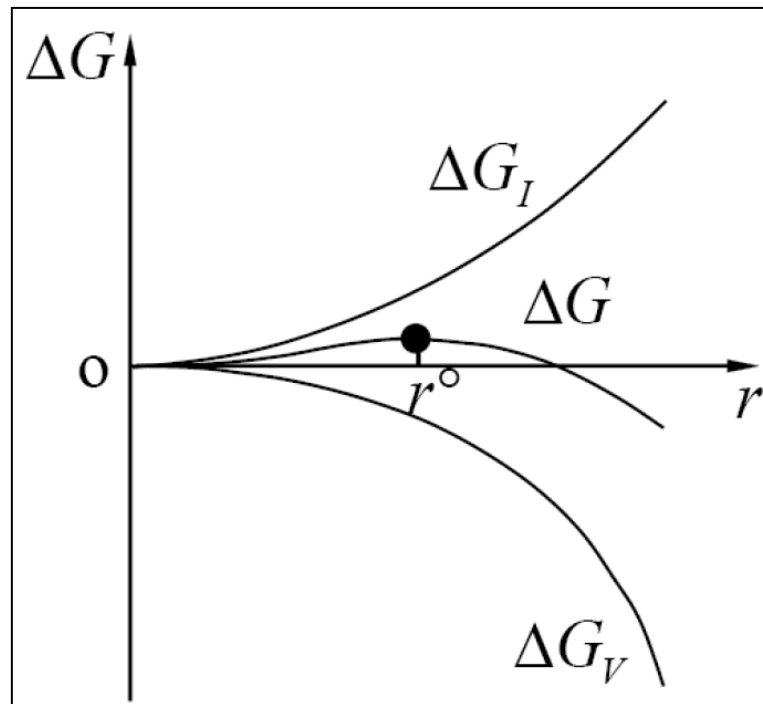


Figure 3-4 – Gibbs free energy change associated with homogeneous nucleation with a spherical shape (Kurz and Fisher, 1998)

Therefore setting  $\frac{d}{dr}(\Delta G) = 0$  in Eq. 3-9, the critical radius,  $r^0$ , can be calculated:

$$\frac{d}{dr}(\Delta G) = 0 = 8\pi r\sigma + 4\pi r^2\Delta g \quad \text{Eq. 3-10}$$

$$r^0 = \frac{-2\sigma}{\Delta g} \quad \text{Eq. 3-11}$$

### 3.1.8.2 Heterogeneous Nucleation:

Homogeneous nucleation in practice is not common, and usually requires a large amount of undercooling to occur. The second type of nucleation is heterogeneous nucleation, which involves the preferential nucleation of a nuclei by the aid of foreign materials (Flemings, 1974); this can be through the sides of the furnace wall, oxides or inclusions etc. as displayed in Figure 3-5 (Kurz and Fisher, 1998). In this instance, the crystal's liquid-to-solid interface ( $A_{LC}$ ) is partly replaced with a low-energy liquid-to-solid interface between the crystal and the foreign material ( $A_{CS}$ ). Therefore, the activation energy required for nucleation compared to homogeneous nucleation is reduced.

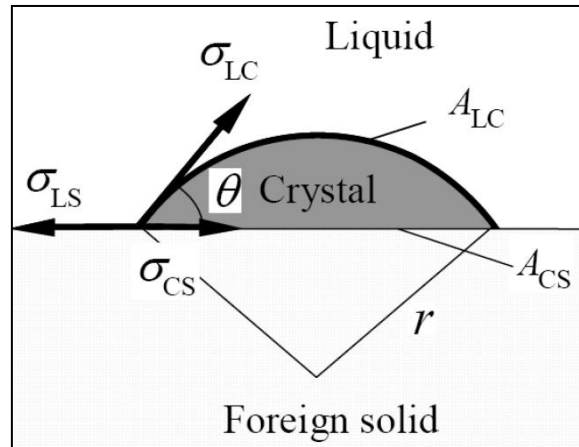


Figure 3-5 – Schematic diagram displaying the heterogeneous nucleation of a nuclei (Kurz and Fisher, 1998).

The energy balance for heterogeneous solidification is given by:

$$\Delta G_{het} = \Delta G f(\theta) \quad \text{Eq. 3-12}$$

$$f(\theta) = \frac{(2 + \cos\theta)(1 - \cos\theta)^2}{4} \leq 1 \quad \text{Eq. 3-13}$$

where  $\theta$  is the wetting angle as displayed in Figure 3-5. Thereby, heterogeneous nucleation can be controlled by selecting crucible material, or including nucleation reagents into the liquid.

### 3.1.9 Growth Kinetics:

Once a crystal has exceeded the critical size and is “stable” it can begin to grow. For pure metals solid growth is governed by the heat of fusion; for alloys, it is the combination of solute diffusion and heat transfer during solidification.

For solute diffusion and neglecting convection:

$$\frac{\partial C}{\partial t} = \nabla(D\nabla C) \quad \text{Eq. 3-14}$$

where  $D$  is the solute diffusion constant and  $C$  the concentration in either the solid or liquid.

Solute can diffuse two to three orders of magnitude quicker in the liquid phase than the solid phase, Eq. 3-14 can therefore be expressed for the equivalent phases:

$$\frac{\partial C_L}{\partial t} = \nabla(D_L \nabla C_L) \quad \text{Eq. 3-15}$$

$$\frac{\partial C_S}{\partial t} = \nabla(D_S \nabla C_S) \quad \text{Eq. 3-16}$$

And for heat:

$$\frac{\partial T}{\partial t} = \nabla(\alpha \nabla T) \quad \text{Eq. 3-17}$$

where  $\alpha$  is the thermal diffusivity and given by:

$$\alpha = \frac{K}{\rho C_p} \quad \text{Eq. 3-18}$$

where  $K$  is the thermal conductivity,  $\rho$  density, and  $C_p$  is specific heat per unit volume.

### 3.1.10 Solute Redistribution Models

As described by Fleming, there are two extreme cases for solute redistribution, the equilibrium and Schiel conditions. The equilibrium condition assumes that complete mixing occurs in both the liquid and the solid, as described by Figure 3-6 (Flemings, 1974).

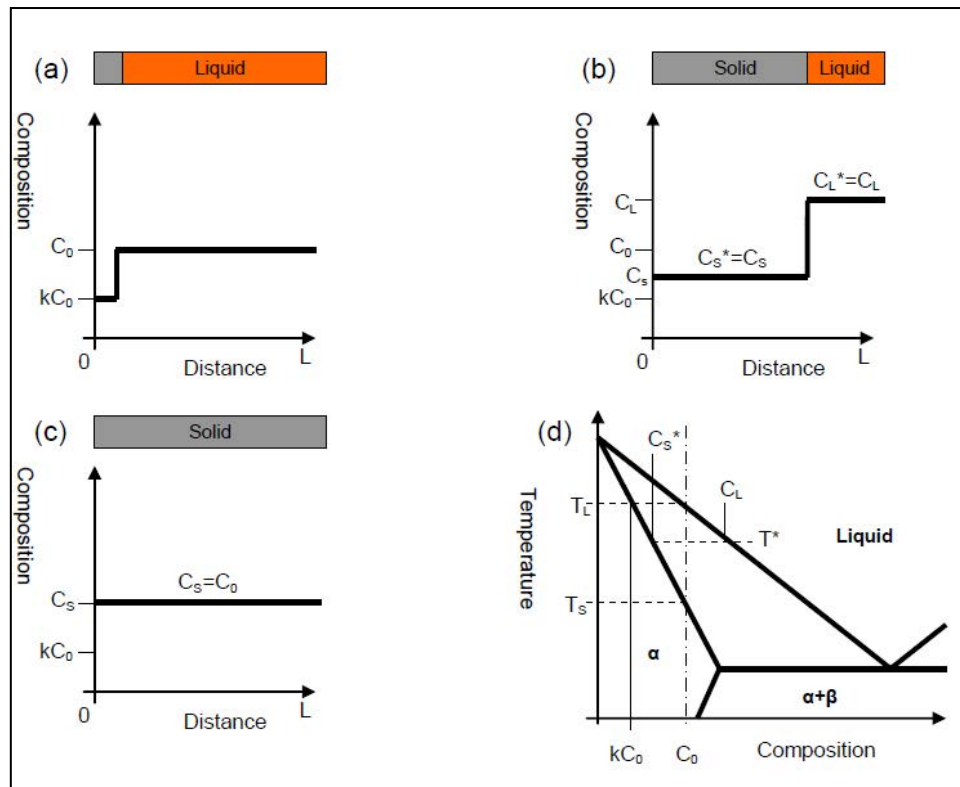


Figure 3-6 – Solute redistribution during equilibrium solidification: (a) at the start of solidification, (b) at temperature  $T^*$ , (c) when solidification is complete, (d) the corresponding phase diagram (Flemings, 1974)

The Scheil model only considers complete mixing in the liquid, and that no diffusion occurs in the solid state. Because of this, the increase in the concentration of the liquid melt is equal to that of the rejected solute as can be shown by the illustration in Figure 3-7 (Dantzig and Rappaz, 2009) where  $\lambda_2$  is the secondary dendrite arm spacing.

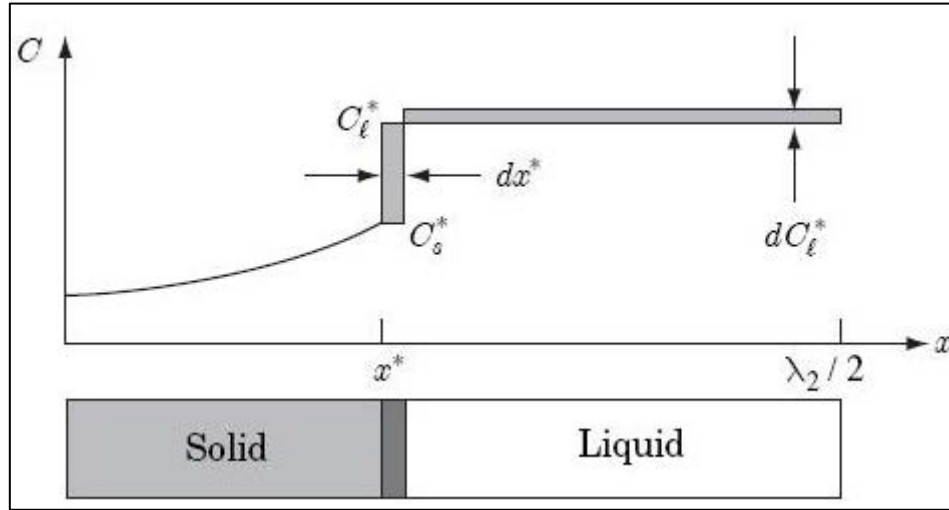


Figure 3-7 – An construct demonstrating the partitioning of liquid from the interface to the liquid in the Gulliver-Scheil model of segregation (Dantzig and Rappaz, 2009).

### 3.1.11 Effect of Solidification Rate

It is well understood that an increased rate of solidification provides a finer as-cast microstructure, and this in turn improves the final mechanical properties of the material by the well known Hall-Petch relationship, Eq. 1-19 (Hansen, 2004). It is also important to consider the cooling rate after solidification, as this will limit the grain movement and growth which occurs to minimise the free energy of the material (Stefanescu and Ruxanda, 2004).

$$\sigma_y = \sigma_0 + kd^{-1/2} \quad \text{Eq. 3-19}$$

where  $\sigma_y$  is the yield stress of the material,  $\sigma_0$  is a friction stress, which includes contributions from solutes and particles but not from dislocations  $k$  is a constant and  $d$  is the grain diameter.

For wrought products the same relationship applies; however, the cooling rate is less important as the finer grain structures are provided through the thermo-mechanical work the material receives. In addition to a finer grain structure, an increased cooling rate also helps promote the heterogeneous nucleation of grains providing an equiaxed grain structure which is usually preferred over a columnar grain structure. This provides uniform mechanical properties as well as the better overall strength, increased fatigue life, more finely dispersed second phases and porosity, less macrosegregation, improved feeding to compensate for shrinkage and less hot cracking, improved surface properties, and improved machinability and fabricability (Beckermann, 1997).

Many of the improvements from a higher cooling rate stated above are not relevant to wrought product; however, the reduction in macrosegregation is beneficial as this can cause the non-uniform properties of an ingot, which may be subject to rejection. Due to the low diffusivity of solutes within the solid, the macrosegregation cannot be recovered through processes such as a homogenisation heat treatments (Stefanescu et al., 1988). Therefore the cooling rate still needs to be considered and Chapter 6 will discuss the non-uniform properties of a single as-worked ingot due to the macrosegregation of oxides and niobium carbides.



# Chapter 4. Air-Gap Formation and Heat Transfer between Casting and Mould Interface

## 4.1 Introduction

The heat transfer between a solidifying object and a mould is a fundamental process parameter for the users and designers of casting processes, including static castings, Vacuum Arc Re-melt, Electro Slag Re-melt, directional solidification etc.

The amount of heat that can be transferred from the melt to the mould per degree temperature difference is known as the Interfacial Heat Transfer Coefficient (IHTC) as described by several authors. (Zhang et al., 2010, Arunkumar et al., 2008, Ho and Pehlke, 1985, Nishida et al., 1986, Hu et al., Spinelli et al., 2012, Zhi-peng et al., 2008, Santos et al., 2001). It has been found that the IHTC is dependent on many factors including mould/chill material (Şahin et al., 2006), alloy composition (Kim et al., 2006), alloy superheat (Coates and Argyropoulos, 2007, Ferreira et al., 2005), surface roughness (Coates and Argyropoulos, 2007), surface coatings (Konrad et al., 2011, Broucuret et al., 2001), applied pressure (Zhi-peng et al., 2008), and casting surface orientation (Griffiths, 1999). Control of the IHTC is desirable for many reasons, including controlling solidification rates to prevent cracking and minimize segregation, minimize unwanted phases such as the Laves phase, controlling the location of the last material to solidify avoiding unwanted features such as piping and for mass produced parts the minimum amount of time before ejection from the mould is permissible.

Fundamentally, the majority of all alloys and metals will contract on cooling from the liquidus temperature and will expand on heating from room temperature. As discussed by Kron (Kron and Fredriksson, 2005) and Lagerstedt (Lagerstedt et al., 2005) the total

amount of shrinkage within the alloys cast is due to a combination of thermal shrinkage, condensation of vacancies and solid state phase changes. In this study the experimental measurement of shrinkage will capture all three of these aspects, although for the alloys cast solid state phase changes are not deemed to be significant.

Commonly metal permanent moulds are used for casting alloy ingots, and the overall effect of the contracting ingot and the expanding mould is the formation of an air-gap. Air is an extremely good insulator, relative to the conductivity of the mould material, and therefore will dramatically decrease the IHTC between the metal and the mould; this is in agreement with Nishida and Ho (Nishida et al., 1986, Ho and Pehlke, 1984). Therefore to achieve the maximum IHTC, perfect contact between the melt and the mould is sought-after. Casting processes such as high-pressure die casting can get close to this; however even during the liquid stage voids between the melt and the mould are present due to mould surface roughness as found by Coates et al (Coates and Argyropoulos, 2007).

During the first stage of casting, there are three contributing heat transfer mechanisms as described by Ho (Ho and Pehlke, 1984), as illustrated in Figure 4-1 (Campbell, 2011b). Convective heat transfer can be neglected due to the small size of the gap; however, it is found to increase as the gap widens allowing circulation (Nishida et al., 1986).

1. Solid conduction through the points of contact (annotated as 1 in figure below).
2. Gas conduction across the void (annotated as 2 in figure below).
3. Radiation across the void (annotated as 3 in figure below).

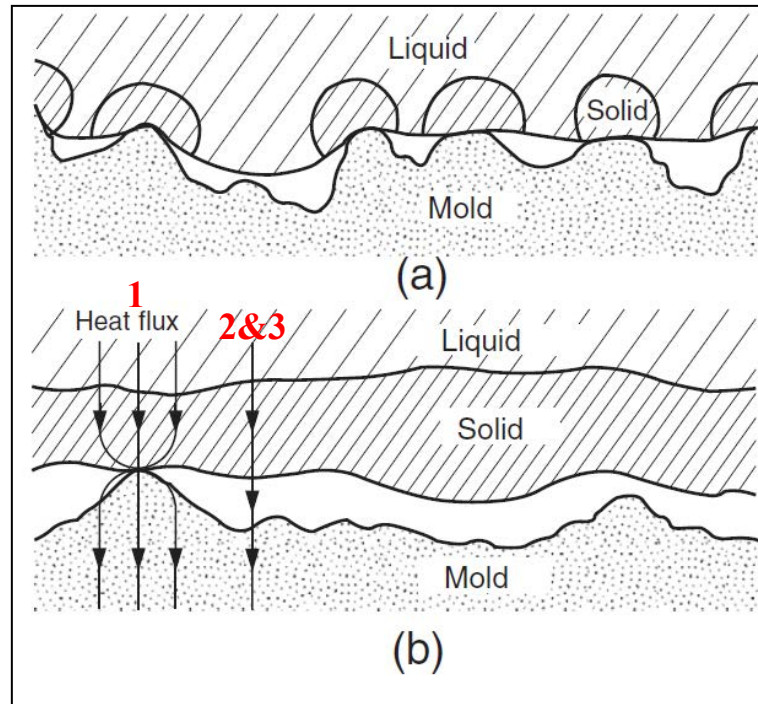


Figure 4-1 – Metal–mould interface at an early stage when solid is nucleating at points of good thermal contact. Overall macroscopic contact is good at this stage (a). Later (b) the casting gains strength, and casting and mould both deform, reducing contact to isolated points at greater separations on non-conforming rigid surfaces (Campbell, 2011b).

Throughout this stage the solid conduction through the points of contact dominates the heat transfer, but as the melt begins to cool further and contract it pulls away from the moulds' surface; simultaneously the mould is heating up and expanding resulting in a continuous void or air-gap. Heat energy can now only be transferred from the melt to the mould through the newly formed air-gap by gas conduction and radiation. Casting within a vacuum would greatly reduce gas conduction, so in such castings (e.g. solidified ingot in VAR) radiation is the dominant heat transfer mechanism.

There has also been some different approaches to the consideration importance of radiative heat transfer, with Nishida (Nishida et al., 1986) neglecting it, while Dong used a simplified radiative heat transfer term (Dong et al., 2011), and Kim used a combined IHTC representing both radiative and conductive terms (Kim and Lee, 1997).

These are different approaches likely to be due to the use of different casting methods, casting sizes and alloys cast. Radiative heat transfer is not affected by the size of the air-gap; however, conductive heat transfer is dramatically reduced with an increase in the air-gap. A casting method such as high pressure die-casting restricts the formation of the air-gap and thus the conductive heat transfer is not affected so greatly. With small castings such as centrifugally cast valve heads, the air-gap will be minimal and a continuous void is unlikely to form; for large castings such as continuous direct-chill and VAR, an increased air-gap is expected as shown by Vynnycky (Vynnycky, 2009) thus reducing the conductive heat transfer. Radiative heat flux has a power 4 relationship with temperature (Eq. 4-2), and therefore the type of alloy cast will play a major role in the amount of energy transferred by radiation.

Previously the size of the air-gap during solidification has been studied mainly for aluminum alloys (Gunasegaram and Nguyen, 2006, Trovant and Argyropoulos, 1998, Kim and Lee, 1997), with a little work on iron (Lagerstedt et al., 2005) and copper (Kron and Fredriksson, 2005) alloys.

The purpose of this study was to measure the magnitude of the air-gap and how this affects the conductive and radiative heat transfer for a low melting point alloy, aluminium alloy Al-7Si-0.3Mg (identified as LM25 from here onwards), and a high melting point alloy, nickel-based alloy XD1102, when cast independently into the same size mould. The casting experiment of the LM25 alloy has been used to demonstrate the method for a relatively inexpensive, commercially available alloy.

## 4.2 Experimental Set-Up

Casting experiments were performed using the aluminium alloy LM25, superheated by approximately 155°C in an air induction furnace to 770°C, and the nickel-iron alloy, XD1102, superheated by roughly 135°C to 1455°C. For both alloys, the superheated melt was top-poured into a permanent cylindrical, H13 steel, mould held at room temperature with dimensions as shown in Figure 4-2a. The duration of pouring was around 12 seconds and the melt was poured from a height of approximately 50 mm above the mould.

The mould was stood on a slab of fireclay to reduce the heat transfer through the base of the mould into the ground. Both the base of the fireclay slab and the mould were supported by a bed of sand, thus increasing the number of points of contact between mating surfaces giving rise to stability during the filling procedure (Figure 4-4). Temperature and displacement histories for both the mould and the casting were recorded at mid-height of the mould; this allowed the assumption of an infinity long cylinder and the cooling effects from the top and the bottom of the mould could therefore be neglected.

The displacements were measured using Micro-Epsilon OptoNCDT 17-10 laser triangulation sensors with a measuring accuracy of 0.5 µm. The displacement of the outer surface of the mould was measured directly. Other work have used a silica rod through a hole in the mould wall and into the melt to measure the contraction of the casting, by monitoring the position of its outer end using a Linear Variable Differential Transformer (LVDT) sensor. This assumes that the melt solidifies around the rod; that the solidifying skin is strong enough to pull the rod inwards as it contracts and that the

rod does not break, possibly from stress as the casting shrinks vertically. The LVDT sensor applies very little force onto the rod, but may require careful electrical and mechanical setting up for maximum accuracy. Silica rod is chosen as its low thermal expansion coefficient is favourable; however, difficulty in successfully solidifying the melt around the rod, during the initial stages of solidification, has been encountered (Nishida et al., 1986).

In this work, to measure the first stages of solidification, a pig tail on the end of a tungsten rod was positioned up against the inside wall of the mould; the tungsten rod continued through a pre-drilled hole in the mould to the outer surface. The pig tail increased the mechanical keying with the melt, so as it solidifies it does so around the pig tail to ensure the displacement could be accurately measured. A target on the outer end of the tungsten rod then allowed the laser sensor to measure its position without applying any mechanical load (Figure 4-2b). The pig tailing of a silica rod was considered, however for the XD1102 casting the end of the rod would be above the glass transition temperature; on contraction of the melt the quartz rod would then stretch and displacements would not be captured accurately.

Both laser sensors were positioned perpendicular to their target of interest within an air-cooled stainless steel housing for protection. The housing was also coated in refractory wool keeping the temperature increase of the stainless steel to a minimum; this prevented any significant movement within the housing itself which would have been captured by the laser sensors.

The mould temperature, for all experiments, was measured using three Type-K Inconel sheathed thermocouples 1 mm in diameter and with a grounded simplex junction.

These were then slotted into pre-drilled 1.1 mm holes with varying depths of 3, 10 and 18 mm from the mould's outer surface. An approximation of the moulds' inner surface temperature could then be calculated by an inverse method using these temperature measurements.

The casting temperature was measured using a Type-K thermocouple for the LM25 casting and a Type-S thermocouple for the XD1102 casting. For both castings the internal thermocouples were positioned as close to the pig tail in the tungsten rod as practical without distorting the solidification of the ingot; all thermocouples were positioned at the same height as the tungsten rod (Figure 4-3). The outputs of the lasers and the thermocouples were sampled and recorded at 1000 Hz using a National Instruments A-D converter and a personal computer. A medium speed camera (AVT Pike F032) was used to determine the start of the pour, the contact between the melt and the tungsten rod, and the finish of the pour. Any displacement readings captured by the lasers during this transition could be investigated, and instances such as mould rocking could be neglected. For all experiments a minimum of 60 minutes was allowed for the melt to cool. Extensive use of MATLAB has been used to deal with the large amounts of data obtained from the experiments and the code can be found in Appendix B.

Note:

*For all sensor displacements presented a positive value indicates expansion and a negative value contraction. This experimental set-up measures the displacement of the outer surface of the mould and the melts' surface displacement via a tungsten rod. To compensate for both the expansion of the mould wall thickness and change in length of the tungsten rod; a prediction of the expansions, using the average temperature of the three embedded thermocouples, has been subtracted from the sensor readings.*

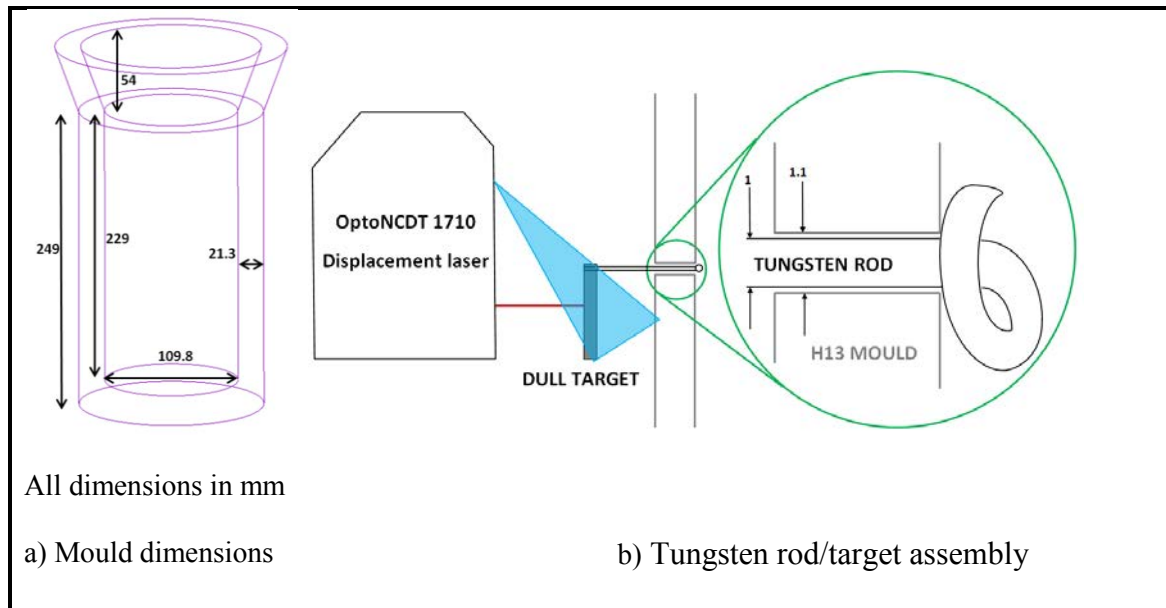


Figure 4-2 – Schematic diagrams displaying the dimensions of the H13 steel mould used during the air-gap experiments and the laser triangulation and tungsten rod set up to capture the displacement of the melt.

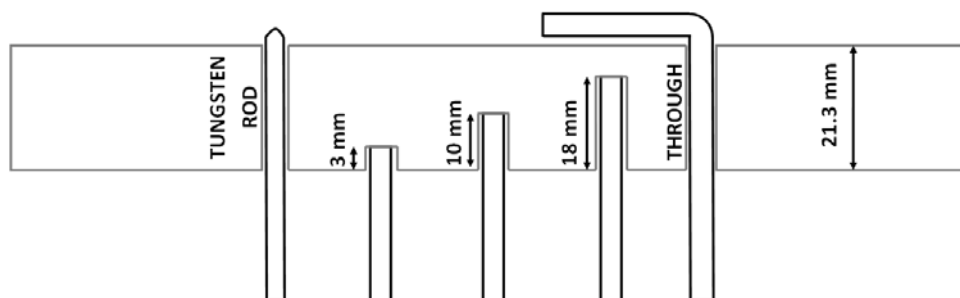


Figure 4-3 – Thermocouple locations set into the mould wall at 3, 10 and 18 mm from the moulds outer surface.





Figure 4-4 – Photograph of the air-gap experimental set-up displaying the mould and housings for the laser triangulation sensors sitting on top of the slab of fireclay.

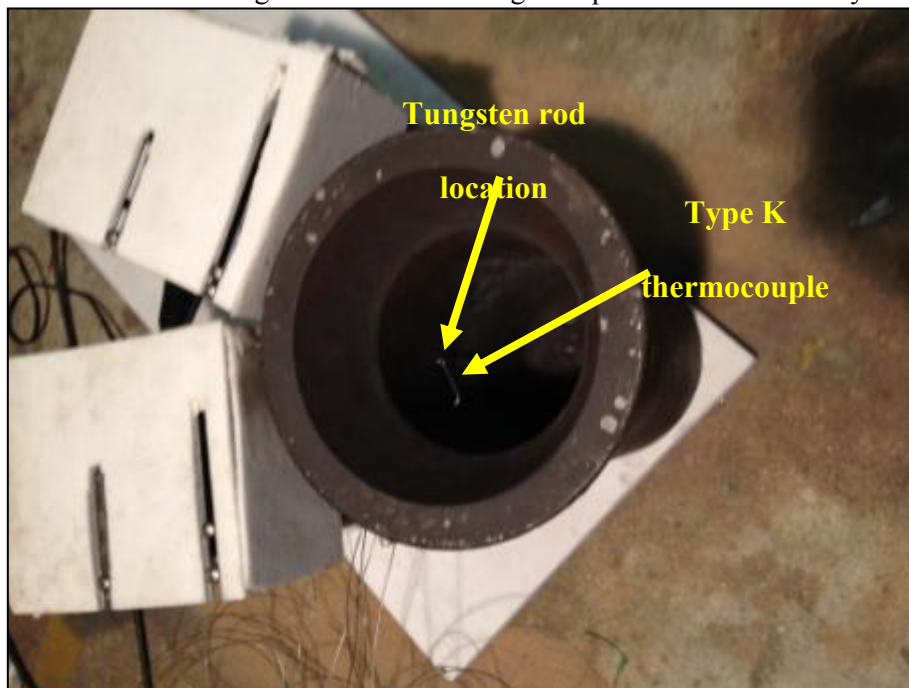


Figure 4-5 – Photograph of the air-gap experiments displaying the internal configuration of the Type K melt thermocouple and the protruding tungsten rod.

### 4.3 Temperature and Displacement Results for LM25

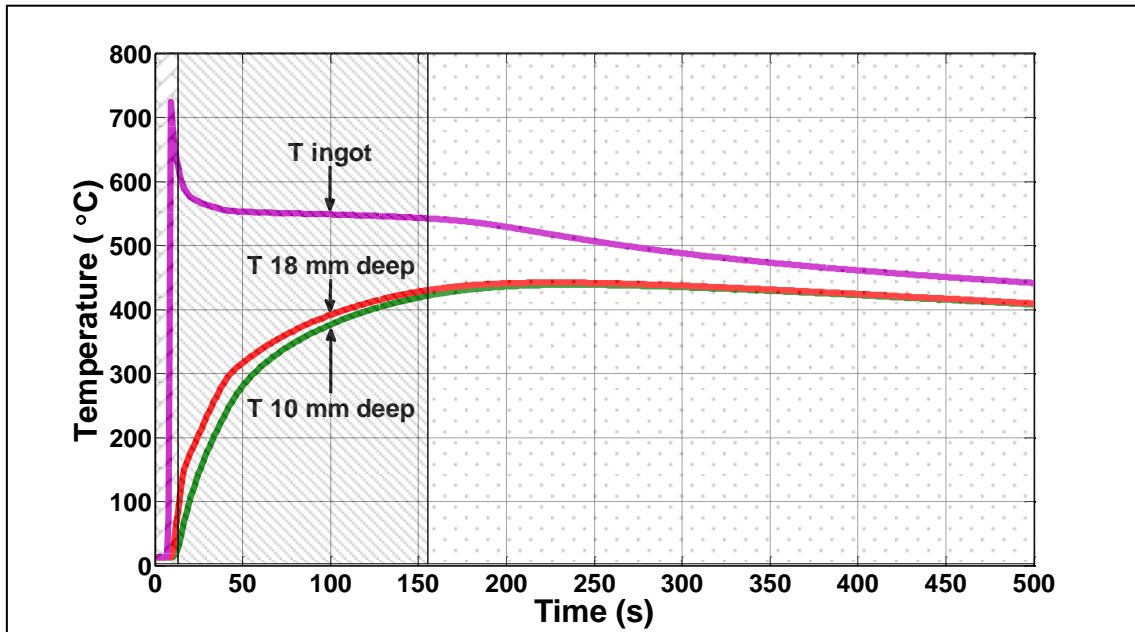


Figure 4-6 – Graph to show the first 500 seconds of the measured temperature readings for the LM25 casting.

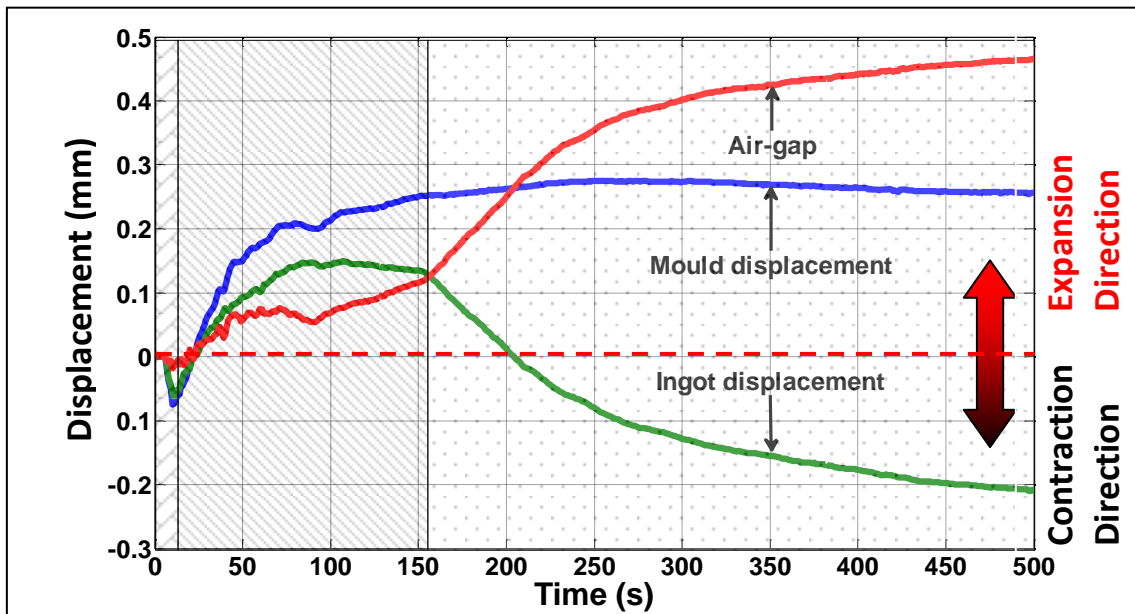
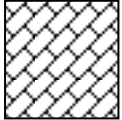
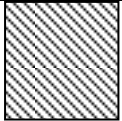
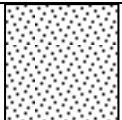


Figure 4-7 – Graph to show the first 500 seconds of the measured experimental displacements for the LM25 casting.

Presented in Figure 4-6 and Figure 4-7 are the first 500 seconds of the experiment for temperature and displacement measurements respectively; as illustrated in the figures by the shading, the initial 500 seconds can be split into three distinct regions as described below:

*( $T_l$  and  $T_s$  represent the liquidus and solidus temperatures of the alloy respectively)*

	<p><math>T_{\text{melt surface}} &gt; T_l</math> - The melt fits to the shape of the inner mould surface with almost liquid to solid contact as described by Ho (Ho and Pehlke, 1984).</p> <p>As the mould heats up and expands the melt follows this expansion, at this point it is likely a thin solidified layer has formed, however with insufficient strength to retain the melts position relative to the mould expansion.</p>
	<p><math>T_l \geq T_{\text{melt surface}} \geq T_s</math> - The mould is still heating up and expanding, but the casting is now likely a combination of a thin solidified skin and a mushy layer (point of a solid-liquid equilibrium in the alloy's phase diagram). The sensor is fluctuating showing that movement of the mushy skin is occurring, and liquid may still be flowing in this region. This layer is continually gaining strength during this period and begins to resist the metallostatic head pressure from the liquid above and the rate of movement following the expansion of the mould is reduced and thus creates the initial stages of an air-gap.</p>
	<p><math>T_s \geq T_{\text{melt surface}}</math> - A sufficiently thick solidified skin is now present with enough mechanical strength to withstand the pressure from the melt above; it begins to contract on cooling and draws the tungsten rod in smoothly.</p> <p>The mould is still expanding but now at a reduced rate and towards the end of the time interval is starting to cool and itself begins to contract.</p> <p>“Contraction is elastic-plastic”</p>

The full duration of the experiment for both temperature and displacements is illustrated in Figure 4-8 and Figure 4-9 respectively.

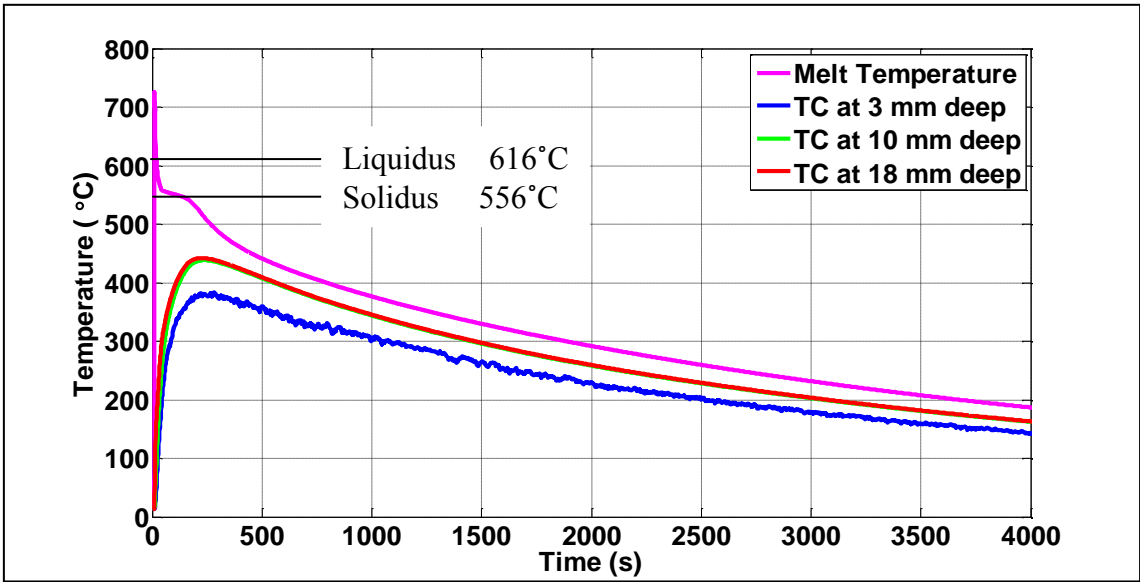


Figure 4-8 – Graph to show the full length of experimental temperature readings for the LM25 casting.

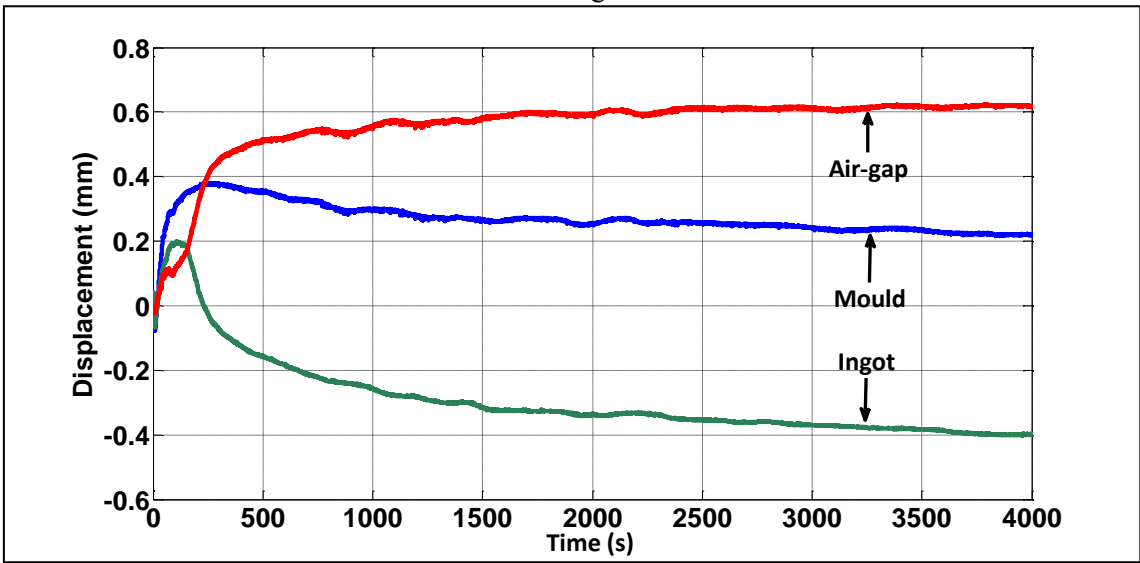


Figure 4-9 – Graph to show the full length of experimental displacement readings for the LM25 casting.

Figure 4-9 demonstrates that the air-gap experiences its greatest enlargement during the early stages of the casting when the mould is still heating up and expanding, and the melt has just begun to cool and contract; thus the two are moving in opposing directions. As the mould then begins to cool, and also contract, the rate of increase in the size of air-gap is reduced. After this point the cooling rate for both the melt and the mould are near equivalent and the gradual increase in air-gap is governed by the increased thermal expansion coefficient of the melt. Although it is difficult to compare the results to literature due to alloy chemistry variations, casting diameter, mould material and mould wall thickness, a similar trend has been observed to the above by Kron (Kron et al., 2005).

What can be seen in Figure 4-8 is that the thermocouple at 3 mm deep is reading approximately 70°C lower than the 10 and 18 mm deep thermocouples. This difference was greater than expected and has been attributed to the thermocouple not having a good fit into the pre-drilled hole unlike the other two thermocouples. It is also possible that the thermocouple is being cooled by the ambient air giving a false reading. The combination of the two has led to a very unstable temperature reading, however for the method chosen, see below, only the two thermocouples at 10 and 18 mm deep were used to approximate the moulds' inner surface temperature.

Three mathematical approaches have been explored for the approximation of the mould's inner surface temperature, these are: extrapolation using the three known temperature readings (Konrad et al., 2011), a finite difference method (Şahin et al., 2006, Lagerstedt et al., 2005) or an inverse model (Broucaret et al., 2001, Arunkumar et al., 2008). All three methods of approximation are presented in Figure 4-10. The extrapolation method seems to over-predict the temperature; this is believed to be due to

using the thermocouple at 3 mm deep within the approximation. The finite difference temperature looks reasonable; however, it displays temperature fluctuations of  $\pm 5^{\circ}\text{C}$  as illustrated in Figure 4-11. The inverse method displays a similar temperature trend as the finite difference method without the fluctuations; hence this method has been used for the approximation of the moulds' inner surface temperature from here on. (See Appendix B.3 for the MATLAB code)

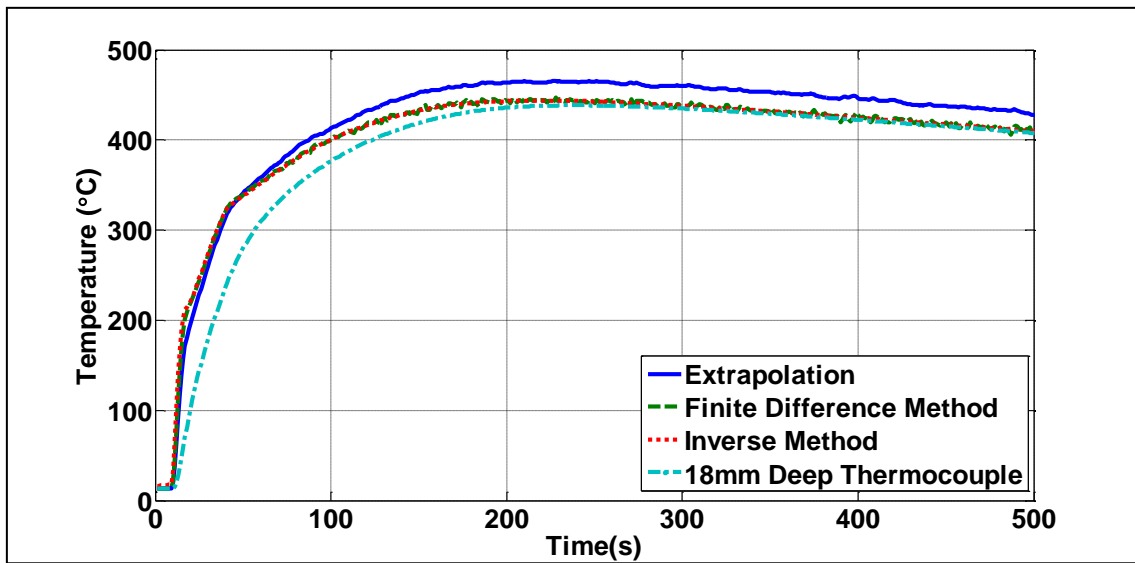


Figure 4-10 – Graph to show the predictions of the internal moulds surface temperature for the first 500 seconds using the inverse, finite difference and extrapolation techniques.

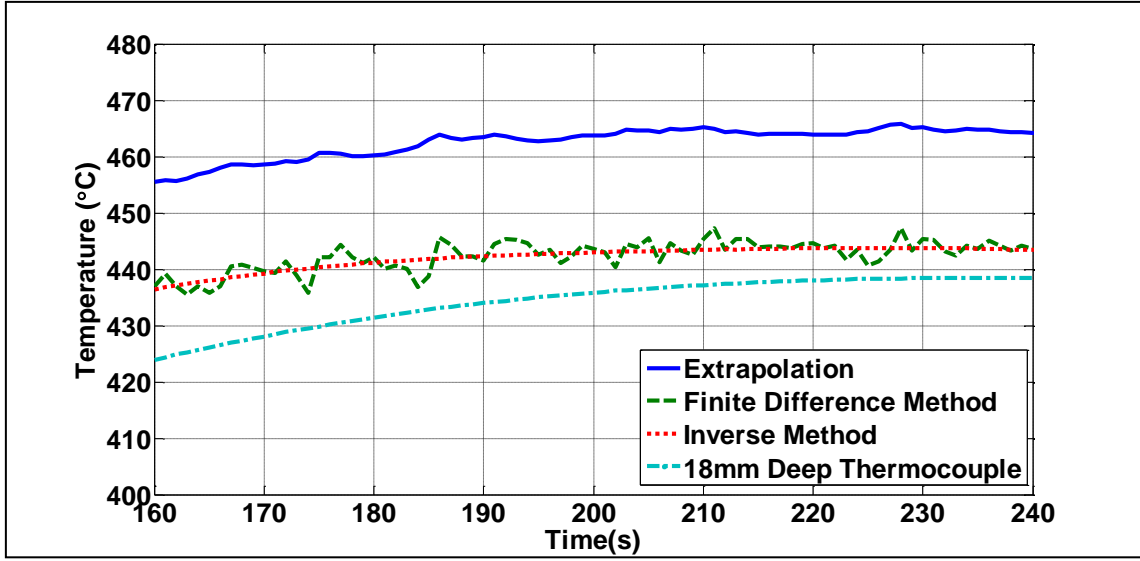


Figure 4-11 – Graph to show the fluctuations of  $\pm 5^{\circ}\text{C}$  when using the finite difference method.

#### 4.3.1 Calculations of IHTC

Using the approximated mould's inner surface temperature and treating the thermocouple in the mould cavity as the melt surface temperature, along with the compensated size of the air-gap, the IHTC can now be calculated by the superposition of the heat flux,  $q$ , of the conductive,  $q_c$ , and radiative,  $q_r$ , terms:

$$q_c = \frac{k_{air}A(T_{cs} - T_{ms})}{\Delta r_{gap}} \quad \text{Eq. 4-1}$$

$$q_r = \frac{\sigma_{sb}A(T_{cs}^4 - T_{ms}^4)}{\frac{1}{\epsilon_{metal}} + \frac{1}{\epsilon_{mould}} - 1} \quad \text{Eq. 4-2}$$

$$IHTC = \frac{q_c + q_r}{A(T_{cs} - T_{ms})} \quad \text{Eq. 4-3}$$

Where  $k_{air}$  is the thermal conductivity of air in the gap (calculated using the average temperature between metal and mould) (Haynes, 2012-2013),  $A$  is the heat transfer area,  $T_{cs}$  and  $T_{ms}$  are the temperatures of the casting and mould surfaces respectively,  $\Delta r_{gap}$  size of the air-gap,  $\sigma_{sb}$  Stefan-Boltzmann constant, and  $\epsilon_{metal}/\epsilon_{mould}$  are the

emissivity of the metal and mould surfaces respectively which are temperature dependent.

As found by Ho and Nishida (Ho and Pehlke, 1985, Nishida et al., 1986), as the air-gap begins to form, creating the continuous void between the melt and the mould, the IHTC is dramatically reduced as the point to point conduction has now been lost. The reduction in IHTC can be seen in Figure 4-12. The undulations present between 25 to 100 seconds is due to the sensitivity of the IHTC with the size of the air-gap; during this time frame the experiment had yet to stabilise and both movements in the mould and the casting were detected by the laser sensors as displayed in Figure 4-7 .

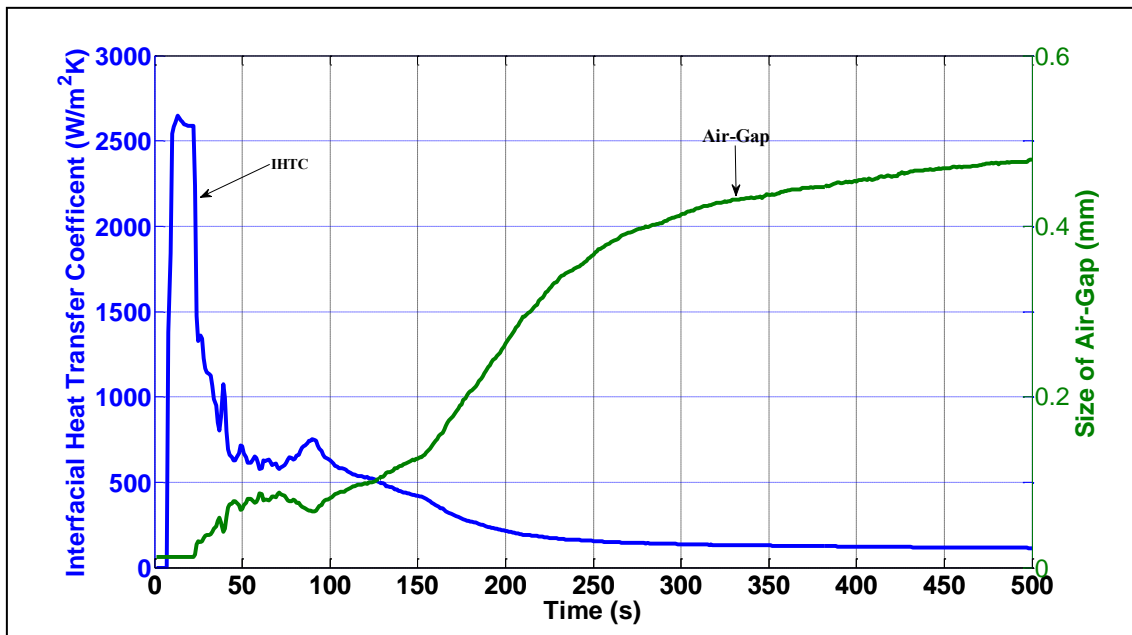


Figure 4-12 – Graph to show the calculated interfacial heat transfer coefficient for the LM25 casting.

#### 4.3.2 Radiative to Conductive Ratio, $Q_r:Q_c$

Using the calculated values from Eq. 4-1 and Eq. 4-2 the ratio of radiative to conductive heat transfer has been calculated per time step. It is found that during the early stages of the casting, when the air-gap has not fully formed, the radiative heat transfer is minimal



and only contributes up to 4% of the heat transfer by heat conduction. However, as the air-gap starts to increase the radiative heat transfer increases towards its maximum for this experiment of 18%. As the melt is allowed to cool, and due to the  $T^4$  relationship for radiation, the contribution of the radiative heat transfer begins to decrease. At this point the air-gap is still increasing but at a slower rate due to the contraction of both the melt and the mould; this relationship can be seen in Figure 4-13.

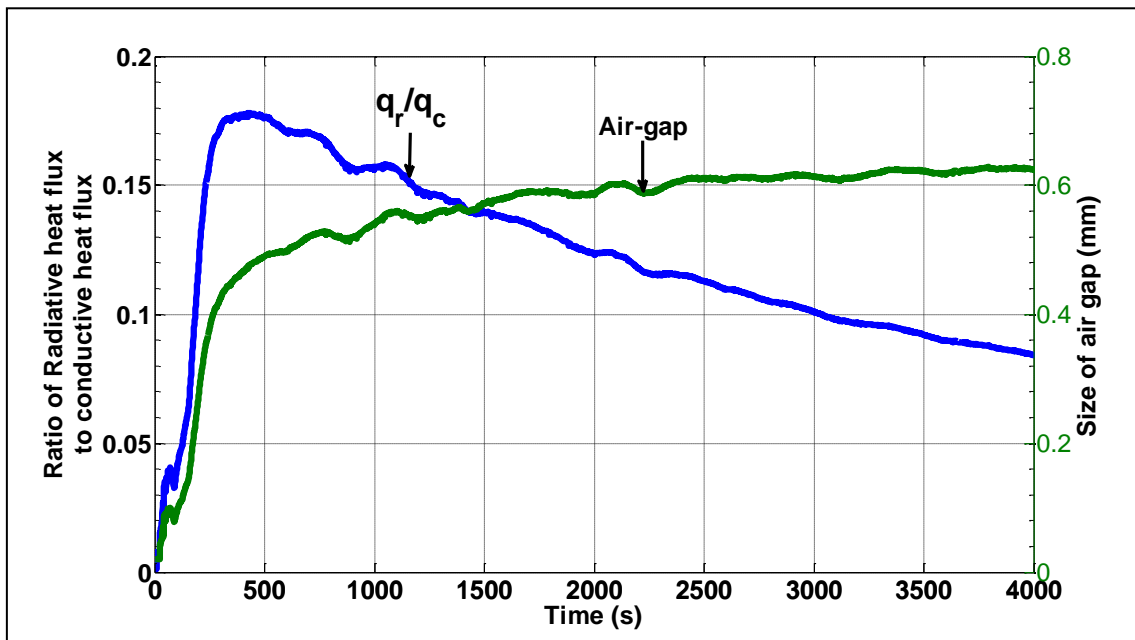


Figure 4-13 – Graph to show the ratio of radiative to conductive heat transfer with the size of air-gap for the LM25 casting.

#### 4.3.3 Including a Numerical Model – ProCAST

The ESI software ProCAST was used to simulate the solidification stages of the described casting in 3-D at the macroscopic level. Initially a CAD model, for both the mould and the volume of fluid, was modelled using the software ProEngineer. This model was then imported into ProCAST as an IGS file so that the inbuilt meshing software could create a constant tetrahedral mesh (Figure 4-14).

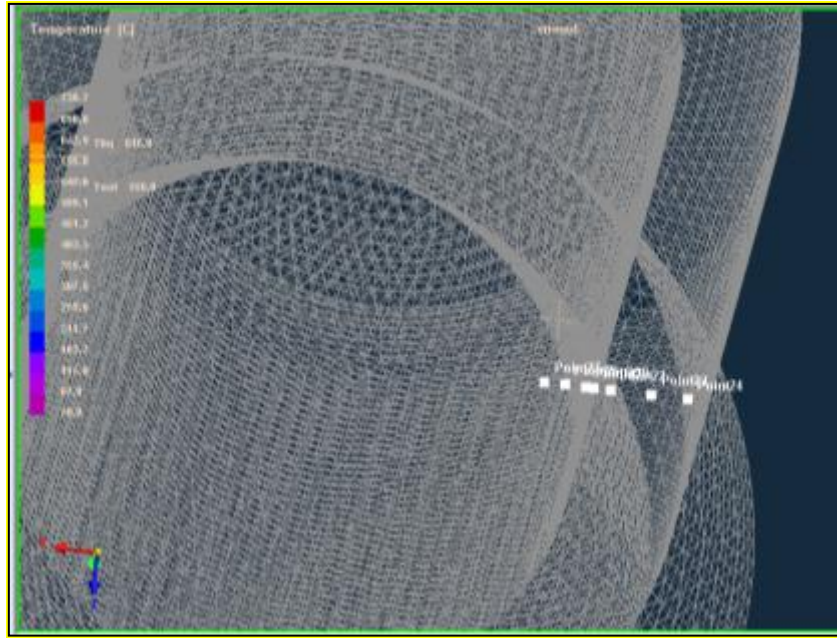


Figure 4-14 – Screen shot of the 4 mm surface mesh used on the H13 mould

Once a mesh was created, ProCAST was used to study the thermal balance and the development of stresses and strains throughout the solidification process. The model incorporates heat transfer with radiation with view factors, fluid flow and stresses fully coupled with the thermal solution.

At each time-step, the heat transfer per cell is calculated by the interpolation of temperature across the nodal points. An enthalpy method is adopted to handle the phase transition problem during solidification.

The underlying calculations used for the heat, radiation and flow module within ProCAST are as described by Dai (Dai, 2009) and summarised below :

Heat Module:

The heat module conserves heat by taking into account both the phase change and the transport of heat through both the fluid and the solid phases.

$$\frac{\partial H}{\partial t} + \vec{U}_s \nabla H + \rho C_p (\vec{u} - \vec{u}_s) \nabla T - \nabla (K \nabla T) = S \quad \text{Eq. 4-1}$$

where  $\rho$  is the density,  $C_p$  is the specific heat,  $K$  is the thermal conductivity,  $S$  is the heat source term,  $T$  is the temperature,  $\vec{u}$  is the average velocity and  $H$  is the volumetric enthalpy field which is assumed to be a function of  $T$  and given by the equation:

$$H(T) = \int_0^T \rho C_p(\theta) d\theta + L(1 - f_s(T)) \quad \text{Eq. 4-2}$$

where  $L$  is the latent heat of fusion and  $f_s$  is the volumetric fraction solid.

Radiation Module:

During casting of high-temperature alloys, radiation plays an important role in the heat transfer from the casting to the environment; this is discussed further in Chapter 4. The emitted flux  $q_N^{\text{out}}$  from each side  $i$  can be written as follows:

$$q_i^{\text{out}} = \varepsilon_i \sigma T^4 + (1 - \varepsilon_i) q_i^{\text{in}} \quad \text{Eq. 4-3}$$

where  $i$  is a given surface,  $\sigma$  is the Stefan-Boltzmann constant,  $\varepsilon$  is the emissivity of the given surface,  $T$  is the given surface temperature, the combined first term represents the radiant heat flux emitted from the surface  $N$  and the second term represents the radiant heat flux absorbed into the surface  $i$  and given by the following:

$$q_i^{in} = \sum_{j=1}^N q_j^{out} F_{ij}, i = 1 \dots N \quad \text{Eq. 4-4}$$

where  $F_{ij}$  is the view factor representing the fraction of the radiant energy leaving the surface  $j$ , which irradiates the surface  $i$ .

Flow Module:

To calculate the fluid flow during solidification, a unit set of average equations are set to solve over the liquid, mushy and solid regions. Assuming that density  $\rho$  is constant and uniform in the liquid and solid phases, the average velocity,  $\vec{u}$ , can be defined as:

$$\vec{u} = f_S \vec{u}_S + f_L \vec{u}_L \quad \text{Eq. 4-5}$$

where  $\vec{u}_S$  and  $\vec{u}_L$  are the velocity fields in the solid and the liquid respectively,  $f_S$  and  $f_L$  are the volumetric fractions of the solid and the liquid respectively. The average velocity  $\vec{u}$  is given by:

$$\rho \left( \frac{\partial \vec{u}}{\partial t} + \frac{1}{f_L} (\nabla \vec{u}) \vec{u} \right) - 2\mu \nabla \dot{\epsilon}(\vec{u}) + \frac{\mu}{K} f_L (\vec{u} - \vec{u}_S) + f_L (\nabla P) = f_L \vec{f} \quad \text{Eq. 4-6}$$

$$\nabla \vec{u} = 0 \quad \text{Eq. 4-7}$$

where  $\dot{\epsilon}(\vec{u})$  is the strain rate tensor,  $P$  is the pressure field,  $\mu$  is the dynamic viscosity,  $K$  is the permeability of mushy zone and  $\vec{f}$  is the sum of any body force given by the user with the buoyancy term.

#### 4.3.3.1 Mesh Size Sensitivity Study

Simulation accuracy usually comes at the expense of computation time and is largely dependent on the number of elements present within the model. ProCAST has the ability to assign boundaries with a finer mesh which can incrementally increase away from the boundary as a percentage of the previous element. During this study it was found that for thermal-only simulations this incremental increase reduced computation time with little to no impact on the perceived accuracy. However, complications arose when stress-modelling was included within the simulation and hence a constant mesh was chosen for this model.

At the interface between the casting and the mould, the coincident mesh setting was chosen to split the node into two allowing the casting and the mould to have independent temperatures at the same location. This mesh setting is a requirement for models which include stress/displacement as the interface between the casting and the mould gradually moves apart as the air-gap forms. To allow for the coincident mesh at the interface, both the mould and the casting volume had the same mesh size.

In order to minimise computation time, but retain accuracy, a mesh sensitivity study was performed using constant mesh sizes of 2, 4, 8 and 16 mm with all other parameters unchanged. The computation times for the differing size meshes are displayed in Table 4-1. As indicated within the table, the 2 mm mesh only completed 22% of the simulation before the computer automatically shut down aborting the run; if the model was to continue at the same rate the simulation would have taken 152 hours. This is a conservative estimate as the model files become progressively larger and therefore are more resourceful on the CPU increasing the time required to perform each step. It is

also demonstrated that the size 16 mm mesh is unstable and the simulation could not be completed; mesh sizes 4 and 8 mm ran to completion.

Table 4-1 – Simulation Time for Differing Mesh Sizes

Mesh size	Steps Complete	% complete	CPU time (hours)	Total time for Completion (hours)	Comments
2	995	22	34.63	157	computer shut down
4	2154	100	7.12	7.12	
8	2052	100	0.94	0.94	
16	1347	66	0.83	1.25	Software crashed

The simulated temperature plots for all mesh sizes are illustrated in Figure 4-15 and due to the increased number of elements in the 2 mm mesh, it is assumed to be the most accurate simulation out of the four repeats. The percentage deviation of the 4, 8 and 16 mm meshes in respect to the 2 mm mesh are plotted in Figure 4-16. This plot is only valid up to 911 seconds after which the 2 mm mesh run was aborted. It was unnecessary to run this model again due to high level of coherence of the 2 and 4 mm mesh sizes after an initial transient within the first 200 seconds. Beyond this point there was less than one percent difference between the 2 and the 4 mm meshes. During the initial 200 seconds the 4 mm mesh deviated, at worst, just three percent from the 2 mm mesh; an acceptable value for a small time frame and importantly a computational time less than seven times that of the 2 mm mesh. It was decided that the use of a mesh size of 4 mm would provide the best accuracy whilst providing a reasonable computation time.

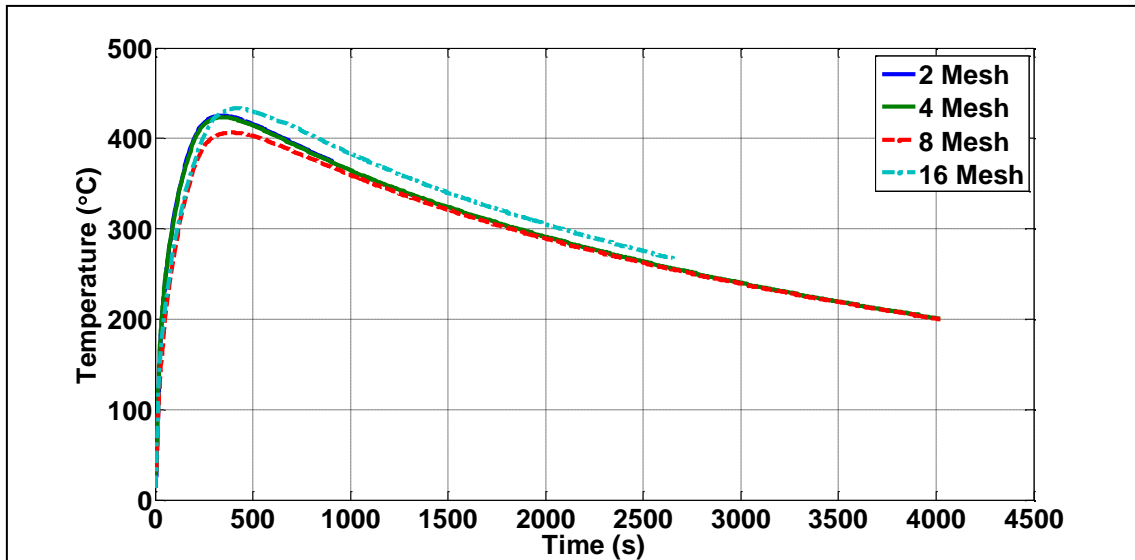


Figure 4-15 – Mesh sensitivity study graphically showing the predicted mould temperatures for the LM25 casting using ProCAST with a constant tetrahedral mesh size of 2, 4, 8 and 16 mm.

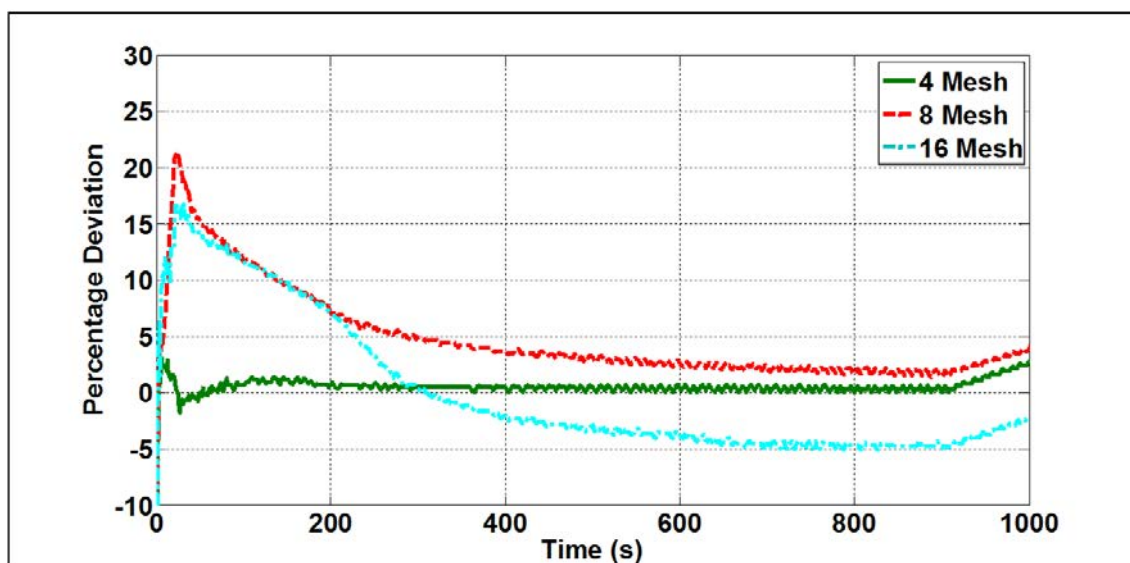


Figure 4-16 – Percentage deviation of the 4, 8 and 16 mm mesh sizes in comparison to the 2 mm mesh size. After 911 seconds the computer shut down for the 2 mm mesh and hence the values start to diverge beyond this point.

#### 4.3.3.2 Stress Sensitivity Study

In a similar manner to the mesh size sensitivity study, an investigation was carried out using the different stress models available in ProCAST; elastic, elastic-plastic and

visco-elastic plastic. Presented in Figure 4-17 are the air-gap predictions for each stress calculation which displays a good agreement between all three models, and unlike the mesh size sensitivity study there was little difference in the computational time for each stress type. Due to the unaffected computational time the visco-elastic-plastic model was chosen for the simulations going forward, as this is the most thorough stress model.

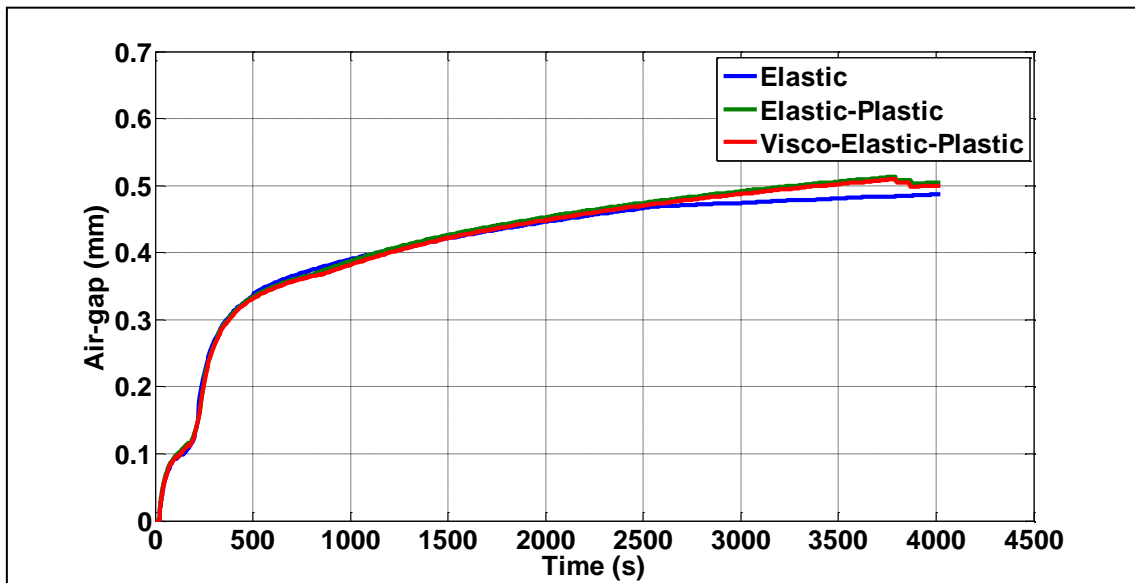


Figure 4-17 – Stress sensitivity study graphically showing the predicted air-gap for the LM25 casting using ProCAST with a constant tetrahedral mesh size of 4 mm and the elastic, elastic-plastic and visco-elastic plastic stress models.

#### 4.3.3.3 Inputs into the Model

In order to simulate the casting process, ProCAST required initial conditions such as the temperature of the melt and mould, the percentage fill of the melt, the length of time for the simulation, the maximum time step and the material types. The inputted values were chosen to correlate with the casting experiments as described above.

Thermo-physical properties are also necessary for both the melt and the mould such as thermal conductivity, emissivity and latent heat of fusion. ProCAST has an inbuilt



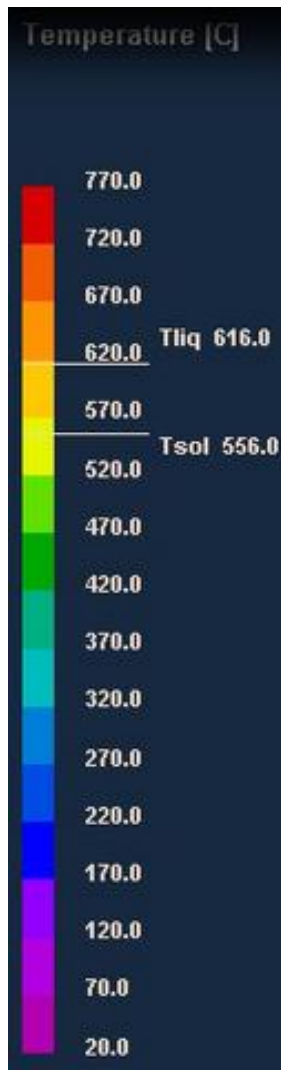
material property database to include information for an LM25 equivalent and H13 steel. These figures were verified against supplier's data and determined to be representative.

Boundary conditions are also essential; this can either be between the mould and the environment or between any two interfaces. At these points IHTCs have to be applied and can be treated in three ways:

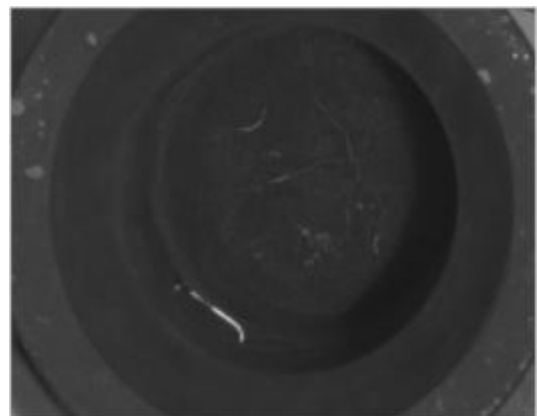
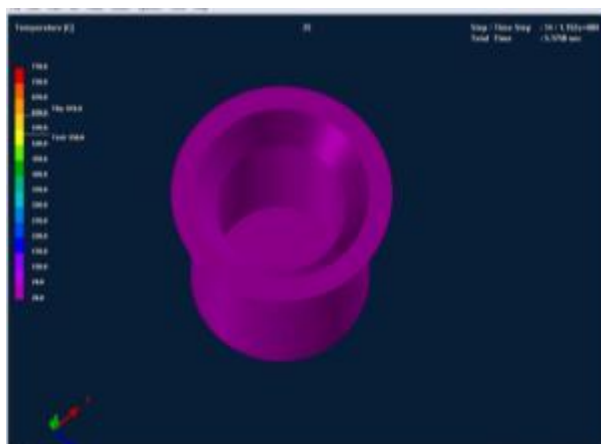
1. As a constant
2. As a proscribed IHTC dependent only on time (i.e. using the data in Figure 4-12)
3. By iteratively predicting the IHTC within the model based upon the size of the air-gap using the initial IHTC from Figure 4-12.

It was found that if the initial IHTC was kept constant, the mould temperature was over-estimated and the melt temperature under-estimated, also seen by Kron (Kron et al., 2004). The time dependant IHTC had to be applied identically across the entire ingot and mould interface. However, in practice the local size of the air-gap will vary, leading to a varying IHTC across different regions of the interface, as found by Arunkumar (Arunkumar et al., 2008). Therefore for the simulation results a gap-dependent IHTC was used with an initial value of  $2569 \text{ W/m}^2\text{K}$ . Typical ProCAST run parameters can be found in Appendix C.

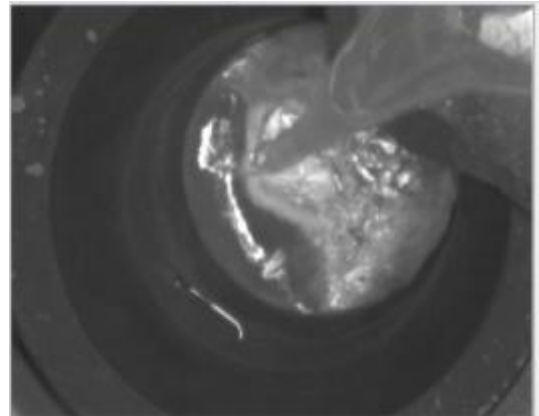
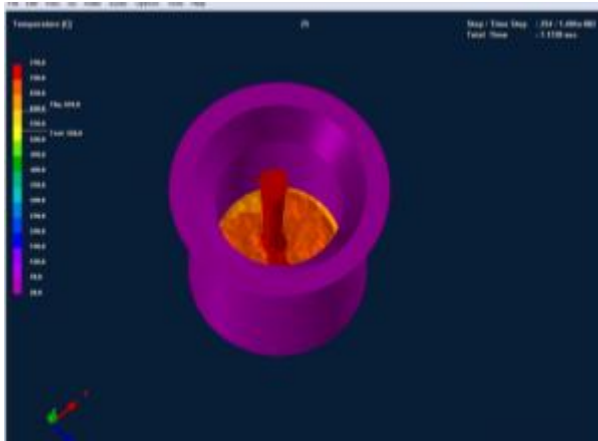
The model was run for the same duration as the casting experiment to include both the pouring and the solidification of the melt. Illustrated in Figure 4-18 are equivalent time steps between the ProCAST simulation and the casting experiment which shows a good agreement with filling time and the formation of pipe on the melt's surface as it solidifies.



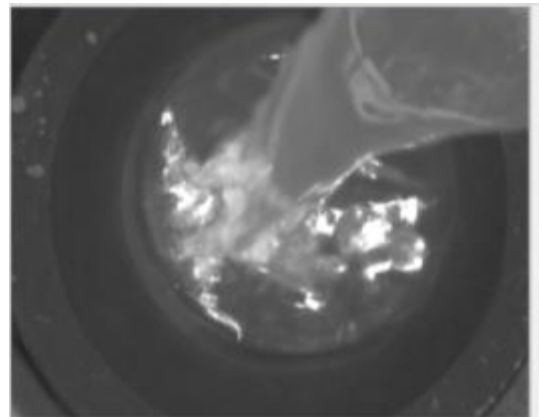
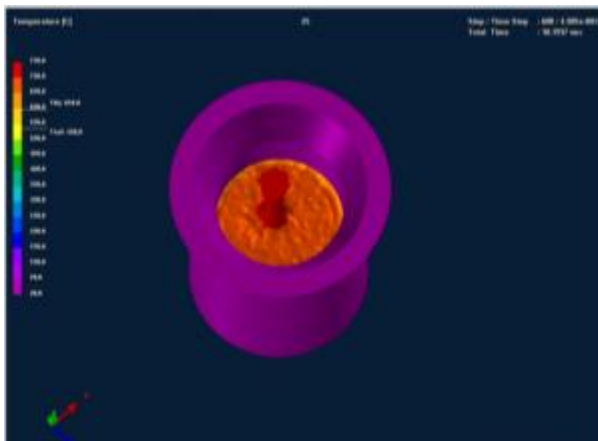
Note constant temperature colour chart throughout all images



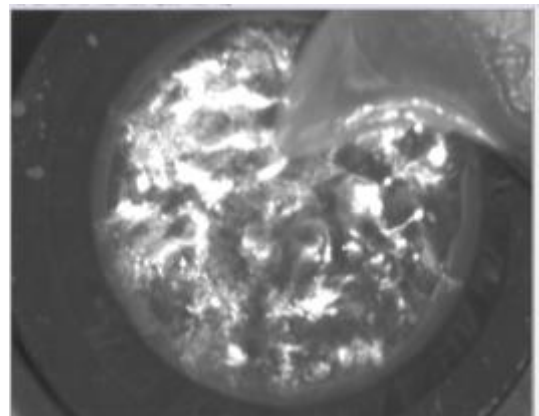
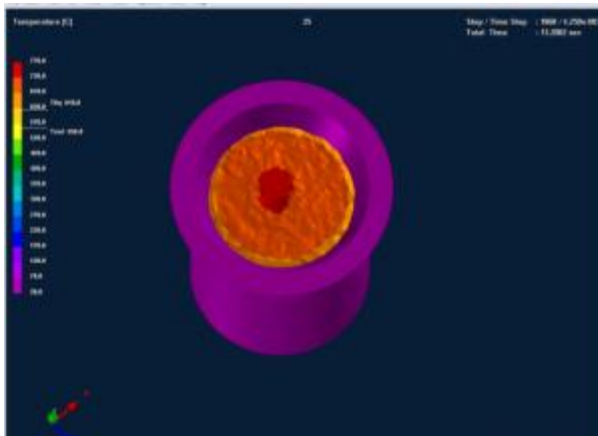
- a)  $t=5$  – Before pour – note the simulation start pour time was offset by 6 seconds so it ran at the same time as the video.



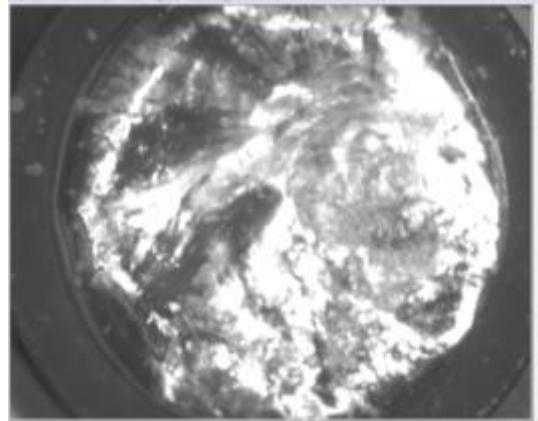
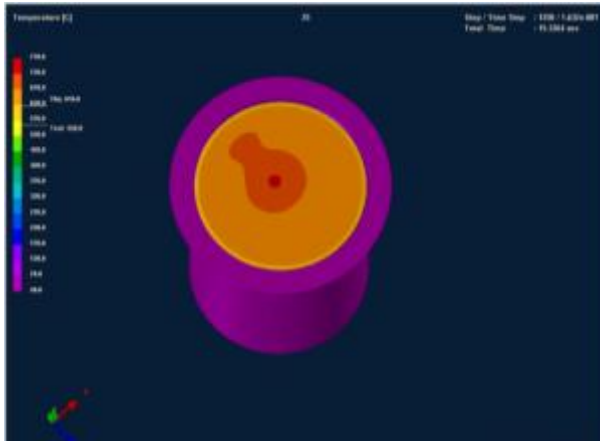
b)  $t=7$  seconds – Start of pour



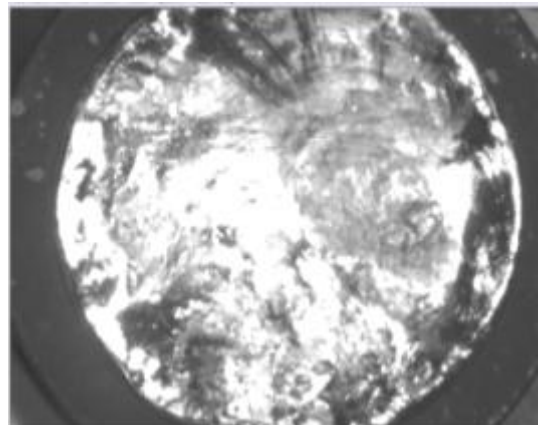
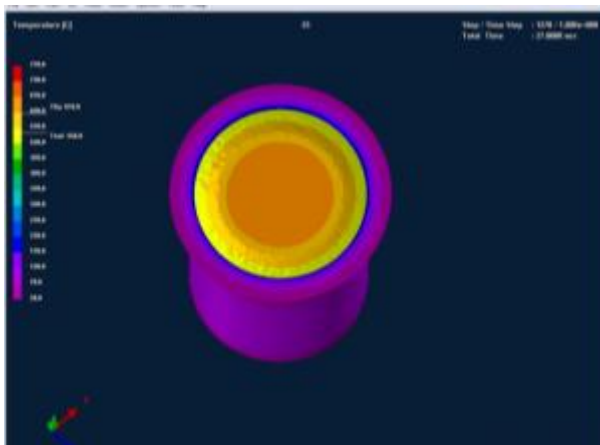
c)  $t=10$  seconds – The mould is half full and has reached the locations of the tungsten rod and internal thermocouple.



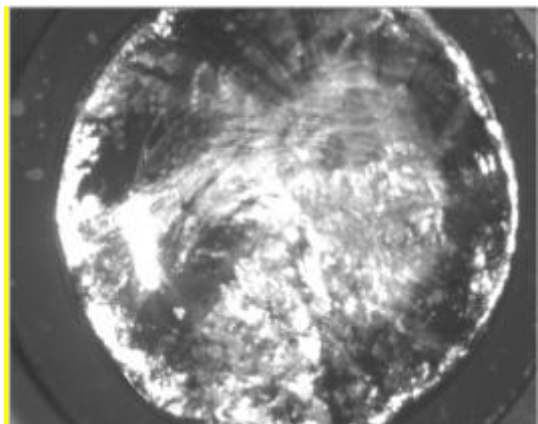
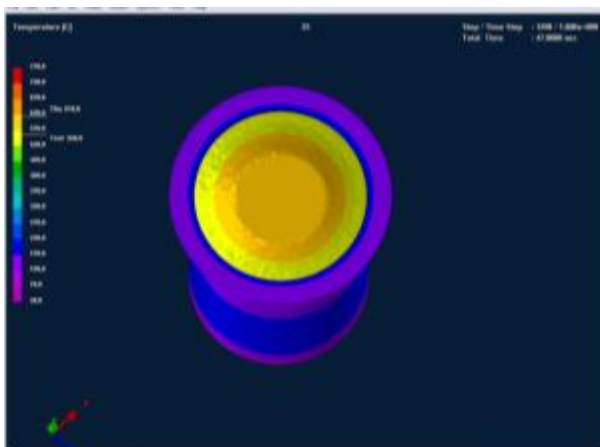
d)  $t=13$  seconds – Pour nearing completion



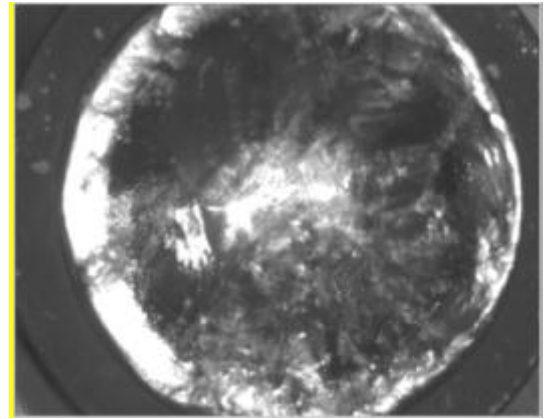
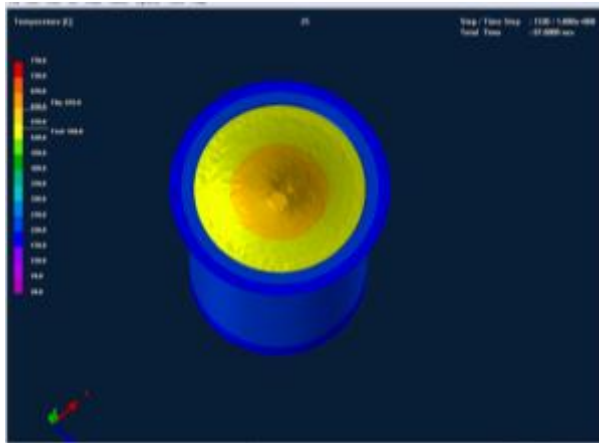
e)  $t=15$  seconds – Pour complete



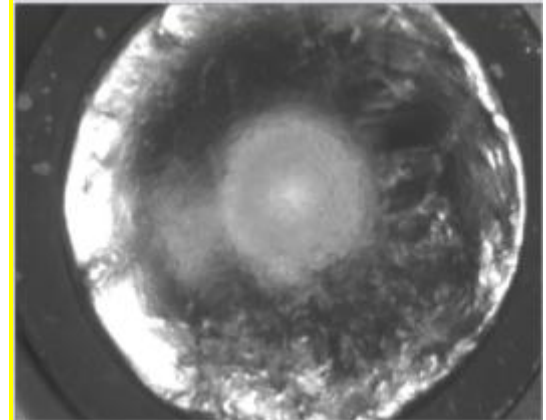
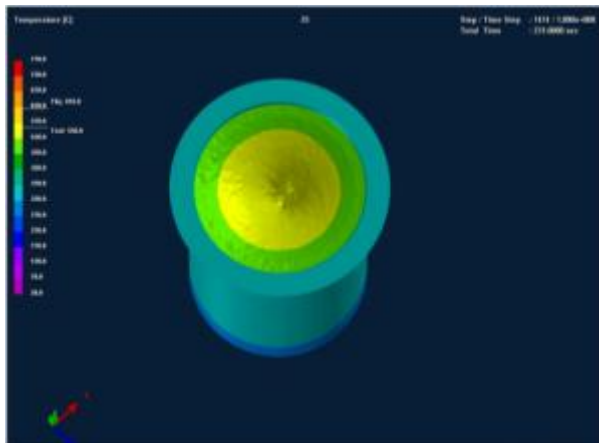
f)  $t=27$  seconds – Formation of pipe begins on the surface of the melt



g)  $t=47$  seconds – Pipe becomes more pronounced as cooling continues



h)  $t=87$  seconds – Last stages of pipe as minimal liquid is left on the surface of the melt



i)  $t=231$  seconds – Pipe is fully formed and surface skin is 100% solid

Figure 4-18 – Time steps taken from ProCAST simulation (left) and the casting experiment (right) for LM25 casting.

Once the simulation was complete, nodes were selected to extract time-temperature histories. Identical positions of the thermocouples, both within the mould's wall and the melt's surface, were chosen and are illustrated in Figure 4-19. This allowed the direct comparison between the experimental data and the simulation predictions; these results are presented in Figure 4-20. The node at the interface was also chosen which allowed for the predicted air-gap to be exported; this is displayed in Figure 4-21.

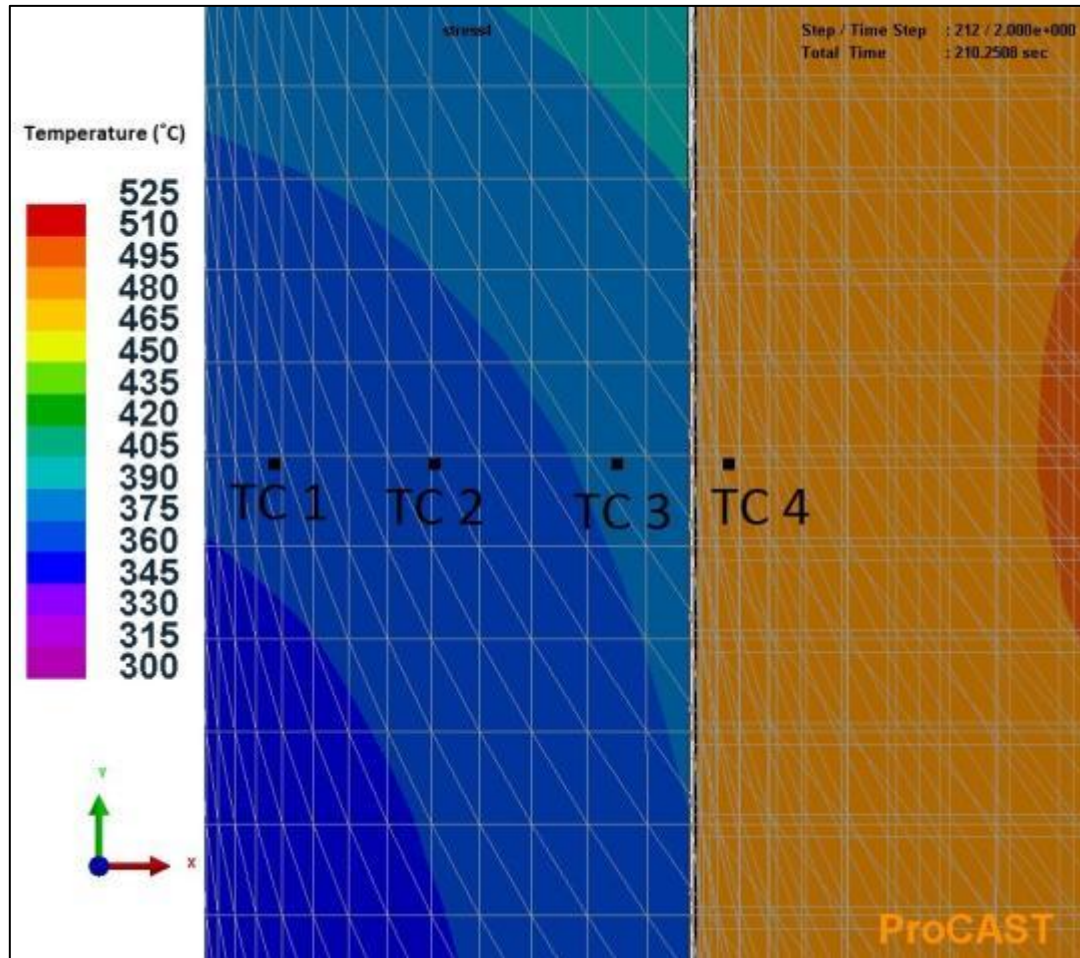


Figure 4-19 – Illustration to show the locations of nodes selected in ProCAST for the extraction of predicted temperatures within the mould's wall and melt concurring with experimental locations.



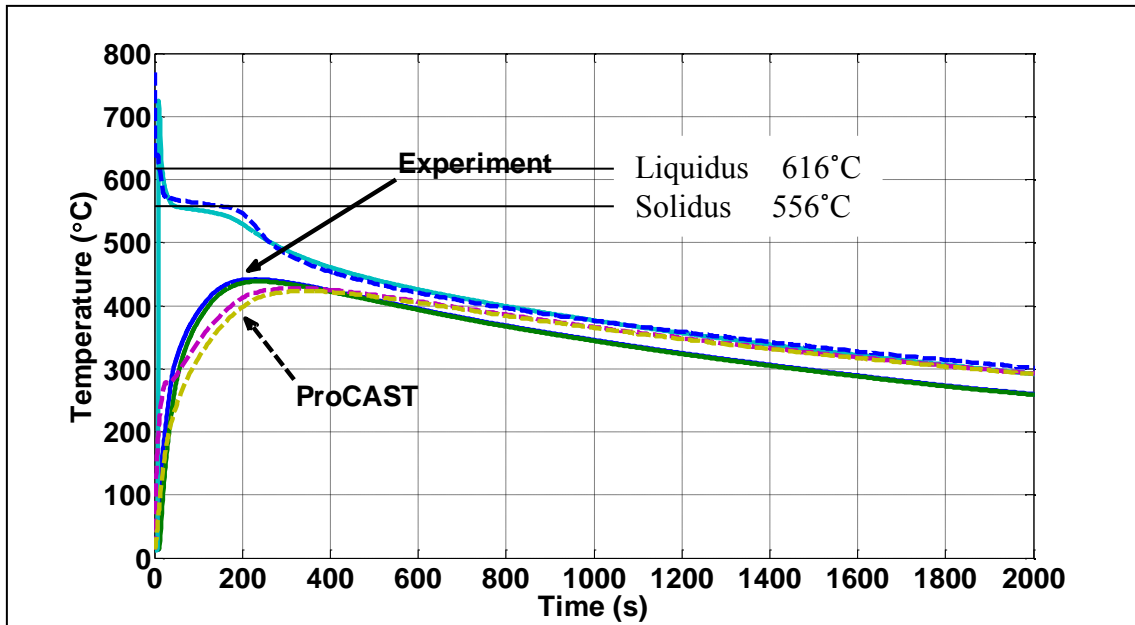


Figure 4-20 – Graph to show the ProCAST temperature predictions (dashed lines) and the experimental measurements of the thermocouples 10 and 18 mm within the mould wall and the melt thermocouples for the LM25 casting.

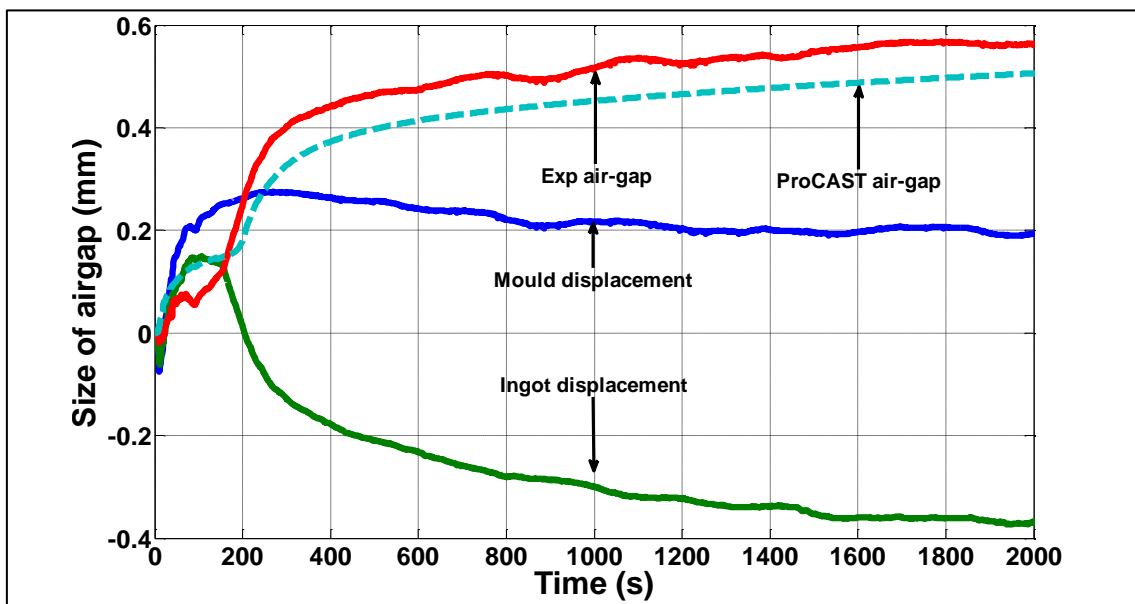


Figure 4-21 – Graph to show the ProCAST air-gap predictions (dashed lines) and the experimentally measured air-gap for the LM25 casting.

As illustrated in Figure 4-20, the simulated and experimental melt temperatures are in close relationship, and the time taken for them to reach the solidus temperature is within 10 seconds.

In both the experimental and the model predictions, reaching the solidus temperature coincides with an increased rate in air-gap formation, which can be seen in Figure 4-20 and Figure 4-21 for temperature and displacement respectively. This increased rate in air-gap formation reflects the presence of the newly solidified skin of the casting, which begins to cool and contract whilst the mould is still gaining heat and expanding.

The rate of increase in air-gap begins to fall after 400 seconds which can be attributed to the peak temperature of the mould is reached. From here, and in agreement with the experimental results, the mould begins to cool and consequently contracts resulting in both the melt and the mould moving in the same direction. The rate of increase in the air-gap from this point onwards is equivalent to the experimental results; even though the magnitude of the predicted air-gap for the model is lower than the measured value.

Some key differences between the predicted and experimental results are observed within Figure 4-20 and Figure 4-21 these are:

1. The melt's super heat for the simulation is immediately lost, however for the experiment this occurs over the first few seconds. For the simulation a surface node was selected, and therefore representative of the true melts' surface. However, for the experiment a thermocouple was positioned in the mould cavity as close as practical to the surface of the melt. After cooling the ingot was removed from the mould and sectioned to determine the location of the



thermocouple tip by a progressive grinding technique. The location of the thermocouple tip was found to be 1.5 mm from the melt's surface (Figure 4-22).

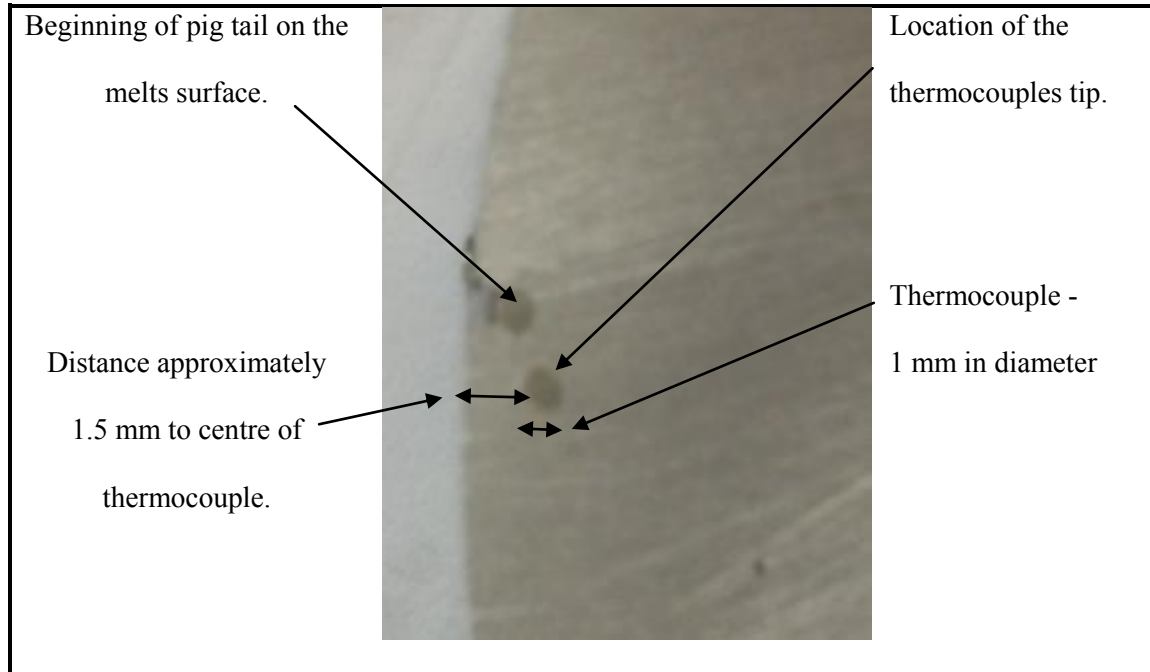


Figure 4-22 – Photograph to show the location of thermocouple tip solidified within the LM25 casting.

2. Once steady state had been reached, approximately after 600 seconds, disagreement in the temperature difference between the melt and the mould is witnessed between experimental and simulated results. This was measured at 25°C and predicted at 14°C. This could also be attributed to the melt's thermocouple measuring the temperature at a depth of 1.5 mm and not the melt's surface.
3. The maximum predicted mould temperature for the simulation was lower and delayed by 150 seconds compared to the experimental results. Parameters within the simulation which have not been explored and may have an influence on this are the mould's thermal conductivity and the initial IHTC. It is predicted that an increase in either/both of these would lead to a better fit between

simulated and experimental results. However the investigation for this is out of the scope of this work.

4. The final measured air-gap is slightly larger than the predicted counter-part. The simulated mould's temperature not reaching the same maximum as the experiment may have contributed to this, as a lower amount of expansion occurs within the mould occurs.

As with the experimental results, the simulated IHTC was calculated using the temperature readings and the size of the air-gap; this is presented in Figure 4-23.

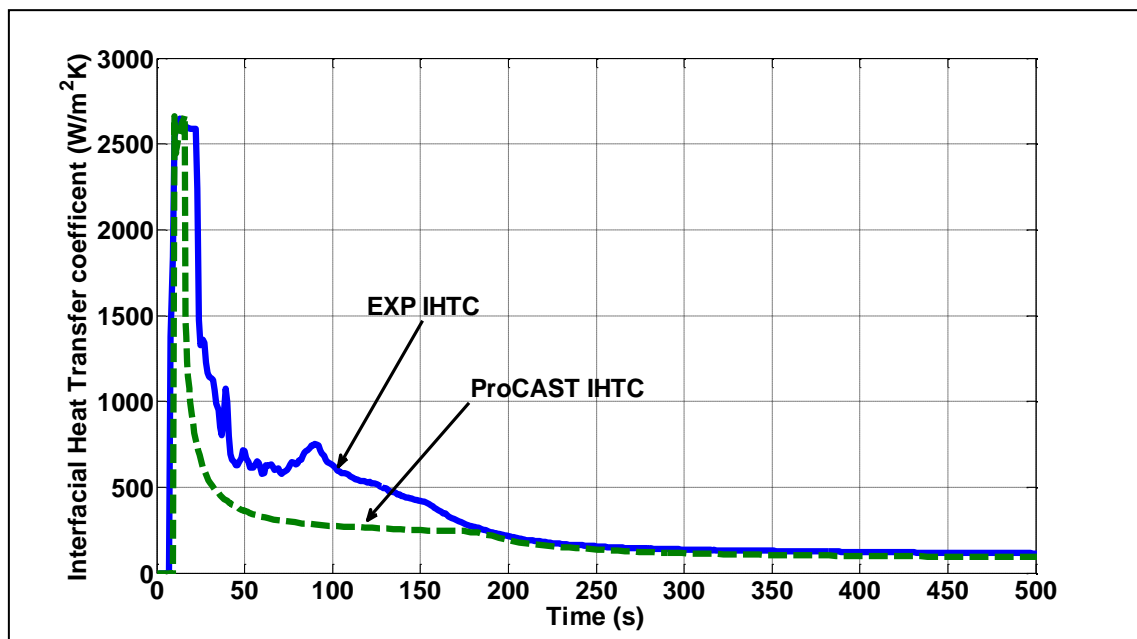


Figure 4-23 – Graph to show the comparison of the predicted interfacial heat transfer coefficient using ProCAST and the calculated values from the LM25 casting.

This section of work was presented at the Liquid Metals Technology conference in 2013 (Swan et al., 2013)

#### **4.4 Temperature and Displacements Results for XD1102**

An identical experiment using the same equipment was then carried out replacing the aluminium alloy with the nickel-based alloy XD1102. Due to the higher melt temperature, the internal Type K thermocouple was replaced with a Type S thermocouple. During the first casting trial the internal Type S thermocouple was pushed out through the hole in the mould wall during pouring; this compromised the accuracy of the temperature reading and therefore the experiment was repeated ensuring the Type S thermocouple was fixed in position preventing this from happening a second time. This was due to a rigid thermocouple being used, where for the LM25 casting a flexible thermocouple was used and could be bent through 90° and rest against the moulds' inner surface. Both the experimental results are displayed and the initial IHTC has been calculated using the second of the two experiments readings only.

The same four graphs for the LM25 experiment are presented for the XD1102 experiments:

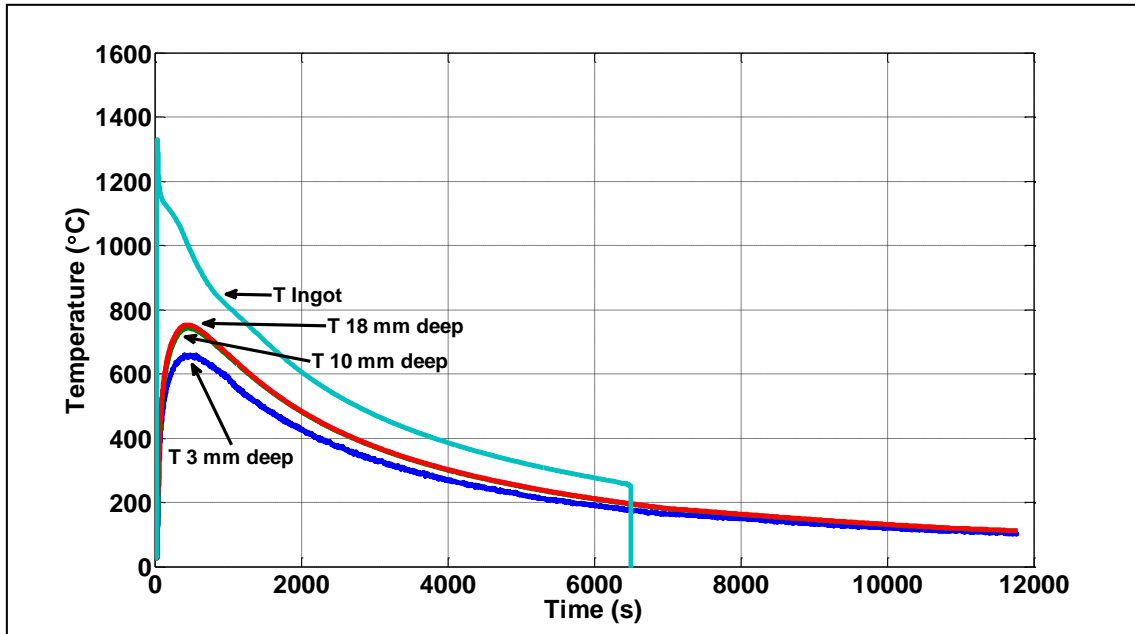


Figure 4-24 – Graph to show the full length of experimental temperature readings for the XD1102 casting.

As before with the LM25 casting the thermocouple within the mould wall at a depth of 3 mm is lagging behind the thermocouples at 10 and 18 mm depths, and as before the temperature readings are fluctuating. The explanation given in section 4.3 is still relevant, and as this thermocouple is not used for the calculation of the inner mould's surface temperature: no concern was made.

After approximately 6,500 seconds the Type S thermocouple failed; however, this was not considered significant as the experiment is in steady state and simply the whole system is cooling.

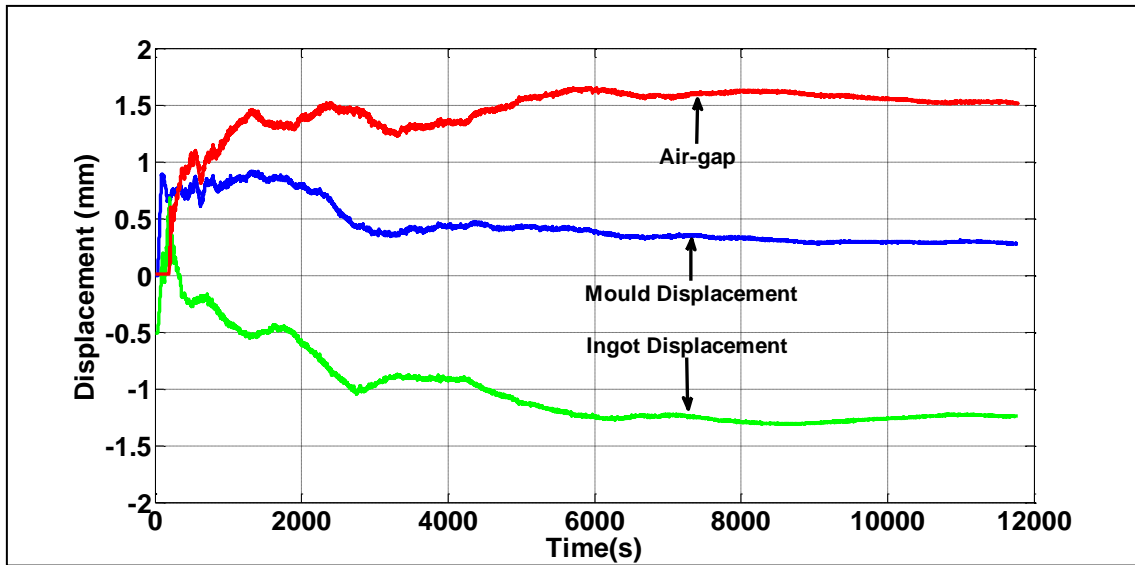


Figure 4-25 – Graph to show the full length of experimental displacement measurements and the magnitude of the air-gap for the XD1102 casting.

Results displayed in Figure 4-25 show a similar behaviour for the XD1102 casting as for the LM25 casting; the largest rate of increase in air-gap was found when the solidified alloy had developed sufficient strength and begun to contract. This is due to the casting and the mould moving in opposite directions. Once the mould begins to cool and contract the size of the air-gap stabilises.

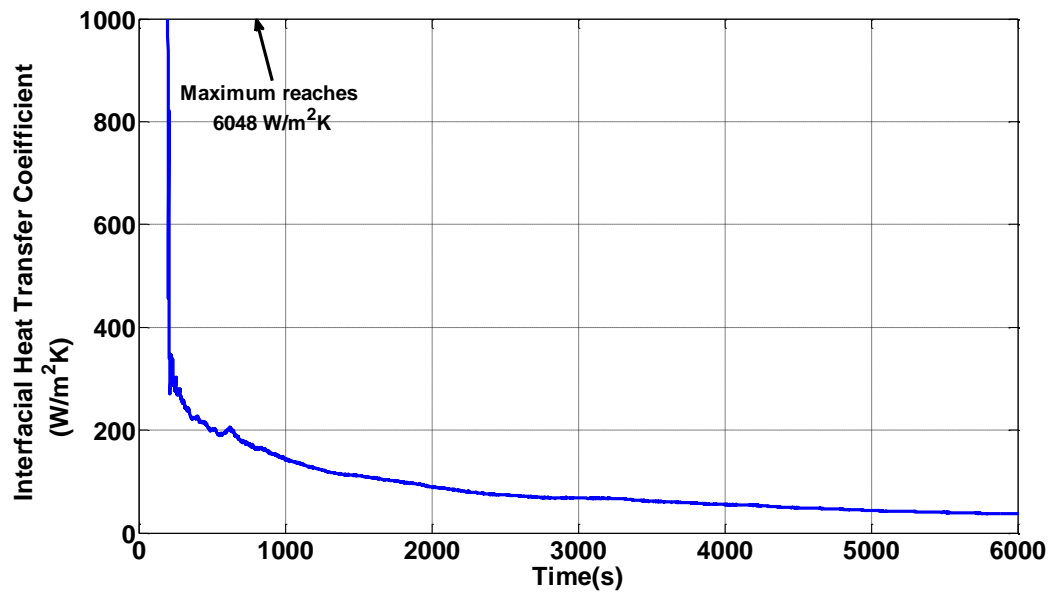


Figure 4-26 – Graph to show the calculated IHTC for the experimental XD1102 casting.

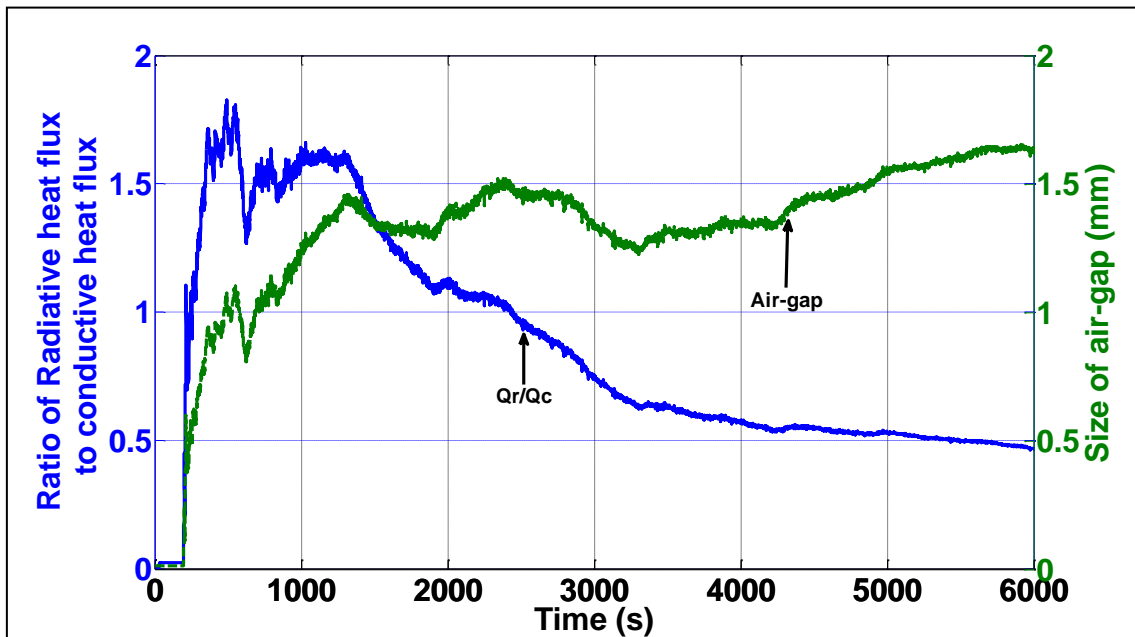


Figure 4-27 – Graph to show the ratio of radiative to conductive heat transfer with the size of air-gap for the XD1102 casting.

#### 4.4.1 $Q_r$ to $Q_c$ Ratio

Comparable to the LM25 casting, during the early stages of the solidification, where a liquid to mould interface is present, the heat transfer is dominated by conductive terms.

However as the air-gap starts to form, and due to the increased temperature of casting XD1102, the energy transmitted through radiation surpasses the amount by conduction. The maximum radiative to conductive ratio occurs approximately after 500 seconds whilst the casting still has sufficient temperature,  $>1000^{\circ}\text{C}$  (casting at the surface completely solid), and the air-gap is increasing at the largest rate; at this point the radiative heat flux is nearly double that of the conductive heat flux. As observed with the LM25 casting, as the casting starts to cool further and the size of the air-gap starts to plateau the ratio starts to decrease. After 2,500 seconds, and at a casting temperature of approximately  $500^{\circ}\text{C}$ , the conductive heat transfer again becomes the dominating heat transfer mechanism.

#### **4.5 Comparing the Two Alloys Cast**

It is found that by using a higher melting point alloy whilst keeping all other parameters the same, a large increase in the size of the air-gap was measured.

When casting XD1102 the recorded air-gap is over two times that of the LM25 casting; factors which are associated with this are the following:

1. The increased melt temperature of XD1102 leads to an increased amount of energy being transferred to the mould which therefore reached an increased temperature compared to that when casting LM25; thus leading to an increased amount of expansion of the mould.
2. As XD1102 has higher liquidus and solidus temperatures than LM25, to reach room temperature the XD1102 casting has further to cool, and therefore has an increased contraction range.

The maximum rate of increase in air-gap formation for the LM25 casting is  $0.002 \text{ mms}^{-1}$  and  $0.0036 \text{ mms}^{-1}$  for the XD1102 casting over the same period of time. Even though the coefficients of thermal expansion are near equivalent the increased melt temperature of XD1102 leads to an increased cooling rate and therefore contracts further over the same time-frame. This can be summarised by Eq. 4-8 when assuming a constant thermal expansion coefficient,  $\alpha$ .

$$\frac{d\varepsilon}{dt} = \alpha \frac{dT}{dt} \quad \text{Eq. 4-8}$$

Where  $\varepsilon$  is the strain,  $T$  is the casting temperature and  $t$  is time.

#### **4.6 Emissivity Trials for Improved Simulation Data, XD1102**

All material above absolute zero emits thermal radiation in all directions and wavelengths. For each given material and temperature, its emissivity is compared to that of a blackbody; a blackbody is defined as a material which absorbs and emits the maximum possible radiation at any temperature, wavelength and direction. The effectiveness which a material emits thermal radiation compared to a black body is known as its emissivity, and has therefore a value between zero and one.

For the ProCAST simulations, emissivity values for H13 steel and LM25 could be found within ProCAST's database; however, as XD1102 is a customer specific alloy the emissivity is unknown and not documented. Approximate values based on widely known nickel-based alloys with a similar chemical composition such as Inconel 718 or 706 could have been used; however, the surface conditions would not be truly representative of the casting process carried out in this study. Unfortunately, emissivity measurements are not simple to accomplish, particularly when the surface properties change with time as is often the case.



#### 4.6.1 Experimental Process

To approximate the surface emissivity of XD1102 the casting was placed into a furnace at a set temperature, verified by three thermocouples, and allowed to soak for a minimum of one hour. The furnace door was then opened and an image was taken using a thermal imaging camera (Flir A40M). The door then closed and the furnace ramped up and again the ingot was allowed to soak. The images were analysed using the software ThermaCAM Researcher Pro 2.10 to marry up the furnace temperature and the ingot's temperature by adjusting the emissivity in the software. For accuracy a random three locations were selected at each temperature that were perpendicular to the cameras view; this was important due to false readings at the edges of the ingot due to reflections from the furnace walls; this can be seen clearly in Figure 4-28. The emissivity at known temperatures is presented in Figure 4-29. The emissivity values have then been incorporated into the ProCAST simulations for the XD1102 castings.

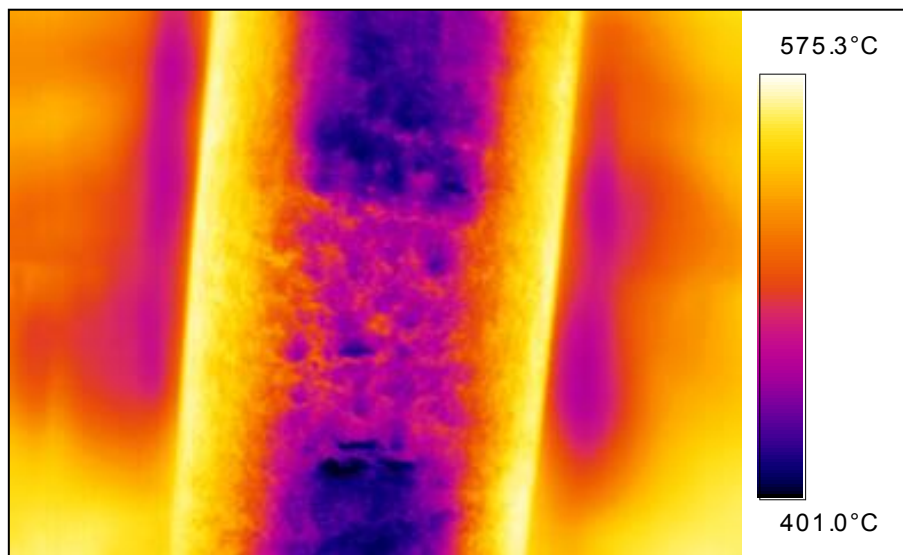


Figure 4-28 – Thermal image of the as-cast XD1102 at temperature.

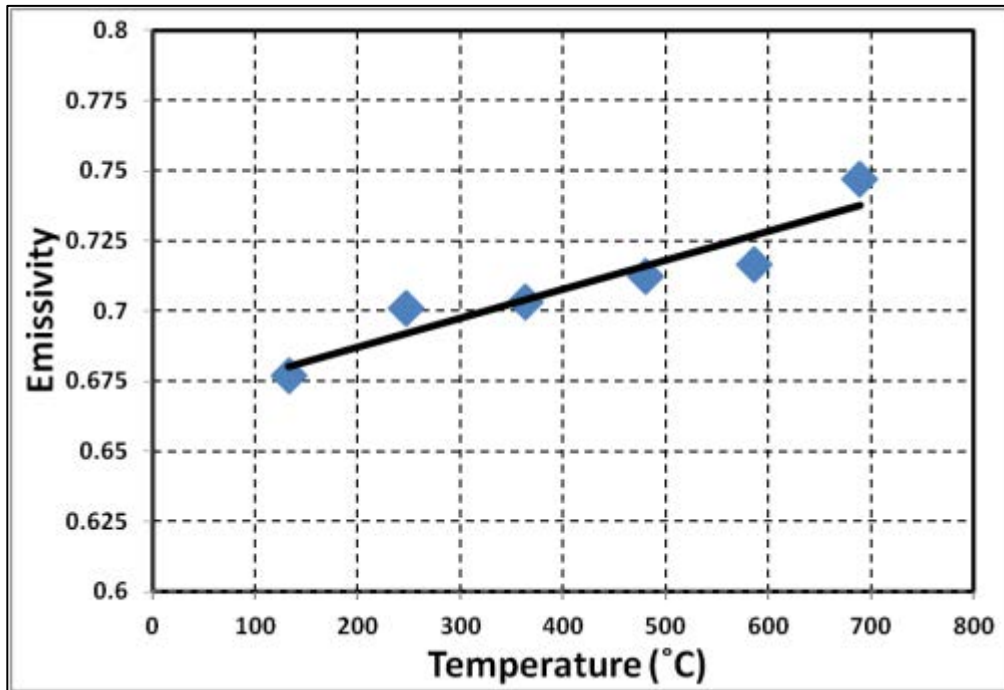


Figure 4-29 – Graph to show the measured emissivity of XD1102 up to 700°C

#### 4.6.2 ProCAST Simulations

As with the LM25 casting a 3D simulation was ran for XD1102 using the maximum IHTC found during the experiments of 6048 W/m<sup>2</sup>K. The results of the first casting trial have also been included which shows repeatability of the experiment itself.

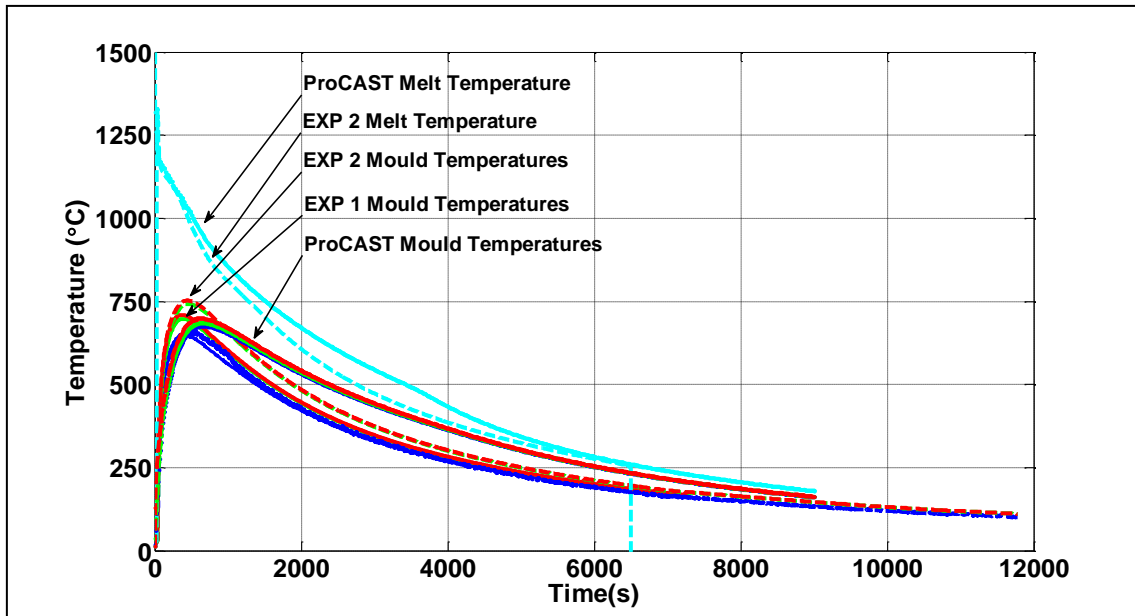


Figure 4-30 - Graph to show the ProCAST temperature predictions (solid lines) and the experimental measurements of the thermocouples 10 and 18 mm within the mould wall and the melt thermocouple for the XD1102 casting.

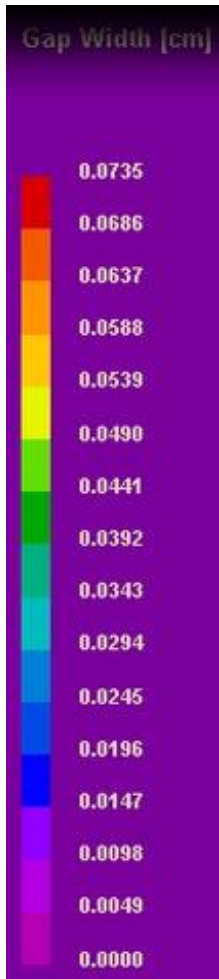
The predicted mould temperature lags behind the temperatures measured experimentally. This may be caused by the determination of the initial IHTC. This is extremely difficult to measure due to the sensitivity of the conditions during the initial stages of solidification. With a larger initial IHTC the rate of increase in the mould temperature is likely to be greater and the maximum temperature would be reached in a shorter time frame. The rate of heat exchange between the outer surface of the mould and the ambient air would also increase but not to the same magnitude of the casting to mould exchange; this is due to energy being spent in heating up the mould's mass. Therefore it is likely to expect an increase in maximum mould temperature.

There is a good agreement between the results from the physical and numerical experiments whilst the casting is above 1000°C; after this point divergence of results is evident. Below 1000°C the cooling rate of the experiment, for both the casting and

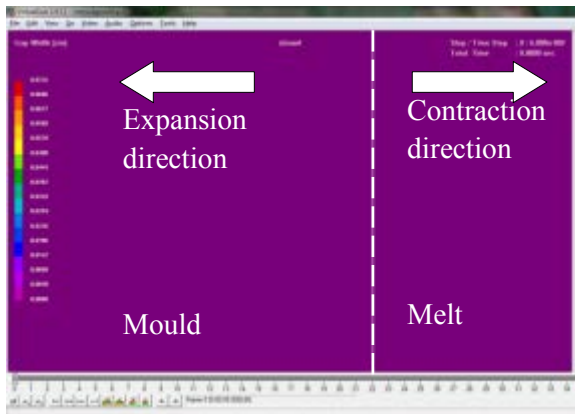
mould, is greater than the simulated results; this suggests that heat is not being exchanged to the environment at the same rate and that for the simulated results energy is being retained. Normal ingot casting operations do not usually experience a controlled environment and the temperature and air flow around the casting can fluctuate by means of doors opening and closing, personnel walking by and draughts. This may lead to an increased rate in cooling of a small ingot compared to a ProCAST simulation which has a controlled environment at a constant temperature. This may explain, in part, the temperature difference observed.

#### 4.6.2.1 Displacement Predictions

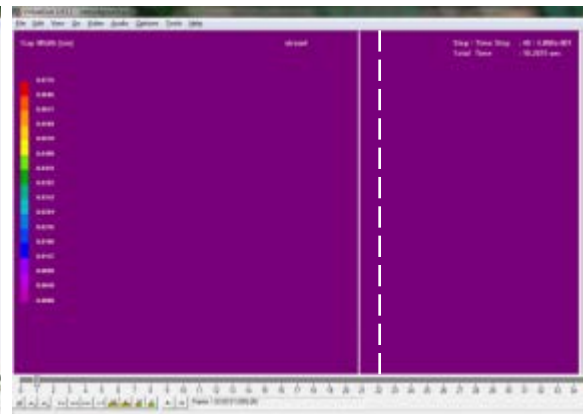
For the displacement predictions, nodes from the model were selected on the ingot's surface and the mould's inner wall at the equivalent height of the experimental measurements. The air-gap as with the experimental results is then the difference between the two. A short video clip, split into screen shots, displays the movements of the interface (Figure 4-31); similar was reported in Figure 4-6 and Figure 4-7.



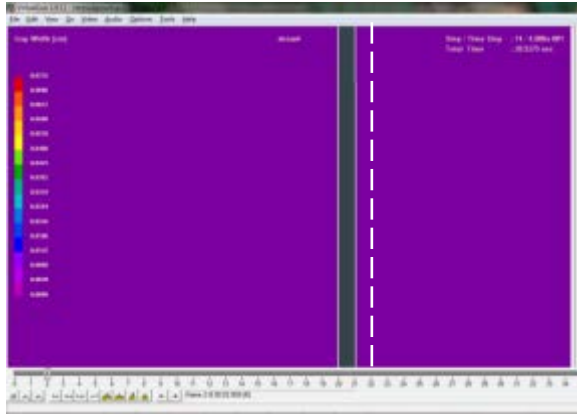
Note constant gap width colour chart throughout all images



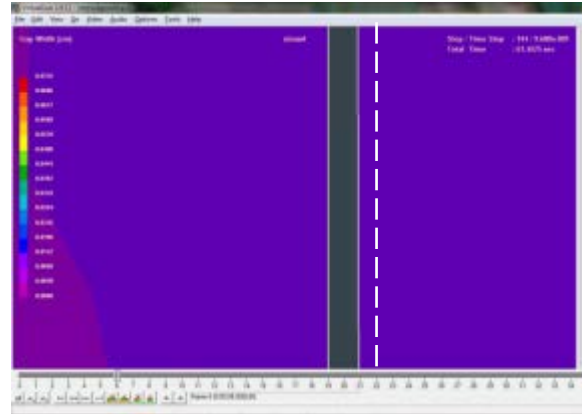
a)  $t = 0$  - Starting position Frame “22” as the reference (White dashed line)



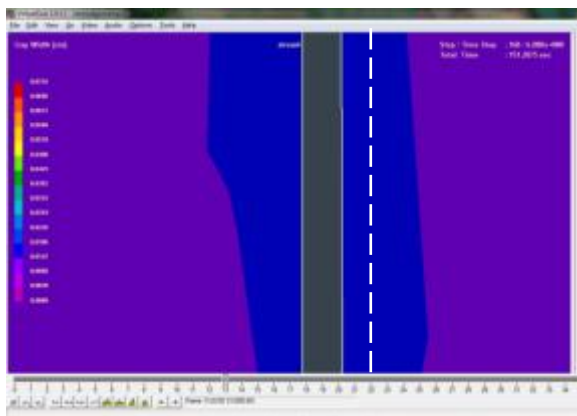
b)  $t = 10$  seconds - Both the mould and the casting with full liquid metal contact move to the left as the mould expands and the liquid metal follows this expansion



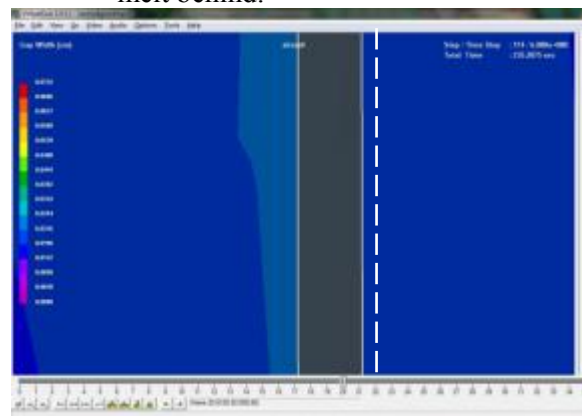
c)  $t = 20$  seconds - Air-gap has formed



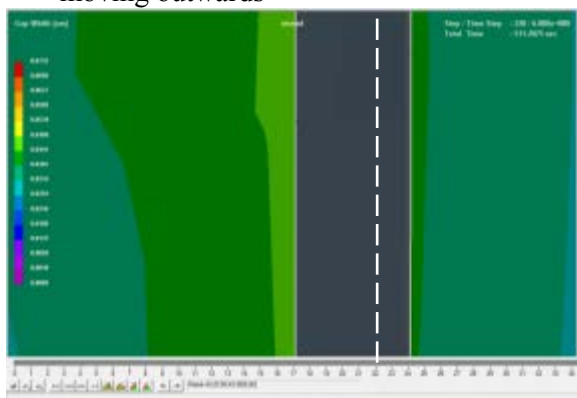
d)  $t = 60$  seconds – Movement of both the mould and the casting surface outwards due to the pressure of the melt behind.



e)  $t = 151$  seconds – The mould is still expanding and the casting is no longer moving outwards



f)  $t = 235$  – The casting begins to contract and the rate of expansion of the mould begins to decrease



$t = 511$  seconds - Casting continues to contract, and the mould has stopped expanding and itself begins to contract as it cools

Figure 4-31 – Illustration of the ProCAST simulation showing the moving interface between the casting and the mould.

Comparison of the considered experimental and predicted results can be seen in Figure 4-32.

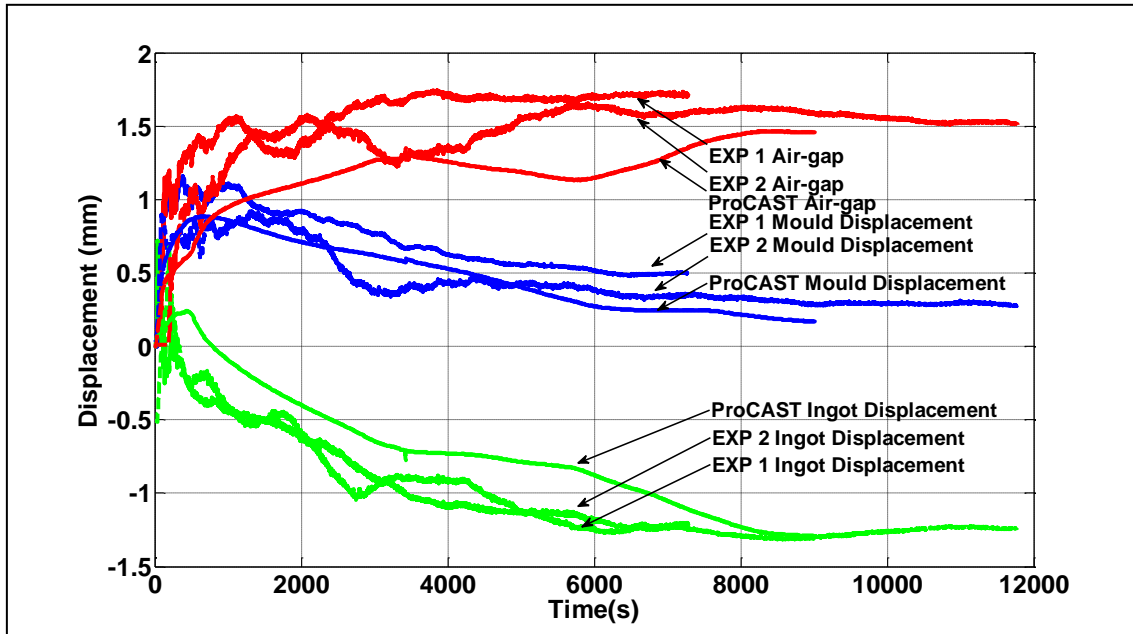


Figure 4-32 – Graph to show the ProCAST predictions for the displacements of the casting and the mould and the magnitude of the air-gap compared to the experimentally measured displacements and size of the air-gap for the XD1102 casting.

Similar to the temperature predictions, the expansion and contraction of the mould and ingot lag behind the experimental readings. This again could be explained by a lower than expected IHTC value and a reduced rate of cooling of the mould to the environment.

## 4.7 Conclusions

The air-gap which forms between the casting and the surface of the mould was investigated for an aluminium and a nickel-based alloy, LM25 and XD1102 respectively. Measurement of the air-gap was successfully achieved by recording the displacements, using laser triangulation sensors, of the ingot and mould surfaces; the air-gap is then the difference between the two. Temperature measurements were

recorded using Type K thermocouples embedded within the mould wall, at varying depths, and either Type K or Type S thermocouples for the aluminium and nickel-based alloys respectively to capture the surface temperature of the casting. The heat transfer through the air-gap could then be calculated in terms of conductive and radiative heat fluxes, which combine to give the IHTC.

It was found that for the nickel-based alloy the magnitude of the air-gap was over twice the aluminium casting. This is due to the increased melting temperature of the alloy subsequently heating the mould to a higher temperature and thus an increased amount of expansion. Secondly, the ingot has a larger cooling range and therefore an increased contraction range.

During the early stages of casting when a liquid to mould interface was present, conductive heat transfer dominated radiative heat transfer. As the air-gap began to form and the metal began to pull away from the mould wall, and whilst the casting was still retaining most of its temperature, the maximum ratio of radiative to conductive heat transfer was found. After this point, and as the whole system began to cool, the ratio of radiative heat flux began to the total heat transferred began to decrease.

Throughout the aluminium casting process conductive heat transfer was the dominating transport method, and the radiative heat flow only contributed to 18% of the total heat flux. However, due to the increased temperature of XD1102 castings and the formation of a larger air-gap the radiative heat transfer dominated after an air-gap of 0.5 mm was formed (after the casting surface temperature had dropped below 500°C). Some literature (Kron et al., 2005, Nishida et al., 1986) has suggested that radiative heat



transfer can be neglected when calculating heat flow, but the evidence from the two castings in this work that this is not the case.

The software PROCAST was used to predict both temperatures and displacements of the ingot and the mould for comparison with the experimental work. A good agreement between the model and experiments was achieved, providing confidence that the model can be extended to areas where destructive temperature and displacement measurements are not practical. Secondly the model can be extended to more intricate casting shapes to allow mould designers to manipulate the design to obtain the most favourable cooling rates and material properties without the need for expensive experiments.

Enhancements in the accuracy of modelling prediction were completed by investigating the emissivity of the mould and the as-cast XD1102 ingot at a range of temperatures. A thermal imaging camera and the software ThermoCAM Researcher Pro 2.10 was used to marry up the known temperature and the temperature of the infrared thermal image by adjusting the emissivity. These were then incorporated into the ProCAST model.

## **4.8 Future Work**

The temperatures and displacements from the experiments were recorded from a single height and orientation of the mould, and it would be beneficial to extend this work to cover the full height and circumference to determine whether the expected homogeneous solidification occurs. The air-gap will always vary in the height direction due to the additional pressures from the melt above as you traverse lower into the mould; however due to the uncontrolled environment variations circumferentially may also occur. This could influence the magnitude of the air-gap formed at a given location, and therefore the experiments where only one measurement of the air-gap was

made may not be a true representation of the full mould displacement and temperature histories.

An added benefit of full displacement history is that any unexpected movements of the mould such as rocking after pouring, if any, would be captured. The effects of these movements can be considered and the decision to neglect any contribution can be validated.

For both alloys the casting temperature was recorded by using a single thermocouple positioned as close to the outer surface of the casting as possible. It would be advantageous to include multiple thermocouples within the casting at set distances, similar to the mould thermocouples, and then the casting surface temperature could be predicted more accurately. These additional temperature readings could then also be used to further validate ProCAST simulations. As can be seen from Figure 4-22 the actual position of the thermocouple tip is set back from the ingots surface. When selecting the nodes in the ProCAST simulation a node that represents the tip location should be used and this may lead to an improved agreement.

Two major factors determine if radiative heat flux can be neglected for a particular casting, one already explored is the casting temperature and the second is the size of the casting. An increased casting size would result in further contraction of the casting and hence an increased air-gap; this in turn would reduce the effectiveness of conductive heat transfer. Decreasing the size of the castings has the opposite of the above and there will become a point where radiation effects can be argued to be insignificant; for the work carried out by Nishida, a casting mould size of just 34 mm diameter was sufficiently small to render radiation insignificant (Nishida et al., 1986). It would be

interesting to explore different casting sizes using the same alloy to determine the transitions between conductive and radiative dominance.

As described in the section 4.3.3.3 a variation in the initial IHTC is likely to influence the simulation outputs; a suite of models could be run to either prove or disprove this. Also it would be of interest to better understand parameters such as the emissivity; in the trial conducted the ingot was sat in the furnace for approximately one hour then ramped up. It is unclear to what extent an oxide build up on the ingot's surface increased the apparent emissivity. To further investigate this, a freshly cast ingot could be kept at a set temperature and then images taken at a given time interval to see what to predict the change in emissivity. This could then be compensated for to represent the true emissivity of the ingot surface during the casting process.

# Chapter 5. Valve Bar Feature – Identification, Origin, Root Cause Analysis and Mitigation

## 5.1 Introduction

The hot extrusion of cylindrical nickel iron ingots is a common practice at Special Metals Wiggin Limited (SMWL) with very high success rates. However, with alloy XD1102 many ingots split on extrusion known in the industry as “crocodiling” (Figure 5-1a). The likely root cause of this was thought to be ingots cracking along their base within the extrusion pre-heat furnace due to thermally induced stresses.

Once a uniform ingot temperature is reached in the extrusion pre-heat furnace they are removed and immediately extruded, with no inspection so as to minimise heat loss to the environment. Because of this, the cracking on the base of the ingots has not been seen, which led to other theories to attempt to prevent the crocodiling of the ingots. These included poor mould quality, due to wear, leaving a protrusion on the base of the ingots and the entrainment of an oxide skin from a return-wave at the base of the mould during filling.

To explore this a trial of pre-heating six ingots was conducted with varying ingot conditions including good quality as-cast ingots, ingots with base features and skimmed ingots (removing the radius from the base of the ingot as illustrated in Figure 5-1). These were then loaded into the pre-heat furnace, allowed to soak for the standard time, withdrawn and inspected. On assessment, five ingots showed centreline base cracks with a single skimmed ingot being the only one to retain defect free (Figure 5-1b). It was hypothesised that if base features were present the crack may open across this as it may act as a stress riser; however, in this particular trial the crack path did propagate

through this base feature and had no relationship with it, as can be seen in Figure 5-1b, ingot number 4. Here the dashed line represents the base feature and the solid line represents the base crack of the ingot. It was concluded that the cracking of the base is initiated through the combination of residual stresses and thermal shock within the furnace regardless of the surface finish of the ingots. The positioning of ingots within the furnace in relation to heating elements and shielding from other ingots could play an important role in the generation of defects. Due to expense these trials have not been carried out

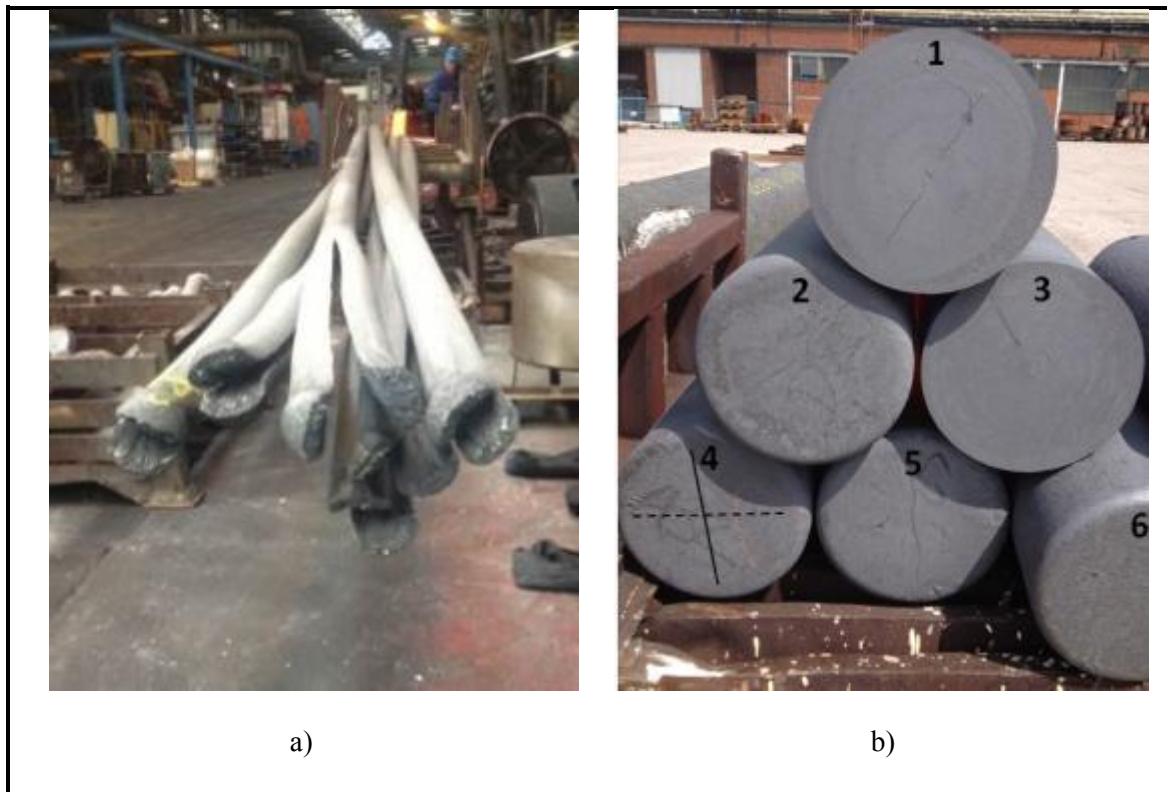


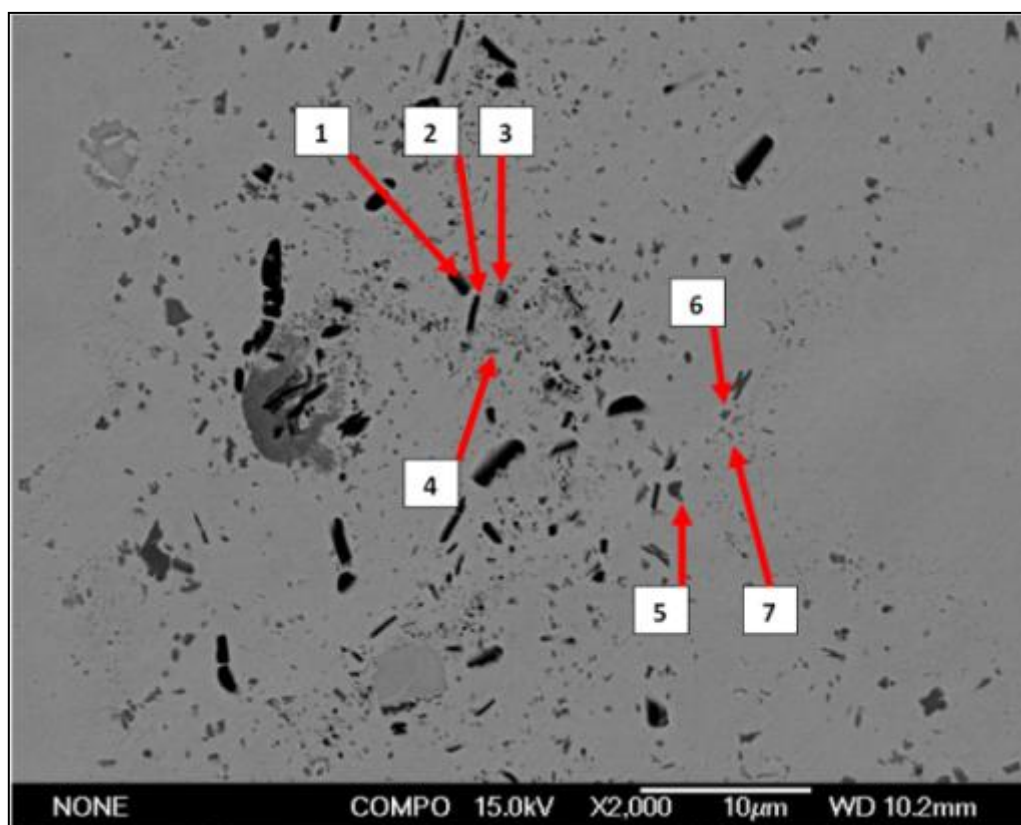
Figure 5-1 –Photographs to show the crocodiling of XD1102 extruded bars (a) and the ingots displaying base cracks with various starting conditions after being withdrawn from the pre-heat furnace prior to extrusion for inspection

It is likely that any cracked ingot will inevitably crocodile on extrusion; the extruded bar is then cut back to the end of the crocodiled region and then processed as usual to produce a valve bar. Features have been previously found within the valve bar that

resembles oxidation/nitridation of the material (Figure 5-2); it was this feature which initiated this investigation. The nature of this work is to link the cracking of the ingot within the pre-heat furnace to this valve bar feature. Hence the results will be presented in reverse from the initial findings of the feature in the valve bar to a crocodiled extruded bar, and finally to a thermal shocked ingot.

## **5.2 The Valve Bar Feature**

Figure 5-2 represents a polished section of a valve bar, which displays a particle rich zone stretching across almost the full diameter passing close to its centre. The width of this zone was approximately 40  $\mu\text{m}$  and was a combination of aluminium and titanium rich oxide or nitride particles. The aluminium rich particles were generally larger than the titanium particles with platelet morphology; these reached up to four  $\mu\text{m}$  in length and approximately 1  $\mu\text{m}$  in width. The titanium particles were typically sub one  $\mu\text{m}$  in size and have a more globular morphology. It can also be seen that the aluminium particles clustered more closely to the centre of the oxidation feature with a bandwidth of approximately 25  $\mu\text{m}$ ; whereas the titanium particles cover the full bandwidth of the feature i.e. 40  $\mu\text{m}$ .



Spectrum	% Deviation from XD1102 average							wt% detected by EDX	
	C	Al	Ti	Cr	Fe	Ni	Nb	N	O
Spectrum 1	1415	1469	-13	-37	-51	-50	15	15.73	
Spectrum 2	4502	1540	8	-45	-60	-61	-30	17.53	
Spectrum 3	2522	645	681	-53	-72	-74	164		24.92
Spectrum 4	2017	-76	635	-18	-33	-29	42	6.57	
Spectrum 6		-68	1096	-27	-45	-51	328	4.69	1.61
Spectrum 7		-52	417	-7	-18	-19	-7	5.59	

Figure 5-2 – SEM back scattered image at 2,000 magnification of the feature region within a valve bar of XD1102. Dark in contrast particles are rich in aluminium – light in contrast are titanium rich particles. *Blank entries within the attached table indicates that no detection of that element was found*

### 5.3 Extruded Bar “Crocodile”

Prior to the furnace trials and the knowledge that the ingots are prone to cracking within the pre-heat furnace, samples of a crocodile extruded bar were analysed as described in Figure 5-3.

#### 5.3.1 Metallographic Technique

All specimens were sectioned using silicon carbide discs, mounted in conductive Bakelite and ground using MD Piano and MD Largo discs using water and six  $\mu\text{m}$  diamond paste respectively. Polishing followed using MD Dac and MD Nap clothes using one  $\mu\text{m}$  and  $\frac{1}{4} \mu\text{m}$  diamond paste respectively. The morphology and compositional analysis was then carried out using the high resolution JEOL 7000F Scanning Electron Microscopy (SEM) with Energy-Dispersive X-ray spectroscopy (EDX).

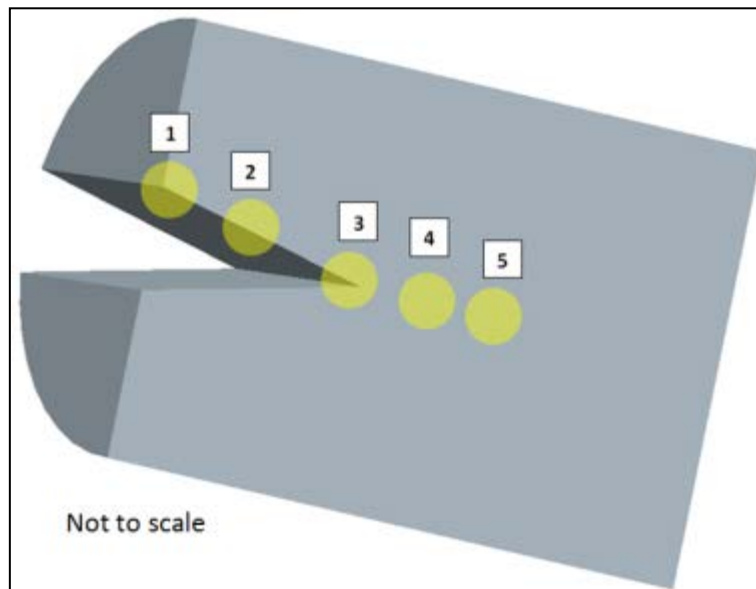


Figure 5-3 – Schematic diagram displaying the sections of a crocodile extruded bar observed by SEM techniques.



Five regions were analysed using SEM and EDX; the first three are within the crocodile region: 1, 2 and 3 going from the opening of the crack, middle to the crack tip respectively. Sections 4 and 5 are both sub crocodile regions.

### 5.3.2 Section 1: Start of Crack

During extrusion the initial part of the ingot may receive minimal deformation, and get pushed through close to the as-cast state. It is not surprising that the surface resembles a typical oxide of a Ni-Fe-Cr alloy (Figure 5-4); similar was found by Pan et al. (Pan et al., 2011). The oxide morphology has various levels with a nickel an iron and chromium protective oxide surface of 10 and 5  $\mu\text{m}$  thick respectively, followed by a sub-surface layer of aluminium and titanium oxides (probably as intergranular fingers) as seen by Taylor et al. (Taylor et al., 2012). The oxide rich regions also show an increased nitrogen concentration, likely indicating that nitridation has also occurred in these regions. The total oxidised region penetrates up to a depth of approximately 60  $\mu\text{m}$ .

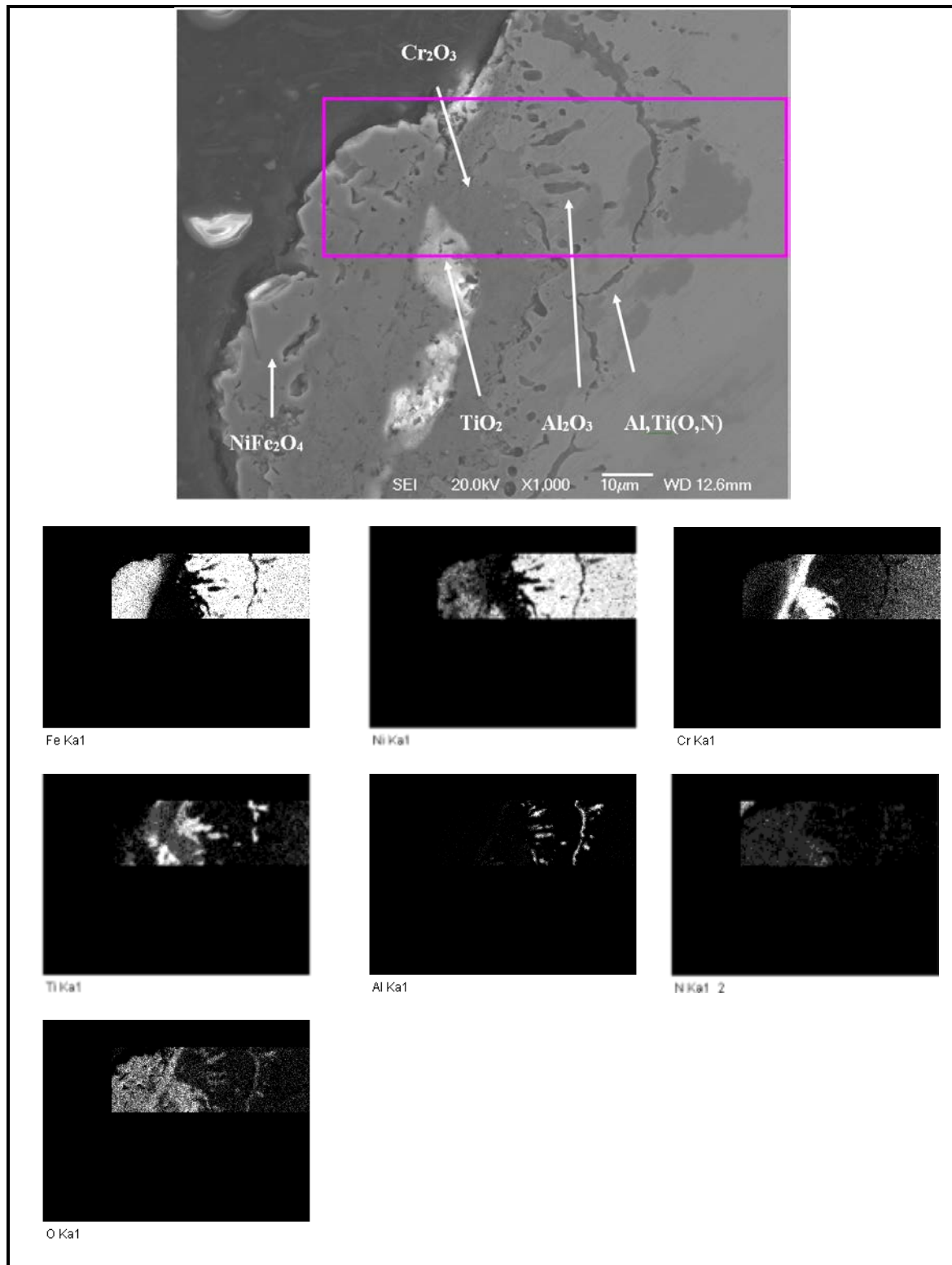


Figure 5-4 – SEM image and elemental mapping at x1,000 magnification of the start of the crocodiled region of an extruded bar - Section 1

### 5.3.3 Section 2: Middle of Crack

The middle region of the crack showed similar characteristics to the base of the crack, although in a much milder form, and the two distinct outer layers of  $\text{NiFe}_2\text{O}_4$  and  $\text{Cr}_2\text{O}_3$  have broken up and delaminated away from the surface (Figure 5-5). The once layered morphology now has a less strongly-defined structure with Al and Ti mixing throughout the oxidised region instead of being sub surface. This is likely to have been caused by the deformation of the material during extrusion. The depth of the oxide layer within this region, including delamination, is approximately 35  $\mu\text{m}$ . It is interesting to note that within this sample there were regions with little or no sign of oxidation. In all probability, when the ingot has opened during extrusion, fresh material may have been revealed leaving a clean surface with insufficient time for it to oxidise, or the oxide scale has become detached on cooling.

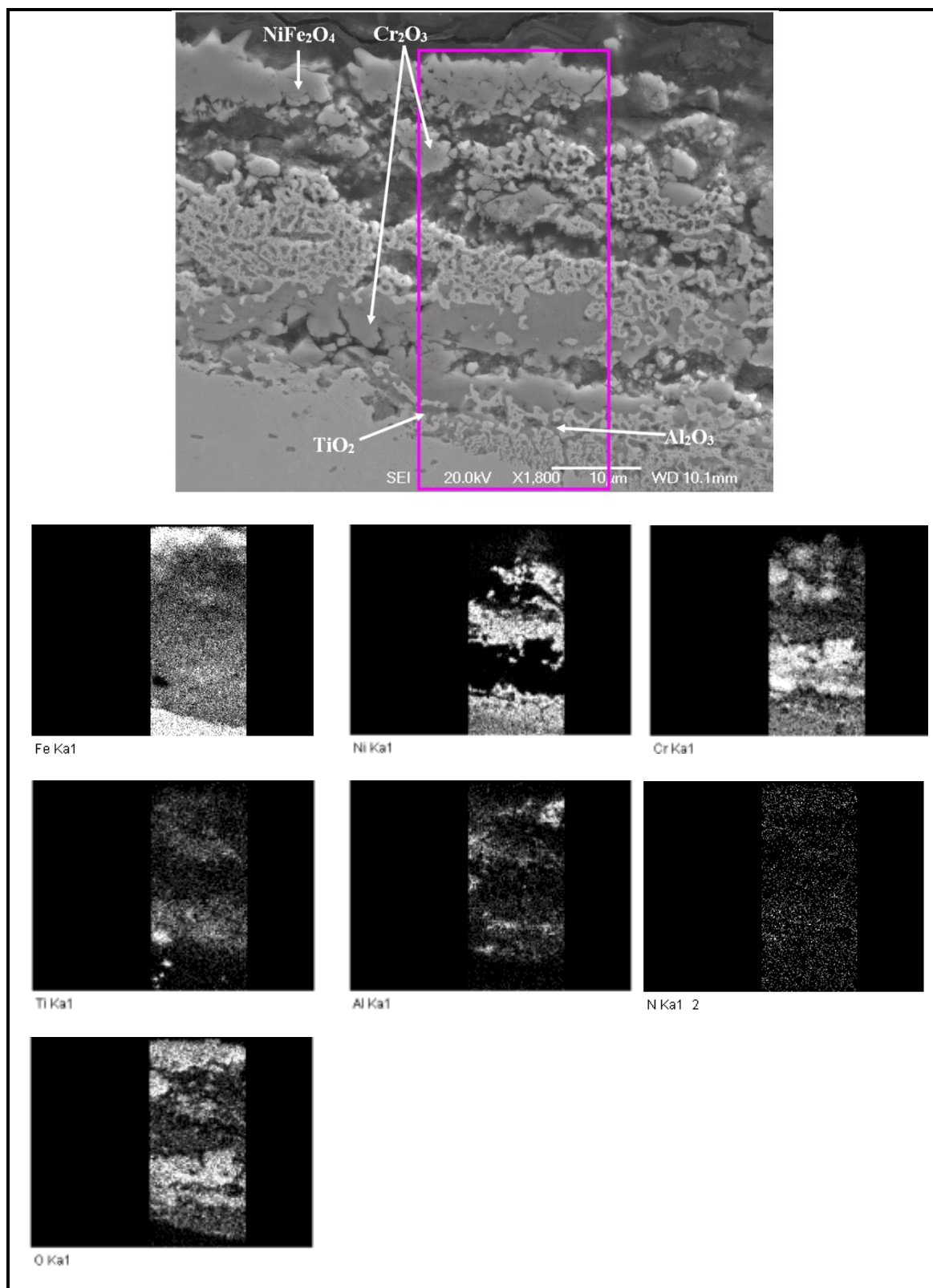


Figure 5-5 – SEM image and elemental mapping at x1,800 magnification at the mid crocodiled region of a extruded bar - Section 2.

### 5.3.4 Section 3: Crack Tip

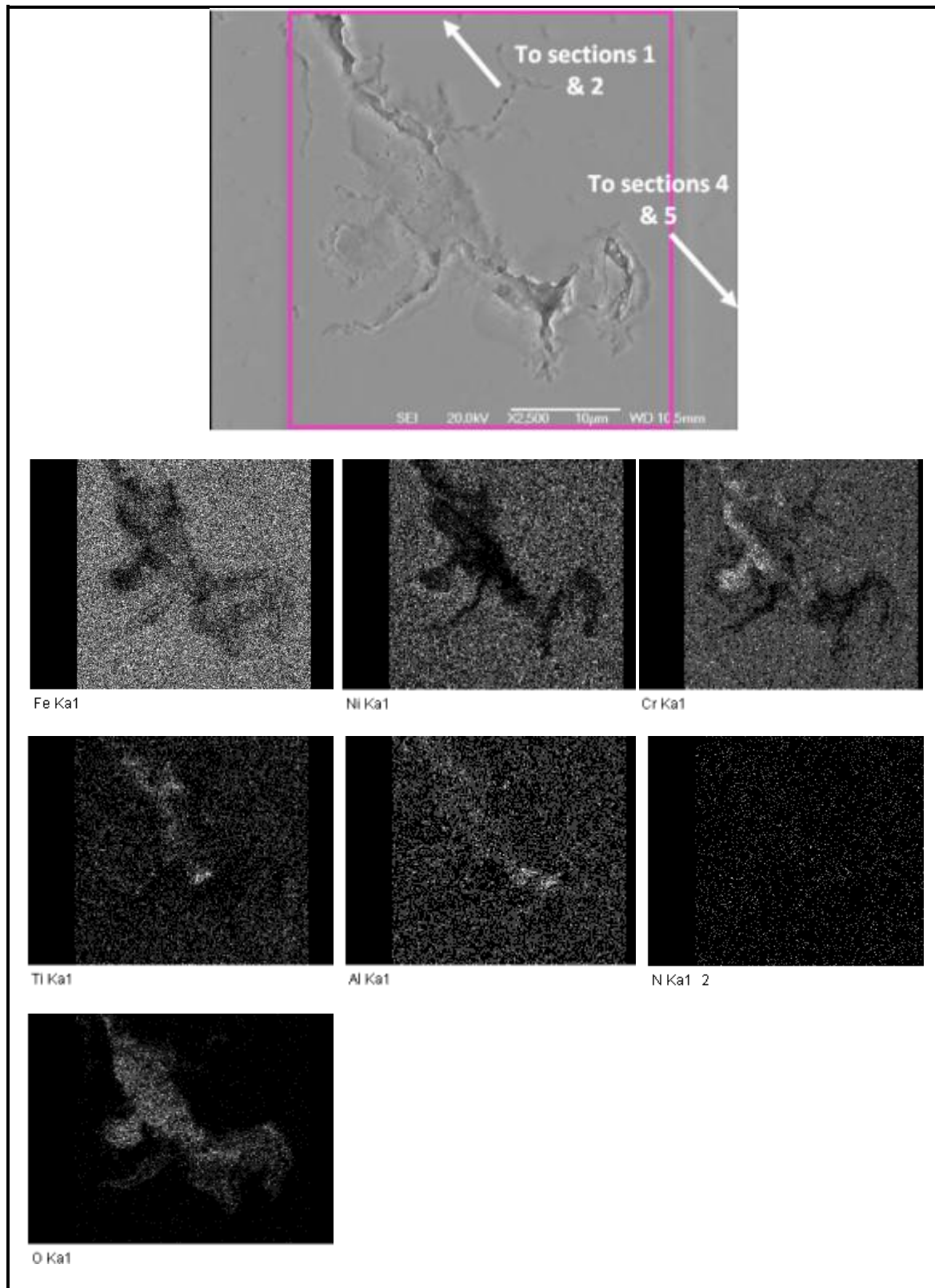


Figure 5-6 – SEM image and elemental mapping at x2,500 magnification at the crack tip of the crocodile extruded bar - Section 3.

At the tip of the crocodile crack, signs of oxidation of the elements Al, Ti, Cr and probably Fe are present within the centre of the oxidation feature shown in Figure 5-6. With no distinct separation of any oxygen rich regions to nitrogen rich regions it is hard to say if nitridation has occurred or not within this region.

#### 5.3.5 Section 4: Sub Crocodile Crack 1

Just in front of the crack tip (section 4), clean material is present with no foreign particles detected. However, traversing further down the length of the extruded bar another feature region is found (Figure 5-7). This is thought to be due to the cracking of the ingot within the pre-heat furnace. This consists of a continuous void with a similar particle distribution either side of it. The surface of the void, which can be seen in Figure 5-8, is rich in Al, Ti and O: likely  $\text{Al}_2\text{O}_3$  and  $\text{TiO}_2$ ; the presence of chromia is also detected here. This region has a thickness of approximately 2  $\mu\text{m}$ .

Approximately 5  $\mu\text{m}$  from the surface a dark in contrast, platelet like AlN particle is present. At greater depths nitrogen rich regions are only observed with very few oxygenated areas; most probably AlN and TiN dark platelet and light globular in contrast respectively (as indicated within Figure 5-7). Figure 5-9 is a high resolution elemental map of a TiN particle approximately 30  $\mu\text{m}$  away from the central void. All particles present are orientated in the direction of the extrusion; confirming they were present before the extrusion process. The total penetration depth of the particle rich zone is over 60  $\mu\text{m}$  with the same observed on the other side of the void.

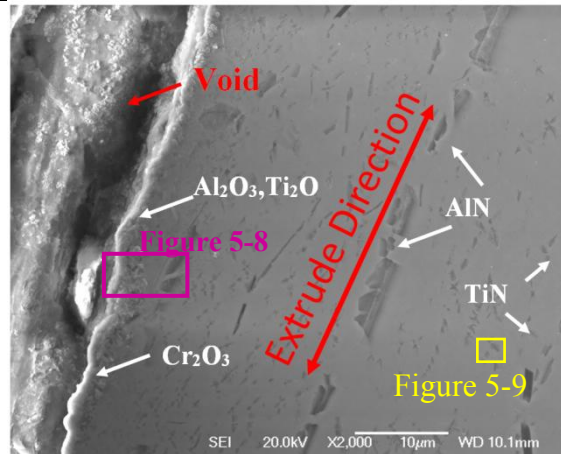


Figure 5-7 – SEM image x2,000 magnification of a sub crocodiled region of a extruded bar -. Section 4.

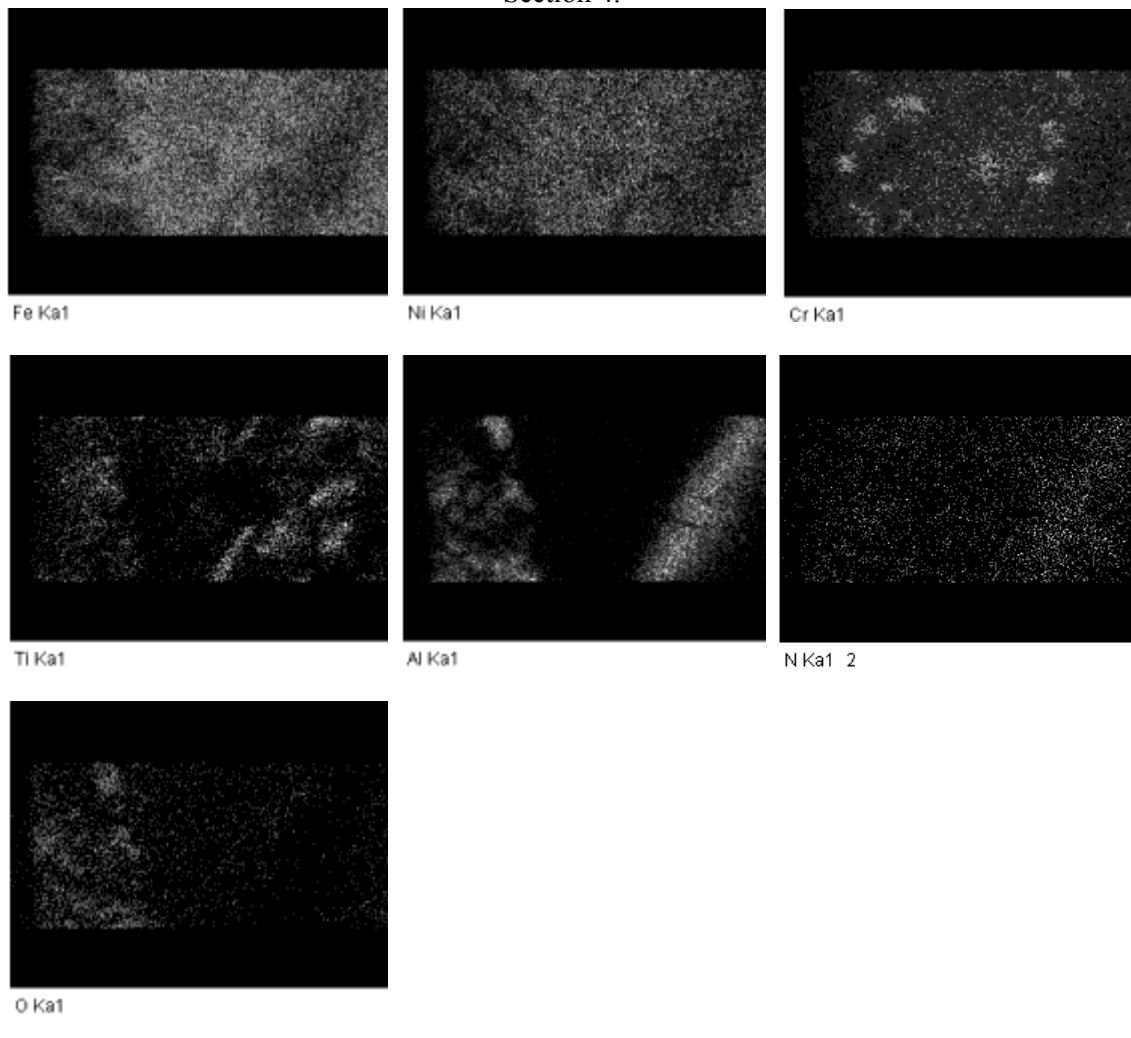


Figure 5-8 – Elemental maps of the surface of the void as shown by the large rectangular purple box annotated within Figure 5-7



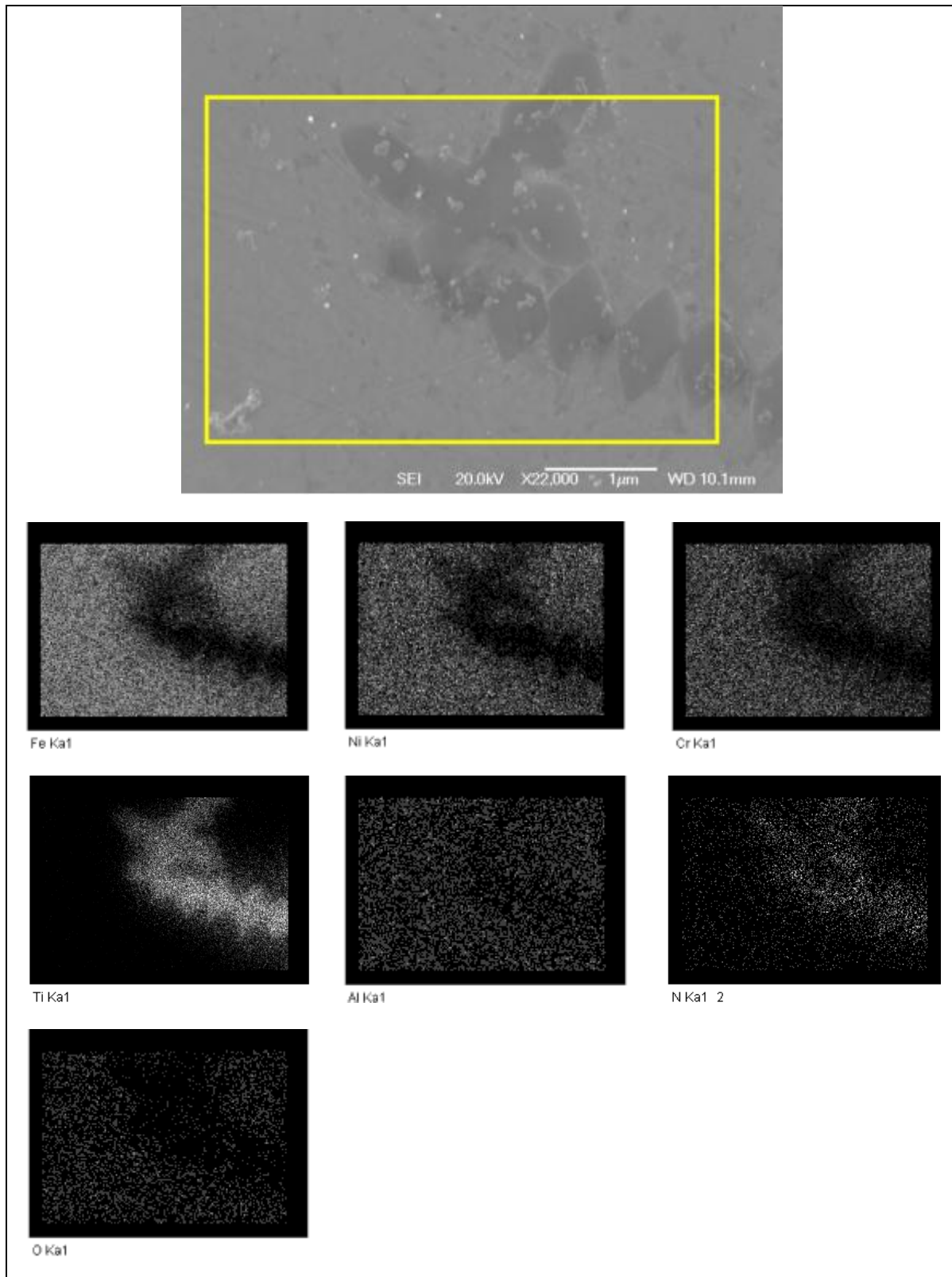


Figure 5-9 – Elemental maps at the location sub-surface of the void as shown by the small yellow square annotated within Figure 5-7.



### 5.3.6 Section 5: Sub Crocodile Crack 2

Continuing down the extruded bar a continuous band of particles is observed; centrally in this band is a distinct uninterrupted line of particles which may represent a weld line. It is quite possible that this is the joining of a void as observed in section 4. As before AlN and TiN rich particles are present which stretch in total approximately 200  $\mu\text{m}$  wide, and as in section 4 the particles are orientated in the extrusion direction. In comparison to the valve bar feature, AlN particles cluster around the centre of the particle rich zone; approximately 100  $\mu\text{m}$  in width in this sample and the TiN particles cover the full breadth.

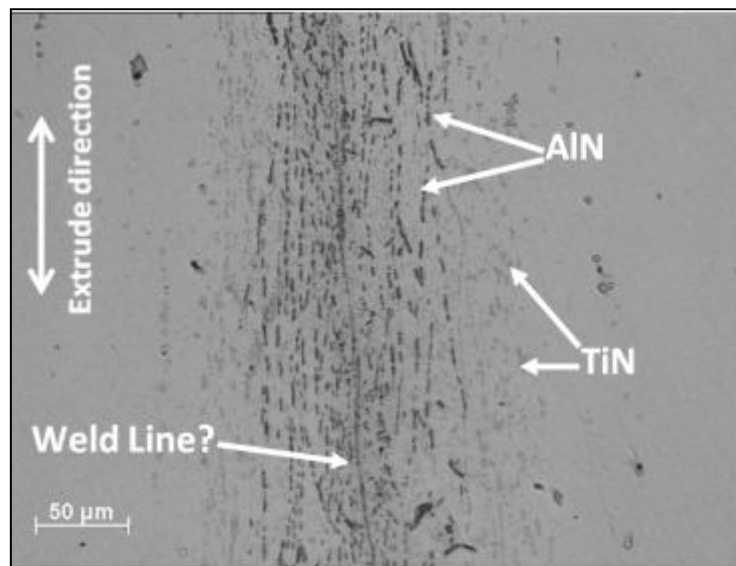


Figure 5-10 – Optical image displaying regions of dark in contrast particles AlN and Light in contrast, TiN particles - Section 5

## **5.4 Oxidation of an Non-Extruded Sample**

The ingots experience large amounts of deformation during the extrusion process, which has caused delamination of the oxide surface; this can clearly be seen within Section 2 of the extruded bar. To fully understand the oxidation characteristics of the alloy a non-extruded bar was studied after exposure to the pre-heat furnace time and temperature. The opportunity has also been taken to investigate the morphology of an oxide lap in the as-cast and oxidised state; this study can be found in Appendix A.

### **5.4.1 Surface Oxidation**

The oxidation of XD1102 under these conditions creates distinct tiers (Figure 5-11) with a dual layer of initially iron and nickel rich with oxygen of 40  $\mu\text{m}$  thickness followed by a chromium and oxygen rich sub layer approximately 20  $\mu\text{m}$  in thickness. Beyond this region, aluminium and titanium enriched with oxygen is observed both as intergranular fingers and some intragranular globular particles. Approximately 70  $\mu\text{m}$  below the chromium and oxygen enriched region enrichment of aluminium and titanium with nitrogen is observed Figure 5-12.

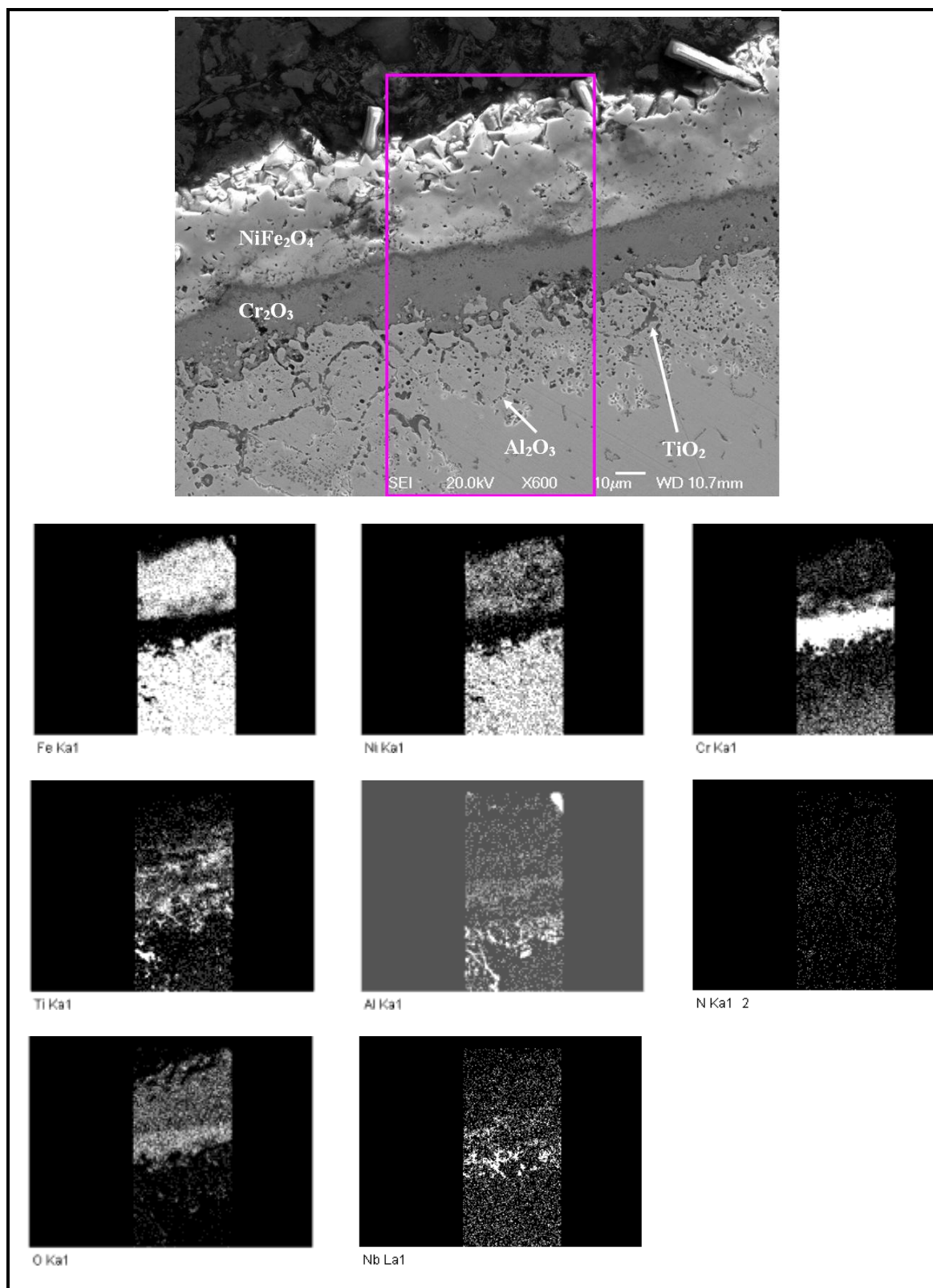


Figure 5-11 – SEM image and elemental mapping at x600 magnification displaying the oxidation characteristics of XD1102.

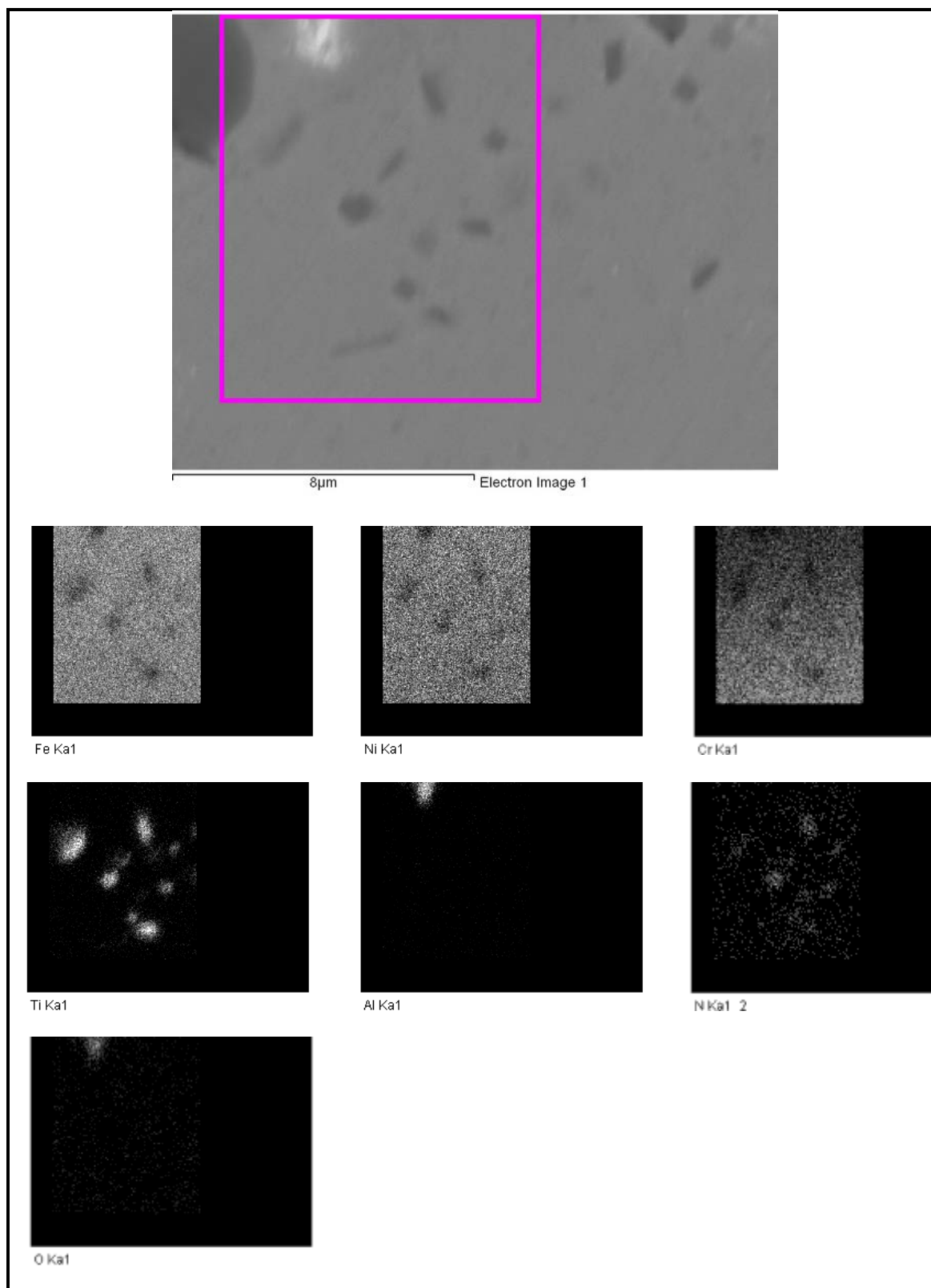


Figure 5-12 – SEM image and elemental mapping at x7,500 magnification displaying sub-surface nitridation.

### 5.4.2 Treating a Lap Defect as a Crack

It is known that the ingots can crack during the pre-heat furnace; oxidation of the surface and the region in front of the crack will then occur. Figure 5-13 shows such a region of a crack tip which has not been extruded. The morphology of the particles at the end of the crack resembles the same as an oxidised surface where an oxidised surface layer of both iron and chromium precedes the oxidation and nitridation of both aluminium and titanium. Annotated within Figure 5-13 is the distance beyond the crack tip that oxidation is observed; this reaches 200  $\mu\text{m}$  which is nearly double the standard depth of oxidation on a flat surface. This phenomenon is known as Stress Accelerated Grain Boundary Oxidation (SAGBO) (Evans et al., 2013) where an increased rate in oxidation is found at the cracked tip over a standard oxidised surface.

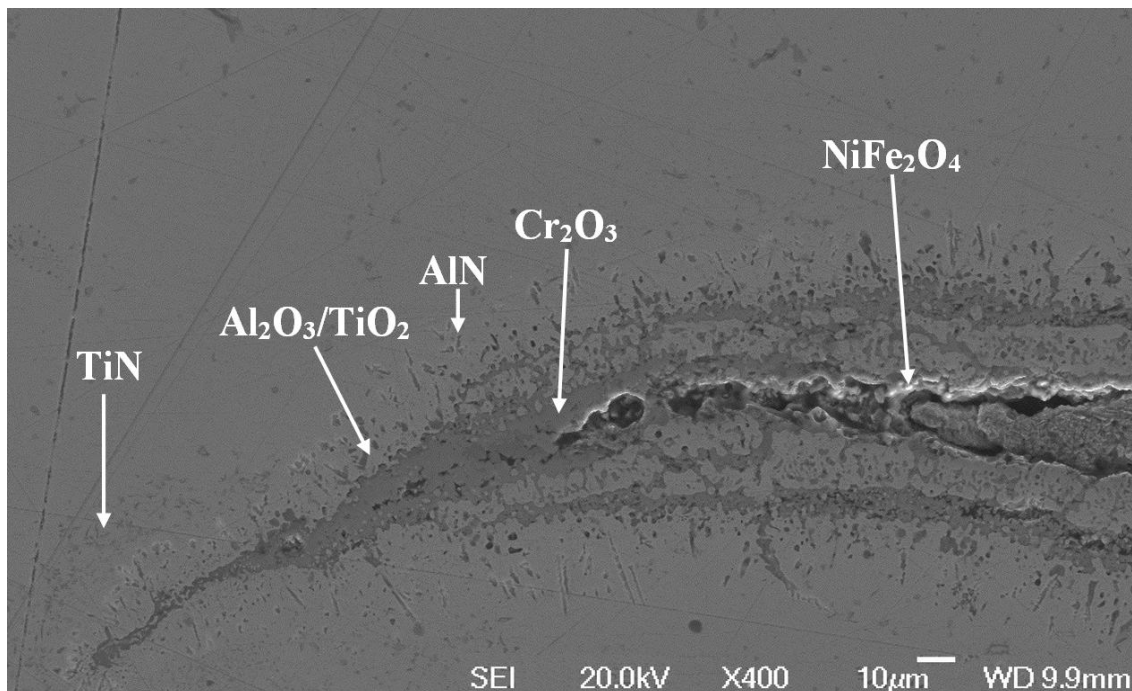


Figure 5-13 – SEM image at x400 magnification displaying oxidation in front of a crack.

## 5.5 Analysis of Thermal Shocked Ingot

An ingot that exhibited a cracked base after heating in the pre-heat furnace was sectioned into cubes as seen in Figure 5-14. The distance between the surfaces of the crack, after cooling, varied from the base of the ingot ( $<0.5$  mm) to the end of the crack ( $<0.010$  mm), which was at a depth of approximately 20 cm from the ingot's base (Material lost to machining is not inclusive). Upon extrusion the reduction ratio would cause a crocodiled region of approximately 2.5 m; something which was observed regularly for XD1102. On further inspection a second crack was observed in the radial direction which did not breach the surface.

### 5.5.1 Longitudinal Crack – “Primary”

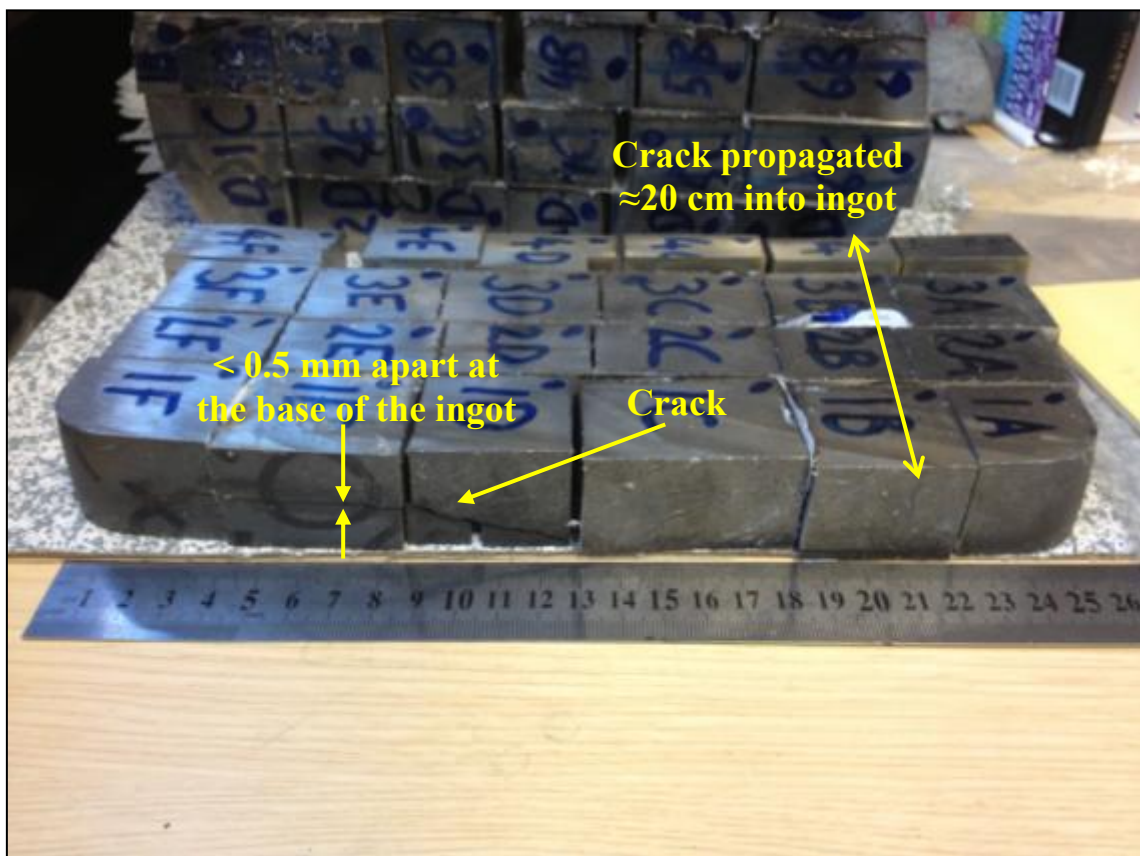


Figure 5-14 – Photograph illustrating the longitudinal crack on the base of an ingot after being withdrawn from the furnace prior to extrusion.

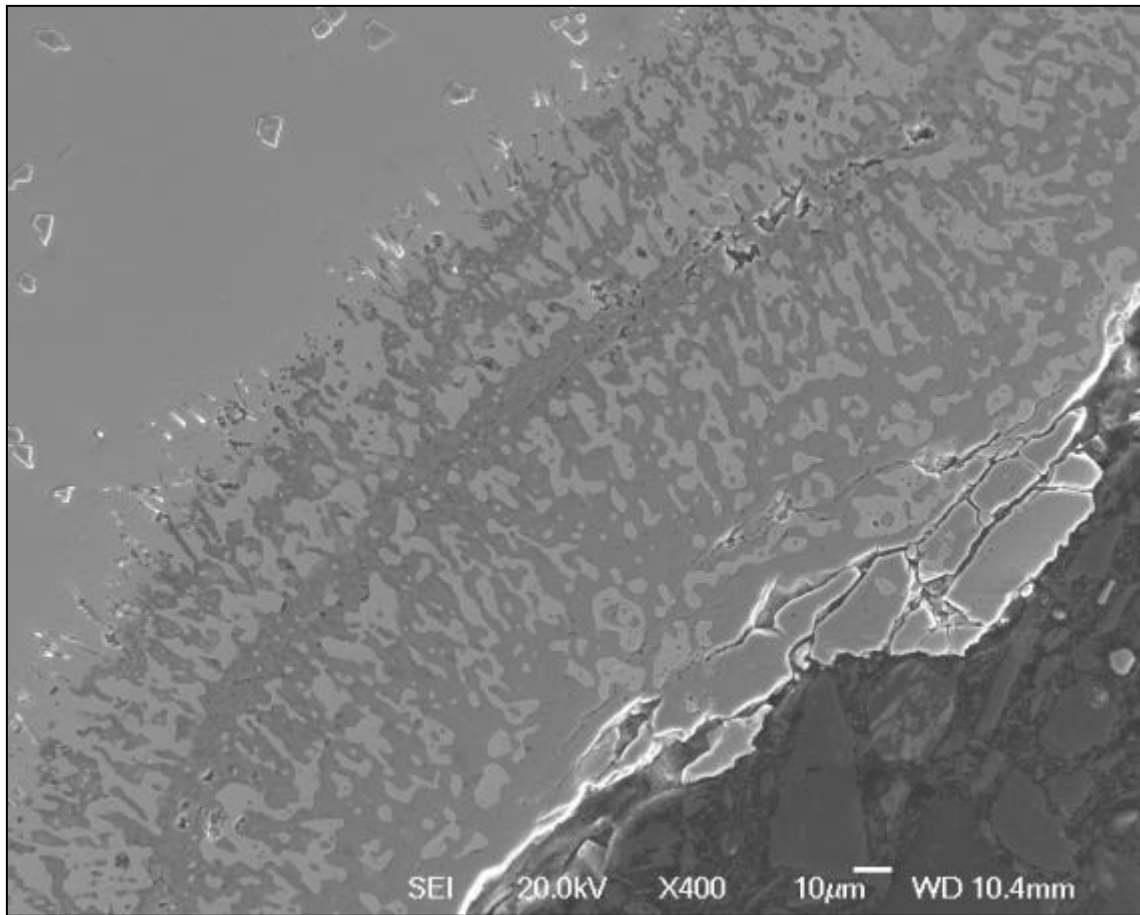


Figure 5-15 – SEM image at x400 magnification illustrating the oxidation at the base of cracked ingot.

Similar characteristics of the front of the crocidiled bar was observed for the cracked ingot, where nickel-iron and chromium oxides forms prior to the formation of aluminium and titanium oxides (Figure 5-15).



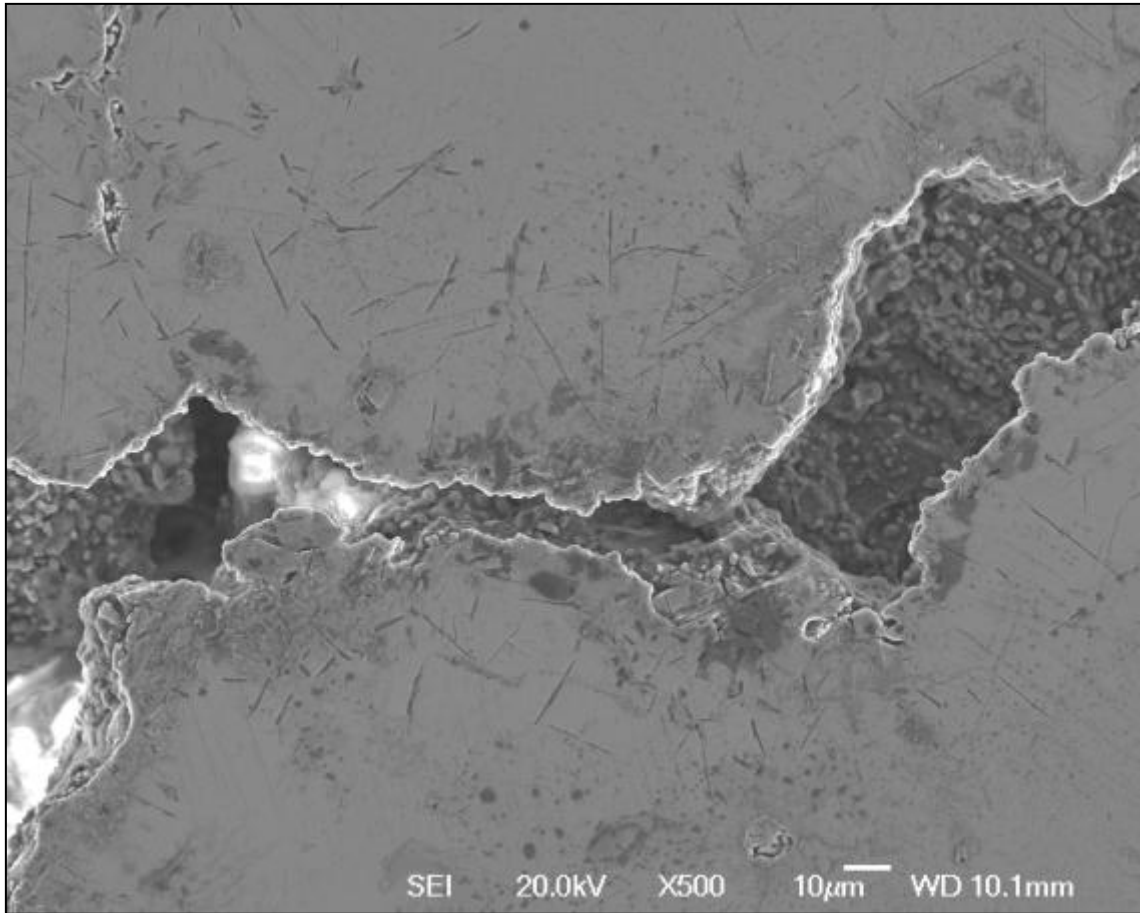


Figure 5-16 – SEM image at x500 magnification displaying the oxidation and nitridation of aluminium and titanium at the end of primary crack.

The amount of oxidation observed on the surface of the crack reduced with increased distance away from the base of the mould. Towards the end of the primary crack, the oxidation of both aluminium and titanium was prominent and in close proximity to the crack surface, Figure 5-16. This is in comparison to Figure 5-15 which shows a strong presence of nickel-iron and chromium oxides near the surface of the crack ( $>70\text{ }\mu\text{m}$  in depth) followed by the oxidation of aluminium and titanium. Only relatively small amounts of oxidation of nickel-iron and chromium is evident within the first  $5\text{ }\mu\text{m}$  of this region. This reduction in oxidation is likely to be due to oxygen being consumed



travelling from the base of the ingot towards the end of the crack, and this argument is strengthened through the large aspect ratio of the crack.

Compiling the evidence from the two sets of analysed samples, the morphology of the crack tip was predicted as illustrated in Figure 5-17. For this study, the morphology of the crack tip was analysed after the ingot had received the full pre-heat treatment prior to extrusion. Therefore, a well developed oxide scale existed which consisted of three distinct tiers.

1. Surface oxides of nickel and iron followed chromium.
2. Intergranular, and some intragranular, oxidation of titanium followed by aluminium.
3. Internal nitridation of aluminium followed by titanium.

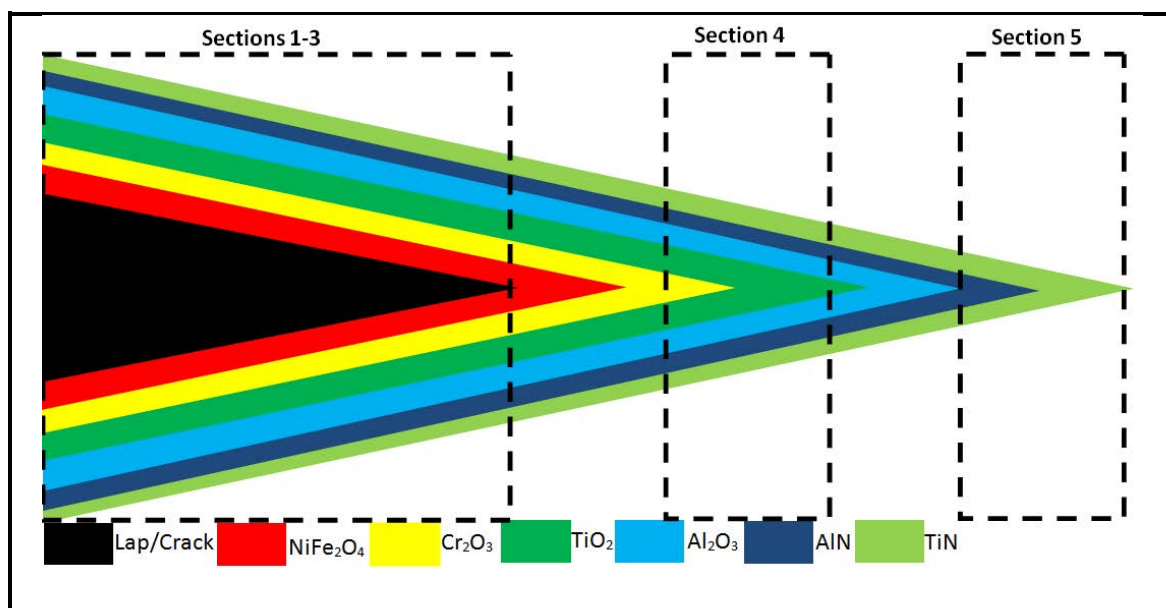


Figure 5-17 – Schematic diagram showing the morphology of an oxidised crack in the alloy XD1102

The first tier consisted of a mixture of oxides of iron and nickel, likely to be a spinel of NiFe<sub>2</sub>O<sub>4</sub> as found by Croll (Croll and Wallwork, 1972) for a Ni-Fe-Cr alloy when containing similar concentrations of iron and nickel as XD1102. This initial surface oxide was followed by a continuous protective layer of chromia (Cr<sub>2</sub>O<sub>3</sub>). The

investigation by Croll illustrated that when a constant chromium content was present and the nickel and the iron content was varied, the passive surface oxide formed was dependant on the nickel and iron concentrations. For nickel compositions lower than two weight percent, it was found that the surface oxide consisted of wustite ( $\text{FeO}$ ). With increasing nickel, a spinel formed on the surface having the formula  $\text{Ni}_x\text{Fe}_{3-x}\text{O}_4$  with islands of  $\text{Fe}_2\text{O}_3$ , which decreased with the increase in the nickel content.

The second tier consisted of the oxidation of titanium ( $\text{TiO}_2$ ) followed by aluminium ( $\text{Al}_2\text{O}_3$ ) within the substrate at predominantly intergranular regions, but with small amounts at intragranular regions. Alumina ( $\text{Al}_2\text{O}_3$ ) is known to increase the oxidation resistance of an alloy as it is a very dense and stable oxide (Lund and Wagner, 1965); however, to be effective a continuous layer must be formed. To form this continuous layer, approximately five to six weight percent minimum of aluminium is required as found by Bensch et.al in the alloy René N5 (Bensch et al., 2012). The aluminium content in XD1102 is not in sufficient supply, and therefore a continuous oxide layer is not formed resulting in the preferential oxidation at the intergranular regions. This selective oxidation agrees with Taylor et al in the alloy RR1000, Trindade on the alloys 625 and 718 (Trindade et al., 2005) and Pettit on various superalloys (Pettit et al., 1984). Unlike the protective nature of a continuous alumina layer, the selective oxidation at grain boundaries is known to reduce the low cycle fatigue life of components (Pineau and Antolovich, 2009), and it was found to be more detrimental than failure through creep mechanisms in two powder-based superalloys (Tong et al., 2001).

The final tier consisted of the nitridation of aluminium ( $\text{AlN}$ ) followed by titanium ( $\text{TiN}$ ) as small globules of nitrides. Taylor et al. observed, and confirmed through

WDX analysis, that the deepest point of penetration was the nitridation of titanium which is in agreement with this study (Taylor et al., 2012).

The tiers concluded from this study were drawn after a well developed oxide was formed through the prolonged exposure at temperature within the pre-heat furnace, and therefore it could not be concluded how the oxide grew. Pettit found that for nickel-based superalloys the selective oxidation of elements to form the protective barrier initially was transient, and the oxidation of multiple elements can be found prior to the formation of the protective barrier (Pettit et al., 1984). In these findings, NiO was the first to form due to the increased weight percentage over other elements; the transient stage. During this period the elements, such as chromium and aluminium, that provide the protective barrier gradually diffuse to the surface and form the protective continuous oxide. In the present study of XD1102, an alloy with a substantial increase in the iron content compared to Pettit's study, it is likely the spinel as described above would have formed before the protective  $\text{Cr}_2\text{O}_3$  layer.

Agreement is made when comparing the above final two tiers with the Ellingham diagram (Ellingham, 1944), which states that:

1. Oxygen is more likely than nitrogen to attach to both aluminium and titanium.
2. Oxygen will react more readily with aluminium than titanium giving the deepest oxide as alumina particles.
3. Nitrogen will react more readily with titanium than aluminium giving the deepest nitride as titanium nitride.

The first tier has not been considered in agreement with the Ellingham diagram due to the transient nature of the formation of the oxides.

The morphology as described above is representative of laps, or in the case of this study a crack within an ingot that has oxidised over time. Extruding a cracked ingot is likely to cause an opening of the extruding bar, “crocodile”, drawing through the features as illustrated in Figure 5-17. Annotated in are dashed boxes which represent the areas which have been analysed through the SEM analysis within the extruded bar study. It is suspected that the valve bar feature, as previously discussed, is representative of the region labelled section 5. The majority of this oxidised bar was easy to detect and discard due to the presence of the crocodiled region. However, if the extruded bar was not cropped back sufficiently beyond this region the feature as described by section 5 may remain in the bar through to hot rolling; as is the case and the cause of initiation of this study.

## **5.6 Crack Formation Hypothesis**

The cause of the base crack in ingots is likely to be due to a combination of two contributing factors.

Firstly, cracks have only ever been witnessed along the bases of the ingots, and due to this fact factor within the casting process must be scrutinised. When casting ingots by the Durville tilt casting technique, the base will have the highest cooling rate; this would lead to this region experiencing an increased amount of residual stress. Additionally, cracks have never been witnessed at the top of the ingot as this region is protected by the insulating collar and the addition of Bitop increasing the solidification time and therefore lowering the predicted amount of residual stress in this region. The head of the ingot is sectioned back so the “top” in the pre-heat furnace is actually material which was within the main body of the cast ingot, and therefore has an increased

solidification time further reducing the residual stresses. Without making changes to the Durville tilt casting method these residual stresses are likely to remain, and may lead to cracking along the base of the ingots within the pre-heat furnace.

Secondly, during the preheat prior to extrusion thermal stresses will be present as a differential in thermal expansion is present, and loading an ingot into a furnace set at higher temperatures will thus lead to increased thermal stresses. It must be noted that although thermal stresses have been simulated, no residual stress measurements prior to the pre-heat furnace were conducted. The residual stress distribution has been hypothesised by the author and would need to be the basis of further work.

#### 5.6.1 ProCAST

ESI's software package ProCAST was used to simulate the stress distribution across the base of the ingot for the standard extrusion pre-heating regime and an alternative heating regime which incorporated a lower load temperature, and an increased amount of time in the furnace prior to extrusion. It is found that for the standard pre-heating regime a 66% increase in the maximum stress can be expected on the base of the ingot as illustrated in Figure 5-18 and Figure 5-19. All data points are taken at the base of the ingot and therefore initially have a compressive stress as the ingot heats up and expands both radially and longitudinally. As the cooler inner material heats up and wants to expand this pushes against the outside surface and flips the stress state into tensile. Even though ProCAST has estimated values for stress, the work should be treated as indicative of the behaviour rather than a determination of the magnitude of the stresses as no experimental stress measurements to validate them have been carried out.

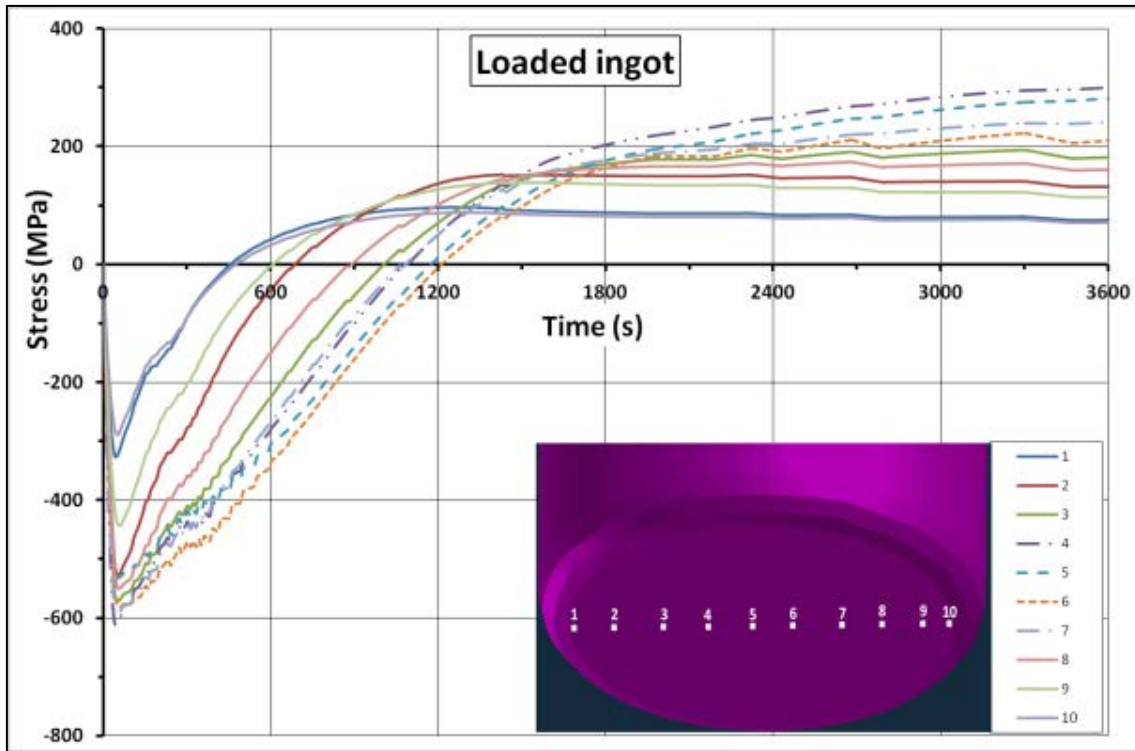


Figure 5-18 – Graph to show the ProCAST simulation predictions of the stress distribution along the base of the ingot which has the standard pre-heating process.

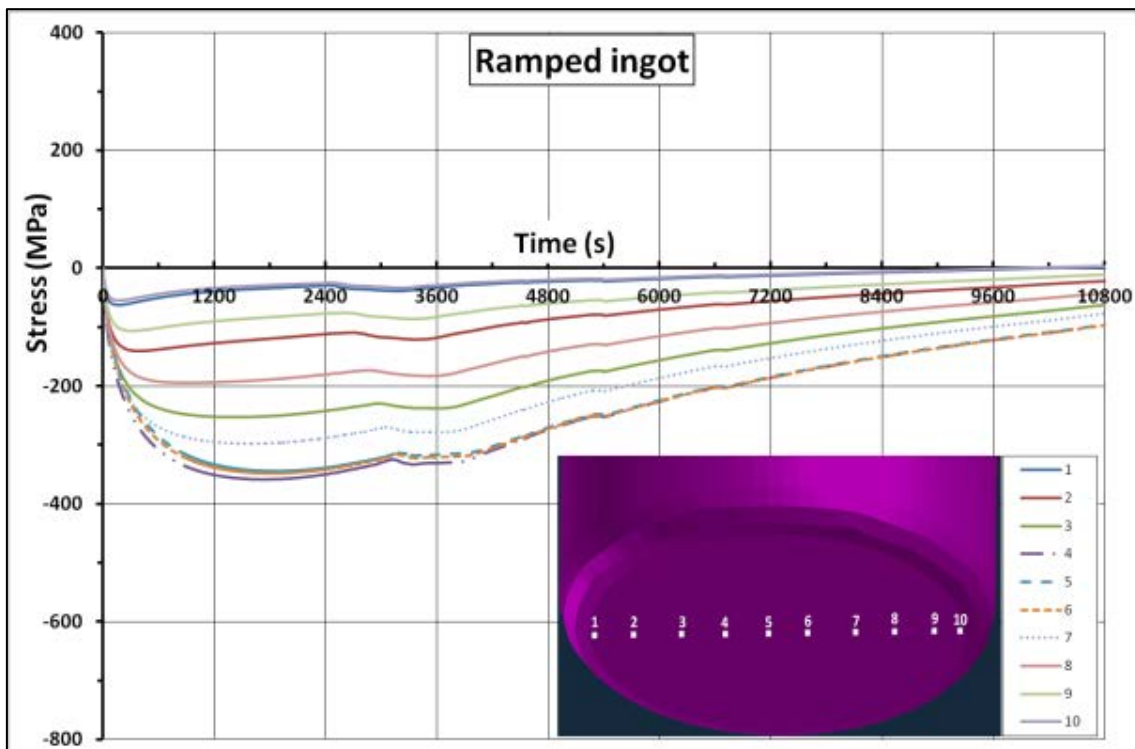


Figure 5-19 – Graph to show the ProCAST simulation predictions of the stress distribution along the base of the ingot which has an alternative heating regime..

The ProCAST simulation was modelled as an ingot suspended within a furnace with uniform heat transfer into the ingot by radiation. However in reality the ingot will not experience uniform heating, as described in Figure 5-20, as large amounts of heat will transfer to the ingot by conduction through the furnace bed via the interface of the ingot. This increased heat transfer will cause a greater drive for expansion within this region as indicated by the blue arrows in the figure.

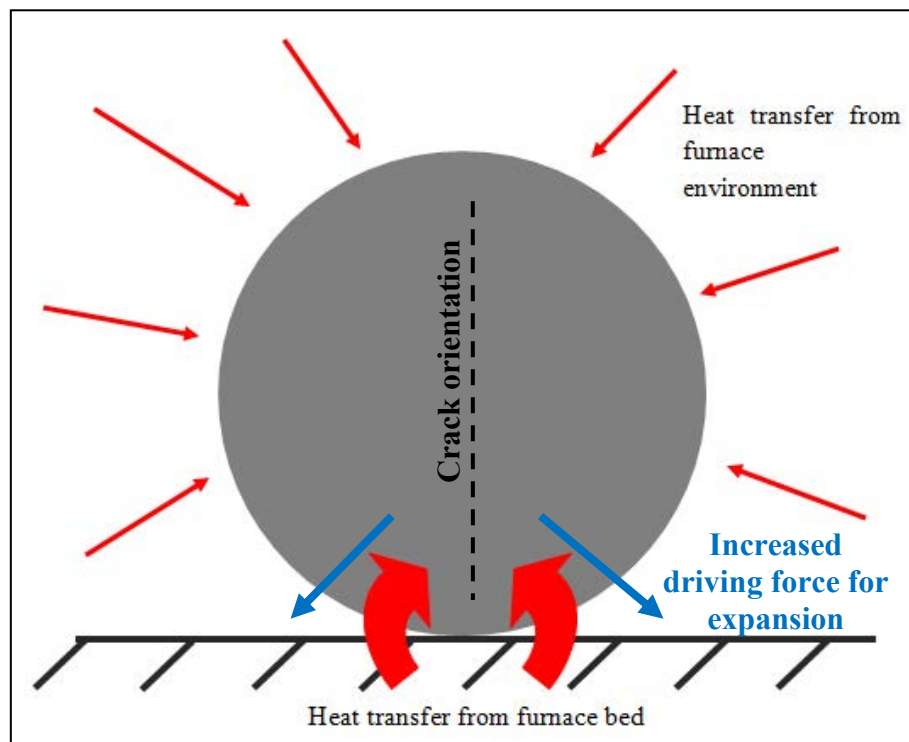


Figure 5-20 – Schematic diagram displaying the heat transfer distribution into the ingot from the furnace environment during the pre-heat furnace prior to extrusion.

The combination of the increased residual stresses at the base of the ingot and the thermal stresses due to loading the ingot into the furnace at the extrusion temperature is too great for the ingot to withstand, and this ultimately leads to a crack. Thereby, if an ingot had the radii removed from its base and therefore removing a region of high residual stresses; the probability of the ingot cracking is reduced. In this study all but

one ingot cracked and the non-cracked ingot had its radii removed before the pre-heat treatment. Although the orientation of the crack with respect to the furnace layout was unknown, a proposed orientation is presented in Figure 5-20. Originally it was predicted that the crack would propagate across a mould base feature due to it being a stress riser; however, this was not the case and the heat flow as described in Figure 5-20 causing preferential thermal expansion could explain this.

### 5.7 Circumferential “Secondary” Crack

In addition to the primary crack a second crack running circumferentially was observed at mid height of the ingot (Figure 5-21). There were no observable cracking on the surface of the ingot and therefore it is assumed to be an internal crack. This was confirmed on inspection as no oxidation of the crack was found (Figure 5-22).

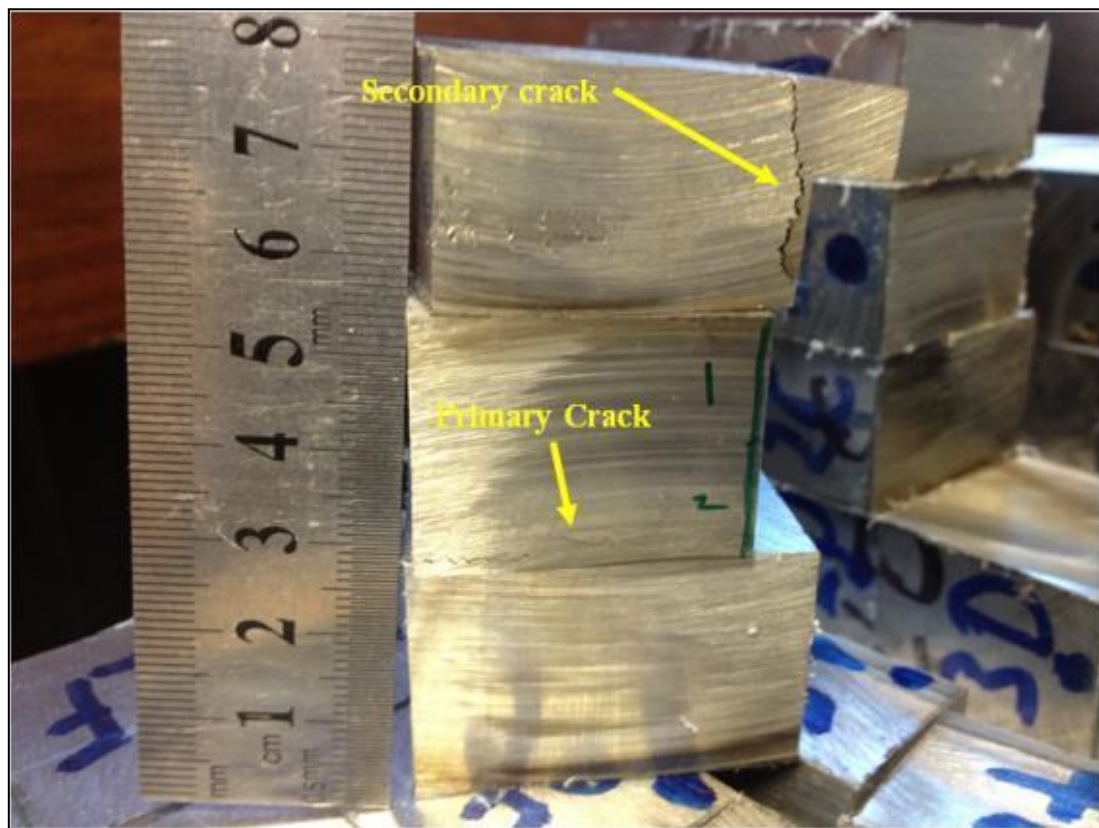


Figure 5-21 – Photograph displaying the primary and secondary crack of an XD1102 ingot which has been withdrawn from the pre-heat furnace prior to extrusion.



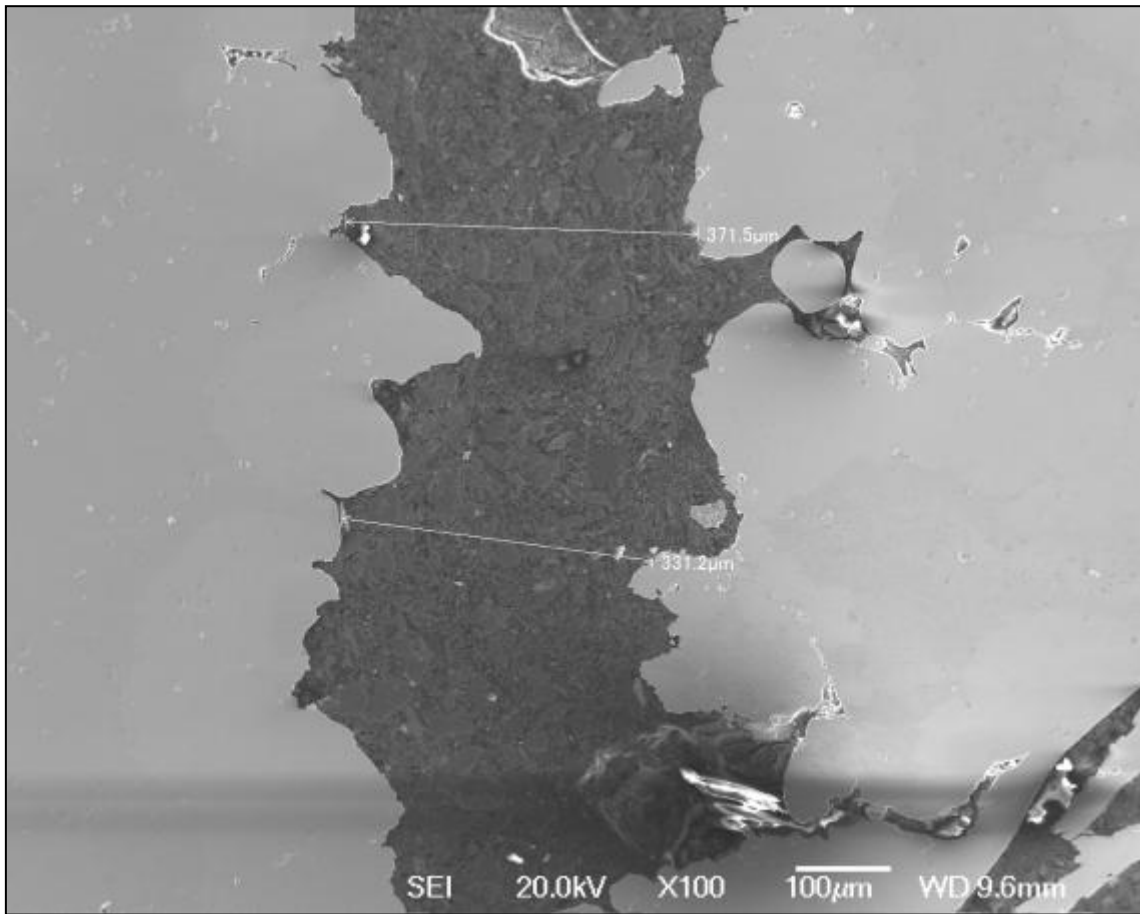


Figure 5-22 – SEM image at x100 magnification displaying that no oxidation of the secondary crack has occurred.

Thermal shock is also the likely cause of secondary cracking; however, unlike the primary crack it is unlikely to open during the extrusion process. This is due to firstly no surface-connected breakages being present and secondly as the material flows through the die a radial force is being exerted on the circumference of the ingot. In comparison, an ingot with a cracked base will crocodile due to the frictional forces present at the ingot die interface causing the crack to open.

As was observed at the end of the primary crack where a weld line was present (Figure 5-10) the secondary crack is also likely to “heal” through compression during extrusion, reducing the potential for any deleterious effects on the final material properties. A similar effect was found on two 706 VAR ingots as discussed by (Minisandram et al.).

## **5.8 Conclusions**

Features observed on the various valve bars have been identified as oxides and nitrides by SEM and EDX techniques. These were likely to be the result of a combination of residual stresses, during solidification, and thermal stresses during the pre heat furnace prior to extrusion causing a longitudinal crack along the bases of ingots. The time within the furnace allowed for the oxidation of the newly formed crack. During extrusion the crack opened widely and the material in this region was discarded, however the entire crack length did not remain open with some of the crack length fused back together from the pressure and temperatures of the extrusion process. This area was not detected and therefore not discarded, and remnants of the oxidation remained within the bar.

The oxidation of the alloy XD1102 was analysed using both SEM and EDX techniques. A sequence of oxides was observed where the penetration of a protective surface oxide, iron and chromium oxides, has led to both intergranular and intragranular oxidation and nitridation of aluminium and titanium. It was observed that nitridation of titanium was the deepest feature to have formed.

The valve bar feature is likely to be a section from an oxidised crack tip where a crocodiled ingot hasn't been cut back sufficiently after extrusion. To prevent this event from re-occurring it is suggested by the author to load the ingots into the furnace at a

lower temperature and then gradually increase the heat input, in a similar manner to the ProCAST simulations in section 5.6.1. However, if this placed too much restriction on the furnace use, due to the additional time required to re-heat the furnace, the ingots could be pre-heated in a separate furnace at a lower temperature before being introduced to the main furnace held at the pre-extrusion temperature.

If neither of these options were viable the ingots could be sectioned further back from the mould radius in order to remove the bulk of base ingot with high residual stress. The crack has been observed to propagate to a depth of at least 20 cm making this whole area unusable; sacrificing a proportion of the bottom of the ingot may prevent the cracking, overall leading to an increased yield of product.

Adjustment of the heat treatment regime is believed to be the most efficient process and would yield the greatest amount of product.

## **5.9 Future Work**

Features observed on the heads of various valves have been traced back to the oxidation of a crack which initiated during the preheat furnace prior to extrusion of the ingots. A hypothesis was offered to suggest that this is the result of both residual stresses from solidification and thermal stresses induced in the furnace through the environment and the furnace bed. Therefore it would be beneficial to understand what the residual stress state of the ingot is after solidification, predominately in four locations:

1. At the base of the mould where it is hypothesised to have the highest amount of residual stress.
2. Just above the base of the mould at the height of the mould radius where one of the six ingots did not crack during the furnace trial.

3. At the top of the ingot after it had been sectioned to remove the material surrounded by the insulating collar.
4. Centrally within the ingot as a reference residual stress state.

The current ProCAST simulation neglects the heat transfer into the ingot from the furnace bed, so the model should be extended to incorporate this. The increased heat transfer through the furnace bed could be influential on the orientation of the crack as an increased driving force for expansion is expected in this region. The crack orientation could then be confirmed if another trial was to take place by allowing the ingots to cool within the furnace and inspecting them before extraction. However, this would be difficult to schedule as the furnace will cool down and not be usable for other applications and an effect on yield would ensue.

# Chapter 6. Is the Bifilm Defect Detrimental to Wrought Product?

## 6.1 Introduction

It is well appreciated in industry that during air melting processes most metals whilst in the melt furnace will react with their environment; whether this is with the gases above, the melt container or slag floating on top of the melt. In this study focus will be concentrated on the reaction with dry air where formation of a non-metallic oxide layer on the surface of the melt is almost instantaneous. It has also been reported that even when casting in a vacuum small amounts of oxidation can still occur (Rashid and Campbell, 2004, Campbell and Tiryakioğlu, 2012, Li et al., 2004).

Oxides of this type that have formed in the melt furnace are commonly known as an “old” oxide film as they have prolonged time at temperature enabling them to grow. If the oxide is left undisturbed it will gradually grow to several tens of microns in thickness (Campbell, 2011a).

“New” oxide films are predominately created during pouring and movement of the melt along mould geometries and runners, where turbulence reveals fresh metal which is subsequently oxidised; due to the short time scales in comparison to old oxides films they are in the order of nanometres in thickness (Divandari and Campbell, 2001).

Within all casting processes, the movement of the melt from the furnace to the final mould geometries is a fundamental process step that usually cannot be avoided; this can lead to the breaking up and/or entraining of an old oxide film, and the creation of new

oxide films through turbulence. A schematic diagram of surface turbulence and entrainment is presented in Figure 6-1 (Campbell, 2006).

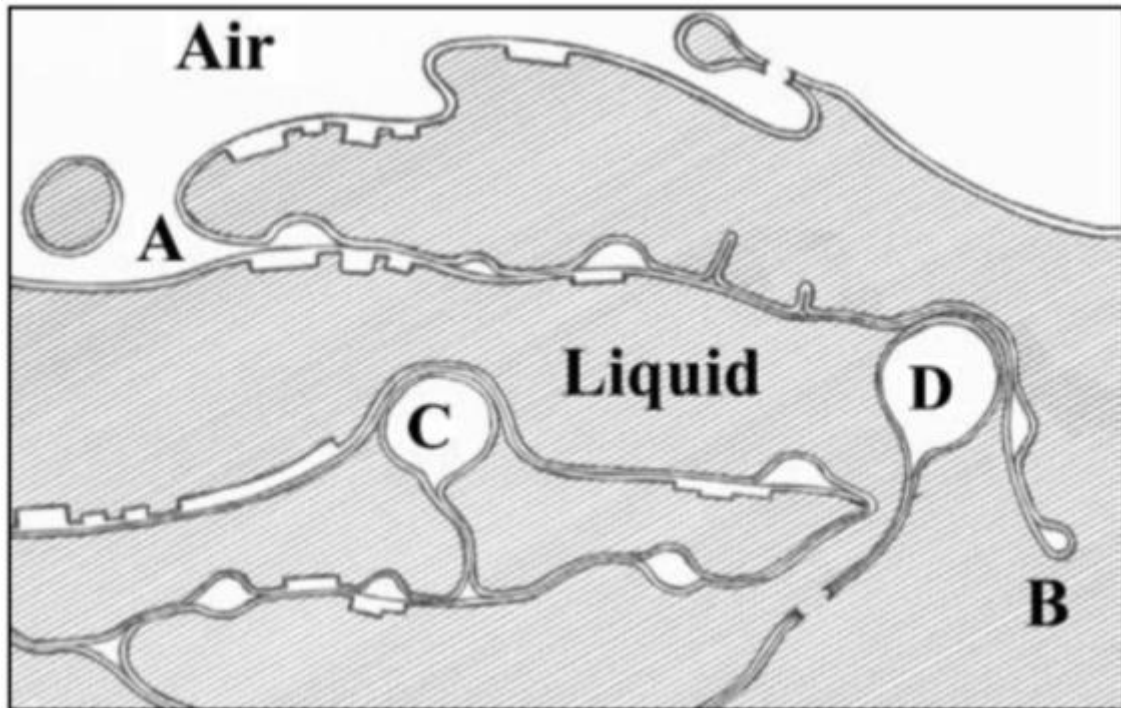


Figure 6-1 – Schematic diagram displaying surface turbulence within a liquid metal causing entrainment of the oxide skin and gas bubbles (Campbell, 2006)

The diagram illustrates numerous entrainment events due to surface turbulence; turbulence can cause the folding of the surface film into the bulk of the melt as displayed by annotations A and B. The entrained film is known as a “bifilm” due to its double nature (Campbell, 2011a). Annotations C and D represent the entrainment of large gas bubbles, and through buoyancy can leave a distinguishable trail behind, known as “bubble trail”, as it floats up through the melt. Entrainment of smaller gas bubbles is unlikely to form such a trail as they stay trapped within the original bifilm. Increased amounts of turbulence can further disrupt the melt’s surface and the once attached bifilm can become detached, subsequently submerging within the melt.

Bifilm entrainment is problematic to the casting industry as the bonding energy across the dry interface is relatively small, and therefore a bifilm can be considered as a crack. The structures from entrainment events can easily flow into moulds and settle within the casting, which is known to have adverse effects on the mechanical properties of the casting.

Wang and Harding demonstrated that a tranquil mould filling of titanium aluminide alloys eliminated gas bubble entrainment and gave better quality casts (Wang et al., 2011, Harding et al., 2011). Where Dispinar has predicted that a reduced number of bifilms found within a casting of aluminium would result in very high ductility (Dispinar and Campbell, 2011).

The majority of research into bifilms has focused on aluminium castings although it is of interest in the nickel casting industry where at least three in service engine failures have resulted from the entrainment of bifilms (Campbell and Tiryakioğlu, 2012).

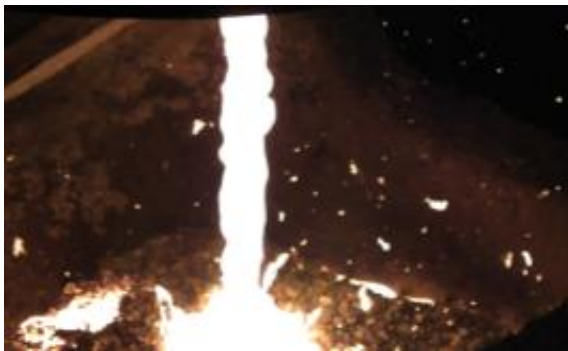
This makes it preferable to prevent entrainment from occurring and foundries have measures in place to eliminate this problem; these include re-melting, treatment of the metal and careful consideration of casting geometries and running systems. Secondary methods such as hot isostatic pressing are hypothesised to heal any pores and thin bifilms as demonstrated by the improved fatigue life of components (Staley Jr et al., 2007); thick bi-films of the spinel type however could not be healed.

Due to the size of the old oxide films they are usually easily detectable by conventional microscopy and by non-destructive techniques such ultrasonic and eddy current methods; however, the new oxide films are somewhat more difficult to detect by microscopy and near impossible to detect by non-destructive techniques.

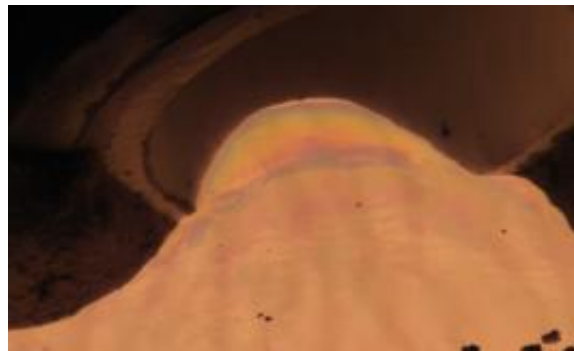
## 6.2 Entrainment of Oxides in the Production of XD1102 ingots

Special Metals Wiggin Limited (SMWL) melt XD1102 in an air induction furnace and the creation of an “old” oxide film on the melt is inevitable. When tilting from the furnace crucible into the ladle the old oxide layer will be transferred; this is likely to be broken up and mix within the melt due to turbulence. The instability and splashing during pouring will also create several thousands of new oxide films.

Once the ladle was craned above the Durville machines, the melt was bottom poured into the receiver from a height of approximately 1 metre. Additional new oxides films will be created due to further turbulence as highlighted in Figure 6-2 picture a).



a) bottom pouring of the liquid melt from the ladle into the receiver



b) The first volume of liquid enters the mould displaying an oxide film is present on the surface.

Figure 6-2 – Photographs taken during the Durville tilt casting process.

As described in section 2.2.6 the melt was allowed to dwell in the receiver until it reached the tilt temperature, this gave the opportunity for any oxides to float to the top of the receiver melt. Tilt filling of the mould was then employed to retain the oxides and vermiculite within the receiver’s volume instead of being transferred into the mould. It was observed that a new oxide film covered the melt as the Durville machine



was tilted over (Figure 6-2 image b)). Turbulence during tilt, either through vibrations in the tilting system or as the melt hit the base of the mould, increased the probability of the surface oxide becoming entrained. It was also possible for any vibrations to disrupt the oxide films held within the receiver and cause them to be transferred into the mould.

As the mould and receiver were mechanically joined the final stages of tilt transferred the vermiculite and the oxide films into the upper region of the mould. This was the location of the insulating collar that was subsequently discarded after solidification and before any further thermo-mechanic work was received. However the casting process was occasionally found to entrain some vermiculite within the main body of the ingot. This was a cause for concern as the relative size of vermiculite in comparison to the oxide films suggested a high probability of these also becoming entrained.

As identified the Durville tilt casting process provided many opportunities for the entrainment of oxide films. In the remainder of this chapter the life cycle of oxides through the manufacturing steps of a valve bar has been explored and the subsequent effects on the mechanical properties have been considered.

### 6.2.1 Dip Sample

For every cast of material produced at SMWL a “dip” sample is taken from the pouring ladle flume (Figure 2-1) to verify the chemistry of the cast. Such a sample was analysed where it was expected that oxide films would either be transferred from the ladle on pouring or created through turbulence within the sample. Due to the small volume of melt captured a high proportion of material was in contact with the cold dip pot causing it to solidify quickly. This increased the probability that oxide films solidified within the sample instead of floating to the top where they could have been misinterpreted as a surface oxide film. Sectioning and using microscopy techniques, as described in 5.3.1, led to numerous oxide films being detected, as shown in Figure 6-3 and Figure 6-4, with the corresponding percentage chemical deviations from the bulk given found in Table 6-1. It is worth noting that the two areas shown are not an exhaustive observation; within approximately 1 cm<sup>2</sup> section at least eight areas had a similar morphology to that shown in Figure 6-3 and Figure 6-4.

The oxide films have a combined morphology of thin continuous strands and larger porous regions (confirmed through optical microscopy). These were likely to have been caused by the oxide film encasing a gas pocket, which has subsequently been entrained within the film; this is in agreement to the schematic diagram presented by Campbell (Campbell, 2006) in Figure 6-1.

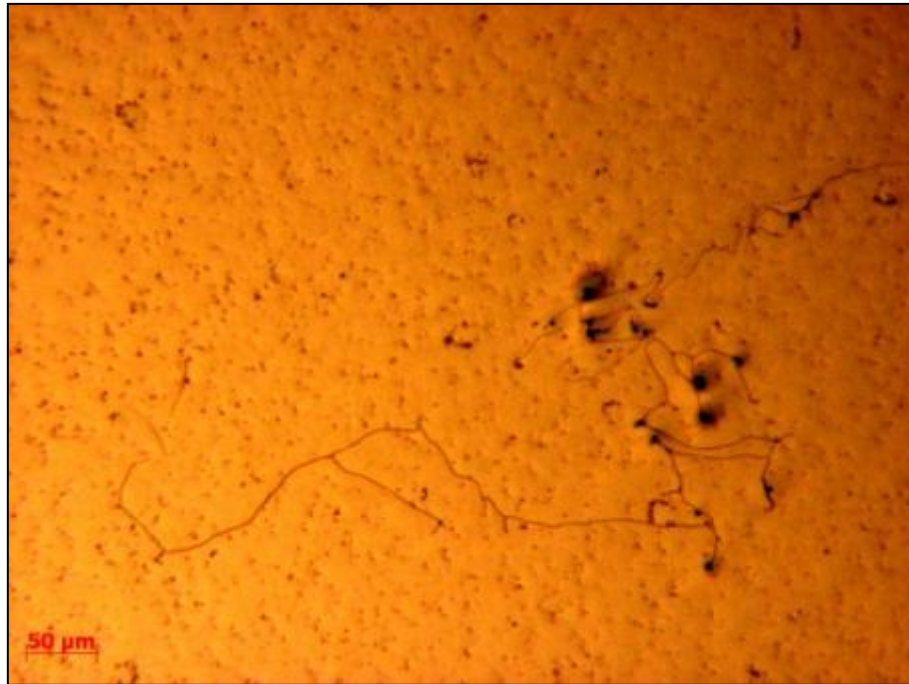
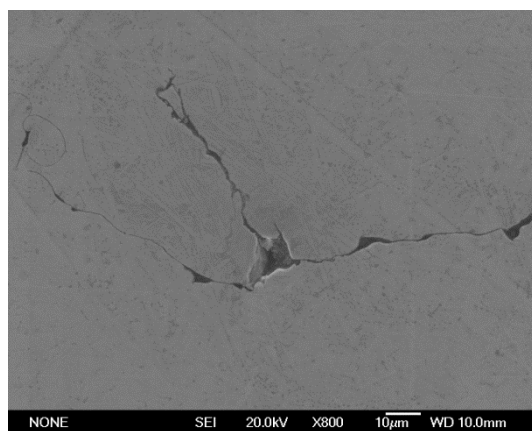
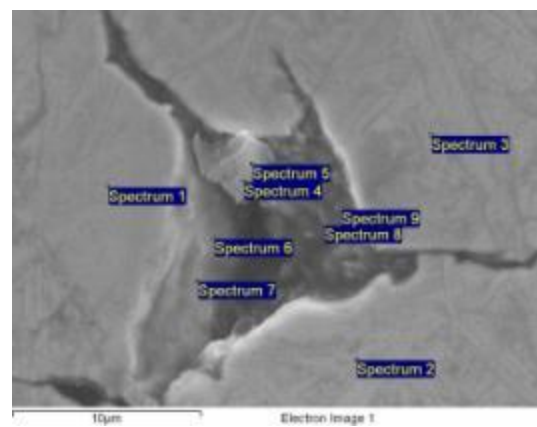


Figure 6-3 – Optical macrograph x10 magnification displaying an example of an “old” oxide film entrained within a dip sample of the XD1102 alloy.



a) SEM image x800 magnification



b) SEM image x4000 magnification

Figure 6-4 – SEM images illustrating the entrainment events witnessed within the dip sample of a XD1102 casting

Table 6-1 – EDX analysis of points identified within Figure 6-4b).

Spectrum	% Deviation from XD1102 average							Wt% detected by EDX
	Al	Si	Ti	Cr	Fe	Ni	Nb	O
1	3		-12	11	2	1		
2	3	47	82	-3	-12	2	134	
3	9		1	8	-3	3	-32	
4	654		27	-61	-69	-70	64	42.62
5	725		43	-63	-70	-72	135	40.67
6	775	622	88	-49	-54	-43	265	21.79
7	759	225	110	-48	-51	-46	295	21.7
8	310	578	30	-24	-25	-31		18.73
9	697	606	82	-18	-22	-32		8.39
10	385	425	56	-25	-26	-35		19.22

The first three EDX points displayed in Figure 6-4 were taken from the bulk material as reference chemistry. It is noted that EDX point 2 displayed an increased niobium and titanium weight percentage; although it cannot be determined by this SEM image, the EDX analysis suggested that a combination of [Nb, Ti]C was detected below the surface.

EDX points 1 and 3 closely resemble the bulk average of SMWL cast material albeit the niobium content which was either undetectable or below expected.

EDX points 4-10 were all taken within the feature observed and show strong enrichment in aluminium and oxygen, with a small enrichment of titanium. The remaining constituent elements were depleted; it is highly probable that the feature was an alumina film.

The presence of silicon within the pore was also detected, however this was believed to be residue from the polishing process.

## 6.2.2 Entrainment within the Durville Machine

It was clear that entrainment of oxides within the receiver volume were present and equating the observation within the dip sample a total of 47 million entrainment events within the receivers  $0.7 \text{ m}^3$  of melt was predicted. It is hypothesised by SMWL that the minimum dwell period is sufficient to allow these films to float to the top of the receiver, where they remain during the initial stages of tilt.

However, the tilting technique is not ideal. The current process involves tilting at a constant angle of rotation;  $135^\circ$  in 35 seconds i.e.  $3.86^\circ\text{s}^{-1}$ . Although the machine assembly moves through a controlled, smooth rotation, an important aspect is the flow rate throughout the system over time. The velocity of the flowing fluid front is not constant. As it moves from the receiver into the mould, down the side of the mould, hits the base and then continues up through the other side of the mould the velocity of the fluid front varies from a predicted  $0.003$  to  $0.25 \text{ ms}^{-1}$  (Figure 6-5).

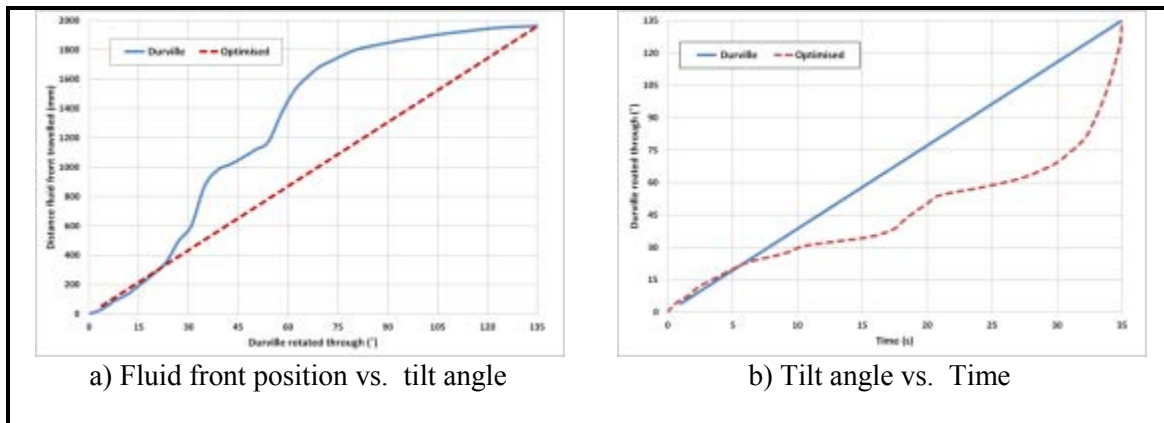


Figure 6-5 – Graph to show a potential improvement to the Durville tilt casting rotation to allow a constant fluid velocity throughout the tilt.

An optimised tilt would consist of a constant fluid front velocity ( $0.056\text{ms}^{-1}$ ) and a variable rate of rotation. This would prevent the acceleration of the flow velocity,

which could lead to strain and/or splitting of the oxide layer revealing fresh melt to be oxidised and the deceleration of the fluid front where the oxide layer may fold back on itself as pictured in Figure 6-1. The maximum velocity is reached when the melt is flowing down the side of the mould before reaching the base. Images from video analysis, illustrated in Figure 6-6, show the presence of a return wave; this can lead to an entrainment event known as a zipping wave (Campbell, 2011a). With the “optimised” flow the velocity of the fluid front at the base of the mould is reduced to a quarter of its’ current speed, which may help prevent or minimise any turbulence induced entrainment.

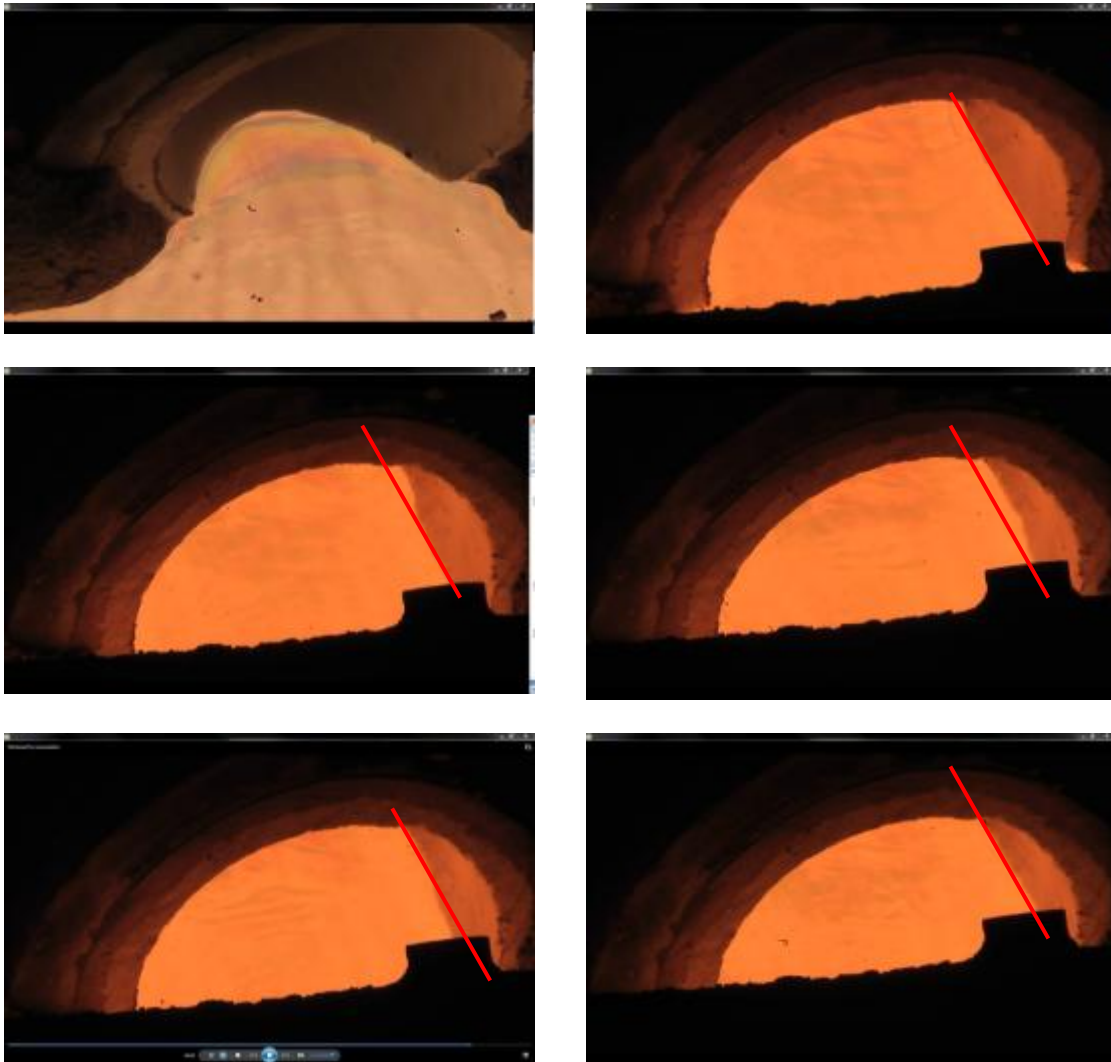
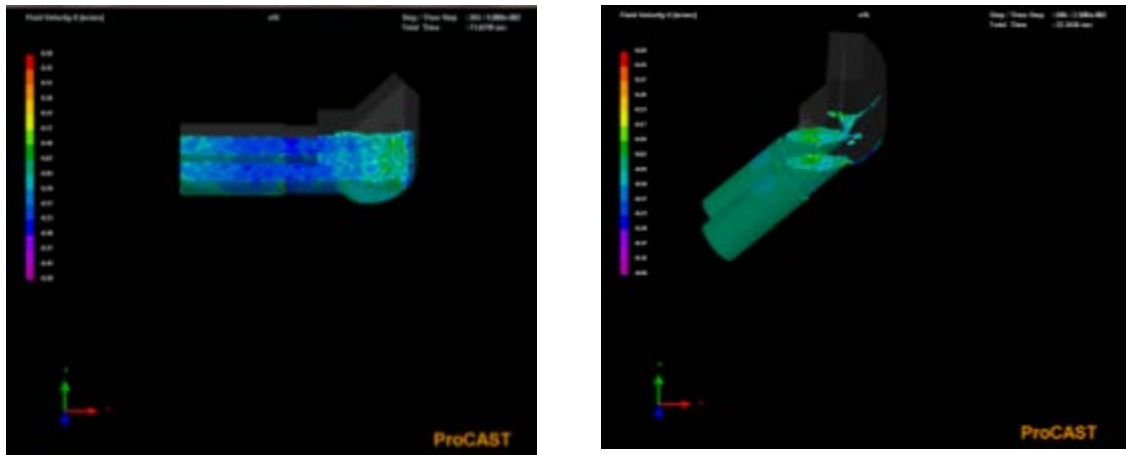


Figure 6-6 – Photographs of the Durville tilt casting process displaying a return wave as the melt hits the base of the mould and back up. Note the position of the annotated red line to aid in the visualisation of the return wave

The folding of an oxide film during the tilt was unavoidable as the melts free surface area reduces while the Durville machine moves through the tilt as presented in Figure 6-7. This was no cause for concern if the crumpled film remained on the top of the melt as the ingot discard has sufficient height for it to be removed. However, during the

crumpling if the oxide film adhered to the mould's wall or became encapsulated within the solidifying melt it may have become entrained.

Further investigation to tilt time and flow entrainment could prove to be beneficial but is out of the scope of this project.



a) Large free surface

b) Small free surface

Figure 6-7 – Screen shot of a simulation displaying the free surface area of melt during the Durville tilt casting method.

### 6.2.3 Cast Ingot Slice

As mentioned earlier the entrainment of oxides can be difficult to observe due to their small size relative to the casting. However one such event was located on a sample of a sectioned XD1102 ingot. This particular feature was confirmed as a pore (Figure 6-8), but unlike the observation made within Figure 6-3 little to no continuous strand region was witnessed. This pore was found 2.5 mm away from the ingots' surface and therefore likely to have been trapped within the solidifying melt before it had chance to float to the top of the ingot.

Element mapping of this feature displayed enriched areas of Al, Ti and Cr with O likely to be oxides (Figure 6-9). The edge of the pore displayed an increase in niobium and



carbon likely to be niobium carbides to be discussed in more detail in 6.4.3. Just beyond the periphery of the pore a large number of small particles were found and identified mainly to be  $\text{Al}_2\text{O}_3$ , with small amounts of titanium also detected. This further supports the suggestion that a gas bubble was entrained, and on cooling some of this gas has diffused out of the bubble into the bulk material where it has oxidised aluminium.

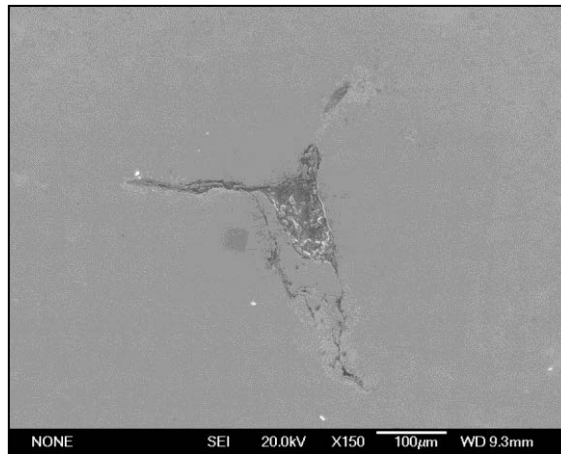


Figure 6-8 – SEM image at x150 magnification illustrating the entrainment of an oxide/pore in an as-cast XD1102 ingot.

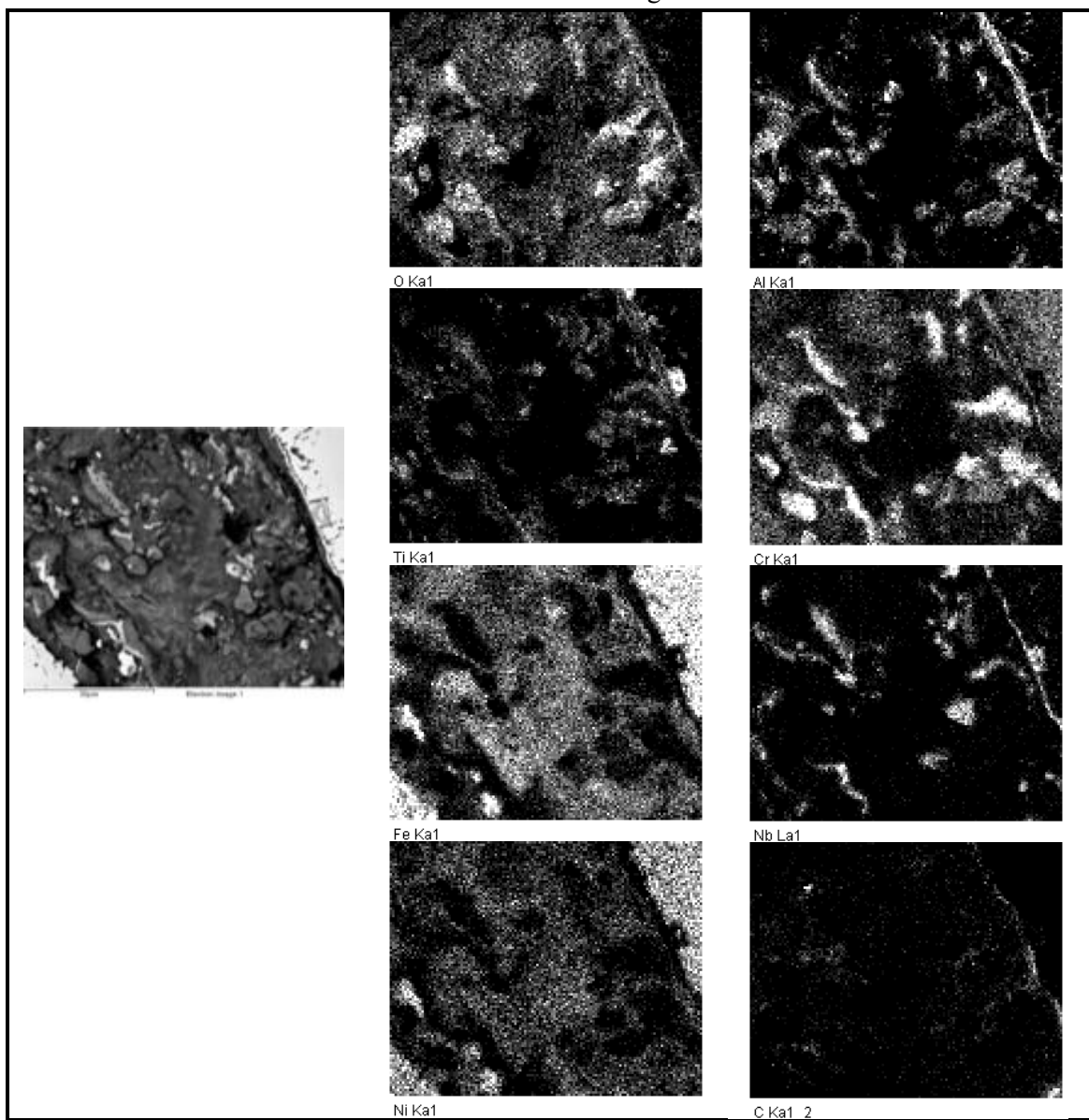


Figure 6-9 – SEM image (left) and Element mapping of the entrained oxide/bubble feature as illustrated in Figure 6-8.

#### 6.2.4 Ingot After Extrusion Pre-Heat – But not Extruded

On a second ingot which was withdrawn out of the pre-heat furnace, prior to extrusion, an entrainment event was observed (Figure 6-10). This particular event has similar morphology to the observations made within the dip sample comprising of a thin continuous strand of alumina. However, due to the extended time at temperature niobium carbides have nucleated on the oxide; similar features have been observed by (Rashid and Campbell, 2004).

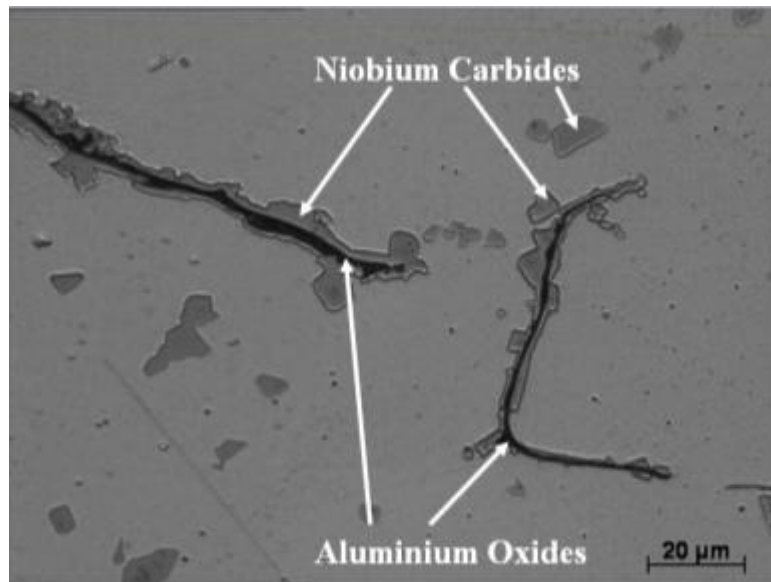


Figure 6-10 – Optical image at x50 magnification of a section of a cracked ingot displaying an oxide film decorated with niobium carbides.

#### 6.2.5 Forward

It was clear that entrainment of oxides during the Durville tilt casting process occurred and it may be unavoidable; the following work was to explore whether these entrainment events proved to be detrimental to the final mechanical properties of the valve bar after extrusion and rod milling has taken place.

## 6.3 Casting Trials

### 6.3.1 Method

Investigation into whether oxide film entrainment during casting played an important role in the final, as delivered, mechanical properties of an XD1102 valve bar was performed using two ingots cast using different techniques. The first ingot was cast by the previously described Durville tilt casting method, and the second ingot was produced by top pouring from the ladle into an upright ingot. The Durville process as previously indicated allows the melt to dwell in the receiver to allow migration of oxides to the top of the melt before it is tranquilly tilted over to avoid turbulence. The top poured ingot did not include a dwell period or apply a tilt, leading to an increased chance that any oxide films would have been entrained within the solidifying melt.

For both casting methods the experimental approach was identical to that of a production ingot with the application of mould pre-heat, and the addition of the insulating collar and Bitop. After solidification the ingots were extruded and hot rolled to the final product diameter using the standard heating cycles prior to working.

Tensile test samples were machined from the valve bar to the dimensions given in Figure 6-11 at the lead, middle and discard ends of the bar, which is representative of the bottom, middle and top of the cast ingots. 14 samples were machined from the lead and discard ends and 12 from the middle for both casting methods. Tests depicted with a “D” represent samples made by the Durville method and tests with a “T” represent top poured samples.

All tensile samples were then tested to destruction at room temperature. The 0.2% Yield strength, Ultimate Tensile Strength (UTS) and elongations were recorded for each tensile sample. The initial 3 tensile tests, T1, T2 and D1, had an extensometer connected, which was later removed due to uncertainty about whether the grips of the extensometer played a role in the failure of the test piece. This was due to the fractures being in close proximity to the grips. The subsequent tests therefore had machine movement incorporated into the results which would affect the 0.2% yield strength and elongation results. The UTS of the sample was unaffected by the removal of the extensometer and was taken from the maximum load applied to the test piece.

The average machine movement was calculated using results from tensile tests D2, T3 and T4 which were chosen as they were all from the lead end of the valve bar, and had similar UTS to each of the tensile test pieces which had the extensometer connected. Curves D1, T1 and T2 were then subtracted from the curves D2, T3 and T4 respectively to predict the amount of strain incorporated in the results from the machine movement, at both the 0.2% yield point and the failure strain, as illustrated in Figure 6-12. The amount of strain from machine movement was found to be exponential as once the sample had yielded and began to plastically deform the resistance provided by the sample reduced and therefore the rate of increase in strain of the machine rig decreased. The average contribution to strain from machine movement and thread deformation at the yield point was approximately 1.4% and 2% strain at failure. This average machine movement was then subtracted from the remainder of test results.

This enabled the 0.2% yield strength of the 77 tensile tests without the extensometer attached to be calculated, by plotting a parallel line to the elastic region of the

stress-strain curve at 0.2% strain. The corresponding stress value at the intersection of these two curves was the 0.2% yield strength. The failure strain was the total strain the sample exhibited at failure and could be read directly from the stress-strain curve.

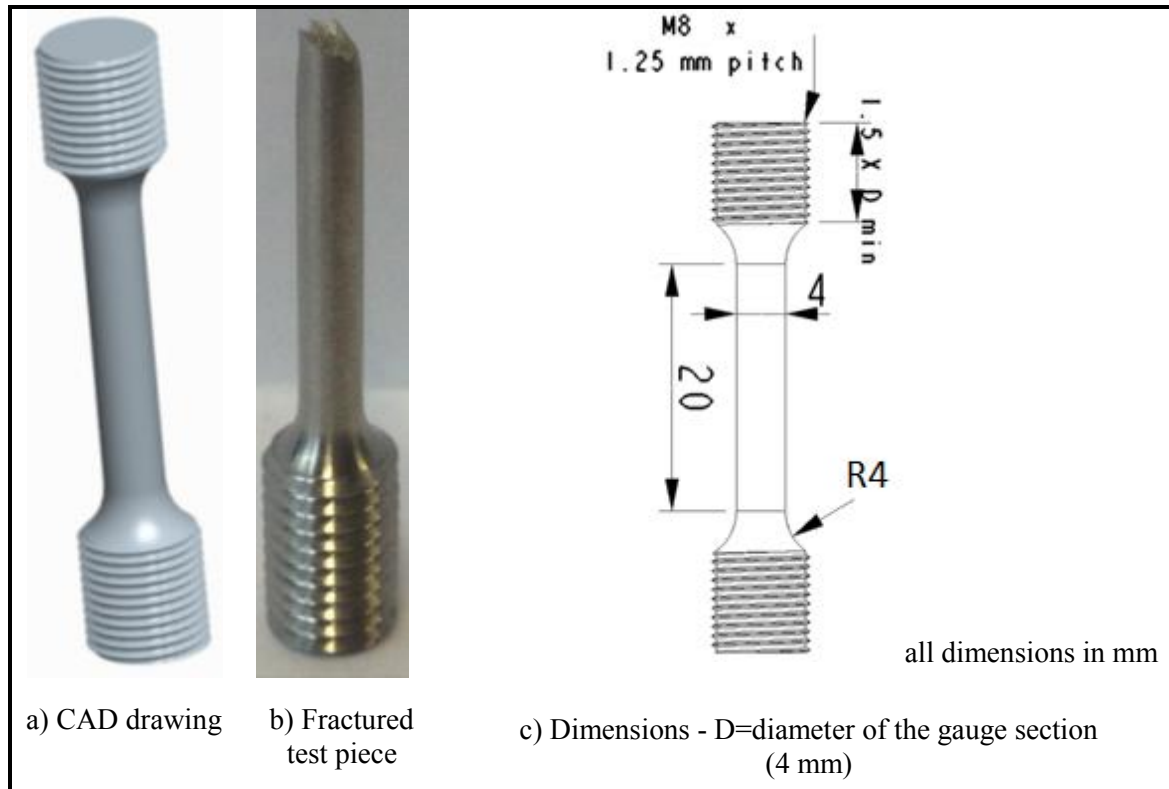


Figure 6-11 – Schematic diagram of the tensile test piece dimensions

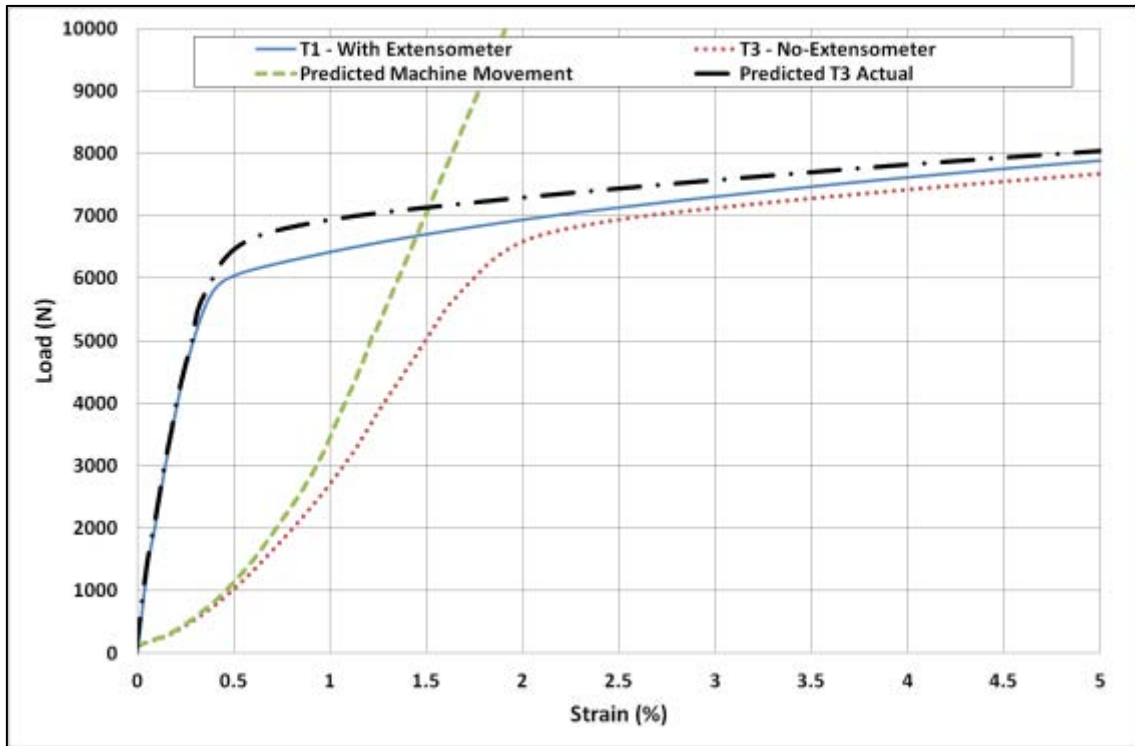


Figure 6-12 – Graph displaying the predicted machine strain during tensile testing.

## 6.3.2 Results

### 6.3.2.1 Tensile Tests

All 80 tests results are displayed in Table 6-2.

Table 6-2 - Results from the tensile testing  
*\*Indicates the 3 tensiles which had the extensometer attached*

	Specimen ID	0.2% Yield Strength (MPa)	UTS (MPa)	Failure Strain (%)	Specimen ID	0.2% Yield Strength (MPa)	UTS (MPa)	Failure Strain (%)
Lead	T1*	474	845	46.4	D1*	489	875	44.8
	T2*	502	860	43.4	D2	549	871	46.9
	T3	467	873	46.2	D3	460	868	46.6
	T4	488	901	42.7	D4	487	902	42.6
	T5	498	917	46.6	D5	522	933	45.4
	T6	495	903	44.9	D6	534	937	40.1
	T7	517	928	46.6	D7	529	932	41.2
	T8	527	936	43.2	D8	551	950	40.4
	T9	527	931	42.5	D9	549	962	40.3
	T10	538	941	42.7	D10	563	974	40.2
	T11	518	908	45.7	D11	573	967	41.2
	T12	531	945	45.9	D12	571	966	38.4
	T13	544	954	44.3	D13	518	890	41.4
	T14	546	962	45.0	D14	595	986	44.1
Middle	T15	656	1049	36.9	D15	613	1012	41.3
	T16	564	970	41.7	D16	603	1015	41.5
	T17	643	1042	38.4	D17	619	1029	40.3
	T18	660	1060	37.1	D18	629	1026	39.3
	T19	619	1037	37.6	D19	628	1029	38.7
	T20	622	1027	36.0	D20	576	990	41.3
	T41	623	1021	39.0	D41	623	1022	38.6
	T42	637	1037	37.7	D42	606	1001	37.5
	T43	641	1038	37.9	D43	610	1006	40.4
	T44	648	1045	39.2	D44	624	1018	38.5
	T45	657	1050	36.5	D45	623	1010	36.8
	T46	645	1031	35.8	D46	595	990	35.7
Discard	T47	681	1073	35.0	D47	603	992	34.9
	T48	691	1078	34.9	D48	567	955	40.1
	T49	696	1081	35.2	D49	594	990	39.9
	T50	692	1076	35.0	D50	584	992	38.5
	T51	689	1072	35.1	D51	592	988	38.2
	T52	675	1070	35.4	D52	594	989	37.7
	T53	678	1057	34.1	D53	587	981	39.3
	T54	675	1061	34.7	D54	589	980	38.0
	T55	669	1052	39.6	D55	577	968	38.4
	T56	681	1071	39.1	D56	579	977	36.5
	T57	687	1076	37.5	D57	596	990	36.3
	T58	681	1067	36.2	D58	590	981	36.9
	T59	692	1081	36.7	D59	597	984	36.1
	T60	683	1070	36.0	D60	602	991	37.1



#### 6.3.2.2 Weibull Modulus

The Weibull modulus is a dimensionless parameter that is often used to describe the variability within a data set. A low modulus, approximately 5, is symbolic of large variability within the data set whereas a high modulus, approximately 50, represents low variability; when referring to a materials' property a high modulus indicates high reliability. A typical top poured Weibull modulus for investment cast Inconel 939 was found to be 30 (Cox et al., 2000).

The Weibull moduli were calculated for the individual casting methods and the locations of the tensile samples and are summarised in Table 6-3. The value  $R^2$  is the confidence in the fit of results. i.e. 1 represents a perfect fit and 0 is no fit to the data.

Table 6-3 – Calculated Weibull modulus of Durville cast and top poured tensile properties.

		Top-Poured		Durville	
		Weibull Modulus	R <sup>2</sup>	Weibull Modulus	R <sup>2</sup>
0.2% Yield Strength	All 40 samples	8.9	0.89	16.8	0.97
	Lead	24.0	0.97	16.9	0.98
	Middle	26.7	0.88	46.5	0.97
	Discard	104.0	0.96	70.7	0.99
UTS	All 40 samples	16.1	0.92	27.0	0.95
	Lead	30.9	0.98	26.2	0.91
	Middle	46.8	0.88	80.5	0.95
	Discard	149.3	0.97	108.4	0.93
Failure Strain	All 40 samples	10.8	0.80	15.2	0.88
	Lead	14.1	0.98	12.2	0.73
	Middle	18.3	0.70	18.4	0.94
	Discard	16.0	0.59	22.5	0.90

What can be identified when the casting methods as a whole are compared, i.e all 40 samples, the Durville process provided the more consistent mechanical properties on all aspects over the top poured casting method. This was also reflected in the increased R<sup>2</sup> values. Displayed in Figure 6-13 is a survival chart which illustrates the proportion of a population which will survive past a certain yield strength. It also illustrates that 80% of the top poured samples were likely to be of an increased strength compared to Durville samples; however the 20% of samples which were likely to be of lower yield strength, and hence the Durvilled product would be selected.

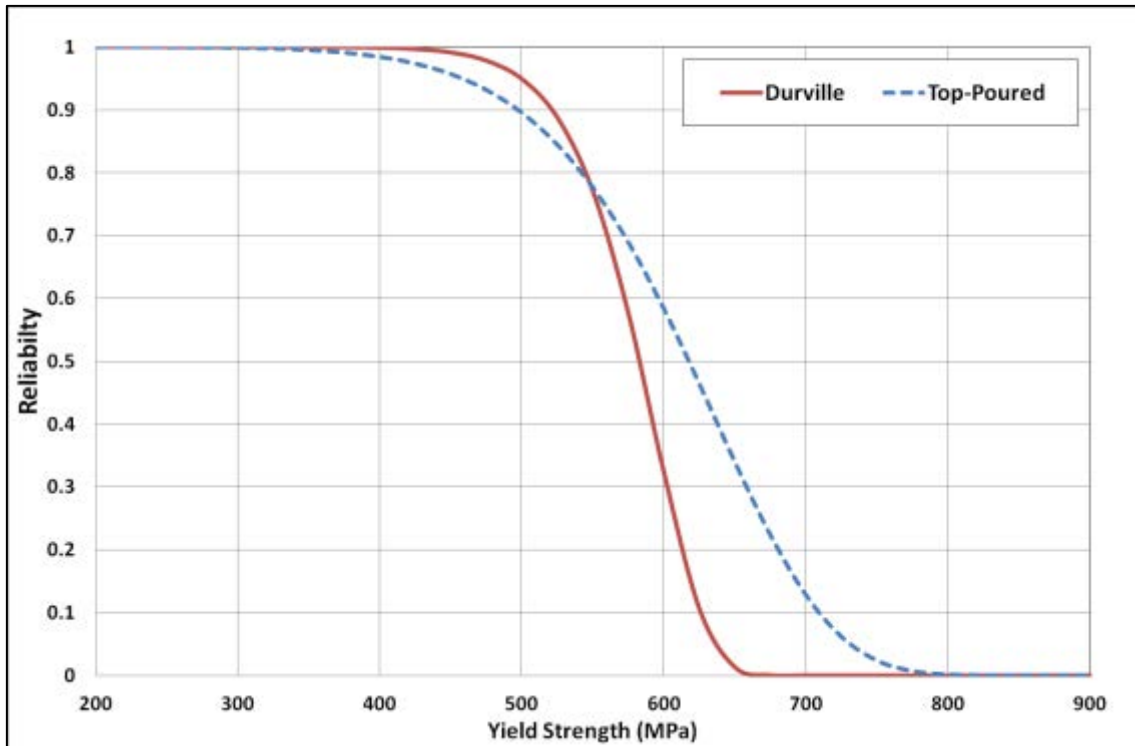


Figure 6-13 – Graph to display the probability of survival for Durville cast and top poured cast tensile properties.

However, different results were found when breaking down the sample regions into the lead, middle and discard ends as tested, and calculating the Weibull modulus for each individual area. In both casting methods the discard end (top) has a significantly higher Weibull modulus; 104 for the top poured and 71 for the Durville test pieces, compared to the lead end of the casting, which produced figures of only 24 and 17 respectively. This indicated that not only was there variation across the different casting methods, but also variation within a single cast ingot.

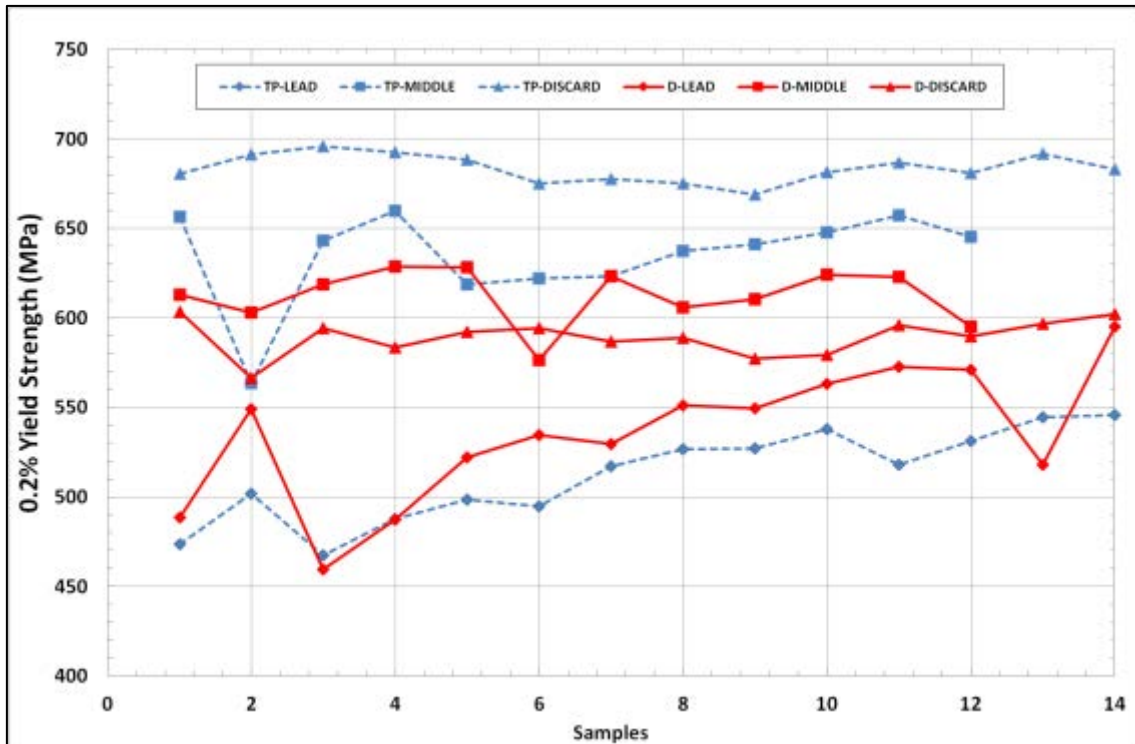


Figure 6-14 – Graph to display the 0.2% yield strength of Durville and top poured tests split into lead, middle and discard ends.

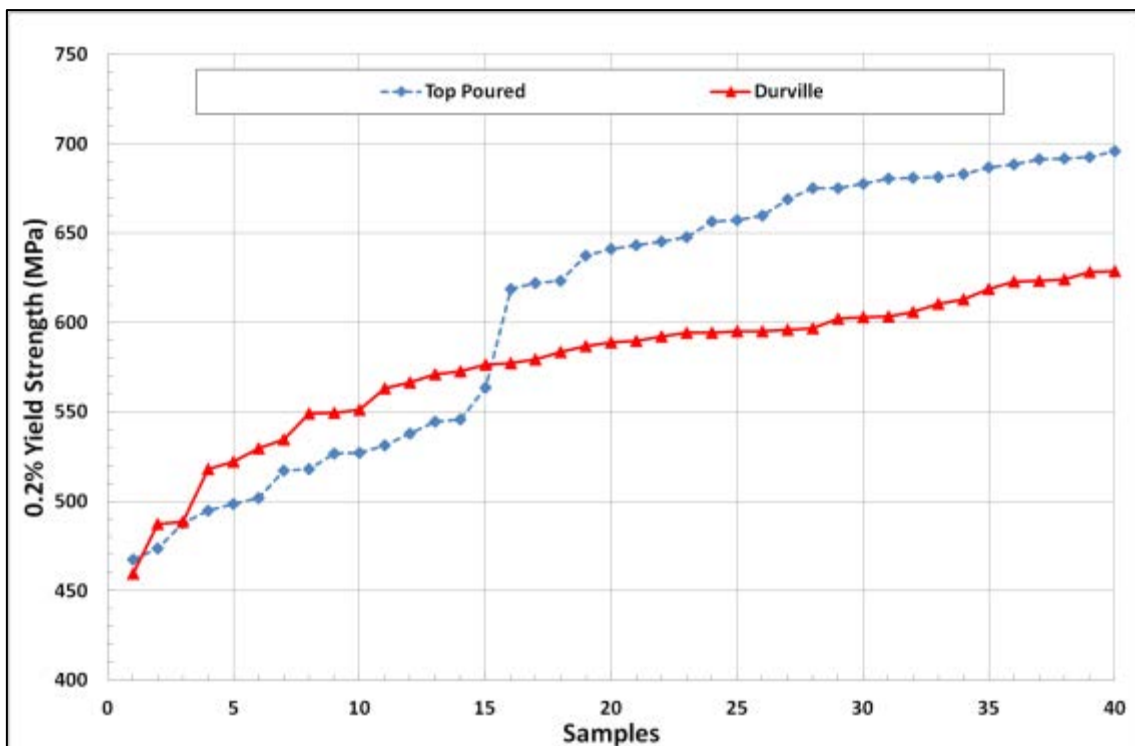


Figure 6-15 - Graph to display the ascending 0.2% yield strength of Durville and top poured tests.

Figure 6-14 presents the 0.2% yield strength results given in Table 6-2.

Table 6-2 and Figure 6-15 shows a combined ascending plot to compare the different casting methods. An observation made from both figures is that the Durville has a closer spread of results, hence the increased Weibull modulus when all 40 samples are considered. The range in strength for the Durvilled samples was 169 MPa compared to the Top Poured samples of 228 MPa.

For the lead end for both casting experiments the mechanical properties were in reasonable relationship with each other with the Durvilled samples having slightly increased 0.2% yield strength, 23 MPa on average.

However, for the middle and the discard end of the bars the top poured samples were consistently stronger than any Durville sample by an average of 60 MPa; a 10% increase in 0.2% Yield Strength.

The results displayed the following trends (Table 6-4), which are in agreement with literature. The table indicates that an increase in the parameter in row one will cause either the increase or decrease in the parameters in column one.

Table 6-4 - Trends in mechanical properties of the tensile tests

Increase in leads to →	Elongation	Hardness	Ductility	0.2% Yield Strength
Elongation		↓	↑	↓
Hardness	↓		↓	↑
Toughness	↑	↓		↓
0.2% Yield Strength	↓	↑	↓	

## 6.4 Investigation into the Differences in Strength between Casting Methods

### 6.4.1 Chemistry

The increase in strength was investigated initially through analysing the chemistry of each test location using EDX and plasma optical emission spectroscopy techniques, but no significant amount of segregation within the bulk material was found which may have caused the additional strength. The results were random and within the accuracy of the testing techniques of  $\pm 2\%$  for most elements tested. The percentage deviation from the average wt% of each individual element is displayed, with the error bands, in Figure 6-16.

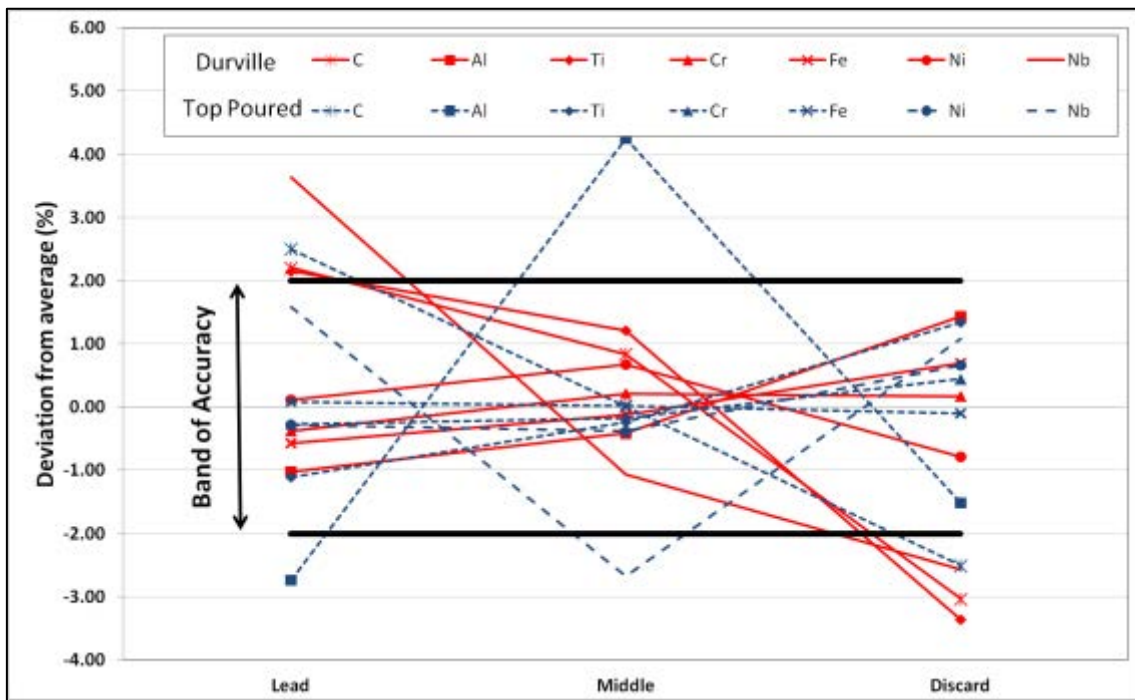


Figure 6-16 – Graph to show the percentage chemistry deviation from the elemental average wt% in the lead, middle and discards ends of both Durville and top poured end of test pieces.

### 6.4.2 Fractured Surface

Also, the fractured surfaces were examined to determine whether any re-occurring features, such as oxide films or inclusions, were present which may have lead to the premature failure of the tensile test pieces. However, there was only the single sample which displayed an abnormality on the fractured surface as displayed in Figure 6-17, with the corresponding EDX analysis provided in Table 6-5.

Spectra 1 and 2 are EDX measurements from the feature and in comparison to the bulk average indicated that this was an alumina particle. Due to the interaction volume associated with this technique only a slight increase in aluminium and oxygen was found.

It could be argued that such a feature would have been a site for crack initiation and ultimately the premature failure of this sample. However, this test piece had a 0.2% yield strength of 657 MPa, which was the second strongest within its' own top poured, middle location, the 15<sup>th</sup> strongest overall and stronger than any Durville test piece. The area covered by the oxide film was approximately 400  $\mu\text{m}^2$  and the surrounding pores were approximately 8  $\mu\text{m}$  in diameter. Therefore the oxide film was effectively equivalent to the coalescence of 8 pores; only 8 individual pores would have been needed to join together to create a similar sized void to that of the oxide film. Therefore it was suggested that the presence of this oxide film has had minimal impact on the mechanical properties of this sample.

Spectrum 3 of Figure 6-17 was taken at the base of a pore, and as indicated within the EDX analysis table, Table 6-5, it represented a niobium carbide particle which will be discussed later in 6.4.3.

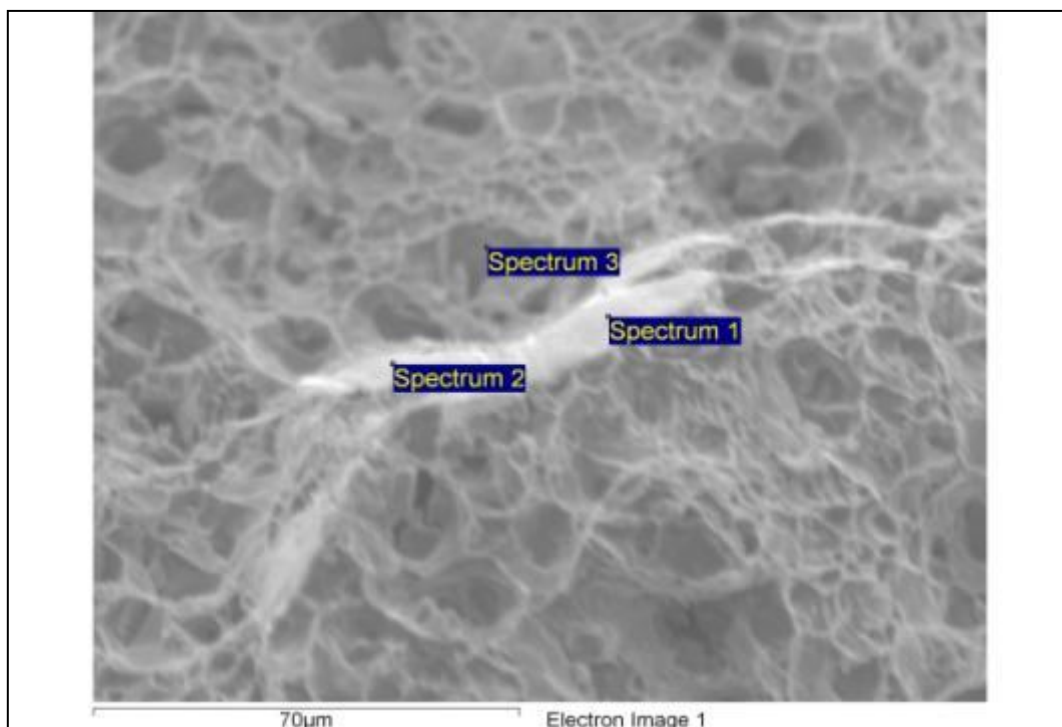


Figure 6-17 – SEM image of an oxide film on the fractured surface middle location top poured test piece.

Table 6-5 – EDX analysis corresponding to the points annotated in Figure 6-17

Spectrum	% Deviation from XD1102 average							Wt% detected by EDX
	C	Al	Ti	Cr	Fe	Ni	Nb	O
Spectrum 1	16	25	-2	-1	-2	-6	10	2.35
Spectrum 2	-1	28	7	-3	-2	-5	27	2.25
Spectrum 3	283	-90	795	-86	-88	-90	1799	

The remaining fractured samples provided no evidence to suggest premature failure had occurred, with each of them exhibiting a combination of ductile and brittle failure regions. This is typical for most materials with high ductility, such as XD1102, where initially the failure mode was ductile in nature (Porous - Figure 6-18a), and as it



becomes over-stressed the failure mechanism converts to brittle (Shears - Figure 6-18b). This produced a clean sharp fracture as the material could no longer plastically deform and hence ruptured.

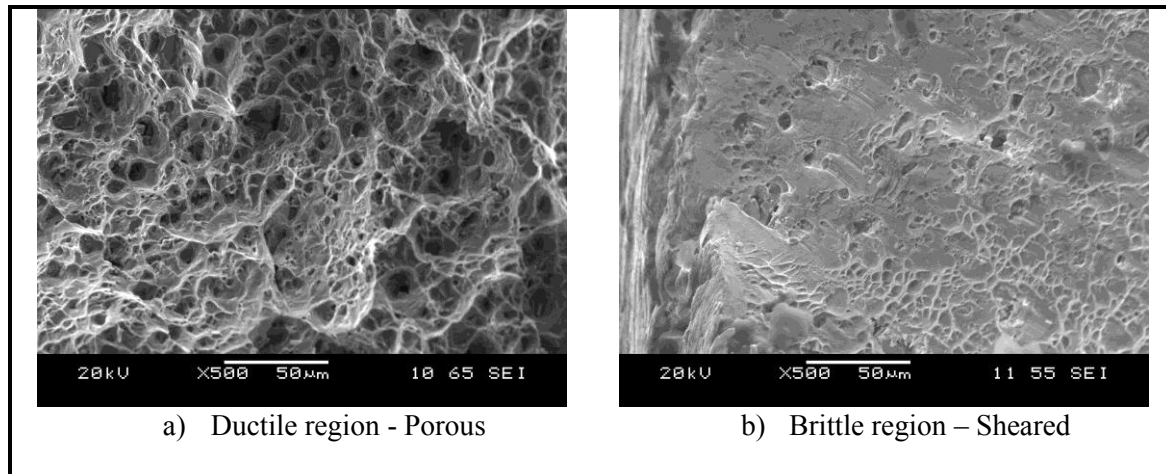


Figure 6-18 – SEM images at x500 magnification displaying regions of ductile and brittle failure mechanisms on a fractured surface.

Figure 6-19 illustrates typical stress-strain curves for brittle and ductile fractures with characteristic material properties. Typical examples of brittle materials include ceramics, glass and martensitic stainless steels whilst typical ductile materials include polymers, pure aluminium and copper.

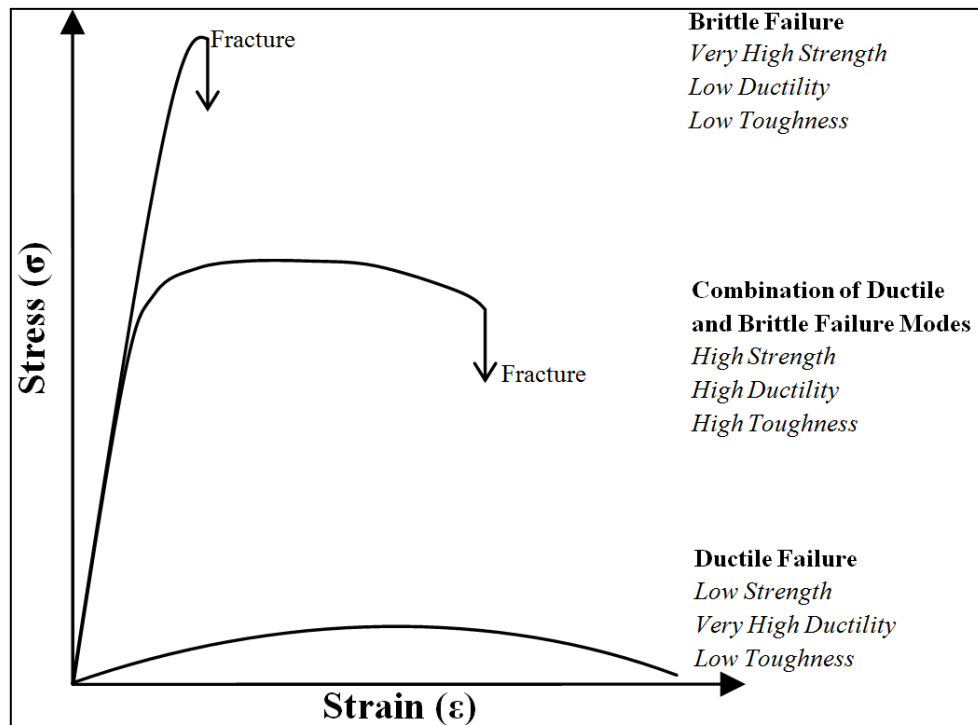


Figure 6-19 – Graph illustrating the typical types of fracture during tensile testing.

### 6.4.3 Carbides

On further investigation of the ductile regions within the fractured surfaces, two types of features of pore were found; small pores of approximately 1  $\mu\text{m}$  in diameter, as well as large pores ranging from 5-20  $\mu\text{m}$  in diameter. Each large pore was seen to open up around a particle, as illustrated in Figure 6-20. The particles were identified as niobium carbides, as previously seen in Figure 6-17. This would be expected as the carbides are hard, brittle phases and the more ductile parent material will plastically deform around the resisting carbide creating the pore as described by Hull (Hull, 1999).

On first inspection from the SEM analysis, it could not be determined whether the carbides present at the base of the large pores were the clustering of smaller carbides, or a larger carbide which had fractured due to applied stress. The investigation of carbide

distribution in the next section displays that most carbides did not cluster, so therefore it was likely that a larger carbide had fractured.

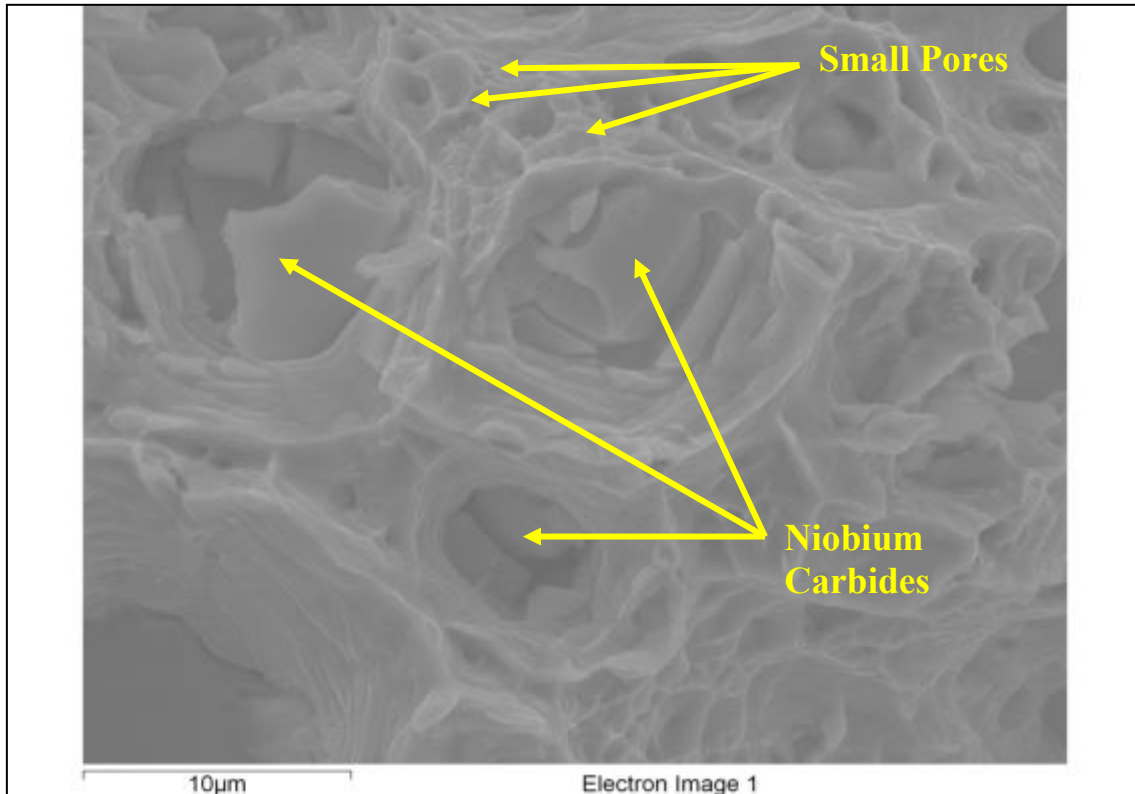


Figure 6-20 – SEM image of a fracture surface displaying the existence of niobium carbides at the base of each large pore.

#### 6.4.3.1 Niobium Carbide Volume Fraction

Further examination into the differences in strength was focused on the niobium carbides. Samples from the tensile tests were prepared for optical analysis; taking into account that the tensile test had already been carried out, the fractured samples were sectioned as close to the threaded end of the test piece as possible. This gave a larger cross sectional area to the gauge length and hence less strain in the region to be examined was expected. The samples were mounted and polished to  $\frac{1}{4}$  µm following the same procedure as described in section 5.3.1. Four samples were chosen from each test location and for each casting method, and a random six images per sample were

captured using an optical microscope at x20 magnification to view the carbide distribution.

To characterise the carbides a public domain, java-based image processing program ImageJ was used. A user-defined function to intensity threshold objects was used to differentiate between the parent material and the carbides in combination with an edge detection tool, which was then used to determine the location and the size of the carbides, as revealed in Figure 6-21.

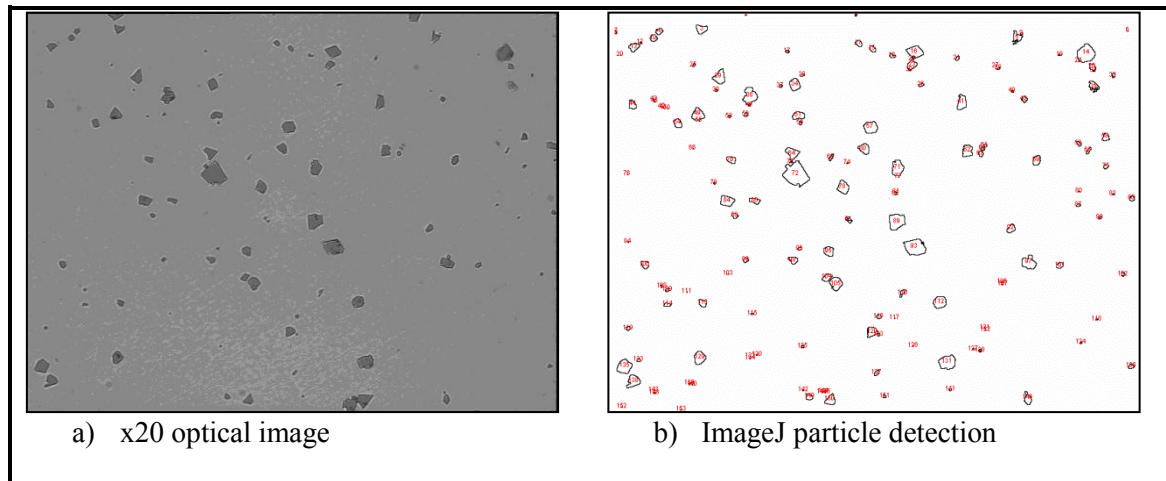


Figure 6-21 – Illustration of particle detection using ImageJ.

Any carbides that came into contact with the edge of the image were dismissed as the full scale of the carbide present could not be determined. A data set was then generated with the total count, total area, average size, volume fraction of carbides and maximum size per image.

It is well understood that the addition of carbon and the carbide forming elements will result in the increase in strength of the material (Bramfitt and Benscoter, 2001); hence

the relationship between the average volume fraction of niobium carbides and the yield strength for the examined samples has been plotted (Figure 6-22).

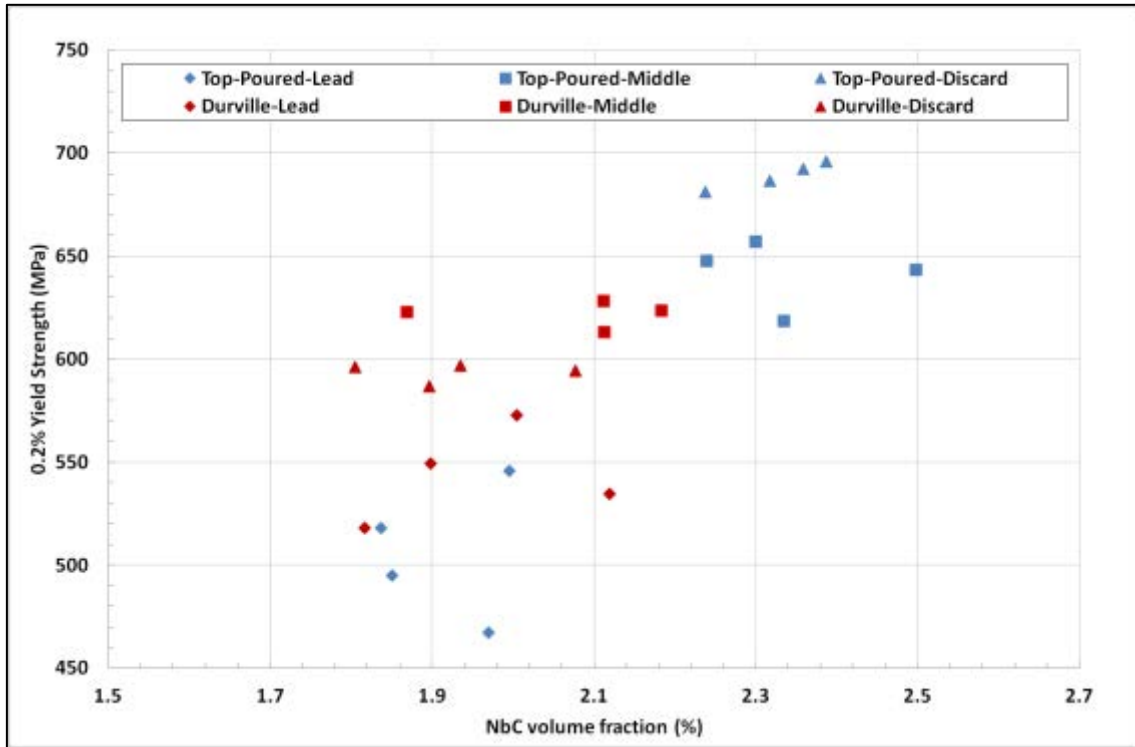


Figure 6-22 – Graph to illustrate 0.2% yield strength vs. NbC volume fraction for both Durville and top poured casts.

This figure displays that the Durville samples have a smaller spread of carbide volume fraction compared to the top poured samples, similar to the spread of tensile strength data points. Only a weak correlation was present between the volume fraction of niobium carbides and yield strength of the material for the Durvilled samples, but to be certain of this additional testing is required. However, for the top poured samples a stronger, positive correlation between the volume fraction of niobium carbides and yield strength of the material was present; where the increased volume fraction of carbides was indicative of increased strength. The middle and the discard locations demonstrated minimal a difference in strength and exhibited a similar volume fraction

of niobium carbides. The lead end had the lowest strength of all areas and it also represented the lowest volume fraction.

The increased niobium carbide volume fraction may be explained by the observation made in Figure 6-10 where carbides have nucleated on an oxide during the pre-heat furnace prior to extrusion. Within the top poured samples it was expected that a larger quantity of oxides were present within the cast ingot in comparison to the Durville process, where any oxides created, or entrained, from the chaotic pour may have settled within the receiver volume and not have transferred into the ingot during tilt. Therefore it was reasonable to assume that an increased amount of carbides would have nucleated within the top poured casting; the average volume fraction of the carbides per casting technique was in agreement to this; an average of 1.99% and 2.17% respectively for Durville and top poured casting techniques. Clearly there is a limit to the volume fraction of carbides that can be present due to the chemical composition of the material. This increase in carbides would also increase the wear resistance of the material, which is of benefit for a valve.

The results show that the carbide volume fraction varies by an increased amount in the top poured casting over the Durville cast samples, with the largest volume fraction found at the discard end followed by the middle location. This observation could be explained by the assumption the oxides gradually floated to the upper regions of the ingot after pouring is complete, in a similar manner the assumption that oxides float to the top of the receiver melt during Durville casting. It is likely that the oxides, by this point, were decorated with niobium carbides, and during the floatation period may have become encapsulated within the solidifying melt; further growth of these carbides would then have been encouraged during the heat cycle prior to extrusion which may

have ultimately led to an increased volume fraction of carbides, than usual, leading to the increased strength of the material in the given location.

#### 6.4.3.2 Carbide Size and Distribution

Observations made from the optical images indicated that the carbides weren't uniformly spread. An etched sample from both the Durville and top poured valve bars revealed a similar grain size for each processing method, and also displayed that the carbides were also of a similar size, approximately 10  $\mu\text{m}$ , and were sparsely spread between the grains as illustrated in Figure 6-23. With this current carbide coverage, minimal grain boundary pinning would be achieved on subsequent heat treatments of the valve bar together with a decreased resistance to grain boundary sliding.

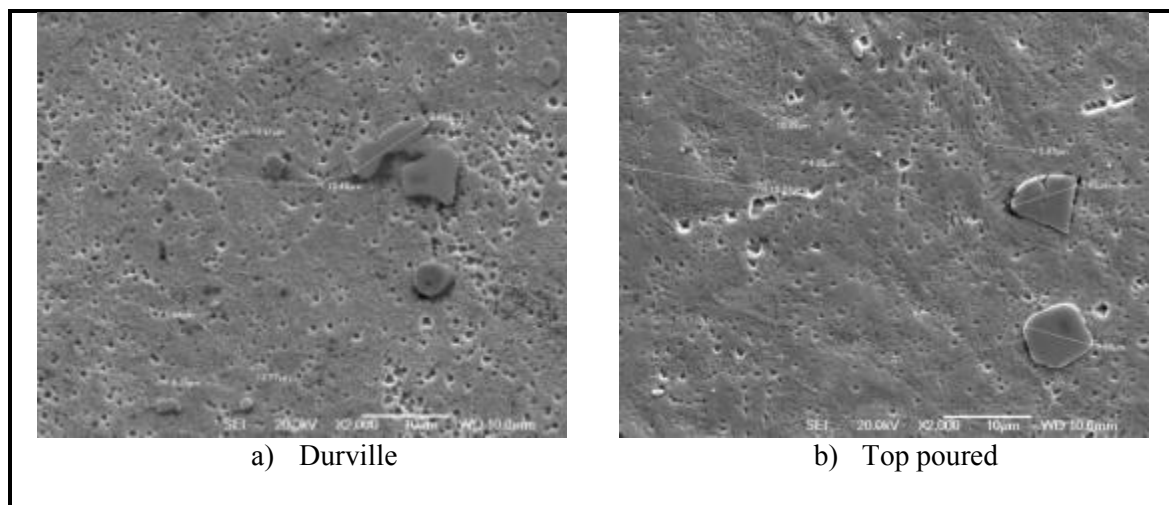


Figure 6-23 – SEM images at x2,000 magnification displaying the grain size in relation to the size of NbC (etched in Kallings No.2 reagent).

It is hypothesised that a finer more evenly distributed number of carbides would further improve mechanical properties of this alloy; a similar effect is evident for cobalt based alloys that are not strengthened through either  $\gamma'$  or  $\gamma''$  precipitation (Davis, 1997). It

would be of interest to investigate the precipitation of the carbides and the key parameters which may affect the microstructure.

#### 6.4.3.3 As Cast Pre-Extrusion Carbides

Due to the stability of the carbides little change is expected in the size, or number of these particles after the heat treatment cycle prior to extrusion (Floreen et al.). The ingot, as observed in Chapter 5, was analysed to characterise the distribution and size of the carbides; 50 optical images were taken from the outer edge to the centre of the ingot at approximately 2.8 mm increments, and ImageJ was used to characterise the carbides.

It was found that the volume fraction of the carbides was highest at the edge of the ingot; likely due to the increased cooling rate reducing the chance of segregation. Due to the drop in the cooling rate from the edge to the centre, any carbides which have formed within the melt are likely to have been pushed towards the centre of the ingot by the solidifying melt, and hence a minimum is found mid-radius before a gradual increase towards the centre was observed. Figure 6-24 illustrates the volume fraction vs. radial position and below this a macrograph of the structure at the edge, middle and central positions.



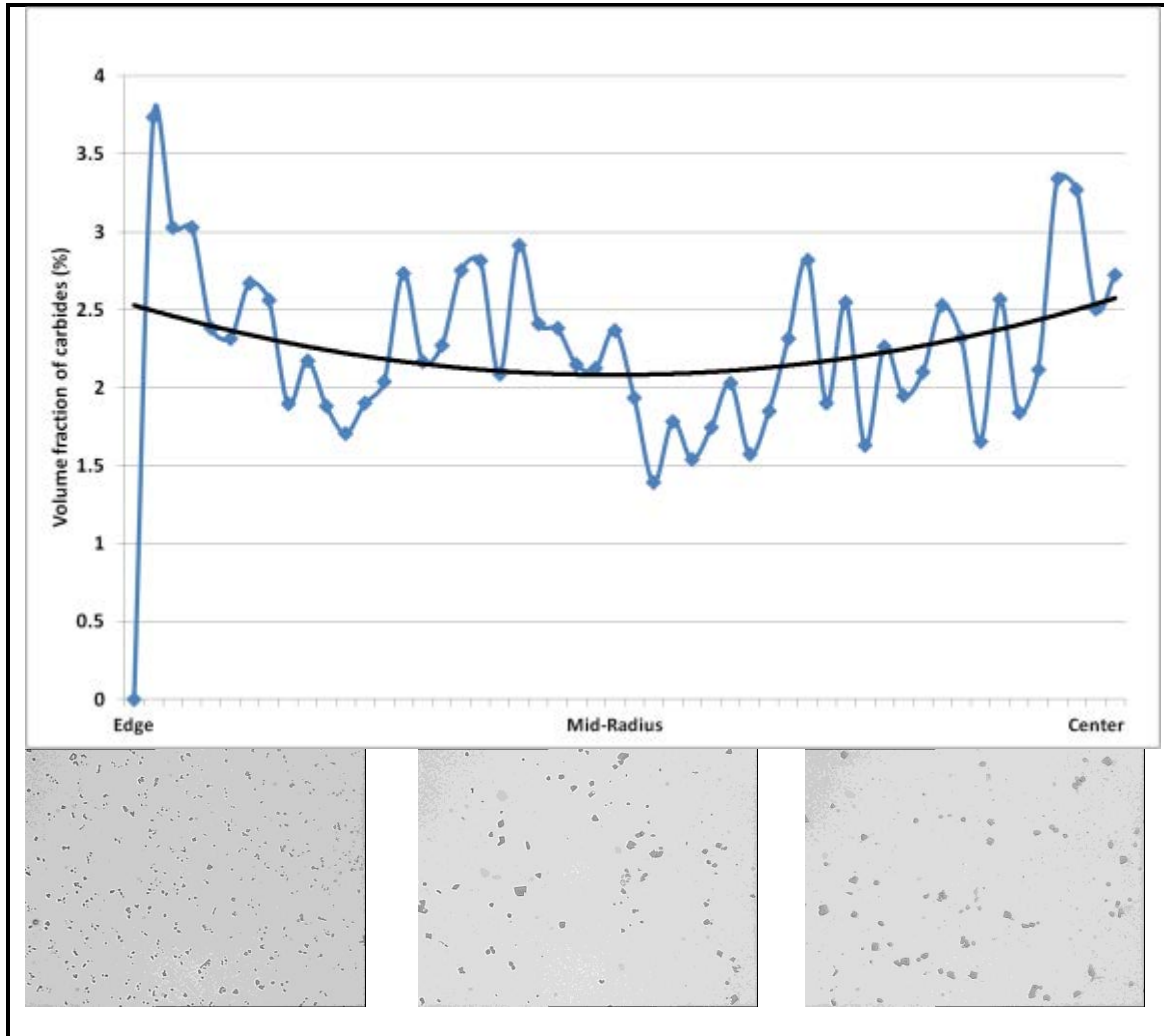


Figure 6-24 – Graph to illustrate the NbC volume fraction vs. radial position of the as-cast ingot

The macrographs in Figure 6-24 illustrates that the carbides at the edge are much finer than the mid-radius and central carbides. This is presented graphically in Figure 6-25 where the top ten largest carbides per image have been plotted against the radial position.

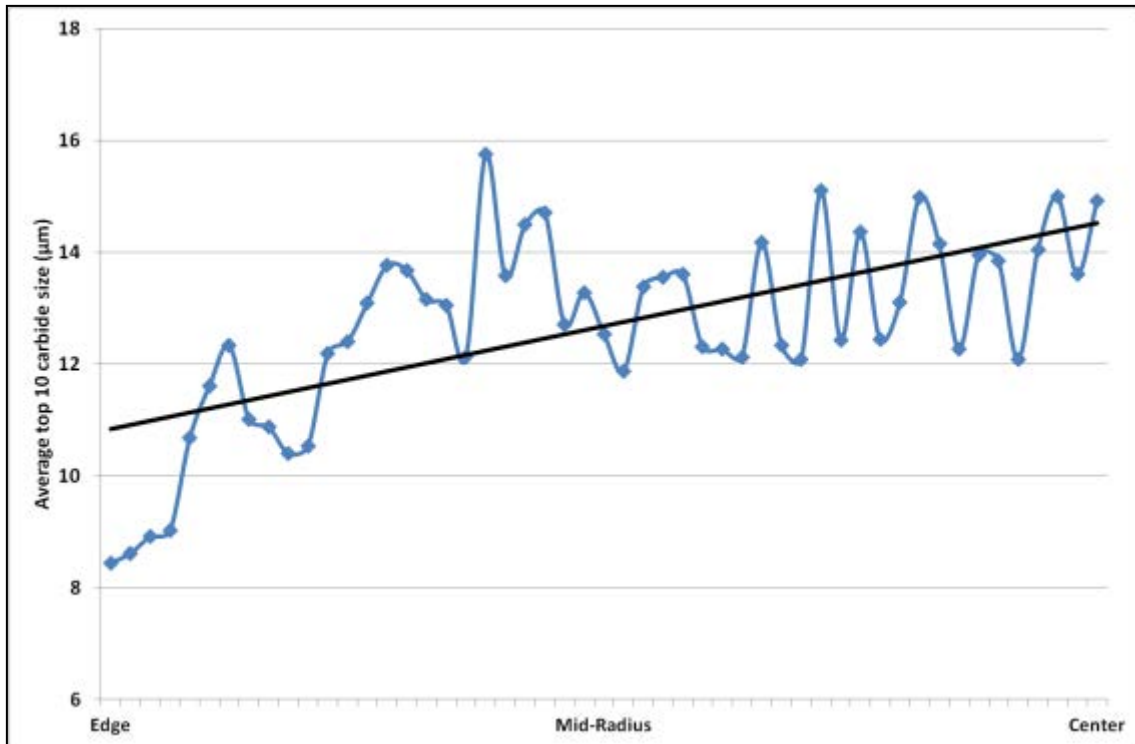


Figure 6-25 – Graph to show the average top 10 largest NbC vs. radial position.

The increased cooling rate at the edge of the ingot was likely to have been the cause for the fine, evenly spaced carbide distribution and is thought to be due to the following reasons; the carbides did not have sufficient time to grow, as well as experiencing a limited supply of melt due to the finer interdendritic structure.

#### 6.4.3.3.1 Cooling rate using MATLAB code

To explore whether an increased cooling rate at the edge of the mould is sufficient to affect the cooling rate in the centre of the ingot, the software MATLAB was used to produce a finite difference model using the Fourier equation in cylindrical co-ordinates with no heat flow in the azimuthal or vertical directions. This allowed the heat transfer to be approximated in 1-D; this was reasonable as the height of the ingot casting was substantially larger than that of its radius (i.e. treated as an infinitely long cylinder). The flow chart shown in Figure 6-26 presents an overview of the MATLAB code developed; the full code can be found in section B.4. Two different boundary

conditions for the mould's outer surface were explored: Firstly, the current air cooled ingot and secondly by water quenching (HTC taken from (Hasan et al., 2011))

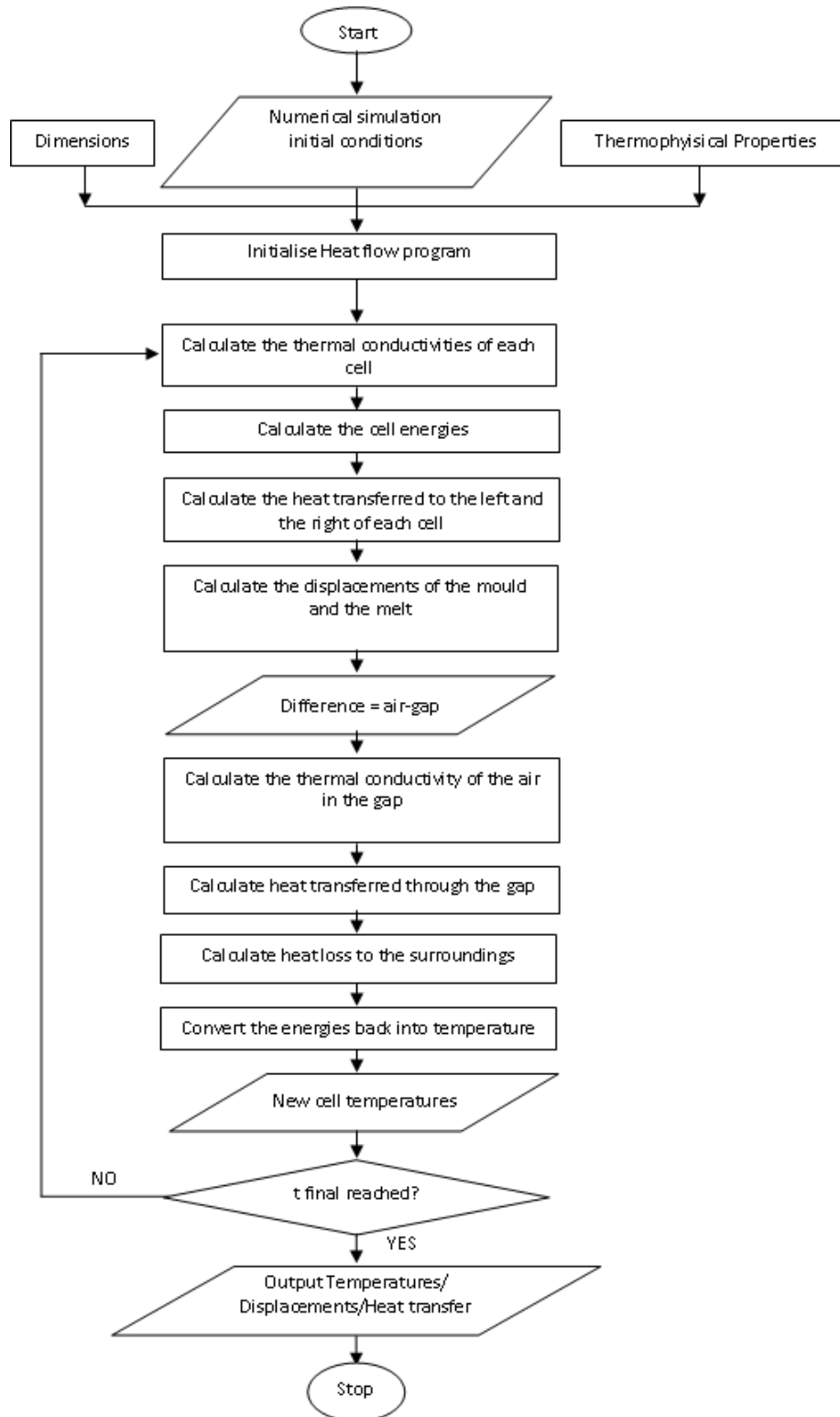


Figure 6-26 – Simplified flow diagram displaying the steps within the MATLAB code

A cell size of 1 mm and a time step of 0.005 seconds were employed and the simulation was run for an hour. The filling of the mould was neglected and the casting was treated at a uniform temperature of the tilt temperature. The mould temperature was set to mirror the temperatures of the Durville moulds prior to tilting. Figure 6-27 displays the time temperature plot for the inner, middle and outer cells of both the casting and the mould.

It was observed that during the early stages of the model's prediction, the temperature of the outer cells of the casting dropped dramatically due to the relatively large heat sink of the cold mould, and were below the solidus temperature of the alloy within the first few seconds. This caused an equivalent sharp rise in the temperature of the moulds inner cells. After this point, the "solidified" outer cells of the casting began to increase in temperature as heat being transported from the liquid into the newly solidified cells was greater than that of heat being transferred from the newly solidified cells to the mould and to the environment. After this transient state, a steady state was reached with a typical cooling curve.

For the water-cooled mould the initial dramatic drop in temperature of the casting outer cells followed by a small increase in temperature occurred in the same manner to the air-cooled mould. This is due to the outer cells of the ingot which are water-cooled have little influence on the inner cells of ingot during this period. However, once this transitional period is complete an increased rate of heat dissipation from the mould to the environment and therefore from within the ingot is observed as expected.

For nodes at the mid-radius and central casting positions, the effect of the cooling mechanism was negligible until the material reached its' solidus temperature due to

sufficient mixing within the liquid. This produced a divergence between the curves, and the rate of cooling for the air-cooled mould slowed in comparison to the water quenched system. This was symbolic of the reduced rate of heat dissipation to the environment in the air-cooled mould, and therefore the casting retained an increased amount of heat over the water-cooled casting.

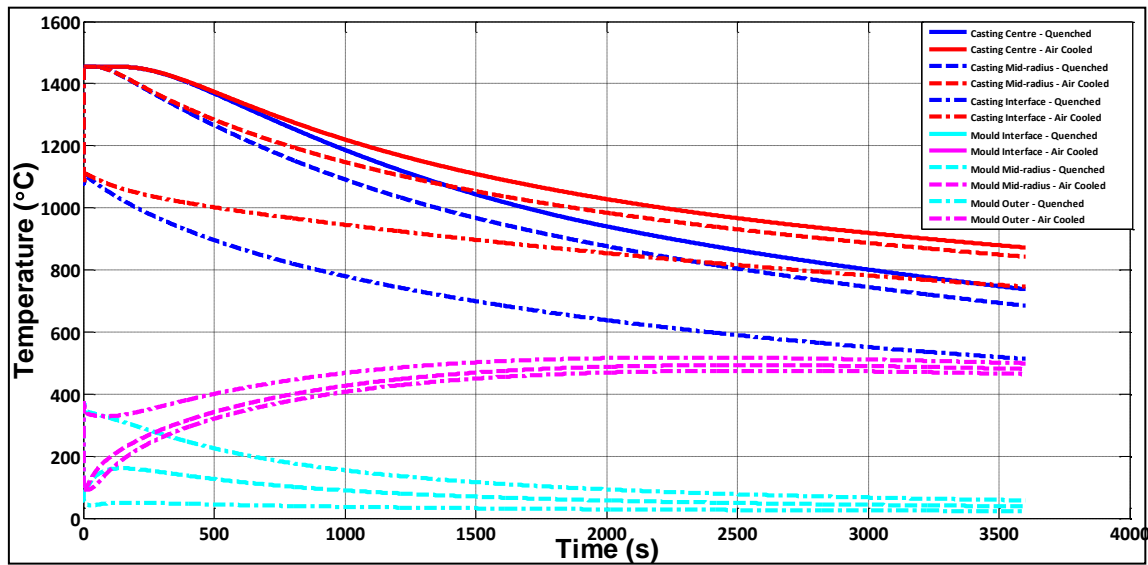


Figure 6-27 – Graph illustrating the predicted time-temperature plot for an air-cooled and water-cooled mould.

Beyond the solidus temperature segregation was minimised as constituent elements can only diffuse through solid state, limiting the distance they can travel. After this point the growth of carbides would be restricted by the availability of elements in the local area, whilst in the liquid phase better mixing allows carbides to grow more rapidly.

Figure 6-28 demonstrates the time taken for all casting cells to reach the solidus temperature of the melt, and Figure 6-29 shows the cooling rates of every casting cell passing through the solidus temperatures respectively.

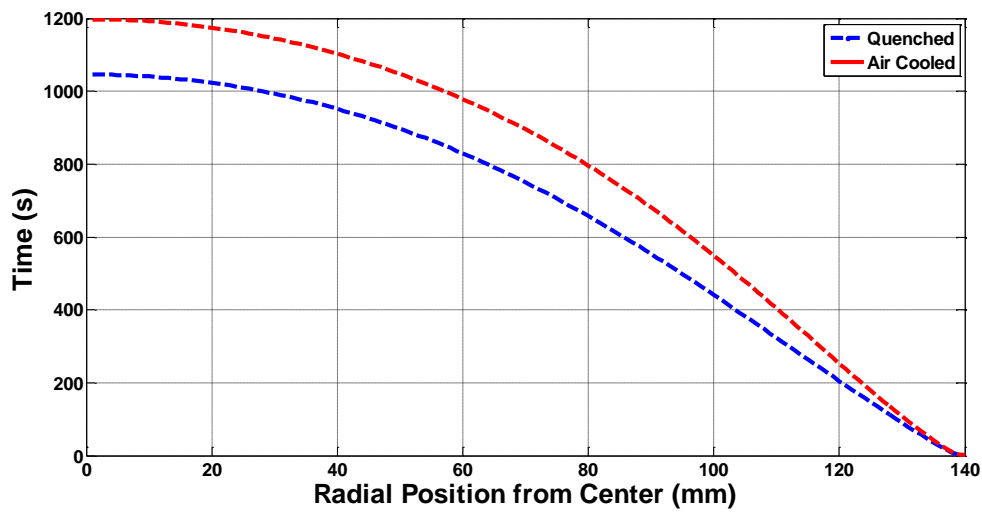


Figure 6-28 – Graph illustrating the time for each cell to reach the solidus temperature of the alloy for an air-cooled and water-cooled mould.

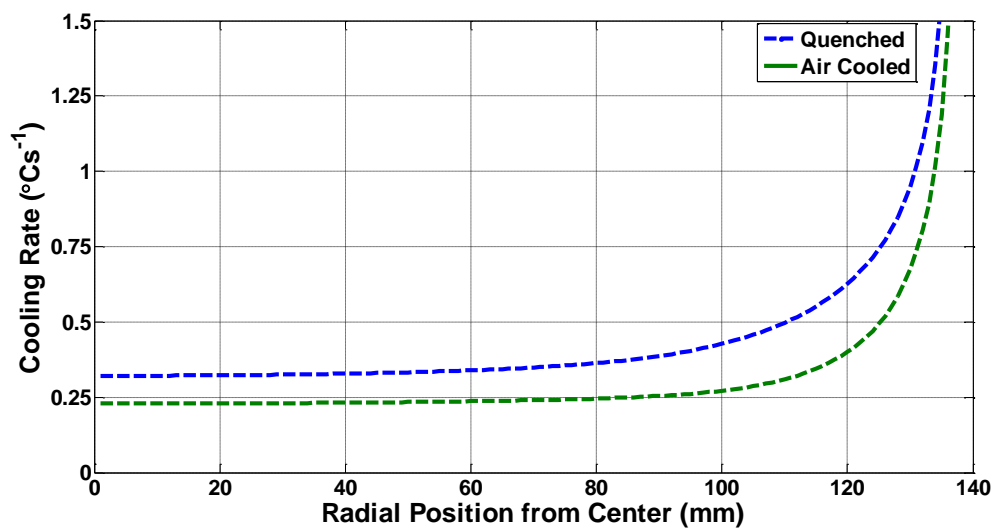


Figure 6-29 – Graph to show the cooling rate going through the solidus temperature for each cell for an air-cooled and water-cooled mould.

Figure 6-28 shows that with the current set-up of an air-cooled mould; the centre of the casting is predicted to reach the solidus temperature just 152 seconds after the water cooled mould. Due to this, it is expected that the carbide size would not be greatly influenced by a water cool, and that the microstructures of each ingot would be similar

to what is pictured in the optical images shown in Figure 6-24 after soaking in the pre-heat furnace prior to extrusion.

From Figure 6-25, and the micrographs used to produce this graph, it shows that the outer four positions displayed a much finer carbide distribution than the remaining positions. The images were taken approximately every 2.8 mm equating to approximately the outer 11 cells of the casting within the model. The predictions from the model show that these 11 outer casting cells had a minimum cooling rate through the solidus temperature of  $0.63^{\circ}\text{Cs}^{-1}$  to over  $50^{\circ}\text{Cs}^{-1}$  for the outer two cells. Therefore to achieve this finer microstructure throughout the casting, it is predicted that a minimum cooling of  $0.63^{\circ}\text{Cs}^{-1}$  is need; however, this rate is unlikely to be achieved throughout the casting even for water-quenched moulds as can be seen in Figure 6-29. This figure shows the majority of the casting cells are cooling at less than half this minimum rate.

The MATLAB code incorporated predictions of the displacement of both the mould and the ingot. It is noticeable that the size of the air-gap formed within the same time period is greater for the air-cooled mould, likely due to the combination of both the mould expanding and the casting contracting. Although the casting cools further for a water quenched mould and therefore contracts further; the mould gains little heat and therefore the expansion is predicted to be minimal in comparison to the air-cast mould. The energy through mould pre-heating is also predicted to be lost within 20 minutes, further constricting the size of the air-gap. The predicted displacements are displayed in Figure 6-30.

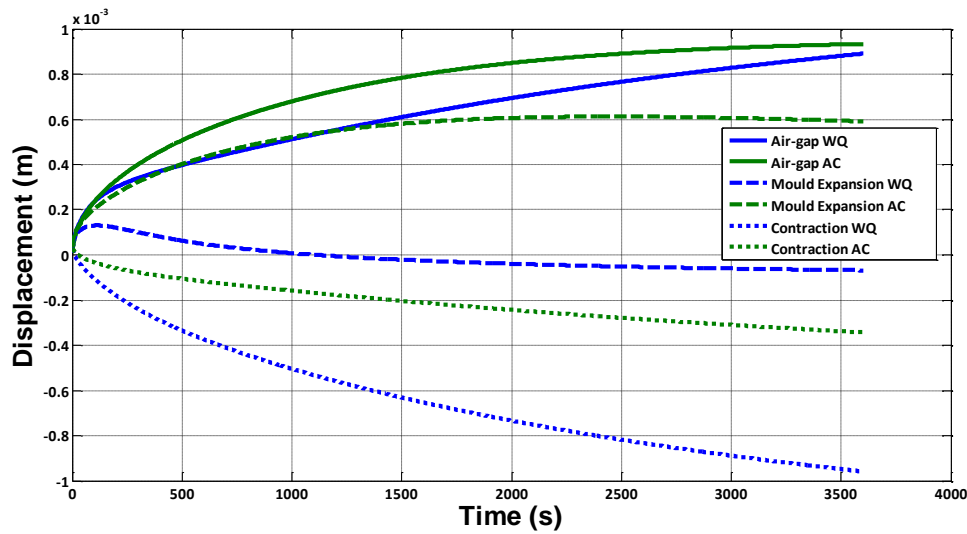


Figure 6-30 – Predicted displacements for the XD1102 ingot comparing the standard air-cooling of the mould and water-cooling.

## 6.5 Conclusions

The effects of tranquil vs. chaotic pouring were studied on ingots of XD1102, after thermomechanical processing. It is known for as-cast products to prematurely fail due to oxide entrainment, so this work was carried out to determine whether the entrainment of oxides is still detrimental to wrought products.

40 tensile test pieces per casting method were machined from the wrought product and pulled to destruction. The 40 samples were split into lead, middle and discard ends of the valve bar which is representative of the bottom, middle and top of the cast ingots.

On balance it was found that oxide entrainment within a casting was not significantly detrimental after the thermomechanical processing used here.

Treating the ingot as a whole, the Durville tilt casting method yielded a higher Weibull modulus than the top poured samples, showing that a more consistent material property could be achieved.



The lead end was the weakest section of material for both casting methods, with the Durville process producing a slightly higher 0.2% yield strength on average at this location. The middle and discard ends of the top poured samples displayed the highest strengths of all samples; and were on average 60 MPa stronger than Durville samples of the same region. It is this increase in strength which has resulted in the lower Weibull modulus as a greater overall spread of 0.2% yield strength was obtained.

It was found that chemical segregation within all samples was minimal and within the analysis accuracy, so therefore is not the reason for the difference in strength grades.

Observation of the fractured surfaces revealed typical ductile to brittle failure mechanisms with only the one sample displaying an abnormal feature, an alumina oxide, but this was considered unlikely to have caused any significant change in the mechanical properties of this sample.

It was found that an increased volume fraction of niobium carbides was associated with the increased 0.2% yield strength of the tensile test samples. This was only a weak relationship in the Durville samples where the carbide distribution was near uniform; however, for the top poured samples the carbide volume fraction and the strength varied considerably from location to location. It has been hypothesised that the increase in niobium carbides in the middle and discard ends of the top poured samples is a result of an increased amount of oxides entrained within the cast ingot due to the chaotic nature of the pour. During solidification the oxides then have the opportunity to float up to the middle and discard locations where they may become trapped within the solidifying melt. The ingots are then raised to extrusion temperature where an increased amount of

nucleation of carbides on the oxides was observed leading to the higher volume fraction.

It is expected that smaller, more finely distributed carbides could be achieved by increasing the cooling rate of the mould. However, calculations suggest that even with a water-cooled mould it is unlikely to sufficiently increase the cooling rate through the solidus temperature, and therefore is not adequate to produce the fine grain structure.

## 6.6 Future Work

Due to all the thermo-mechanical work the material received in the manufacturing of valve bar, the entrained oxide, carbide strings are likely to have been broken up. It is therefore difficult to assess, on the wrought product, which carbides nucleated on an oxide. On numerous optical images the carbides displayed a two phase nature, and it would be of interest to carry out further EDX analysis to determine if the second dark phase, as displayed in Figure 6-31 is the remnants of an entrained oxide.

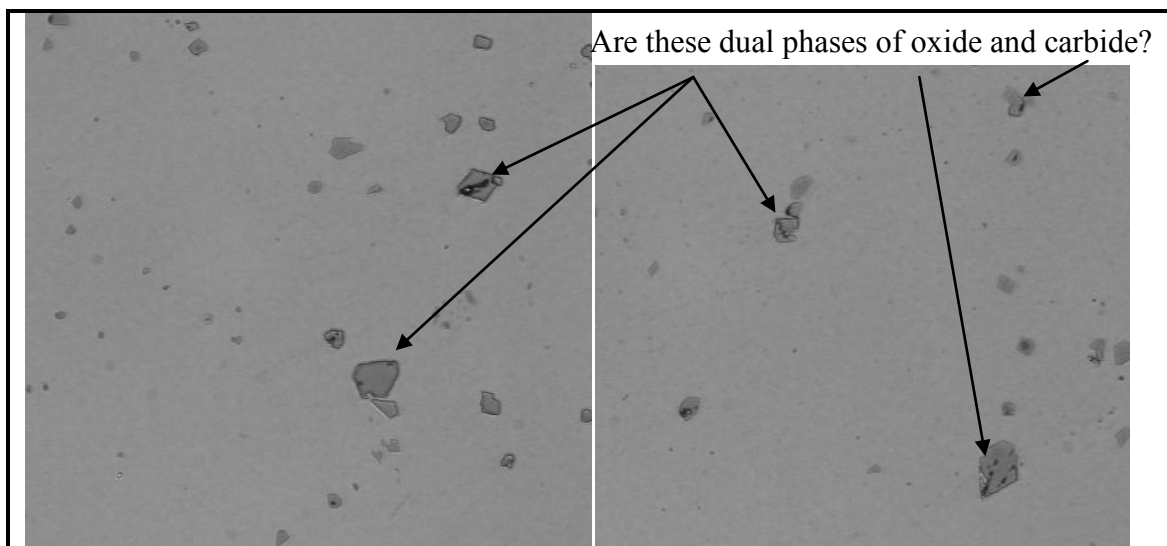


Figure 6-31 – Optical images at x20 magnification displaying a central feature within many of the larger NbC.

### 6.6.1 Nucleation on Oxides True Cause for Increased Strength?

A conclusion was made that the nucleation of niobium carbides on an entrained oxide film led to an increased 0.2% yield strength of wrought XD1102. To further support this additional work would be required. A suggestion of casting two further ingots by the top poured casting method could be employed where one ingot receives the heat treatment cycle prior to extrusion where the carbides are known to nucleate on the entrained oxide film, and the other ingot to be left in the as-cast state. Two ingots of the same casting method would then have differing amounts of carbides present with predicted different strengths. Tensile testing both ingots could then determine the strength which may demonstrate the increased strength of the ingot which has received the heat cycle. This chapter concluded that oxide entrainment was not detrimental to wrought products. The testing of the ingots above will be carried out on the cast structure; therefore any oxides present would not been broken up which could prove to be detrimental to both cast ingots: therefore care must be taken.

### 6.6.2 Chemistry Alterations

It was hypothesised that a finer more evenly distributed carbide coverage would further increase mechanical properties. This could be achieved by increasing the cooling rate during solidification; however, the example of water-cooling the mould displayed an insufficient increase in the cooling rate to lead to a finely distributed carbide coverage.

A high proportion of the niobium carbides observed in XD1102 will have nucleated in the liquid phase, and a second hypothesis if the nucleation temperature of the carbides could be brought down to be below the liquidus temperature then the carbides would have less mixing with the surrounding melt and therefore limiting their size. The

software Thermo-Calc was used to predict the phase transformation temperatures using the average chemical composition of XD1102 as displayed in Figure 6-32.

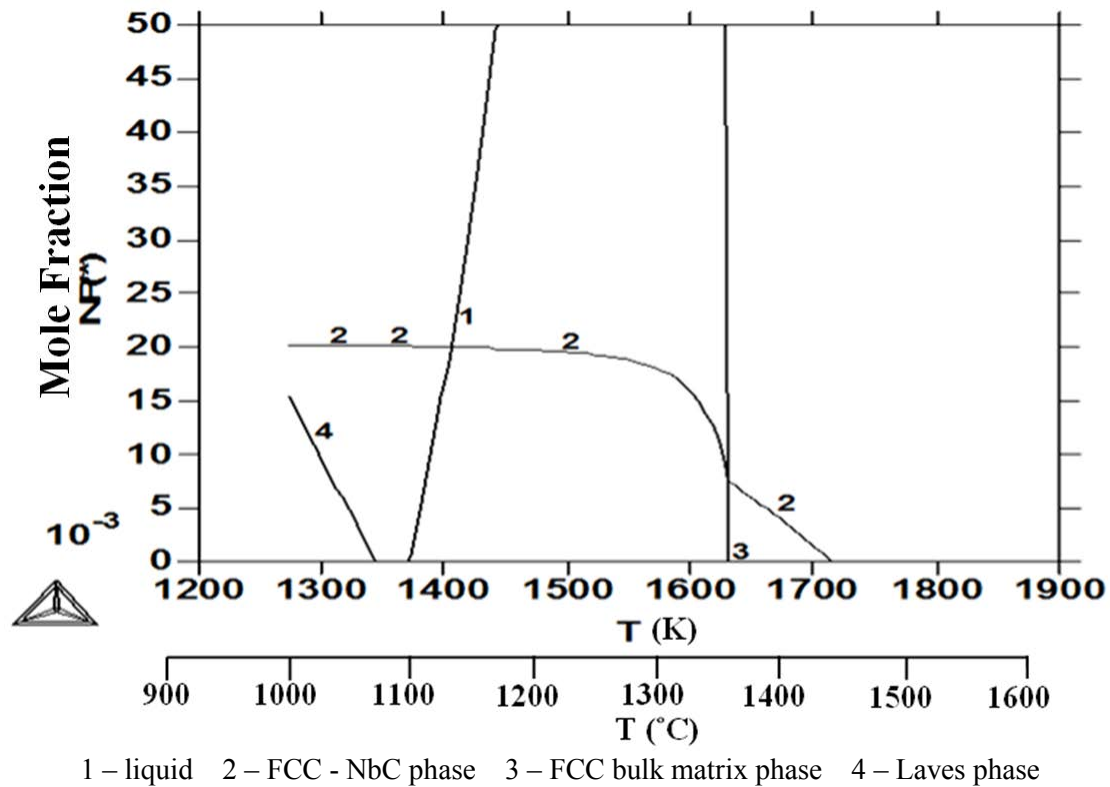


Figure 6-32 – Thermo-Calc phase predictions for XD1102,

With the current Thermo-Calc software code the predicted liquidus and solidus temperatures, 1367°C and 1097°C respectively, compared to the actual values of 1320°C and 1172°C was noted so further investigation using an improved Thermo-Calc prediction would be required before trust in the results could be obtained.

Using the current Thermo-Calc software the NbC phase is predicted, as expected, to form first at a temperature of 1447°C (1720K), illustrated in the Figure 6-32 and Table 6-6. It is also predicted that a volume fraction of 1.5% of the undesirable Laves phase will form.

Using Thermo-Calc the compositions of niobium and carbon have been addressed to achieve two goals:

1. Reduce the precipitation temperature of the niobium carbides to below the liquidus temperature of the melt; thus removing the increased diffusion rate of the niobium and carbon whilst in the liquid phase. This will encourage the carbides to form in the intergranular and interdendritic with a limited supply of niobium and carbon limiting the potential to grow.
2. Prevention of the formation of the Laves phase

Table 6-6 displays the results where only niobium and carbon have been adjusted.

Table 6-6 – Thermo-Calc phase predictions with varying niobium and carbon contents

	% NbC	Liquidus Parent (K)	Precipitation Temperature of NbC (K)	Laves phase form?
Standard	2	1640	1720	Y 1.5%
Double Nb	2	1610	1750	Y 5%
Half Nb	2	1640	1700	N
Double C	4	1640	1820	N
half C	1	1620	1600	Y 3%
1/4 C	0.5	1620	1600	Y <1%
1/2 Nb 1/2 C	1	1650	1640	Y 1%
1/4 Nb 1/2C	1	1650	1630	N

To achieve both of the goals the standard XD1102 would require one quarter of the original niobium content and half of the original carbon content. The corresponding

phase diagram can be seen in Figure 6-34. It should be noted that in having this modified composition the predicted volume fraction of the carbides would decrease to 1% from an original 2% which is expected to bring the strength of the material down. However, would the more finely distributed carbide coverage with a lower volume fraction be comparable to a higher volume fraction but increased size and sparsely spread carbide coverage?

A pseudo ternary equilibrium diagram as described by Floreen (Figure 6-33) for Inconel 718 identifies that the C:Nb ratio dictates the solidification path which would be in a similar manner to XD1102.

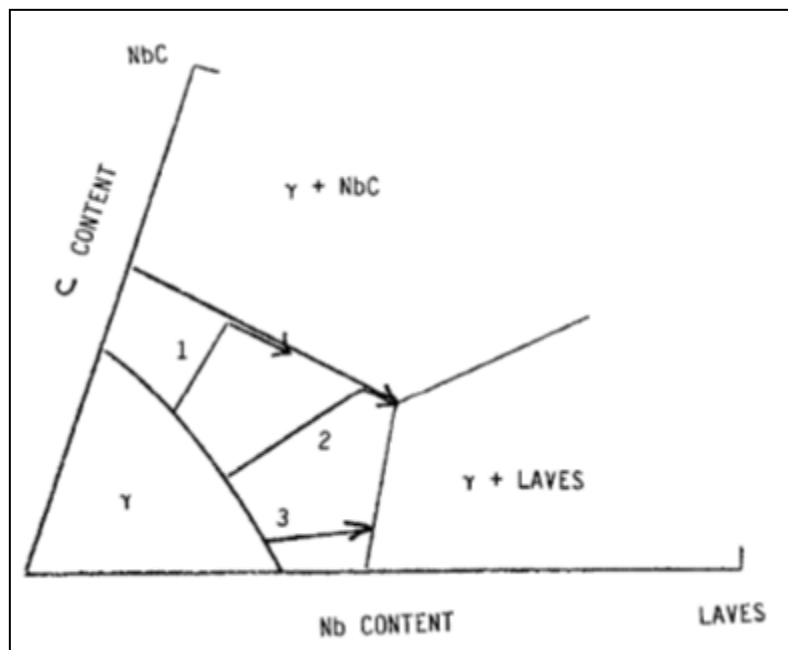
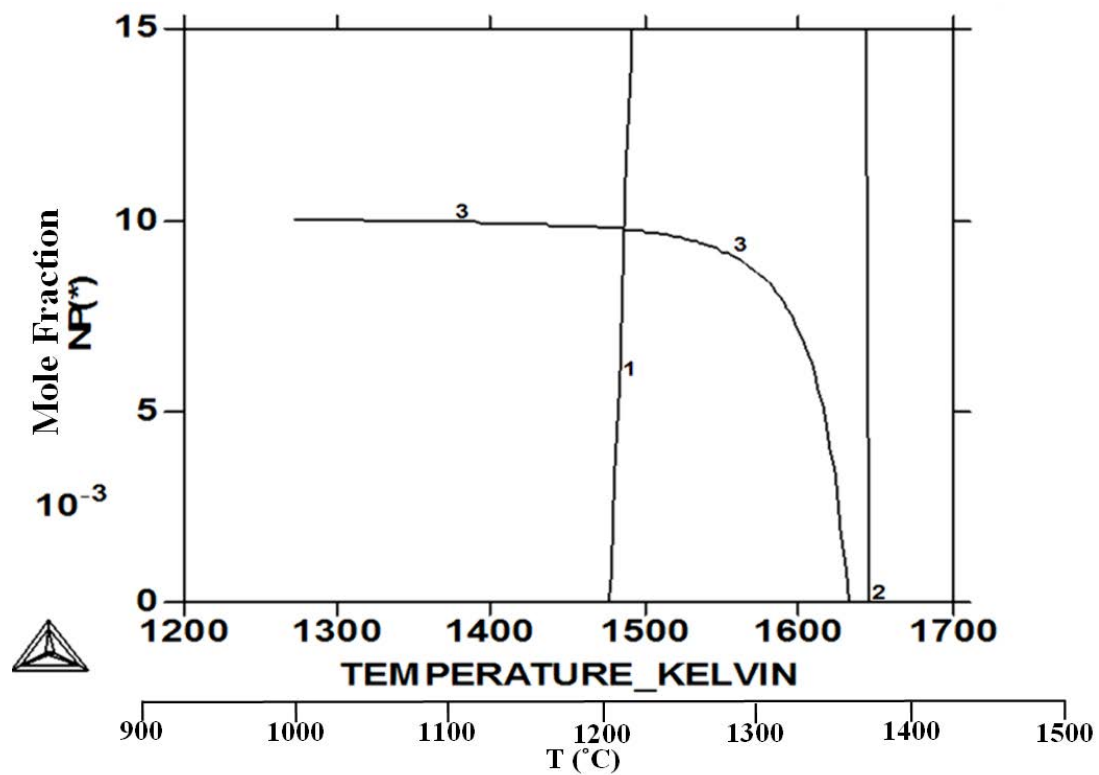


Figure 6-33 – Schematic diagram displaying solidification paths in Alloy 625 (Floreen et al.)



1 – liquid 2 – FCC bulk matrix phase 3 –FCC - NbC phase

Figure 6-34 – Thermo-Calc phase predictions with modified XD1102 composition.

## Chapter 7. Final Remarks

This thesis is written to describe the work carried out over a three year period at the University of Birmingham in collaboration with Special Metals Wiggin Limited (SMWL), a Precision Castparts Corporation company. The focus of this thesis was aimed towards various aspects of the manufacture of a wrought nickel-based superalloy valve bar. The air-cast Durville tilt casting process is the selected method by SMWL for the production of ingots for extrusion; this method provides a platform for the tranquil filling of a mould minimising turbulence within the flowing liquid prior to solidification.

The formation of an air-gap and the heat transfer at the casting-mould interface was measured for the aluminium alloy, LM25, and a nickel-iron alloy XD1102 cast in the same size mould. It was found that for the nickel-iron alloy the magnitude of the air-gap was over twice the aluminium casting. This is due to the increased melting temperature of the alloy subsequently heating the mould to a higher temperature and the alloy has a larger cooling range.

During the early stages of casting, when a liquid to mould interface was present, conductive heat transfer dominated radiative heat transfer for both alloys cast. As the air-gap began to form and pull away from the moulds wall, and whilst the casting still retains most of its temperature, the maximum ratio of radiative to conductive heat transfer was found.

For the duration of the aluminium casting, conductive heat transfer was the dominating transport method; however, due to the increased temperature required for XD1102 castings, and the formation of a larger air-gap, the radiative heat transfer mechanism



dominates after an air-gap of 0.5 mm had formed. 3D simulations of the above castings, using the software ProCAST, displayed a good agreement between the model and experiments. This provided confidence the model could be used where non-destructive techniques are necessary.

After solidification, and prior to extrusion, the XD1102 ingots are pre-heated in an air furnace to slightly below the materials solidus. The furnace is held at this temperature before the ingots are loaded in; this has proved problematic for some ingots in which cracks have been observed along their bases. The time at temperature results in the split subsequently oxidising with the following three tiered morphology; the surface oxide consisting of iron and chromium oxides followed by oxidation within the substrate at inter and intragranular regions of aluminium and titanium and finally the nitridation of both aluminium and titanium is observed.

After extrusion, a large longitudinal split was observed running down the front of many of the bars with the similar morphology to above. Beyond the split a region rich in aluminium and titanium oxides and nitrides were present; this is likely the region of the 2<sup>nd</sup> and 3<sup>rd</sup> tier as discussed above which has oxidised in front of the crack tip. Sufficient discard is therefore required to ensure the oxide and nitride rich regions do not get transferred into the final product.

It is impossible to prevent the formation of an oxide film during the Durville tilt casting process and the entrainment of such films are known to be detrimental to castings. It has been explored whether this is still true for wrought products. The tranquil filling of the moulds by the Durville tilt casting technique, to minimise turbulence, was compared to a top poured mould. Tensile testing of the valve bars was conducted for each casting

method and within the upper, middle and discard regions of product. On balance it was found that oxide entrainment within a casting was not significantly detrimental after the thermo-mechanical processing used here. Treating the ingot as a whole, the Durville tilt casting method yielded a higher Weibull modulus than the top poured samples, showing that a more consistent material property could be achieved. Increased scatter was observed in a chaotically poured ingot where it is found that oxide entrainment has aided in the nucleation of niobium carbides leading to an increased strength over the Durville tilt cast ingot.

The conclusions drawn from this thesis have displayed the capabilities of modelling simulations which can be used to replace multiple costly experiments. It has also provided evidence to SMWL of the importance, and implications, of the furnace heating regime prior to extrusion, as well as highlight that sufficient discard should be taken from a crocodiled extruded bar to ensure remnants of oxidation are not present. The study of tensile testing of Durville and top poured samples has given confidence that a consistent material property is achieved when casting through the Durville tilt casting process.

## Appendix A. Oxidation of a Lap Defect

The following work was carried out to investigate the morphology and chemical composition of an oxide lap in the as cast and the oxidised state with the aim to strengthen the oxidation characteristics of the alloy XD1102, and the interaction of an oxide lap with the pre-heat furnace. For this an ingot was cast which purposely entrained an oxide skin creating a lap defect. Half was analysed in the as-cast state and the other half was placed within an air furnace, where oxidation was allowed to commence. 2 samples, Figure A-1, were analysed using the same preparation and observation techniques as before. Firstly an as-cast oxide lap was analysed and secondly the analysis of an oxidised lap after the pre-heat furnace.

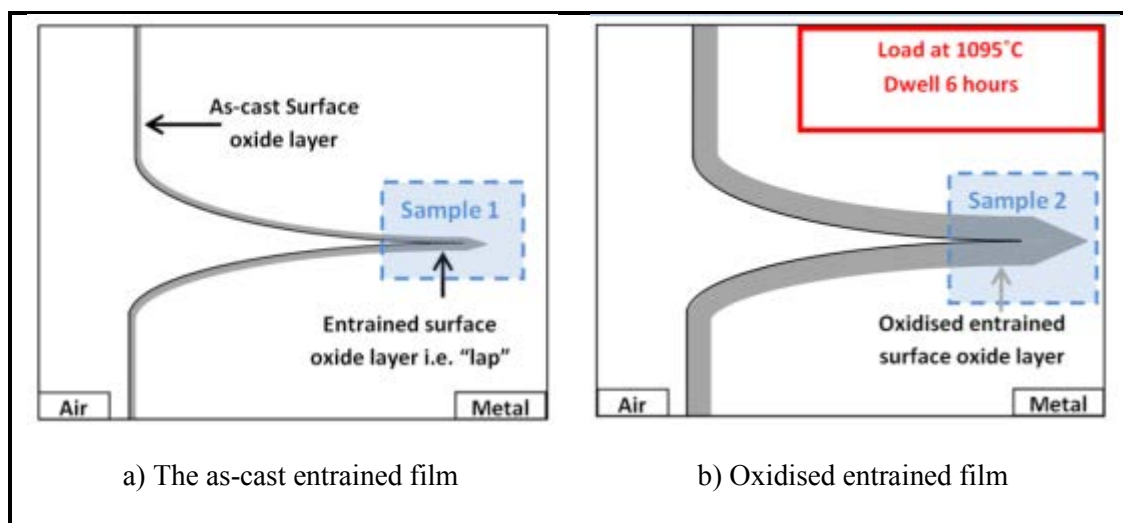


Figure A-1 – Schematic diagram of the samples analysed

### A.1.1 Experimental Set-Up

Approximately 10 Kg of the alloy XD1102 was melted in an induction furnace to the temperature of 1455°C. The melt was then poured in stages into a mould to allow for a skin of sufficient strength to form on the surface before more molten material was poured on top of this i. e. creating a fully entrained oxide skin. The melt was then

transversely poured up and down the mould to create laps along the side walls. As can be seen in the as-cast ingot many laps have been able to form (Figure A-2)



Figure A-2 – Photograph of an as-cast billet containing entrained oxide surfaces (i.e. laps)

The ingot was then sectioned with half being analysed in the as-cast state and the second half placed within a furnace held at the extrusion temperature and allowed to soak.

## **A.1.2 Results**

### **A.1.1.1 As-Cast**

The as-cast sections mainly consist of aluminium and titanium oxides/nitrides, as during the melting phase these two elements are highly reactive with air in this environment. Small amounts of CrO are observed and little evidence of FeO is found (Figure A-3).

The lap itself is approximately 2 $\mu$ m in width including a central void which takes up more than half of this.

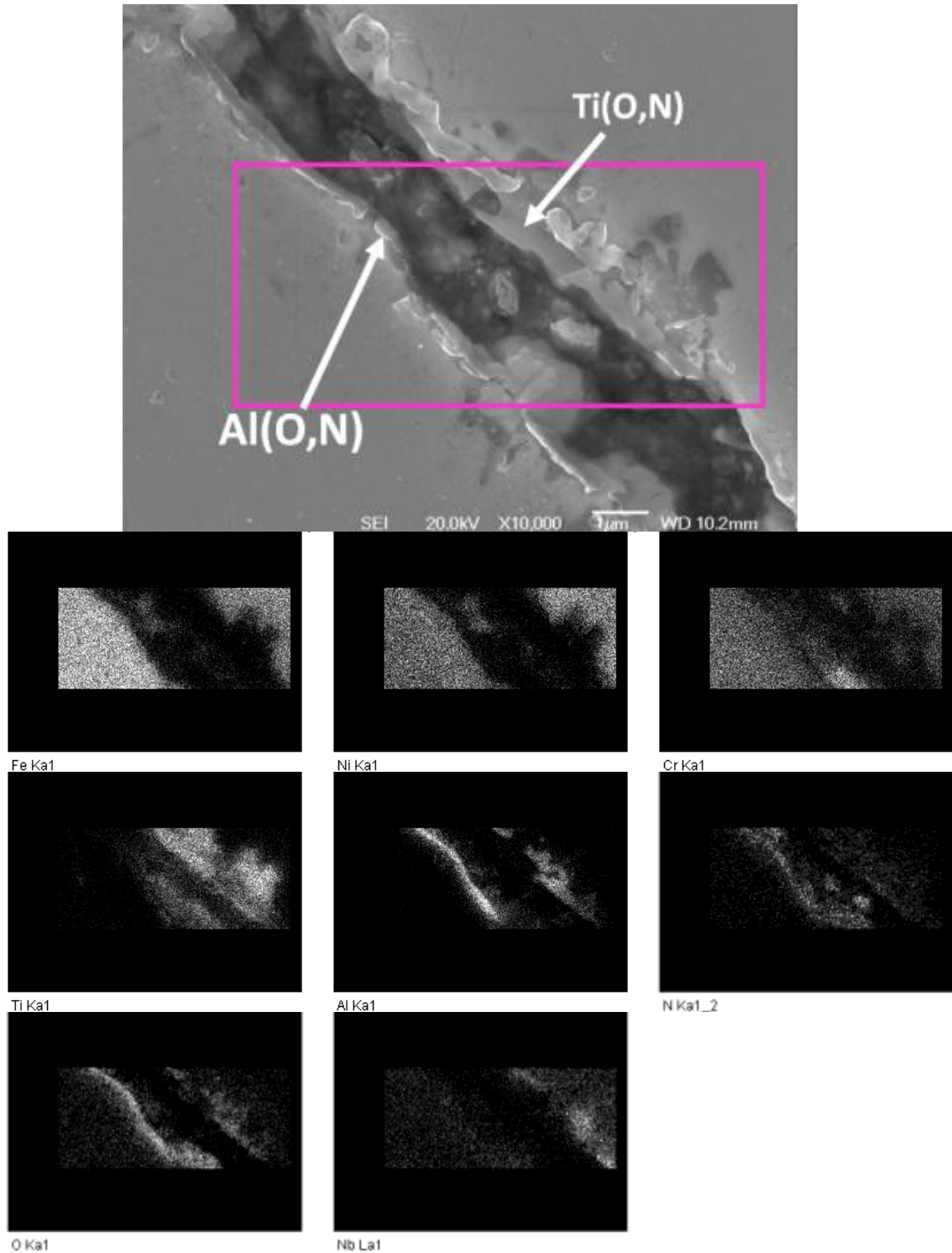


Figure A-3 – SEM image and elemental mapping at x10,000 magnification of the middle of as-cast lap

#### A.1.1.2 Oxidised Entrained Film

After dwelling in the furnace the oxide lap has changed morphology considerably; from less than 2  $\mu\text{m}$  in width to a feature region of approximately 100  $\mu\text{m}$ . Within the main region of the lap indicated by the large rectangular purple box in Figure A-5, oxidation is the predominant mechanism with an inner band resembling FeO and small amounts of CrO. Similar to section 1 this is followed by the oxidation of titanium and then aluminium. Similar to section 4 & 5 a nitrogen rich region is found, shown here by the small yellow box in Figure A-5.

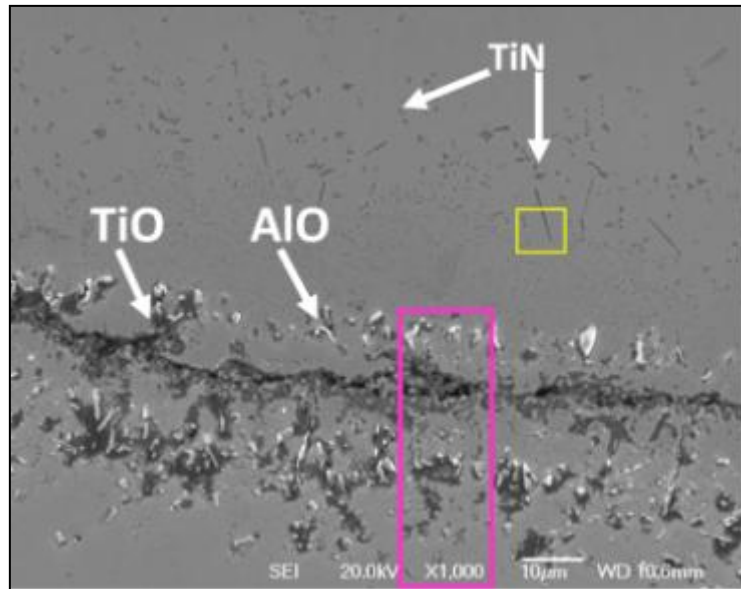


Figure A-4 – SEM image at x1,000 magnification middle of an oxidised lap.

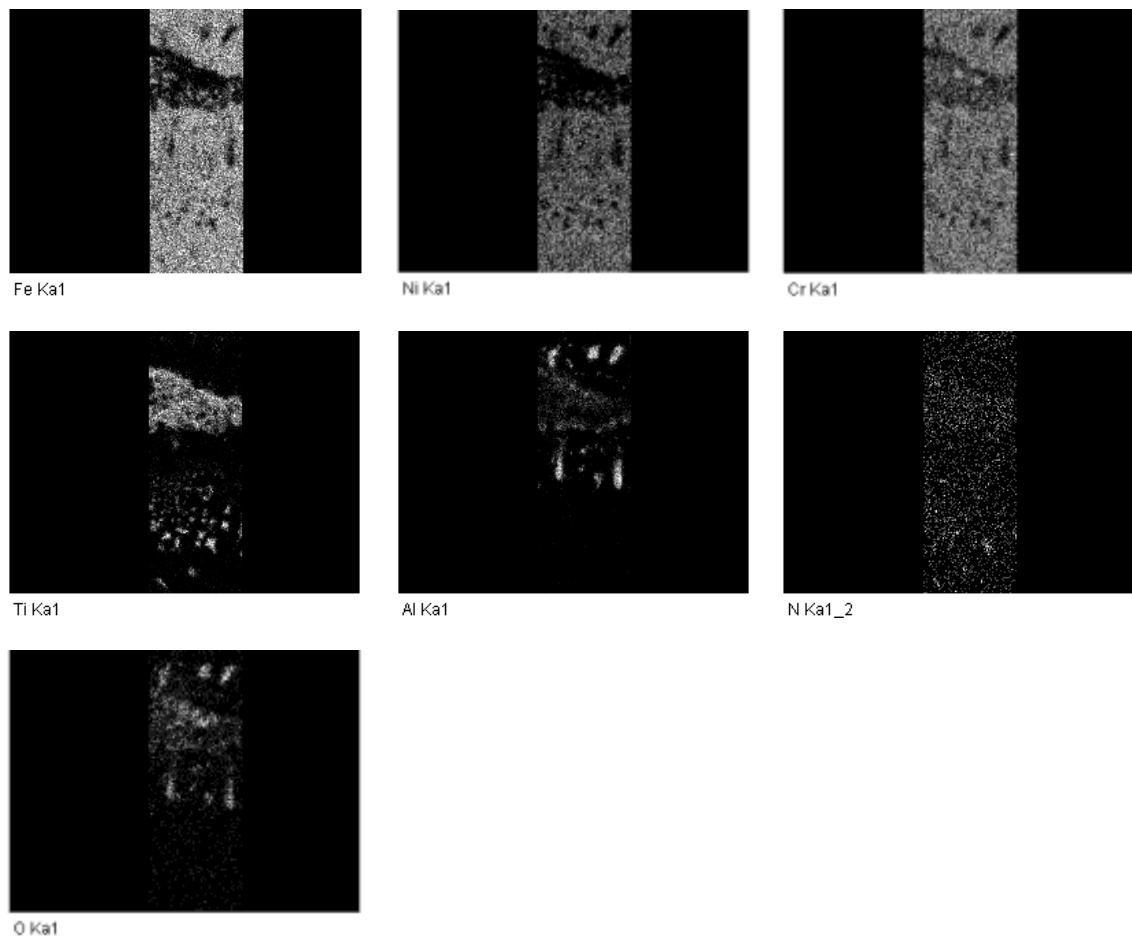


Figure A-5 – Elemental mapping of an oxidised surface of lap (large purple rectangular box within Figure A-4)

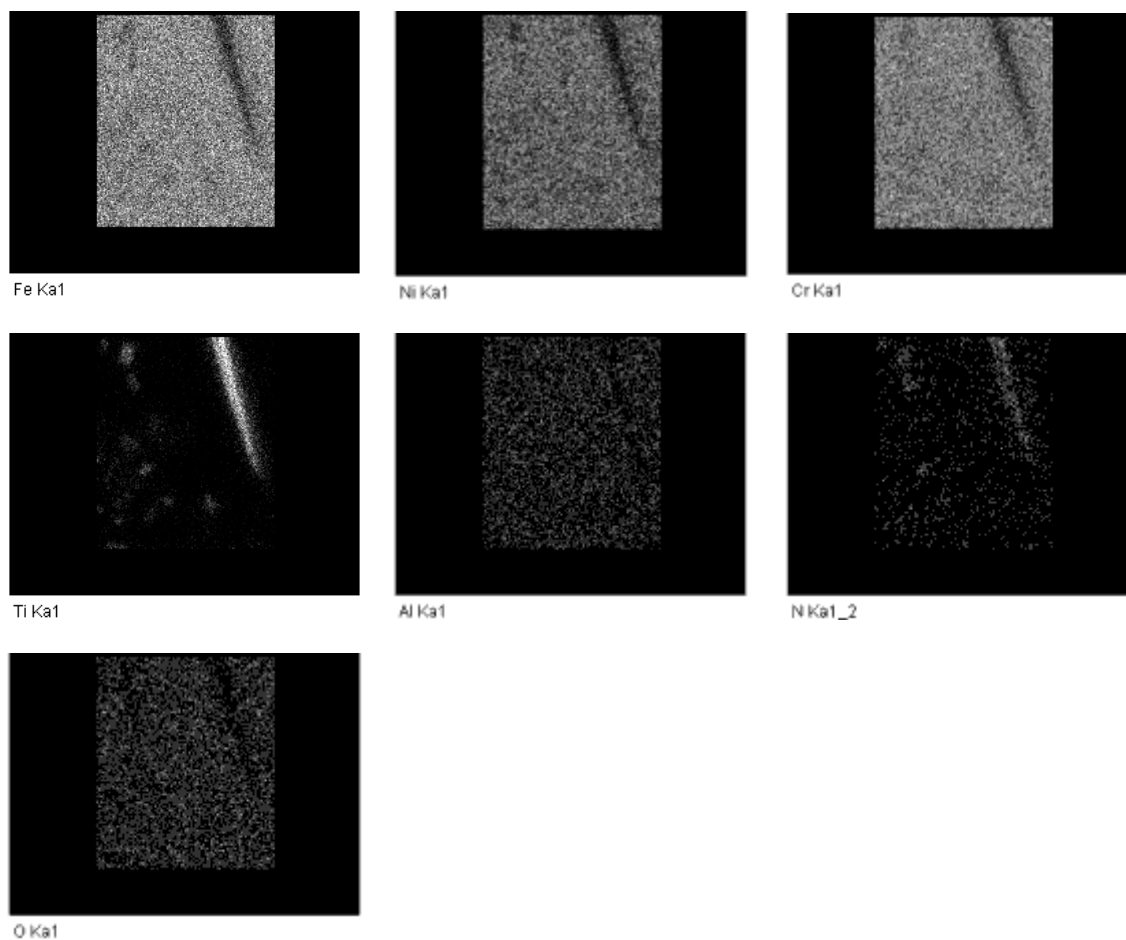


Figure A-6 – Elemental mapping displaying sub-surface of oxidised lap (small yellow box within Figure A-4)



## Appendix B. MATLAB

### B.1 Introduction

The software MATLAB was used extensively during the three year period to deal with large sets of data and to develop and perform 1-D solidification calculations efficiently.

### B.2 Converting Thermocouple Voltage into Temperature

The following code was created to convert raw thermocouple voltages data, recorded during the air-gap experiments, into temperature and displacements respectively. Both Type K and Type S calculations are displayed which is representative of the XD1102 air-gap trials.

```
clear all
close all
load raw;
nrows=length(a);
%a=video frames,b=cjtemp,
%c=typeK3mmdeepdeep ,d=typeK10mmdeep e=TypeK18mm
%lasers f=tungsten sensor, g=mould sensor
%h=Type S
%no scaling required for the XD1102 as already scaled in LABView -
needed so just make bb=b to follow through on a previous code
%used.
bb=b;cc=c;dd=d;ee=e;ff=f;gg=g;hh=h;
%%
%*****calculating CjTemp by given equations on datalogging
software*****
r1=5000;vref=2.5;irt=(vref-bb)/r1;x=1.295361e-3;y=2.343159e-
4;z=1.018703e-7;lnrt=log(bb ./irt);
CjT=1 ./ (x+lnrt.*(y+z*(lnrt.^2)));
CjT=CjT-273; % output temperature in C
%%
%*****TYPE K CALCULATIONS*****
%changing cold junction temp into Type K voltage "millivolts"

TtoVtypeK=[ -1.7600413686E-2
            3.8921204975E-2
            1.8558770032E-5
            -9.9457592874E-8
            3.1840945719E-10
            -5.6072844889E-13
            5.6075059059E-16
            -3.2020720003E-19
            9.7151147152E-23
```

```

        -1.2104721275E-26    ];
TtoVtypeK=flipud(TtoVtypeK);

VrefCjTempK = polyval(TtoVtypeK,CjT);

%changing type K thermocouples voltages into millivolts
ccmv=cc*1000;ddmv=dd*1000;eemv=ee*1000;

%TC voltage plus cold junction voltage
cc=ccmv+VrefCjTempK;dc=ddmv+VrefCjTempK;ec=eemv+VrefCjTempK;
cc=decimate(cc,1000);dc=decimate(dc,1000);ec=decimate(ec,1000);

%*****TYPE K VOLTAGE TO TEMP
COEFFICIENTS*****
%Temperature range 500 deg C to 1372 deg C Voltage range 20.644 mV to
54.886 mV
HighTempK =[    -1.318058E2
                4.830222E1
               -1.646031
                5.464731E-2
               -9.650715E-4
                8.802193E-6
               -3.110810E-8    ];
HighTempK=flipud(HighTempK);

% Temperature range 0 deg C to 500 deg C or Voltage range 0 mV to
20.644 mV
LowTempK =[    0
                2.508355E1
                7.860106E-2
               -2.503131E-1
                8.315270E-2
               -1.228034E-2
                9.804036E-4
               -4.413030E-5
                1.057734E-6
               -1.052755E-8    ];
LowTempK=flipud(LowTempK);

nrows=length(cc);
UpperLimitK = 20.644;
Tc=cc*0;    %sets up a matrix with zeros present to save time for
MATLAB to keep adding and reading the lines in.
for kk=1:nrows, %This is for any thermocouples which range between
more than one coefficient matrix
    if cc(kk)>=UpperLimitK
        Tc(kk)=polyval(HighTempK,cc(kk));
    else
        Tc(kk)=polyval(LowTempK,cc(kk));
    end
end
Td=dc*0;    %sets up a matrix with zeros present to save time for
MATLAB to keep adding and reading the lines in.
for kk=1:nrows, %This is for any
thermocouples which range between more than one coefficient matrix
    if dc(kk)>=UpperLimitK
        Td(kk)=polyval(HighTempK,dc(kk));
    else

```

```

Td(kk)=polyval(LowTempK,dc(kk));
end
end
Te=ec*0; %sets up a matrix with zeros present to save time for
MATLAB to keep adding and reading the lines in.
for kk=1:nrows, %This is for any
thermocouples which range between more than one coefficient matrix
    if ec(kk)>=UpperLimitK
        Te(kk)=polyval(HighTempK,ec(kk));
    else
        Te(kk)=polyval(LowTempK,ec(kk));
    end
end
%changing into Kelvin
Tck=Tc+273;Tdk=Td+273;Tek=Te+273;
t1=(1:length(Tc));
%%
%*****TYPE S Thermocouple*****
%
%converting cjtemp into type s voltages between temp range -50 deg C
to 1064.180
TtoVtypeS=[
    0
    0.540313308631E-2
    0.125934289740E-4
    -0.232477968689E-7
    0.322028823036E-10
    -0.331465196389E-13
    0.255744251786E-16
    -0.125068871393E-19
    0.271443176145E-23 ];
TtoVtypeS=flipud(TtoVtypeS);

VrefCjTempS = polyval(TtoVtypeS,CjT);

%
%*****CHANGE VOLTAGE INPUT INTO MILLIVOTS*****

hhmv=hh*1000;

%TC voltage plus cold junction voltage
hc=hhmv+VrefCjTempS;
hc=decimate(hc,1000);
% Temperature range -50 deg C to 250 deg C or Voltage range -0.235 to
1.874mV
LowTempS=[
    0
    1.8494946E2
    -8.00504062E1
    1.0223743E2
    -1.52248592E2
    1.88821343E2
    -1.59085941E2
    8.2302788E1
    -2.34181944E1
    2.7978626 ];
LowTempS=flipud(LowTempS);

```

```

% Temperature range 250 to 1200 deg C or Voltage range 1.874 to
11.950mV
MidTempS=[ 1.291507177E1
           1.466298863E2
          -1.534713402E1
           3.145945973
          -4.163257839E-1
           3.187963771E-2
          -1.2916375E-3
           2.183475087E-5
          -1.447379511E-7
           8.211272125E-9      ];
MidTempS=flipud(MidTempS);

% Temperature range 1064 to 1664.5 deg C or Voltage range 10.332 to
17.536mV
HighTempS=[ -8.087801117E1
            1.621573104E2
           -8.536869453
            4.719686976E-1
           -1.441693666E-2
            2.081618890E-4      ];
HighTempS=flipud(HighTempS);

LowerLimitS= 1.8874;
UpperLimitS=10.332;

Th=hc*0;
for kk=1:nrows,
    if      hc(kk)>=UpperLimitS
        Th(kk)=polyval(HighTempS, hc(kk));
    elseif hc(kk)>=LowerLimitS
        Th(kk)=polyval(MidTempS, hc(kk));
    else
        Th(kk)=polyval(LowTempS, hc(kk));
    end
end

%changing into Kelvin
Thk=Th+273;

```

### B.3 Prediction of the Mould's Inner Surface Temperature

The following code was used to predict the mould's inner surface temperature by differing prediction techniques of linear extrapolation, finite difference method and the inverse method (as supplied by Fredrick for this reason the sub MATLAB codes have not been presented).

### B.3.1.1 Code

```

close all
clear all
load Td; load Te; load Tf; %Load in the thermocouple data which has
already been converted from a voltage into a temperature reading in a
separate code
%Td=3mm deep, Te=10mm deep, Tf=18mm deep
t1=1:length(Td); %No. of iterations required
Cp=450; %J/Kg/K - Specific Heat Capacity
Di=0.1098; %inner mould diameter
WallThickness=21.3;%mm
%%
%Linear extrapolation

n=length(Td);
OuterTempL = zeros(1, n);
InnerTempL = zeros(1, n);
for ii=1:n
x = [3 10 18];
y = [Td(ii) Te(ii) Tf(ii)];
p = polyfit(x,y,1);%linear
x2 = 0:21;
y2 = polyval(p,x2);
OuterTempL(ii)=p(2);
InnerTempL(ii)=(p(1)*WallThickness)+p(2);
end
%%
%Finite difference
nr=length(Td);Tdt1=Td(2:nr)-Td(1:nr-1);Tdt1(nr)=Tdt1(nr-1);%time
derivative
%=====CYLINDRICAL GEOMETRY=====
R2=(Di/2+0.0066);%diameter at inner element point
QFD=(1/(Di/2)).*((conductivityGCiron((Td+Te+Tf)/3)).*(Tf-
Te)/0.008).*R2+ densityGCiron((Td+Te+Tf)/3).*Cp.*Tdt1.* ( R2^2-
(Di/2)^2 ).*0.5 ); %heat flux going in through mould inner wall
InnerTempFD=((QFD*0.0033)./conductivityGCiron((Td+Te+Tf)/3))+Tf;
%inner surface temp
%%
%Inverse model
%Experiment - Surface Temperature and heat-flux computed using two
% thermocouples inside the material.

% Define physical quantities
rho=7800; % kg/m^3
k=28; % W/m/K
L1=(21.3-18)*10^-3; % mm Distance from inner mould surface to first TC
L2=(21.3-10)*10^-3; % mm Distance from inner mould surface to second
TC

% Load measured data. Also change the scale so the initial temperature
is
% zero. This is needed because of how the codes are written.

BASE_TEMPERATURE=mean(Tf(1:5));
G=Tf-BASE_TEMPERATURE; % G(t)=T(L1,t);
W=Te-BASE_TEMPERATURE; % H(t)=T(L2,t);

```

```

Tend=length(G); % 1 measurement/second
t=Tend*(0:length(G)-1)/(length(G)-1);

% Step 1: Compute the heat-flux at the thermocouple x=L1. This is by
% solving a well-posed boundary value problem in the interval L1<x<L2.
kappa=k/rho/Cp;
N=256;x=L1+(L2-L1)*(0:N-1)/(N-1);
[dG,dW]=SHEForwardSolv(x,t,G,W,kappa);
% plot(t,k*-dG,t,k*-dW); % Plot the two heat-fluxes...

% Step 2: Solve the inverse problem in the region 0<x<L1.
xi_c=120;
N=12;x=L1*(0:N-1)/(N-1);
[T,Tx,x]=SHESolver(x,t,G,dG,kappa,xi_c);
Fode=T(end,:);dFode=k*Tx(end,:);
%figure(2),plot(t,Fode+BASE_TEMPERATURE,'b',t,Te,'k',t,Tf,'m'); %
Surface temperature and at the two thermocouples

InnerTempIn=Fode+BASE_TEMPERATURE;

%%
set(0,'defaultlinelength',4)
plot(t1,InnerTempL,t1,InnerTempFD,'--',t1,InnerTempIn,':',t1,Te)
legend('Extrapolation','finite Difference','Inverse','18mm Deep
Thermocouple')
xlabel('Time(s)','FontSize',24,'FontWeight','bold');ylabel('Temperatur
e (\circC)','FontSize',24,'FontWeight','bold');
set(gca,'FontWeight','bold','FontSize',24)
grid

```

## B.3.1.2 Calculations for Finite Difference Method

### B.3.1.2.1 Nomenclature

		Subscripts	
$c_p$	Specific heat (J/kgK)		
$h$	Heat transfer coefficient (W/m <sup>2</sup> K)	a	alloy
$K$	Thermal conductivity (W/mK)	air	air
$Q$	Heat flux (W/m <sup>2</sup> K)	c	conduction
$t$	time (s)	m	mould
$T$	Temperature (K)	r	radiation
$\rho$	Density (kg/m <sup>3</sup> )	s	surface
$\varepsilon$	Emissivity		
$\sigma$	Stefan-Boltzmann constant (5.67x10 <sup>-8</sup> W/m <sup>2</sup> K <sup>4</sup> )		

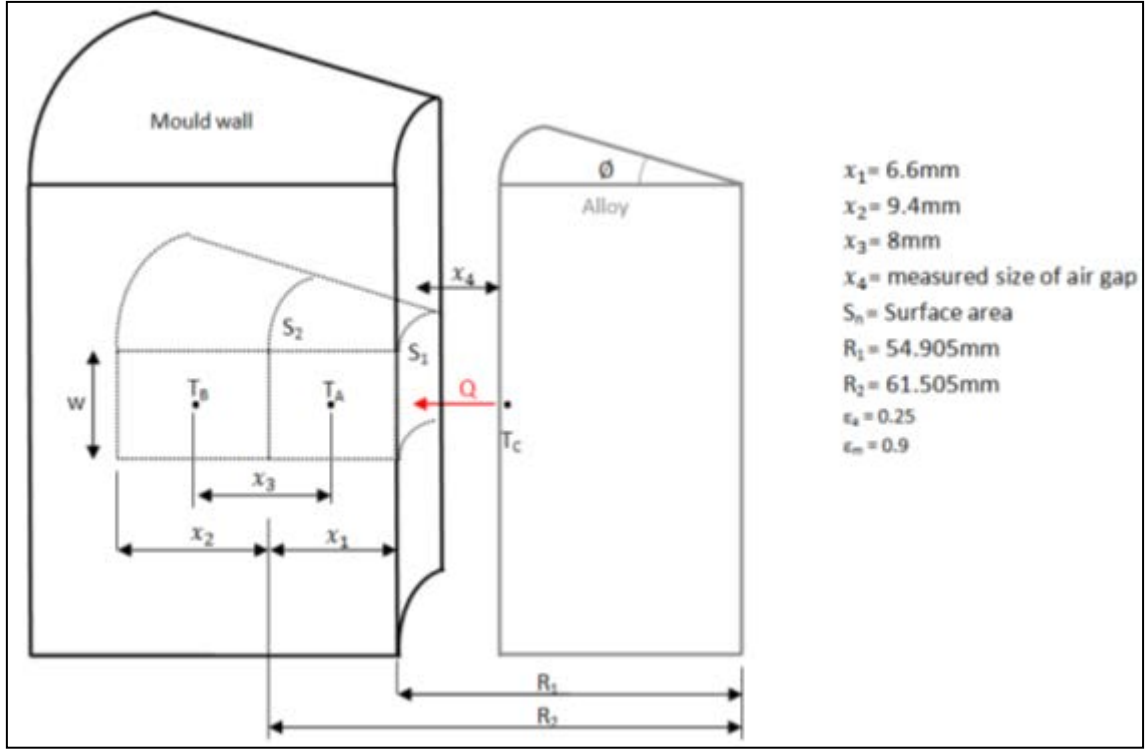


Figure B-1 – Schematic diagram displaying the variables used for the finite difference calculation

The heat flux passing in through the surface of element A transferred from the melt (combination of conduction and radiation):

$$QS_1 = k_m \left. \frac{dT}{dx} \right|_{R_2} \cdot S_2 + \rho c_p V_A \frac{dT}{dt}$$

$$QR_1 w \phi = k_m \left. \frac{dT}{dx} \right|_{R_2} \cdot R_2 w \phi + \rho c_p \frac{dT}{dt} \frac{\phi \pi}{2\pi} (R_2^2 - R_1^2) w$$

$$Q = \frac{1}{R_1} \left[ k_m \left. \frac{dT}{dx} \right|_{R_2} \cdot R_2 + \frac{1}{2} \rho_m c_{p_m} \frac{dT}{dt} (R_2^2 - R_1^2) \right]$$

With the known heat flux and the temperature,  $T_A$ , the inner surface temperature of the mould wall can be predicted by the well known heat conduction equation:

$$Q = k_m \frac{dT}{dx}$$

$$T_s = \frac{Qx_1}{k_m} + T_A$$

#### B.3.1.2.2 Assumptions

1. The heat problem is treated as one-dimensional
2. The temperature distribution within each element is treated as uniform
3. The measured temperature of the casting,  $T_C$ , is assumed to be the surface temperature of the ingot.
4. The air-gap temperature and respective thermal conductivity is taken as the average of the mould and alloy surface temperatures and assumed no increase in hydrogen content.
5. The surface of the alloy is assumed heavily oxidised

### B.4 Air and Water Quenching of the XD1102 at SMWL

The following code was created to predict the temperature of each cell within a SMWL mould by either the standard air cooling on the outer surface or by water quenching. “Q” within represents the water quenched side of the code and “A” Air-cooled. The schematic in Figure B-2 is presented for clarity over the initial calculations. The main code, during the iterative calculations, calls up many sub-functions to speed up calculations and to help with clarity and any de-bugging issues.



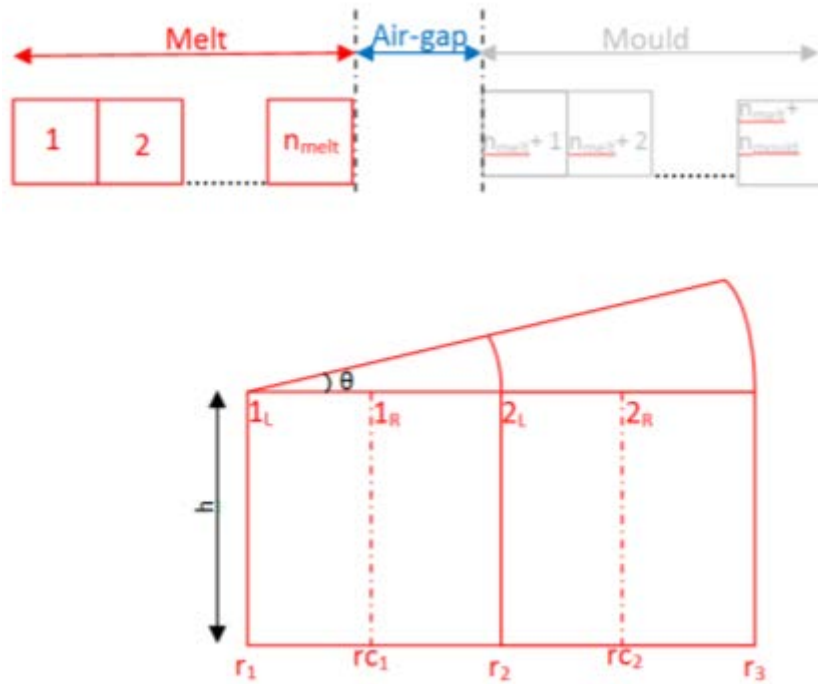


Figure B-2 – Schematic diagram displaying cell sizes used in the MATLAB code

#### B.4.1.1 Main Code

```
% close all
% close all
clear all
%dimensions
widthcell=.001; cellheight=.001; %1mm
%material properties
Rho1102=7300;RhoGCiron=7000; %Using constant density else loss of
energy conversion
StefanBoltzmann=5.6704E-8;
EGCiron=0.6;Emetal=0.25;Emould=0.95; %code for GC iron emissivity
available
Tamb=13;
Tliquidus=1320;Tsolidus=1172;Tmiddle=(Tliquidus+Tsolidus)./2;T620=620;
Fraction=0.7;SolidFrac=Tliquidus - Fraction*(Tliquidus-Tsolidus);

%how long?
dt=0.005;minutes=60;n=(minutes*60)/dt;%/m/s
% n=6000;
% n=length(g1)/dt; %too match the time for the experiment

tstart=1;

%Initial conditions
TmeltQ=1455;Tmetal=92;TmeltA=1455;
nmeltQ=140;nmetal=64;nmeltA=140;
meltcellsQ=ones(1,nmeltQ);metalcells=ones(1,nmetal);
```

```

allcells=[meltcellsQ metalcells];
T0Q=[meltcellsQ*TmeltQ metalcells*Tmetal];
T0A=[meltcellsQ*TmeltA metalcells*Tmetal];
theta=2*pi;
IAG=20E-6;
%zero the vectors
RADoutQ=0*n;RADoutA=0*n;ConvOutQ=0*n;ConvOutA=0*n;EoutQ=0*n;EoutA=0*n;
Tot2EQ=0*n;TotEQ=0*n;TotEA=0*n;
GradQ=0*nmeltQ+nmetal;GradA=0*nmeltQ+nmetal;TempQ=0*nmeltQ+nmetal;Temp
A=0*nmeltQ+nmetal;
GradientsQ=zeros(n, nmeltQ+nmetal);GradientsA=zeros(n, nmeltQ+nmetal);Te
mperaturesQ=zeros(n, nmeltQ+nmetal);TemperaturesA=zeros(n, nmeltQ+nmetal
);
CoolingRateQL=0*nmeltQ;CoolingRateAL=0*nmeltQ;CoolingRateQM=0*nmeltQ;C
oolingRateAM=0*nmeltQ;CoolingRateQS=0*nmeltQ;CoolingRateAS=0*nmeltQ;
CoolingRate620QS=0*nmeltQ;CoolingRate620AS=0*nmeltQ;

r=[(0:nmeltQ)*widthcell (1:nmetal)*widthcell+nmeltQ*widthcell];
r(1)=1E-6;
% VolMelt=pi*(nmelt*widthmetal)^2;
% VolMetal=(pi*((nmelt+nmetal)*widthmetal)^2)-
(pi*(nmelt*widthmetal)^2);
rc=0.5*(r(1:end-1) + r(2:end));
T1Q=T0Q;T1A=T0A;
cellmass=0*rc;

Breakaway=0;
for ii=tstart:n,

T2Q=T1Q;T2A=T1A;
KcQ=[conductivity1102(T1Q(1:nmeltQ))
conductivityGCiron(T1Q(nmeltQ+1:nmeltQ+nmetal))];
KcA=[conductivity1102(T1A(1:nmeltA))
conductivityGCiron(T1A(nmeltA+1:nmeltA+nmetal))];

RRQ=0*r;RRA=0*r;
%to the left of the interfaces
RRQ(2:end)=log(r(2:end)./rc(1:end))./(KcQ(1:end)*cellheight*theta);
RRA(2:end)=log(r(2:end)./rc(1:end))./(KcA(1:end)*cellheight*theta);

%to the right of the interfaces
RRQ(1:end-1)=RRQ(1:end-1)+(log((rc(1:end)./r(1:end-
1)))./(KcQ(1:end)*cellheight*theta));
RRA(1:end-1)=RRA(1:end-1)+(log((rc(1:end)./r(1:end-
1)))./(KcA(1:end)*cellheight*theta));

cellmass=[ pi*(r(2:nmeltQ+1).^2-r(1:nmeltQ).^2)*cellheight*Rho1102
pi*(r(nmeltQ+2:nmeltQ+nmetal+1).^2-
r(nmeltQ+1:nmeltQ+nmetal).^2)*cellheight*Rho1102 ];

KKQ=1./RRQ;KKA=1./RRA;

```

```

dERlQ=0*T0Q;dERrQ=0*T0Q;dERlA=0*T0A;dERrA=0*T0A;

dERrQ(1:end-1)=(TlQ(2:end)-TlQ(1:end-1)).*KKQ(2:end-1);dERrA(1:end-1)=(TlA(2:end)-TlA(1:end-1)).*KKA(2:end-1);
dERlQ(2:end)=(TlQ(1:end-1)-TlQ(2:end)).*KKQ(2:end-1);dERlA(2:end)=(TlA(1:end-1)-TlA(2:end)).*KKA(2:end-1);

avmouldTempA(ii)=mean(TlA(nmeltA:end));%average of mould temp
ExpansionMouldRingA(ii)=r(nmeltA+(nmetal)/2)*10.8E-6*(avmouldTempA(ii)-Tmetal);
ExpansionMouldWallA(ii)=nmetal*10^-3*10.8E-6*(avmouldTempA(ii)-Tmetal);
ExpansionTotA(ii)=(ExpansionMouldRingA(ii)-ExpansionMouldWallA(ii)/2);

avmeltTempA(ii)=mean(TlA(nmeltA-2:nmeltA));
if avmeltTempA(ii)>SolidFrac
    ContractionA(ii)=ExpansionTotA(ii);
    Breakaway=ExpansionTotA(ii);

elseif avmeltTempA(ii) < SolidFrac && avmeltTempA(ii)> Tsolidus
    ContractionA(ii)=Breakaway;

else

    ContractionA(ii)= Breakaway +(r(nmeltA)*6.6E-6.*(avmeltTempA(ii)-Tsolidus)); %using TE
    % Contraction(ii)= Breakaway +
    (r(nmelt)*(density1102(Tsolidus)./density1102(avmeltTemp(ii))).^0.5))
    ;% using density shrinkage
end
AirgapA(ii)=ExpansionTotA(ii)-ContractionA(ii);
if AirgapA(ii)<=IAG
    AirgapA(ii)=IAG;
else
end

avmouldTempQ(ii)=mean(TlQ(nmeltQ:end));%average of mould temp
ExpansionMouldRingQ(ii)=r(nmeltQ+(nmetal)/2)*10.8E-6*(avmouldTempQ(ii)-Tmetal);
ExpansionMouldWallQ(ii)=nmetal*10^-3*10.8E-6*(avmouldTempQ(ii)-Tmetal);
ExpansionTotQ(ii)=(ExpansionMouldRingQ(ii)-ExpansionMouldWallQ(ii)/2);

avmeltTempQ(ii)=mean(TlQ(nmeltQ-2:nmeltQ));
if avmeltTempQ(ii)>SolidFrac
    ContractionQ(ii)=ExpansionTotQ(ii);
    Breakaway=ExpansionTotQ(ii);

elseif avmeltTempQ(ii) < SolidFrac && avmeltTempQ(ii)> Tsolidus
    ContractionQ(ii)=Breakaway;

else

    ContractionQ(ii)= Breakaway +(r(nmeltQ)*6.6E-6.*(avmeltTempQ(ii)-Tsolidus)); %using TE

```

```

%      Contraction(ii)= Breakaway +
(r(nmelt)*(density1102(Tsolidus)./density1102(avmeltTemp(ii))).^0.5))
;% using density shrinkage
end
AirgapQ(ii)=ExpansionTotQ(ii)-ContractionQ(ii);
if AirgapQ(ii)<=IAG
    AirgapQ(ii)=IAG;
else
end

%conductivity of air in newly formed gap
KairQ(ii)=(1.5207E-11*((T1Q(nmeltQ)+T1Q(nmeltQ+1))/2).^3)-(4.8574E-
8*((T1Q(nmeltQ)+T1Q(nmeltQ+1))/2).^2)+(1.0184E-
4*((T1Q(nmeltQ)+T1Q(nmeltQ+1))/2))-0.00039333;
KairA(ii)=(1.5207E-11*((T1A(nmeltA)+T1A(nmeltA+1))/2).^3)-(4.8574E-
8*((T1A(nmeltA)+T1A(nmeltA+1))/2).^2)+(1.0184E-
4*((T1A(nmeltA)+T1A(nmeltA+1))/2))-0.00039333;

%Conduction through gap
QcbetQ(ii)=((KairQ(ii)*cellheight*2*pi*r(nmeltQ)*(T1Q(nmeltQ)-
T1Q(nmeltQ+1)))./AirgapQ(ii)); %using avexpansions from thermal
expansion equations
QcbetA(ii)=((KairA(ii)*cellheight*2*pi*r(nmeltA)*(T1A(nmeltA)-
T1A(nmeltA+1)))./AirgapA(ii)); %using avexpansions from thermal
expansion equations

%radiation through airgap
QrbetQ(ii)=(StefanBoltzmann*cellheight*2*pi*r(nmeltQ)*((T1Q(nmeltQ)+27
3).^4-(T1Q(nmeltQ+1)+273).^4))/((1/Emetal)+(1/Emould)-1);
QrbetA(ii)=(StefanBoltzmann*cellheight*2*pi*r(nmeltA)*((T1A(nmeltA)+27
3).^4-(T1A(nmeltA+1)+273).^4))/((1/Emetal)+(1/Emould)-1);

dERlA(nmeltA+1)=QcbetA(ii)+QrbetA(ii);
dERrA(nmeltA)=-dERlA(nmeltA+1);

dERlQ(nmeltQ+1)=QcbetQ(ii)+QrbetQ(ii);
dERrQ(nmeltQ)=-dERlQ(nmeltQ+1);

E0Q=0*rc;E0A=0*rc;

E0Q=[ cellmass(1:nmeltQ).*enthalpy1102(T1Q(1:nmeltQ))
cellmass(nmeltQ+1:nmeltQ+nmeltQ+nmetal).*enthalpyGCiron(T1Q(nmeltQ+1:nmeltQ+n
metal)) ];
E0A=[ cellmass(1:nmeltA).*enthalpy1102(T1A(1:nmeltA))
cellmass(nmeltA+1:nmeltA+nmeltA+nmetal).*enthalpyGCiron(T1A(nmeltA+1:nmeltA+n
metal)) ];

%TotE0Q(ii)=sum(E0Q);%TotE0A(ii)=sum(E0A);
RADoutQ(ii)=StefanBoltzmann*EmissivityGCiron(T1Q(end))*cellheight*pi*r
(end)*2*((T1Q(end)+273)^4-(Tamb+273)^4);
RADoutA(ii)=StefanBoltzmann*EmissivityGCiron(T1A(end))*cellheight*pi*r
(end)*2*((T1A(end)+273)^4-(Tamb+273)^4);

```

```

ConvOutQ(ii)=cellheight*pi*r(end)*2*htcQ(T1Q(end))*(T1Q(end)-
Tamb);%coefficient used to mimic the cooling of the temperature
measurements
ConvOutA(ii)=cellheight*pi*r(end)*2*15*(T1A(end)-Tamb);%coefficient
used to mimic the cooling of the temperature measurements

EoutQ(ii)=(RADoutQ(ii)+ConvOutQ(ii));EoutA(ii)=(RADoutA(ii)+ConvOutA(i
i));

dERrQ(end)=dERrQ(end)-EoutQ(ii);dERrA(end)=dERrA(end)-EoutA(ii);
%Right(ii)=sum(dERr);Left(ii)=sum(dERl);

EQ= E0Q+(dERrQ+dERlQ)*dt;EA= E0A+(dERrA+dERlA)*dt;

% TotEQ(ii)=sum(EQ);TotEA(ii)=sum(EA);

T1Q(1:nmeltQ)=temperaturel102(EQ(1:nmeltQ)./cellmass(1:nmeltQ));
T1Q(nmeltQ+1:nmeltQ+nmetal)=temperatureGCiron(EQ(nmeltQ+1:nmeltQ+nmeta
l)./(cellmass(nmeltQ+1:nmeltQ+nmetal)));
T1A(1:nmeltA)=temperaturel102(EA(1:nmeltA)./cellmass(1:nmeltA));
T1A(nmeltA+1:nmeltA+nmetal)=temperatureGCiron(EA(nmeltA+1:nmeltA+nmeta
l)./(cellmass(nmeltA+1:nmeltA+nmetal)));

% E1Q=[ cellmass(1:nmeltQ).*enthalpyl102(T1Q(1:nmeltQ))
cellmass(nmeltQ+1:nmeltQ+nmetal).*enthalpyGCiron(T1Q(nmeltQ+1:nmeltQ+n
metal))] ;
% Tot2EQ(ii)=sum(E1Q);

for jj = 1:nmeltQ+nmetal,
    GradQ(jj)=(T2Q(jj)-T1Q(jj))/dt;        %cooling rate water bath
    TempQ(jj)=T1Q(jj);

    GradA(jj)=(T2A(jj)-T1A(jj))/dt;        %cooling rate air cooled
    TempA(jj)=T1A(jj);
end

GradientsQ(ii,:)=GradQ;GradientsA(ii,:)=GradA;
TemperaturesQ(ii,:)=TempQ;TemperaturesA(ii,:)=TempA;

end
t=(1:ii)*dt;
%%

for kk=1:140,
lowerQL= find(TemperaturesQ(:,kk)<= Tliquidus,1,'first');
lowerAL= find(TemperaturesA(:,kk)<= Tliquidus,1,'first');
CoolingRateQL(kk)=GradientsQ(lowerQL,kk);
CoolingRateAL(kk)=GradientsA(lowerAL,kk);
lowerQM= find(TemperaturesQ(:,kk)<= Tmiddle,1,'first');
lowerAM= find(TemperaturesA(:,kk)<= Tmiddle,1,'first');
CoolingRateQM(kk)=GradientsQ(lowerQM,kk);
CoolingRateAM(kk)=GradientsA(lowerAM,kk);
lowerQS= find(TemperaturesQ(:,kk)<= Tsolidus,1,'first');
lowerAS= find(TemperaturesA(:,kk)<= Tsolidus,1,'first');

```

```

CoolingRateQS(kk)=GradientsQ(lowerQS,kk);
CoolingRateAS(kk)=GradientsA(lowerAS,kk);
% PreQS= find(TemperaturesQ(:,kk)<= T620,1,'first');
% PreAS= find(TemperaturesA(:,kk)<= T620,1,'first');
% CoolingRate620QS(kk)=GradientsQ(PreQS,kk);
% CoolingRate620AS(kk)=GradientsA(PreAS,kk);
end

```

## B.5 Sub functions of the Code

### B.5.1.1 Conductivity GCIron

```

function E=ConductivityGCiron(T)
E=0*T;
i1=T<=800;
i2=T>800;
E(i1)=-0.0141*T(i1) + 45.429;
E(i2) = 0.0171*T(i2) +19.556;

```

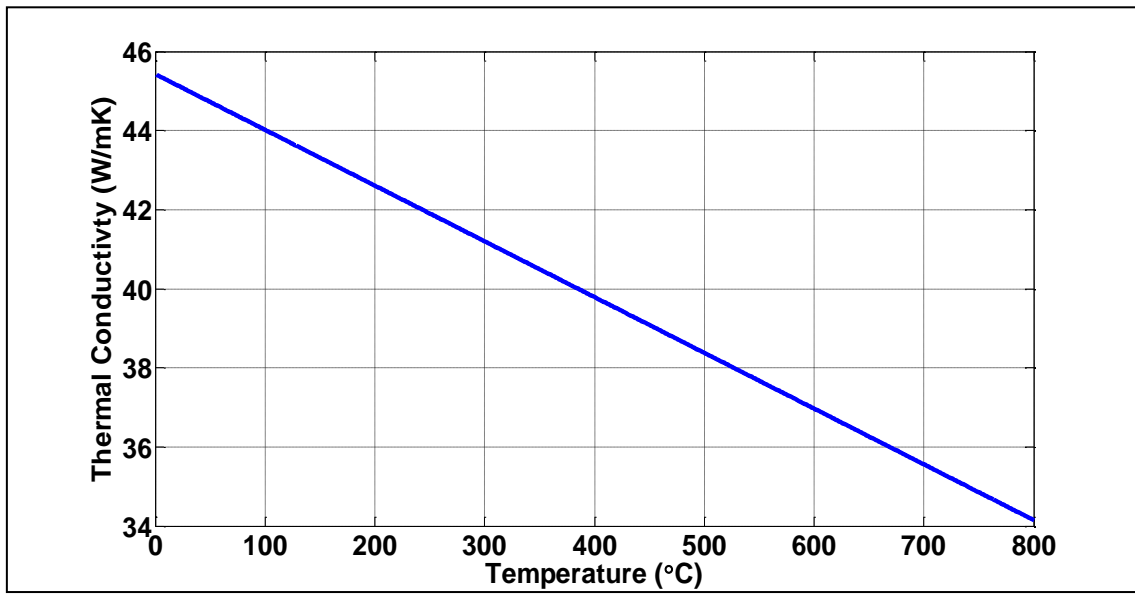


Figure B-3 – Thermal Conductivity of Grey Cast Iron used in the MATLAB code

### B.5.1.2 Conductivity 1102

```

function E=conductivity1102(T)
E=0*T;
i1=T<=452;
i2=T>452 & T<962;
i3=T>=962 & T<=1335;
i4=T>1335;

```

```

E(i1)=8.869;
E(i2)=4e-5*T(i2).^2 - 0.0385*T(i2) + 18.101;
E(i3) = 0.013493333*(T(i3)-961) + 18.04;
E(i4)=(0.0097*T(i4)+10.139);

```

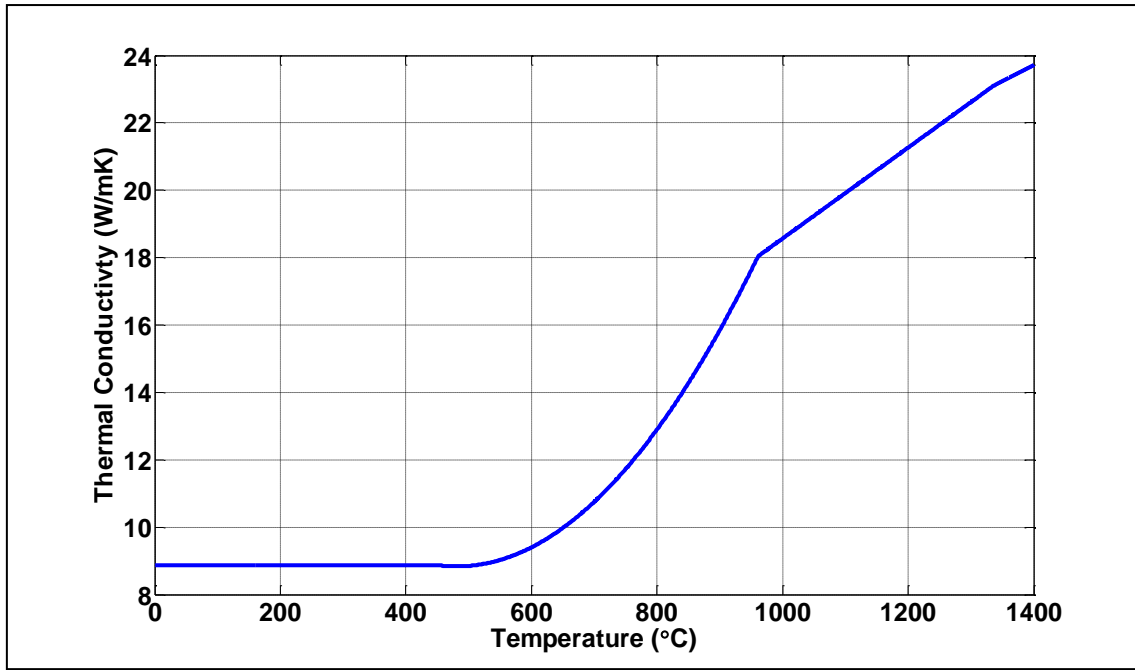


Figure B-4 – Thermal Conductivity of XD1102 used in the MATLAB code

### B.5.1.3 Enthalpy of GCIron

```

function E=enthalpyGCiron(T)
%extrapolated enthalpy back from 797 using an intercept of zero
E=0*T;
i1=T<1149;
i2=T>=1149 & T<=1165;
i3=T>1165;
E(i1)=(0.6115*T(i1))*1000;
E(i3)=(0.8198*T(i3) + 64.523)*1000;
E(i2) = (15.937*T(i2) -17593)*1000;

```

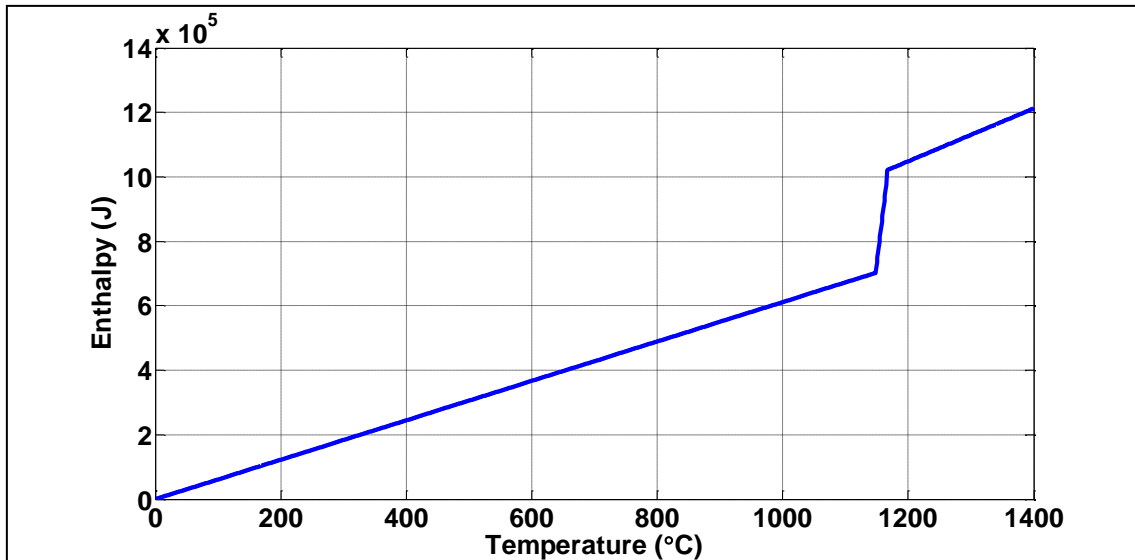


Figure B-5 – Enthalpy of Grey Cast Iron used in the MATLAB code

#### B.5.1.4 Enthalpy of XD1102

```
function E=enthalpy1102(T)
E=0*T;
i1=T<1172;
i2=T>=1172 & T<=1322;
i3=T>1322;
E(i1)=(0.7895*T(i1)-321.19)*1000;
E(i2) = (1.911184211*(T(i2) - 1171)+6.033e2) *1000;
E(i3)=(0.7741*T(i3)-130.33)*1000;
```

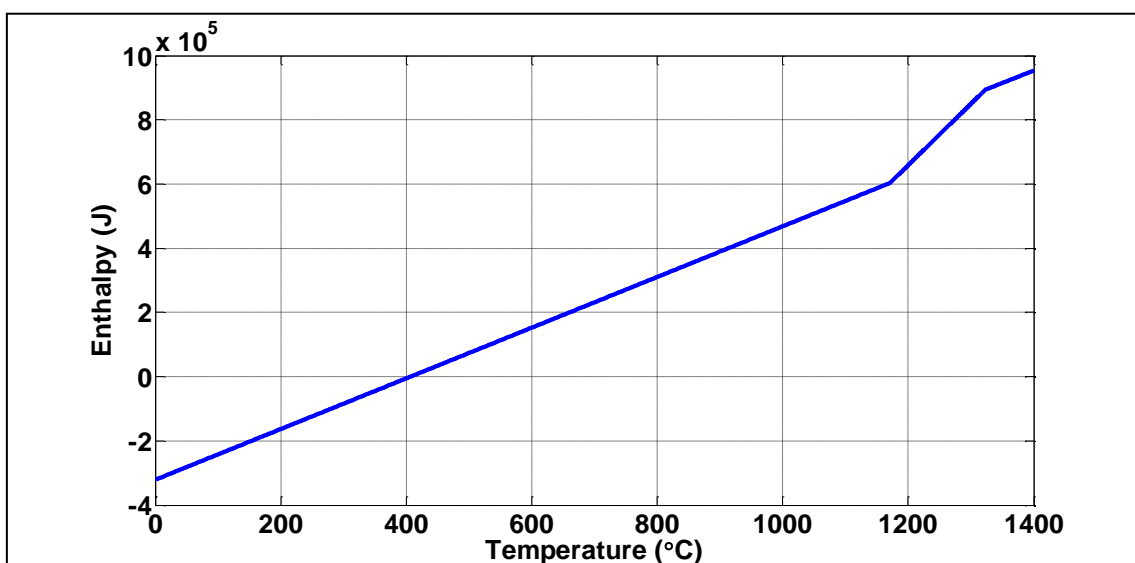




Figure B-6 – enthalpy of XD1102 used in the MATLAB code

### B.5.1.5 Emissivity of GCiron

```
function E=EmissivityGCiron(T)
E=0*T;
i1=T<600;
i2=T>=600;
E(i1)=- 0.0001666667*T(i1) + 0.9;
E(i2) = 0.8;
```

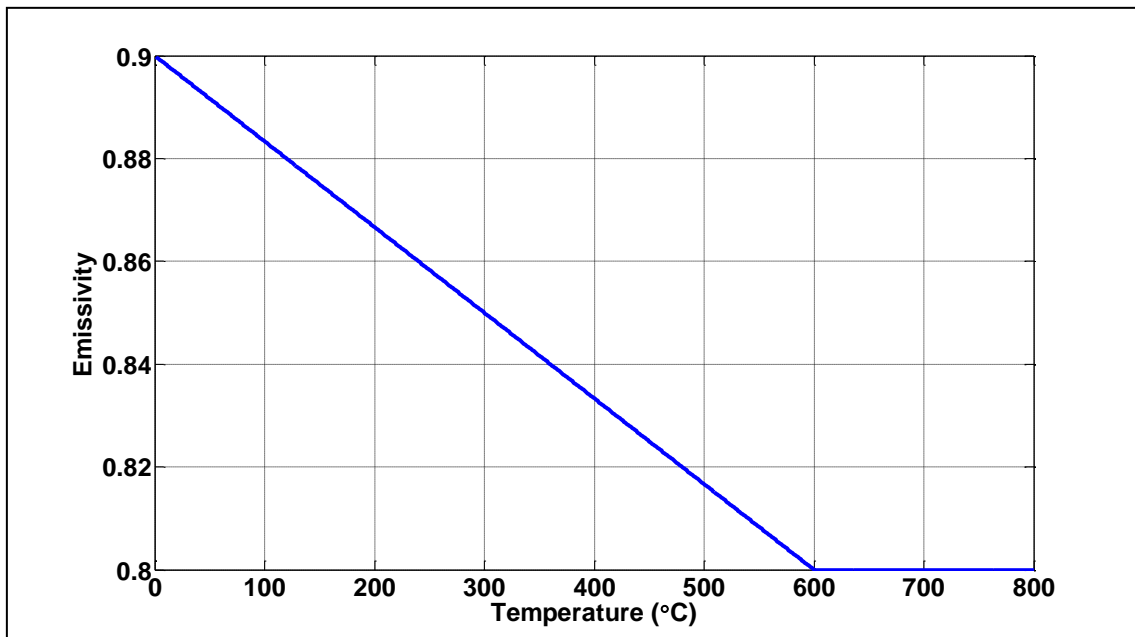


Figure B-7 – Emissivity of Grey Cast Iron used in the MATLAB code

### B.5.1.6 Emissivity of 1102

This was derived experimentally as described in section 4.6.

```
function E=Emissivity1102(T)
E=0*T;
i1=T<600;
i2=T>=600;
E(i1)=- 0.0001666667*T(i1) + 0.9;
E(i2) = 0.8;
```

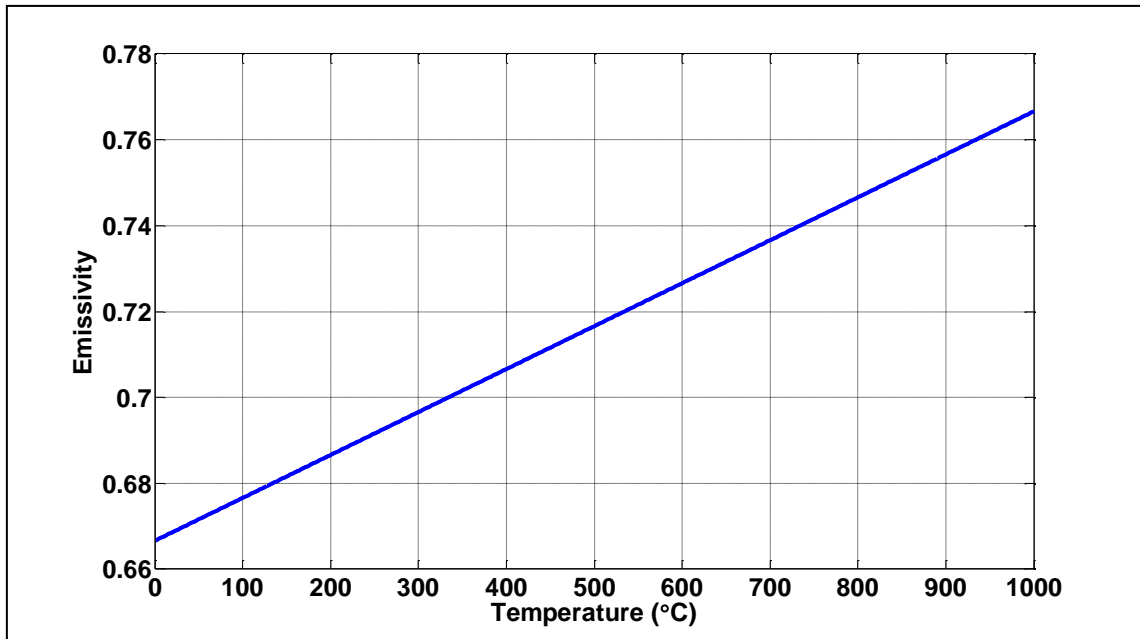


Figure B-8 – Emissivity of XD1102 used in the MATLAB code

### B.5.1.7 Conductivity of Air

```
function E=conductivityAir(T)
E=0*T;
E=(1.527E-11*(T.^3))-(4.8574E-8*(T.^2))+(1.0184E-4*T)-0.00039333;
```

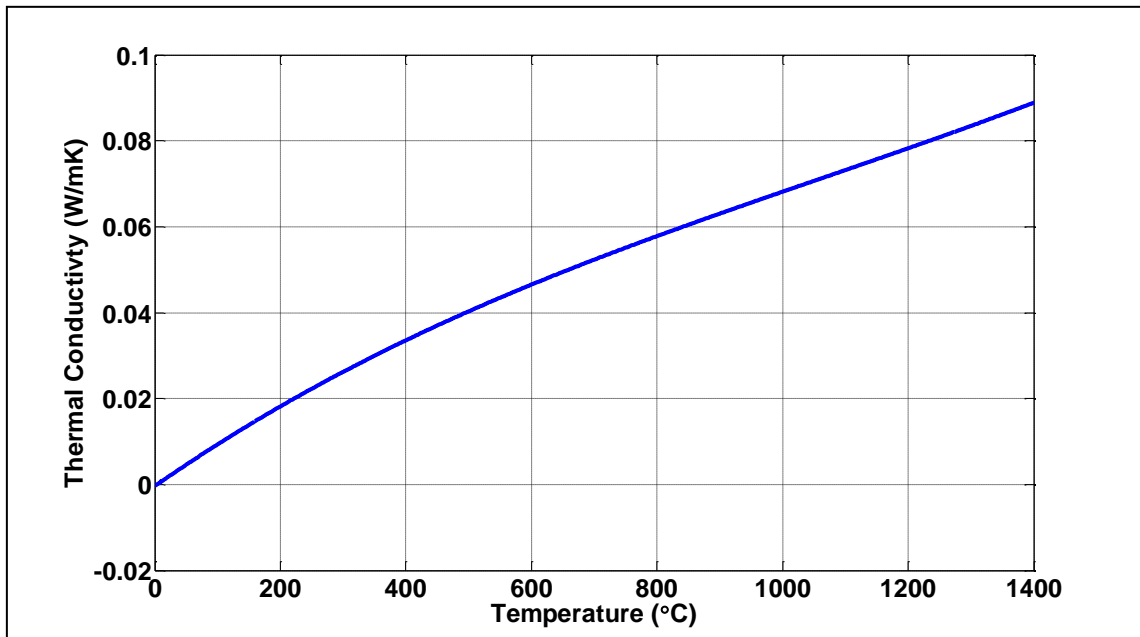


Figure B-9 – Conductivity of air used in the MATLAB code

### B.5.1.8 Heat Transfer Coefficient Water

The heat transfer coefficient for a water quench varies dramatically with temperature from the liquid turning into steam and effectively creating a gas pocket lowering the HTC.

```
function E=htcQ(T)
E=0*T;
i1=T<377;
i2=T>=377;
E(i1) = 0.00035233*T(i1).^3 - 0.37367513*T(i1).^2 +
97.2668809*T(i1);
E(i2)=0.00588284*T(i2).^2 - 11.10548630*T(i2) + 5550.59848305;
```

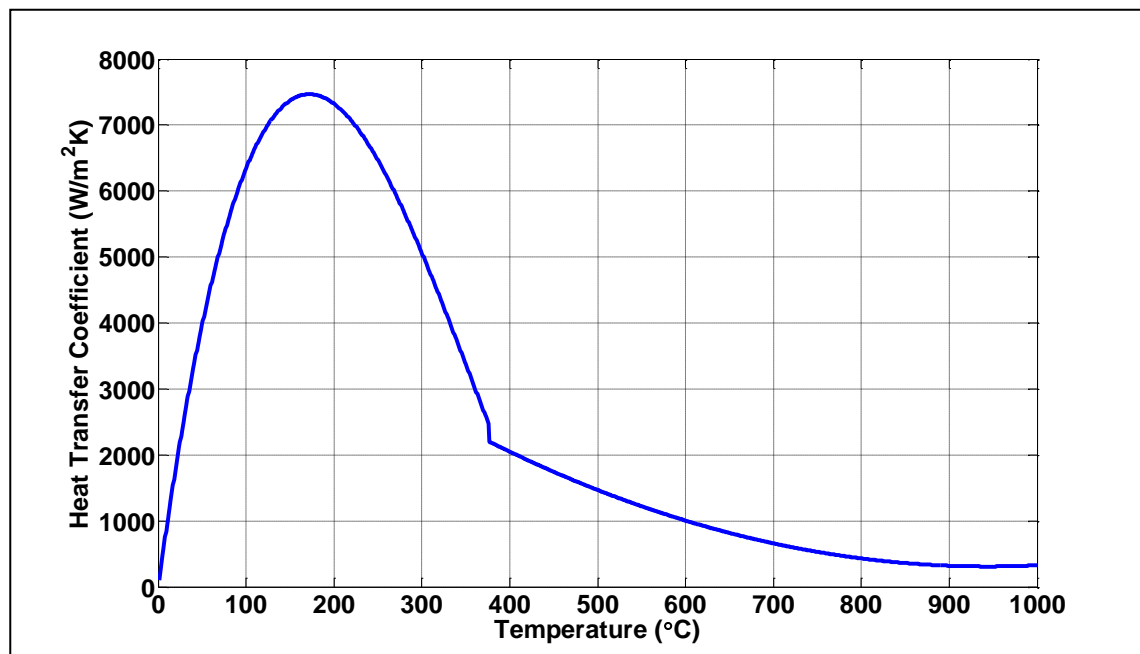


Figure B-10 – Heat Transfer Coefficient during water quenching used in the MATLAB code

### B.5.1.9 Decimate – (Supplied by Dr R M Ward)

```
function b=decimate(a,n)
%function b=decimate(a,n)
% decimates vector / column matrix 'a' in sections of 'n', taking
averages

[nra,nca]=size(a); % how big is the matrix?

if nca>nra, a=a';end % if it's wider than tall it's probably a mistake
so transpose it
[nr,nc]=size(a);
```

```

l1 = floor(nr/n); %how many rows will there be after decimation by
'n'?
b=zeros(l1,nc); % pre-allocate an empty matrix to put them into, to
save calling the memory manager too often
for i=1:l1,
    b(i,:) = mean(a( ((i-1)*n+1):(i*n),: )); % put the mean of each
chunk of data into an output row
end

if nca>nra, a=a';end % if we transposed it, swap it back

```

## B.6 Possible Extension to the MATLAB Code

An extension to the MATLAB code could include the carbon layer which lines the inner surface of the moulds through the yellow sooty flame pre-heat. This would further retard the heat transfer from the melt and through to the mould (Figure B-11).

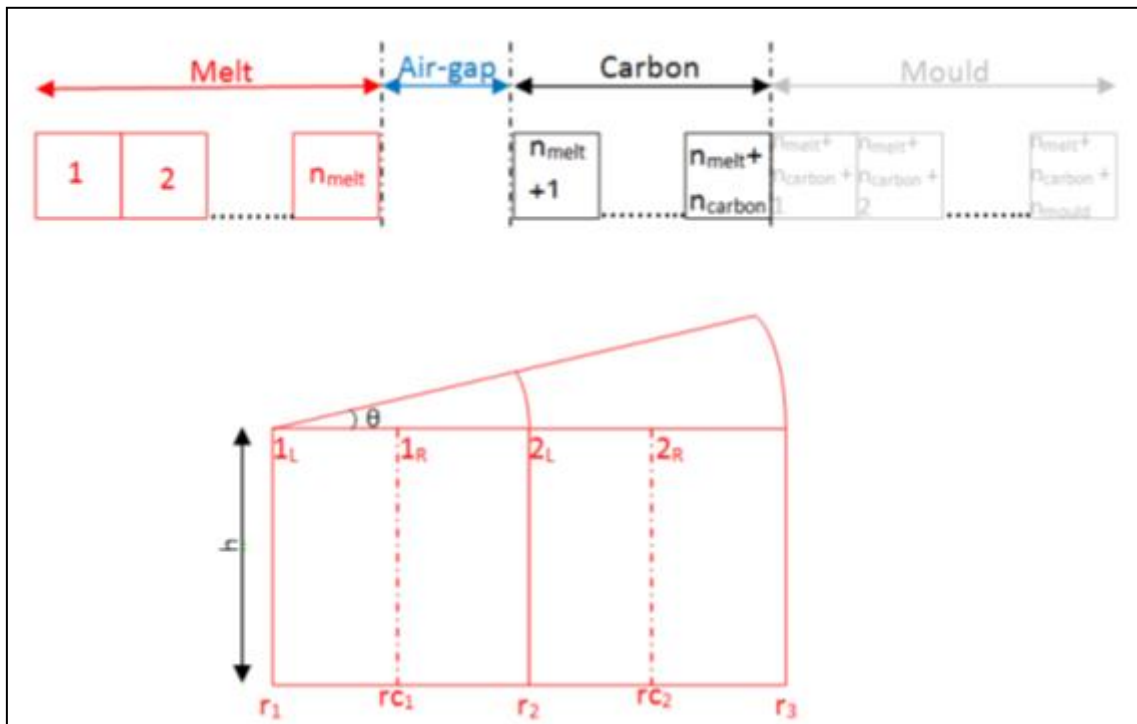


Figure B-11 – 1-D finite difference model including the air-gap formation and the carbon layer

## Appendix C. ProCAST Run Parameters

Please refer to the ProCAST user manual for a description of the parameters.

COM ** None **	TPROF 1	TMODS 2.00e+000	TBRELAX 1.00e+000
TUNITS 2	VPROF 0	TMODR 5.00e-001	MRELAX 1.0e+000
VUNITS 1	HEAD_ON 0	CONVT 1	ADVECTW 0.0e+000
PUNITS 5	WSHEAR 2	1.00000e+000	BETA 5.00e-001
QUNITS 1	PINLET 0	CONVV 5.00e-002	MLUMP 1.00e+000
INILEV 0	PENETRATE 0	CONVS 1.00e-002	CLUMP 1.00e+000
NSTEP 100000	SDEBUG 1	CONVTOL 1.00e-004	GAPMOD 1
NCYCLE 0	PRNLEV 0	COURANT 1.00e+002	TRI2QUAD 1
NRSTAR 5	NPRFR 1	LVSURF 1.00e+000	GATEFEED 0
TFREQ 2	RDEBUG 0	MACROFS 7.00e-001	GATENODE 0
VFREQ 100	CGSQ 0	PIPEFS 0.0e+000	GATEFS 0.9500
QFREQ 2	DIAG 1024	FEEDLEN 1 5.00e-003	THMODULE 0
SFREQ 2	LUFAC 1	MOLDRIG 1.00e+000	HOTSPOTS 0
RFREQ 1	NEWTONR 0	MOBILE 3.00e-001	ACCORDION 0
EFREQ 1	LINSRC 0	PLIMIT 1 1.00e+025	FREESFBAL 0
FFREQ 1	USER 0	PREF 1 0.00e+000	JUNCTION 0
PFREQ 50	POROS 1	FLOWDEL 1 1.0e+020	RELVEL 0
SCALC 2	ENCLID 0	TSOFF 1 0.0e+000	USERHO 1
THERMAL 1	EMITER 100	CINIT 3.0e-001	CRITFS 5.00e-001
MICRO 0	BEM 0	CMU 9.000e-002	AVEPEN 1 1.00e-004
TTTMIC 0	ISEED 0	SIGMAK 1.00e+000	FOAMHTC 0.0200
MICCP 0	DT 1 1.00e-003	SIGMAE 1.30e+000	FOAMHTCMAX
FLOW 1	DTMAX 1	CONE 1.440e+000	0.2500
STRESS 1	2.00e+000	CTWO 1.920e+000	BURNZONE 1.00
EM 0	DTMAXFILL 1	KAPPA 4.000e-001	GASFRAC 0.10
TURB 0	2.00e+0	VFTIME 1 0.00e+000	TOFRSF2 1.00e+020
HIVISC 0	TFINAL 1 4.015e+3	VFDISP 1 0.00e+000	MLDUPDT 1
COMPRES 0	TENDFILL 1 0.0e+0	VFLIM 0.00e+000	TOPFILL 0
COUPLED 0	TSTOP 1 2.73e+002	EPTOL 8.00e-001	CYCLESF 0
AVEPROP 0	TCYCLE 1 0.0e+0	ANGTOL 4.50e+001	ENDFILL 1.00
GAS 0	TFILL 1 1.0e+0	PENALTY 1.00e-002	COLDSHUT 1
FREESF 1	TOPEN 1 0.0e+0	CFREQ 0.00e+000	
FREESFOPT 1	TCLOSE 1 0.0e+0	CELLSZ 1 1.00e-003	
NNEWTON 0	TEJECT 1 0.0e+0	TRELAX 1.00e+000	
WALLF 8.00000e-001	TBSPRAY 1 0.0e+0	CRELAX 1.00e+000	
	TESPRAY 1 0.e+0	PRELAX 1.00e+000	

# REFERENCES

- [http://www.micro-epsilon.co.uk/displacement-position-sensors/laser-sensor/optoNCDT\\_1710-1000/index.html](http://www.micro-epsilon.co.uk/displacement-position-sensors/laser-sensor/optoNCDT_1710-1000/index.html).
- ARUNKUMAR, S., SREENIVAS RAO, K. V. & PRASANNA KUMAR, T. S. 2008. Spatial variation of heat flux at the metal–mold interface due to mold filling effects in gravity die-casting. *International Journal of Heat and Mass Transfer*, 51, 2676-2685.
- BAUSER, M. & SIEGERT, K. 2006. *Extrusion: Second Edition*, ASM International.
- BECKERMANN, C. 1997. Modeling segregation and grain structure development in equiaxed solidification with convection. *JOM*, 49, 13-17.
- BENSCH, M., SATO, A., WARNKEN, N., AFFELDT, E., REED, R. & GLATZEL, U. 2012. Modelling of high temperature oxidation of alumina-forming single-crystal nickel-base superalloys. *Acta Materialia*, 60, 5468-5480.
- BOUSE, G. 1989. Application of a modified phase diagram to the production of cast alloy 718 components. *Superalloy*, 718, 69-77.
- BRAMFITT, B. L. & BENSCOTER, A. O. 2001. *Metallographer's Guide: Practice and Procedures for Irons and Steels*, ASM International.
- BROOKS, J. & BRIDGES, P. 1988. Metallurgical stability of inconel alloy 718. *Superalloys*, 88, 33-42.
- BROUCARET, S., MICHRAFY, A. & DOUR, G. 2001. Heat transfer and thermo-mechanical stresses in a gravity casting die: Influence of process parameters. *Journal of Materials Processing Technology*, 110, 211-217.
- CAMPBELL, J. 2006. Entrainment defects. *Materials Science and Technology*, 22, 127-145.
- CAMPBELL, J. 2011a. Chapter 2 - Entrainment. *Complete Casting Handbook*. Oxford: Butterworth-Heinemann.
- CAMPBELL, J. 2011b. Chapter 5 - Solidification Structure. *Complete Casting Handbook*. Oxford: Butterworth-Heinemann.
- CAMPBELL, J. & TIRYAKIOĞLU, M. 2012. Bifilm defects in Ni-based alloy castings. *Metallurgical and Materials Transactions B*, 43, 902-914.
- CHANG, K.-M., LAI, H.-J. & HWANG, J.-Y. 1994. Existence of Laves phase in Nb-hardened superalloys. *Superalloys 718, 625, 706 and various derivatives*, 683-694.
- CHILTON, R. A. 2002. *Experimental Study and Modelling of the Cell-dendrite Transition*, University of Oxford.
- CIESLAK, M., KNOROVSKY, G., HEADLEY, T. & ROMIG JR, A. 1989. The solidification metallurgy of alloy 718 and other Nb-containing superalloys. *Superalloy*, 718, 59-68.
- COATES, B. & ARGYROPOULOS, S. 2007. The Effects of Surface Roughness and Metal Temperature on the Heat-Transfer Coefficient at the Metal Mold Interface. *Metallurgical and Materials Transactions B*, 38, 243-255.
- COCKS, A. 1985. The nucleation and growth of voids in a material containing a distribution of grain-boundary particles. *Acta Metallurgica*, 33, 129-137.
- COX, M., WICKINS, M., KUANG, J., HARDING, R. & CAMPBELL, J. 2000. Effect of top and bottom filling on reliability of investment castings in Al, Fe, and Ni based alloys. *Materials Science and Technology*, 16, 1445-1452.

- CROLL, J. E. & WALLWORK, G. R. 1972. The high-temperature oxidation of iron-chromium-nickel alloys containing 0–30% chromium. *Oxidation of Metals*, 4, 121-140.
- DAI, H. 2009. *A Study of Solidification Structure Evolution during Investment Casting of Ni-based Superalloy for Aero-Engine Turbine Blades*. University of Leicester.
- DANTZIG, J. A. & RAPPAZ, M. 2009. *Solidification*, EPFL press.
- DAVIS, J. R. 1997. *ASM specialty handbook: heat-resistant materials*, ASM International.
- DISPINAR, D. & CAMPBELL, J. 2011. Porosity, hydrogen and bifilm content in Al alloy castings. *Materials Science and Engineering: A*, 528, 3860-3865.
- DIVANDARI, M. & CAMPBELL, J. 2001. Mechanisms of bubble damage in castings. *Department of Metallurgy and Materials*.
- DONACHIE, M. J. 2002. *Superalloys: a technical guide*, ASM international.
- DONG, Y., BU, K., DOU, Y. & ZHANG, D. 2011. Determination of interfacial heat-transfer coefficient during investment-casting process of single-crystal blades. *Journal of Materials Processing Technology*, 211, 2123-2131.
- DURVILLE, P. H. G. 1914. An Improved Process of Casting Ingots of Metals and Alloys and Apparatus therefor. *GB191323719 (A)*.
- ELLINGHAM, H. 1944. Reducibility of oxides and sulphides in metallurgical processes. *Journal of the Society of Chemical Industry*, 63, 125-134.
- EVANS, H. E., LI, H. Y. & BOWEN, P. 2013. A mechanism for stress-aided grain boundary oxidation ahead of cracks. *Scripta Materialia*, 69, 179-182.
- FERREIRA, I. L., SPINELLI, J. E., PIRES, J. C. & GARCIA, A. 2005. The effect of melt temperature profile on the transient metal/mold heat transfer coefficient during solidification. *Materials Science and Engineering: A*, 408, 317-325.
- FLEMINGS, M. C. 1974. *Solidification Processing*, McGraw-Hill.
- FLOREEN, S., FUCHS, G. E. & YANG, W. J. The metallurgy of alloy 625.
- FU, P. X., KANG, X. H., MA, Y. C., LIU, K., LI, D. Z. & LI, Y. Y. 2008. Centrifugal casting of TiAl exhaust valves. *Intermetallics*, 16, 130-138.
- GEDDES, B., LEON, H. & HUANG, X. 2010. *Superalloys: alloying and performance*, Asm International.
- GORDINE, J. Welding of inconel 718.
- GRIFFITHS, W. D. 1999. The heat-transfer coefficient during the unidirectional solidification of an Al-Si alloy casting. *Metallurgical and Materials Transactions B*, 30, 473-482.
- GUNASEGARAM, D. R. & NGUYEN, T. T. 2006. Effect of cooling rate on air gap formation in aluminium alloy permanent mould casting. *International Journal of Cast Metals Research*, 19, 116-122.
- HANSEN, N. 2004. Hall–Petch relation and boundary strengthening. *Scripta Materialia*, 51, 801-806.
- HARDING, R., WICKINS, M., WANG, H., DJAMBAZOV, G. & PERICLEOUS, K. 2011. Development of a turbulence-free casting technique for titanium aluminides. *Intermetallics*, 19, 805-813.
- HASAN, H., PEET, M., JALIL, J. & BHADESHIA, H. 2011. Heat transfer coefficients during quenching of steels. *Heat and mass transfer*, 47, 315-321.
- HAYNES, W. M. 2012-2013. *CRC Handbook of Chemistry and Physics*.
- HECK, K. 1994. The Time-Temperature-Transformation Behavior of Alloy 706. *Superalloys 718, 625, 706 and various derivatives*, 393-404.

- HERLACH, D. M. 2006. *Solidification and Crystallization*, Wiley.
- HO, K. & PEHLKE, R. 1985. Metal-Mold interfacial heat transfer. *Metallurgical Transactions B*, 16, 585-594.
- HO, K. & PEHLKE, R. D. 1984. Mechanisms of Heat Transfer at a Metal-Mold Interface. *Americam Foundrymen's Society*, 92, 587-598.
- HU, P., YING, L., LI, Y. & LIAO, Z. Effect of Oxide Scale on Temperature-dependent Interfacial Heat Transfer in Hot Stamping Process. *Journal of Materials Processing Technology*.
- HULL, D. 1999. *Fractography: observing, measuring and interpreting fracture surface topography*, Cambridge University Press.
- K. L. NARAYANA, S. V. R. P. V. K. 2010. *Production Technology*, I.K. International Publishing House Pvt. Limited.
- KIM, D.-J., KIM, Y.-S., KIM, S.-H., KIM, J.-H., YANG, J.-H., LEE, Y.-W. & KIM, H.-S. 2006. The linear thermal expansion and the thermal diffusivity measurements for near-stoichiometric (U, Ce)O<sub>2</sub> solid solutions. *Thermochimica Acta*, 441, 127-131.
- KIM, T.-G. & LEE, Z.-H. 1997. Time-varying heat transfer coefficients between tube-shaped casting and metal mold. *International Journal of Heat and Mass Transfer*, 40, 3513-3525.
- KIRMAN, I. & WARRINGTON, D. H. 1970. The precipitation of Ni<sub>3</sub>Nb phases in a Ni-Fe-Cr-Nb alloy. *Metallurgical Transactions*, 1, 2667-2675.
- KONRAD, C. H., BRUNNER, M., KYRGYZBAEV, K., VÖLKL, R. & GLATZEL, U. 2011. Determination of heat transfer coefficient and ceramic mold material parameters for alloy IN738LC investment castings. *Journal of Materials Processing Technology*, 211, 181-186.
- KRON, J., BELLET, M., LUDWIG, A., PUSTAL, B., WENDT, J. & FREDRIKSSON, H. 2004. A Comparison of Numerical Simulation Models for Predicting Temperature in Solidification Analysis with Reference to Air Gap Formation. *International journal Cast Metals Research*, 17, 295-310.
- KRON, J. & FREDRIKSSON, H. 2005. Measurements and modelling of air gap formation in Cu-based alloys. *International Journal of Cast Metals Research*, 18, 21-28.
- KRON, J., LAGERSTEDT, A. & FREDRIKSSON, H. 2005. Measurements and modelling of air gap formation in aluminium based alloys. *International Journal of Cast Metals Research*, 18, 29-40.
- KURT, L. & HELMUT, S. 1976. Extrusion. *American Society for metals*.
- KURZ, W. & FISHER, D. J. 1998. *Fundamentals of solidification*, Trans Tech Publications.
- LAGERSTEDT, A., KRON, J., YOSEF, F. & FREDRIKSSON, H. 2005. Measurements and modeling of air gap formation in iron-base alloys. *Materials Science and Engineering: A*, 413-414, 44-51.
- LI, D., CAMPBELL, J. & LI, Y. 2004. Filling system for investment cast Ni-base turbine blades. *Journal of Materials Processing Technology*, 148, 310-316.
- LUCAS JR, M. 1970. The Weld Heat Affected Zone in Nickel Base Alloy 718. *Welding Journal*, 46s.
- MATYSIAK, H., ZAGORSKA, M., ANDERSSON, J., BALKOWIEC, A., CYGAN, R., RASINSKI, M., PISAREK, M., ANDRZEJCZUK, M., KUBIAK, K. & KURZYDŁOWSKI, K. J. 2013. Microstructure of Haynes® 282® Superalloy



- after Vacuum Induction Melting and Investment Casting of Thin-Walled Components. *Materials*, 6, 5016-5037.
- MINISANDRAM, R. S., JACKMAN, L. A., ADASCZIK, C. B. & SHIVPURI, R. Thermal cracking of large-diameter 706 ingots.
- MITCHELL, A., SCHMALZ, A., SCHVEZOV, C. & COCKROFT, S. 1994. The precipitation of primary Carbides in Alloy 718. *Superalloys*, 718, 625-706.
- NISHIDA, Y., DROSTE, W. & ENGLER, S. 1986. The air-gap formation process at the casting-mold interface and the heat transfer mechanism through the gap. *Metallurgical Transactions B*, 17, 833-844.
- NOVOVIC, D., DEWES, R. C., ASPINWALL, D. K., VOICE, W. & BOWEN, P. 2004. The effect of machined topography and integrity on fatigue life. *International Journal of Machine Tools and Manufacture*, 44, 125-134.
- PAN, T. J., LI, Y. S., YANG, Q., FENG, R. F. & HIROSE, A. 2011. Internal oxidation and phase transformations of multi-phase Fe–Ni–Al and Fe–Ni–Al–Cr alloys induced by KCl corrosion. *Corrosion Science*, 53, 2115-2121.
- PELLOUX, R. M. & STOLOFF, N. Creep-fatigue-environment Interactions: Proceedings of a Symposium. 1980. American Society of Civil Engineers.
- PETTIT, F., MEIER, G., GELL, M., KARTOVICH, C., BRICKNEL, R., KENT, W. & RADOVICH, J. 1984. Oxidation and hot corrosion of superalloys. *The Metal Society AIME, Warrendale, PA*, 651.
- PICKERING, F. 1976. Physical metallurgy of stainless steel developments.
- PINEAU, A. & ANTOLOVICH, S. D. 2009. High temperature fatigue of nickel-base superalloys—a review with special emphasis on deformation modes and oxidation. *Engineering Failure Analysis*, 16, 2668-2697.
- RADHAKRISHNA, C. & RAO, K. P. 1997. The formation and control of Laves phase in superalloy 718 welds. *Journal of Materials Science*, 32, 1977-1984.
- RASHID, A. & CAMPBELL, J. 2004. Oxide defects in a vacuum investment-cast Ni-based turbine blade. *Metallurgical and Materials Transactions A*, 35, 2063-2071.
- REED, R. C. 2006. *The superalloys*, Cambridge Univ. Press.
- REED, R. C. & RAE, C. M. F. 2014. 22 - Physical Metallurgy of the Nickel-Based Superalloys. In: HONO, D. E. L. (ed.) *Physical Metallurgy (Fifth Edition)*. Oxford: Elsevier.
- SAHA, P. K. 2000. *Aluminum extrusion technology*, Asm International.
- ŞAHİN, H. M., KOCATEPE, K., KAYIKCI, R. & AKAR, N. 2006. Determination of unidirectional heat transfer coefficient during unsteady-state solidification at metal casting–chill interface. *Energy Conversion and Management*, 47, 19-34.
- SANTOS, C. A., QUARESMA, J. M. V. & GARCIA, A. 2001. Determination of transient interfacial heat transfer coefficients in chill mold castings. *Journal of Alloys and Compounds*, 319, 174-186.
- SCHILKE, P. W., PEPE, J. & SCHWANT, R. C. 1994. Alloy 706 metallurgy and turbine wheel application. *Superalloys*, 718, 1.
- SCHIRRA, J., CALESS, R. & HATALA, R. 1991. The effect of Laves phase on the mechanical properties of wrought and cast+ HIP inconel 718. *Superalloys 718, 625, 706 and various derivatives*, 375-388.
- SCOTT, C. G., RIGA, A. T. & HONG, H. 1995. The erosion-corrosion of nickel-base diesel engine exhaust valves. *Wear*, 181-183, 485-494.

- SHINGLEDECKER, J. P. & PHARR, G. M. 2012. The Role of Eta Phase Formation on the Creep Strength and Ductility of INCONEL Alloy 740 at 1023 K (750° C). *Metallurgical and Materials Transactions A*, 43, 1902-1910.
- SMITH, F. 1999. *Industrial Applications of X-Ray Diffraction*, Taylor & Francis.
- SMITH, G. & PATEL, S. 2005. The role of niobium in wrought precipitation-hardened nickel-base alloys. *Superalloys 718, 625, 706 and various derivatives*.
- SPINELLI, J. E., CHEUNG, N., GOULART, P. R., QUARESMA, J. M. V. & GARCIA, A. 2012. Design of mechanical properties of Al-alloys chill castings based on the metal/mold interfacial heat transfer coefficient. *International Journal of Thermal Sciences*, 51, 145-154.
- STALEY JR, J. T., TIRYAKIOĞLU, M. & CAMPBELL, J. 2007. The effect of hot isostatic pressing (HIP) on the fatigue life of A206-T71 aluminum castings. *Materials Science and Engineering: A*, 465, 136-145.
- STEFANESCU, D. M., COMMITTEE, A. I. H. & METALS, A. S. F. 1988. *Casting - Macrosegregation*, ASM International.
- STEFANESCU, D. M. & RUXANDA, R. 2004. Fundamentals of solidification. *Materials Park, OH: ASM International, 2004.*, 71-92.
- SUN, W., QIN, X., GUO, J., LOU, L. & ZHOU, L. 2015. Thermal stability of primary MC carbide and its influence on the performance of cast Ni-base superalloys. *Materials & Design*, 69, 81-88.
- SWAN, J., WARD, M. & REED, R. C. Determination of the Magnitude of Interfacial Air-Gap and Heat Transfer during Ingot Casting into Permanent Metal Moulds by Numerical and Experimental Techniques. *Materials Science Forum*, 2013. Trans Tech Publ, 276-280.
- TAKEYAMA, M., MATSUO, T., MORITA, S., YAMANAKA, M. & YAMAUCHI, A. 2001. Phase Equilibria Among  $\gamma$ ,  $\text{Ni}_3\text{Nb}$ - $\delta$  and  $\text{Fe}_2\text{Nb}$ - $\epsilon$  Phases in Ni-Nb-Fe and Ni-Nb-Fe-Cr Systems at Elevated Temperatures. *Superalloys 718, 625, 706 and Various Derivatives (2001)*, 333 - 334.
- TAYLOR, M. P., EVANS, H. E., STEKOVIC, S. & HARDY, M. C. 2012. The oxidation characteristics of the nickel-based superalloy, RR1000, at temperatures of 700 900 C. *Materials at High Temperatures*, 29, 145-150.
- THERMO-CALC SOFTWARE, A. Available: <http://www.thermocalc.com/products-services/databases/thermodynamic/>.
- TONG, J., DALBY, S., BYRNE, J., HENDERSON, M. & HARDY, M. 2001. Creep, fatigue and oxidation in crack growth in advanced nickel base superalloys. *International Journal of Fatigue*, 23, 897-902.
- TRINDADE, V., KRUPP, U., WAGENHUBER, P. E. G. & CHRIST, H. J. 2005. Oxidation mechanisms of Cr-containing steels and Ni-base alloys at high-temperatures—. Part I: The different role of alloy grain boundaries. *Materials and Corrosion*, 56, 785-790.
- TROVANT, M. & ARGYROPOLOUS, S. A. 1998. The implementation of a mathematical model to characterize mold metal interface effects in metal casting. *Canadian Metallurgical Quarterly*, 37, 185-196.
- VYNNYCKY, M. 2009. An Asymptotic Model for the Formation and Evolution of Air Gaps in Vertical Continuous Casting. *Proceedings: Mathematical, Physical and Engineering Sciences*, 465, 1617-1644.

- WANG, H., DJAMBAZOV, G., PERICLEOUS, K., HARDING, R. & WICKINS, M. 2011. Modelling the dynamics of the tilt-casting process and the effect of the mould design on the casting quality. *Computers & Fluids*, 42, 92-101.
- WAS, G. 1990. Grain-boundary chemistry and intergranular fracture in austenitic nickel-base alloys-a review. *Corrosion*, 46, 319-330.
- WILMES, S. & ZWICK, G. 2002. Effect of niobium and vanadium as an alloying element in tool steels with high chromium content. *The Use of Tool Steels: Experience and Re-search*, 1, 227-243.
- ZHANG, L., LI, L., JU, H. & ZHU, B. 2010. Inverse identification of interfacial heat transfer coefficient between the casting and metal mold using neural network. *Energy Conversion and Management*, 51, 1898-1904.
- ZHAO, K., LOU, L. H., MA, Y. H. & HU, Z. Q. 2008. Effect of minor niobium addition on microstructure of a nickel-base directionally solidified superalloy. *Materials Science and Engineering: A*, 476, 372-377.
- ZHI-PENG, G., SHOU-MEI, X., BAI-CHENG, L., LI, M. & ALLISON, J. 2008. Determination of the heat transfer coefficient at metal–die interface of high pressure die casting process of AM50 alloy. *International Journal of Heat and Mass Transfer*, 51, 6032-6038.
- ZHU, Y., ZHU, Z., XIANG, Z., YIN, Z., WU, Z. & YAN, W. 2009. Microstructural evolution in 4Cr10Si2Mo at the 4Cr10Si2Mo/Nimonic 80A weld joint by inertia friction welding. *Journal of Alloys and Compounds*, 476, 341-347.